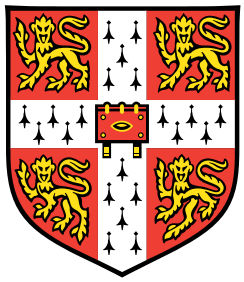

University of Cambridge
Institute of Astronomy

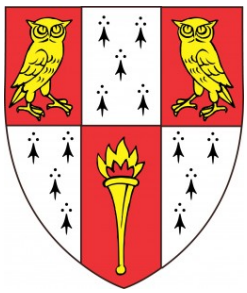

A dissertation submitted to the
University of Cambridge for the degree
of Doctor of Philosophy

The effect of wide-orbit planets on inner planetary systems and debris

Matthew James Read
Hughes Hall College

Submitted to the Board of Graduate Studies
March 2018

Under the Supervision of
Prof. Mark C. Wyatt
Dr Grant M. Kennedy

The Effect of Wide-Orbit Planets on Inner Planetary Systems and Debris

Matthew James Read

SUMMARY

Planetary systems around other stars have been observed to be far more diverse than what would be expected from the example of the Solar System. Exoplanets have been detected with a wide range of sizes and separations from the host star, with a range of orbital properties including large eccentricities and small inter-planet mutual inclinations. How representative these planetary systems are, however, is unclear due to detection techniques being more sensitive to planets on close orbits around the host star. It is possible therefore that a population of wide-orbit planets could be present in these systems and be evading detection. These planets may play a significant role in forming and shaping planetary systems, resulting in the architecture that is observed today.

Currently, one of the major ways of inferring the presence of wide-orbit planets, besides directly detecting them, is to consider the dynamical impact they would have on known planets. In the first part of this thesis I consider how the eccentricities of known planets are affected due to long term dynamical interactions with a wide-orbit planet. I show that the eccentricity of a known planet in a system can periodically be significantly increased due to these interactions, provided that there are a total of two planets in the system. For systems with multiple known planets I show that the inner planets can protect each other against long term eccentricity perturbations from a wide-orbit planet. Following on from this investigation, I show how the inclinations of planets are affected due to long term interactions with a wide-orbit planet. Specifically, I consider how this interaction affects the probability that planetary systems are observed to transit. I find that the presence of wide-orbit planets in transiting planetary systems can help explain the so-called 'Kepler-Dichotomy' which describes the apparent excess of observed single transiting systems compared with multi-planet transiting systems.

Wide-orbit planets do not just dynamically interact with other planets in a system but also with small debris type bodies, akin to the Asteroid and Kuiper belts in the Solar System. In the second half of this thesis, I consider the planetary system HR8799 which is known to host four planets and two populations of debris which lie both internally and externally to the known planets. I find, through suites of N-body simulations, that a hypothetical planet in HR8799 sculpts an outer debris population that agrees more strongly with observations, compared with what would be expected by considering the known planets in isolation.

Finally, for the last part of this thesis, I describe a survey that is looking to observe wide-orbit planets in close-by planetary systems directly. The observations and analysis for this survey is currently on-going, however I show preliminary results including systems with and without potential companion detections.

DECLARATION OF ORIGINALITY

I, Matthew James Read, declare that this thesis entitled *'The effect of wide-orbit planets on inner planetary systems and debris',* is the result of my own work and includes nothing which is the outcome of work done in collaboration except as declared below and clearly specified in the text.

This thesis is not substantially the same as any that I have submitted, or, is being concurrently submitted for a degree or diploma or other qualification at the University of Cambridge or any other University or similar institution. I further state that no substantial part of my dissertation has already been submitted, or, is being concurrently submitted for any such degree, diploma or other qualification at the University of Cambridge or any other University or similar institution. This thesis is within the 60,000 word limit set by the Degree Committee of Physics and Chemistry.

Chapters 1 and **2** introduce relevant concepts related to the topic of this thesis and as such, contain little or no original work. Figures are included from the work of other authors in these Chapters, which are clearly referenced in the associated captions. The following parts of this thesis have already been published, or submitted to academic journals:

- **Chapter 3** was adapted from the published work below and was completed in collaboration with the named authors.
  Dynamical Constraints on Outer Planets in Super-Earth Systems
  Read M. J., Wyatt M. C., 2016, MNRAS, 457, 465.
  I thank Mark Wyatt for an initial script used to calculate the secular interaction between objects, from which my own code used in this Chapter is based.

- **Chapter 4** was adapted from the published work below and was completed in collaboration with the named authors.
  Transit Probabilities in Secularly Evolving Planetary Systems
  Read M. J., Wyatt M. C., Triaud A. H. M. J., 2017, MNRAS, 469, 171

- **Chapter 5** was adapted from the published work below and was completed in collaboration with the named authors.
  Shaping HR8799's outer dust belt with an unseen planet
  Read M. J., Wyatt M. C., Marino S., Kennedy G. M., 2018, MNRAS, 475, 4953.
  I thank Mark Booth for providing the ALMA data of HR8799 presented in Booth M. et al., 2016, MNRAS, 460, L10, which is used in this Chapter. I also thank Sebastian Marino for providing the 1σ rms of the noise per beam of the intensity profile of the ALMA data of HR8799.

Chapter 6 contains work I have completed as a primary investigator of an observational survey, and includes my own preliminary analysis of the observations taken. My collaborators for this survey include: L. Mátra, M.C. Wyatt, J. Milli and G.M. Kennedy. None of the results presented in this Chapter have been submitted to, or published in, an academic journal in any form. I thank Luca Mátra for providing a script used to plot the expected detection threshold of the instrument used in this Chapter. I also thank Julien Milli for providing additional scripts related to the calibration and analysis of the observational data.

Matthew James Read
Cambridge, June 13, 2018

Acknowledgements

First and foremost I offer a huge thanks to my primary supervisor Mark Wyatt. Your guidance and patience has been invaluable throughout my time in Cambridge, and I will carry the vast amount you have taught me long into the future. Thank you also for always having a door open to chat about anything and everything, Astronomy related or not. The advice you have given me during these chats has been extremely helpful. I also thank my second supervisor Grant Kennedy for answering so many of my questions during my PhD and devoting so much time in explaining concepts to make everything seem so clear and exciting. Thank you also for always being available to give advice, I am extremely grateful.

I thank Prof. Jim Pringle and Dr. Sasha Hinkley for taking the time to examine this thesis and conduct a viva. I thank also the Science and Technology Facilities Council for funding my PhD and the University of Cambridge for making me feel so welcome.

To my collaborator and friend Julien Milli, thank you for making me feel so at home during my extended visit to ESO in Santiago, Chile. I will never forget the time you devoted to teaching me about everything observational and the time you spent showing me around Chile.

To my fellow PhD cohort I offer my thanks for all the laughs and the opportunity to detach from all things Astronomy when needs be. Special thanks must go to Bjoern, Dominika, Clare and Christina for being such great housemates, I wish you all the very best. My thanks to the other students in H27: Anjali, Nimisha, Seba and Luca, I hope that my next office is full of people that are just as fun to be around. A special thanks especially to Anjali for the support and second pair of eyes.

Finally, I thank my parents for the unwavering support over the years in all aspects of my life. I hope to keep making you proud in everything I do and offer thanks in advance for all the support I know you will give me in the future. I can only offer to repay the debt one day.

Matthew James Read
Cambridge, June 13, 2018

Contents

List of Figures

List of Tables

1

Introduction

Astronomy is unique amongst the sciences in that it seeks to answer some of the most fundamental of questions that have inspired and confounded humanity since its inception: How did life arrive on our planet? How common is the Solar System? Are we alone in the Universe?

The topic of other worlds in the Universe has been the inspiration for countless stories, books and films across the ages. Planets in our own Solar System have been imbued as the representatives of Gods and all manner of mythical beings, cultivating entire cultures from which we descend. Modern day enthusiasm for this subject shows no sign of abating, evident from the lecture halls around the world that become packed with members of the public, both young and old, when a talk discussing our place in the Universe is announced. Practically, research into Astronomy has led to innovations in technologies and perhaps, just as importantly, fostered relationships between countries that transcend the ebb and flow of politics.

The topic of whether other planetary systems exist in the Universe has historically been reserved for largely philosophical debates. Indeed, before the 20th Century these questions were tackled by some of the most well known minds in Astronomy. Aristotle and Copernicus (384-322BC and 1473-1543, respectively) railed against the possibility of large populations of planetary systems in the Universe, while Epicurus (341-270BC) took the opposite opinion, postulating a possible infinite number of planetary systems (see Dick 1996 for a historical review of the postulations regarding the existence of planetary systems). Fast-forward to the middle of the 20th Century and consensus largely pointed to other planetary systems being a rare occurrence (e.g. Jeans 1919; Eddington 1928). Over the last thirty years however, technological advancements for telescopes and software design has led to the spectacular rise of the field of detecting and characterising worlds around alien stars. We are now therefore entering an age where some of the fundamental questions that have eluded humanity for generations are beginning to be answered.

In this thesis I will present my contribution to the understanding of planetary systems outside our own Solar System. I will mainly concentrate on the dynamical effects that

occur between planets in planetary systems and show how this can be used to place constraints on the types of planets that can exist in a given system. Moreover, I will also present an on-going investigation looking to detect planets around other stars directly, providing context to my previously described work. Before describing the work completed during my PhD however, it is first useful to take a step back and describe what is meant by a 'planetary system' and what constituent parts go into making one. I will frame this explanation in the context of the planetary system that we know best: our own Solar System.

1.1 The Host Star

The host star is the most massive object in a planetary system. Indeed, in the Solar System the host star (the Sun) makes up 99.8% of the total mass of the entire system. Stars are defined as being objects massive enough to fuse hydrogen in the core which can occur when an object exceeds $0.08M_{\odot}$, where $M_{\odot}$ is the mass of the Sun. The energy released from this hydrogen fusion results in the star being the most luminous object in a planetary system. For example, in the Solar System the Sun is roughly nine orders of magnitude brighter than the Earth.

Stars are categorized according to a spectral type, which include O, B, A, F, G, K, M, with O-type stars being the most massive and brightest and M-type stars being the least massive and dimmest. Fundamental parameters which define each of the spectral types are given in Table 1.1. The Sun lies roughly in the middle of this spectral classification scheme as a G-type star. The lower the mass of a star, the more abundant it is observed to be in the Galaxy. M-type stars are therefore the most abundant, making up $\sim$ 80% of main sequence stars. This fraction drops significantly to $\sim$ 8% for G-type stars and down to an almost negligible amount for O stars.

How stars form is a complex field of study in Astronomy, but can be boiled down to a general process starting with a large cloud of material which contains both dust and gas. When this cloud reaches a critical density it begins to collapse under self-gravity to form a core of material known as a protostar. As more gas and dust from the surrounding gas cloud accrete onto the protostar, the following contraction causes the protostar's luminosity and temperature to evolve along Hayashi tracks towards the main sequence (Hayashi, 1961; Hayashi & Hoshi, 1961). Stellar winds begin to be produced at the poles of the protostar, with further in-falling material forming a disk preferentially around the equator of the protostar. Once the contraction of the protostar causes the pressure in the core to become high enough, fusion of hydrogen begins and halts further contraction. At this point the protostar is said to have joined the main sequence and is a fully-fledged star with a spectral type detailed above. Moreover, the disk of material which formed around the star

Type	Temperature (K)	Mass ($M_\odot$)	Radius ($R_\odot$)	Luminosity ($L_\odot$)
O	$\geq$30000	$\geq$16	$\geq$6.6	$\geq$30000
B	10000-30000	2.1-16	1.8-6.6	25-30000
A	7500-10000	1.4-2.1	1.4-1.8	5-25
F	6000-7500	1.04-1.4	1.15-1.4	1.5-5
G	5200-6000	0.8-1.04	0.96-1.15	0.6-1.5
K	3700-5200	0.45-0.8	0.7-0.96	0.08-0.6
M	2400-3700	0.08-0.45	$\leq$0.7	$\leq$0.08

Table 1.1 The spectral type classification scheme for stars (Habets & Heintze, 1981).

during formation can survive for long periods of time, eventually becoming the nursery for planet formation.

The properties of a star has stark implications on the characteristics of any objects which orbit it. For example, the energy that is radiated by the host star goes directly into heating orbiting objects, providing a significant contribution to the surface temperature. This can be simply shown through application of the Stefan-Boltzmann Law, which allows for the calculation of the luminosity, or power output of an object. The luminosity of a star using this law is given by

$$L_\star = 4\pi R_\star^2 \sigma_{SB} T_\star^4, \tag{1.1}$$

where L_* is the luminosity of the star, R_* is the radius of the star and T_* its surface temperature. The value $\sigma_{SB} = 5.67 \times 10^{-8} Wm^{-2}K^{-4}$ is the Stefan-Boltzmann constant. Assuming that the radiation from the star is emitted purely radially, then the amount of power, L_{ob}, that will intercept an orbiting object with radius R_{ob} at a distance of D_{ob} is equal to

$$L_{ob} = L_* \frac{\pi R_{ob}^2}{4\pi D_{ob}^2}. \tag{1.2}$$

Assuming also that the object intercepting the stellar radiation absorbs all energy incident upon it and radiates it perfectly (i.e. acts like a blackbody), then $L_{ob} = 4\pi R_{ob}^2 \sigma_{SB} T_{ob}^4$, where T_{ob} is the surface temperature of the object. Equating this to eq. (1.2), one finds that

$$T_{ob} = T_\star \left(\frac{R_\star}{2D_{ob}} \right)^{1/2}. \tag{1.3}$$

For the example of the Sun and the Earth, $T_\star = 5778K$, $R_\star = 1R_\odot$, where $1R_\odot$ is the radius of the Sun, and $D_{ob} = 1au$, where 1au describes the average distance from the Earth to the Sun. From eq. (1.3) the predicted surface temperature of Earth is $\sim$ 278K, very close to the $\sim$ 288K average recorded today, with the extra $\sim$ 10K largely coming from atmospheric heating effects not included in eq. (1.3).

1.2 Planets

The International Astronomical Union defines a planet as being an object that

- has an orbit that is primarily around the host star
- is massive enough to be in hydrostatic equilibrium, implying a 'round' shape
- has cleared its orbit of all other objects which also initially orbited the host star.

In the solar system eight objects fulfil this criterion, with these eight planets orbiting in roughly the same plane on near-circular orbits. The four planets that orbit closest to the Sun:- Mercury, Venus, Earth and Mars (closest to furthest from the Sun respectively)- are known as the terrestrial planets. These planets are primarily rocky bodies, composed of silicates and metals, with thin atmospheres that make up an insignificant percentage of the overall radius of the planet. The terrestrial planets have a total of three moons: one around the Earth and two around Mars. The orbits of these four planets range from 0.387au for Mercury to 1.52au for Mars. Orbits around these distances are of special interest as they either straddle, or are within, the estimated habitable zone of the Sun. The definition of the habitable zone around a star varies throughout the literature (see Kasting & Catling 2003 and references therein), however the most basic definition is simply a region around a star where water can remain in a liquid state on the surface of a planet.

The next two planets which orbit further out from the terrestrial planets are Jupiter and Saturn. These planets have rocky cores enshrouded by vast atmospheres, mainly comprised of hydrogen and helium. Such large atmospheres have resulted in these planets being known as the gas giants. The orbits of the gas giants are at 5.2au and 9.6au for Jupiter and Saturn respectively. Both gas giants are significantly larger and more massive than any of the terrestrial planets, with the most massive gas giant, Jupiter, having a mass 318 times that of the Earth. Together, the gas giants host at least 131 moons. Notably, the four largest of Jupiter's moons:- Io, Europa, Ganymede and Callisto, also known as the Galilean moons-, have sizes of the order of Mars.

Finally, the two planets that orbit furthest from the Sun: Uranus and Neptune are similar to the gas giants in that they are thought to have rocky cores surrounded by large atmospheres. However, these atmospheres have been found to largely consist of water, ammonia and methane type elements rather than hydrogen and helium. As such, both Uranus and Neptune have been coined as the ice giants. These planets orbit far from the Sun, at 19.2au and 30au respectively, with both planets hosting a total of at least 40 moons. Similarly to the gas giants, both the ice giants are significantly larger and more massive than

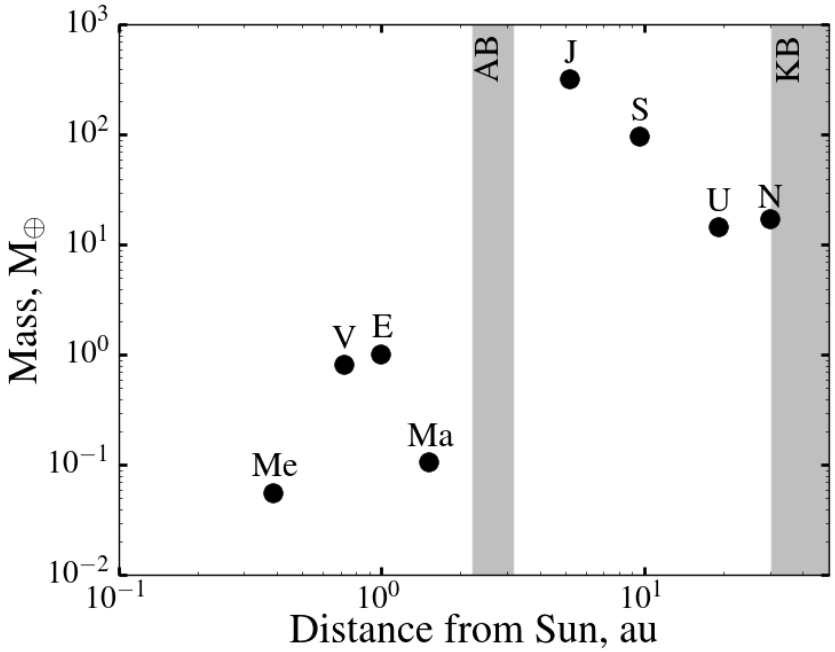

Figure 1.1 Distance from the Sun vs. mass distribution for objects in the Solar System. Each of the planets are referred to by their first letter, apart from Mercury and Mars where the first two letters are used. The Asteroid belt and Kuiper belt are labelled as AB and KB respectively.

the terrestrial planets, with Uranus being 14.5 times more massive than the Earth. Figure 1.1 shows the masses of all the Solar System planets in Earth masses, $M_\oplus$, against the separation from the Sun in units of Earth-Sun separations.

Already therefore, it is evident how diverse planets can be just from the example of the Solar System alone. How representative these planets are of a wider population of exoplanetary systems however is unclear and described later in this section.

1.3 Small Bodies and Debris

In addition to the planets, populations of smaller bodies can also exist in planetary systems. Such populations are thought to be remnant populations of the material that formed in the initial disk around the star, or to be the product of larger bodies that have since been ground down due to repeated collisions with other objects (see Wyatt 2008 and references therein).

In the Solar System populations of small bodies are present in two distinct belts: the Asteroid belt and the Kuiper belt. The Asteroid belt is located between Mars and Jupiter, with objects present between roughly 2.2-3.2au. These objects are thought to range from small pebble (cm) sizes all the way up to larger than 100km, and are largely composed of

rocky-type elements similar to the composition of the terrestrial planets. The largest body in the asteroid belt is Ceres which has a radius of 476km (Thomas et al., 2005), leading to its official designation as a dwarf planet. Despite the huge number of objects present in the Asteroid belt, the total mass is reasonably small at $5.4 \times 10^{-4} M_{\oplus}$ (DeMeo & Carry, 2013; Raymond & Izidoro, 2017).

External to the orbit of Neptune between $\sim 30-50$au lies a population of small bodies known as the Kuiper belt. Compared with the Asteroid belt these bodies are thought to be primarily composed of frozen ices, including water, ammonia and methane. Objects can be ejected from the Kuiper belt and be scattered into the inner solar system. As the object approaches the Sun, the ices present on the surface begin to melt, causing a trail of vapour behind the object. Famous examples of such objects include Halley's comet and 67P/Churyumov-Gerasimenko, which was the target of the recent ESA Rosetta mission. The sizes of objects in the Kuiper belt are estimated to be from small cm-sized bodies up to dwarf-sized planets. The largest of the dwarf planets in the Kuiper belt is Pluto, which has a mass of $0.002 M_{\oplus}$. The total mass of the Kuiper belt is also far in excess of that of the Asteroid belt, estimated at $\sim 0.1 M_{\oplus}$ (Gladman et al., 2001). For reference, the positions of both the Asteroid and Kuiper belts with respect to the Solar System planets are shown in Figure 1.1.

Before any detections of worlds around other stars, a typical planetary system was therefore thought to be comprised of a Sun-like host star, small rocky planets which orbit close to the star, larger planets which orbit at greater distances and inter-spaced populations of debris. However, planetary systems other than the Solar System can be far more diverse than this picture, which I discuss in the next section.

1.4 The Population of Exoplanets

The commonly quoted first detection of a planet around another star (or 'exoplanet' for brevity), was made in 1992 around the pulsar PSR B1257+12 (Wolszczan & Frail, 1992). Soon after in 1995, the first detection of an exoplanet around a solar-type star was made in the system 51 Peg (Mayor & Queloz, 1995). Interestingly, analysis of archival data taken before either of the aforementioned detections showed that signatures of planetary objects were present. For example, Campbell et al. 1988 suggested from observations of γ Ceph that stellar activity signals were present in their data, however on re-analysis Hatzes et al. 2003 confirmed these signals to be indicative of planetary type objects. Regardless of when the first exoplanet was detected however, a fundamental question that has puzzled humanity for generations was answered: the Solar System is not the only planetary system in the Universe. This question now, therefore, has become how many planetary systems

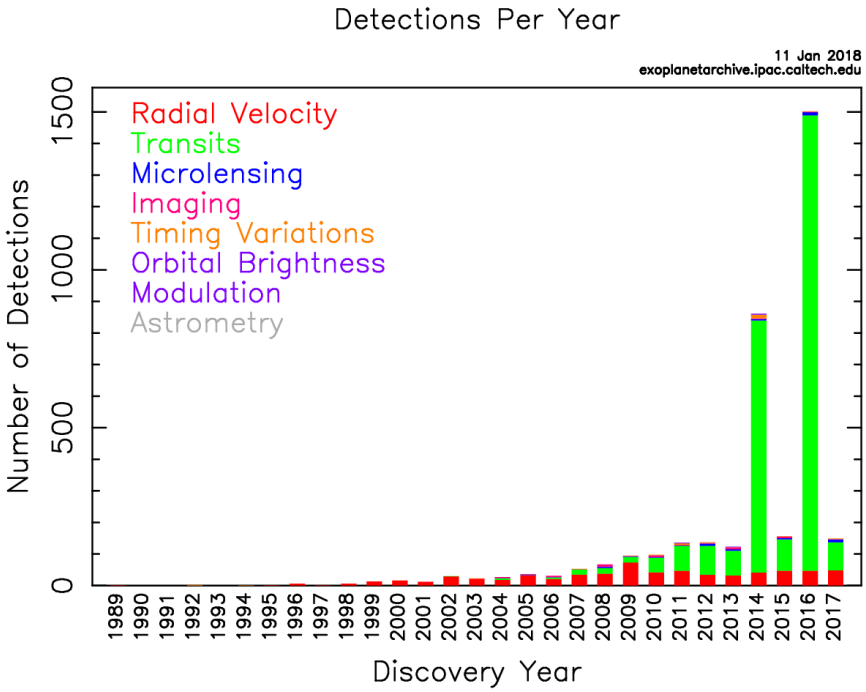

Figure 1.2 The number of exoplanets detected as a function of time. Figure sourced from NASA exoplanet archive.

are there? And how do they compare to the Solar System?

In recent years the number of exoplanet discoveries has steadily increased, as shown in Figure 1.2. Notably, the *High Accuracy Radial velocity Planet Searcher* (HARPS) and the *Kepler* space telescope have led to huge spikes in the number of exoplanet detections (Lissauer et al., 2011; Mayor et al., 2011), with this number increasing by roughly a factor of 9 from 2013-2014 alone. The current distribution of the mass and semi-major axes of confirmed exoplanets, detected using a sub-set of detection methods, is shown in Figure 1.3 (a discussion of these different detection methods is given later in this section). The masses in this Figure are in units of Jupiter masses, with the separation from the host star described by the semi-major axis in units of au. From these detections it is evident that exoplanet systems are much more diverse than what might be expected from the Solar System, with exoplanets having a much wider range of masses and distances from the host star.

A notable population of exoplanet systems are those which contain Jupiter mass objects on orbits extremely close to the host star, at less than a tenth of the size of Earth's orbit. These planets have been described as 'Hot Jupiters' due to their extremely high surface temperatures, which is expected based on eq. (1.3). How planets of this size form so close to the host star initially posed a major problem for planet formation models, as not enough material is present at these distances to form such large objects. It has since been theorized that these objects form further away from the star and then migrate in-

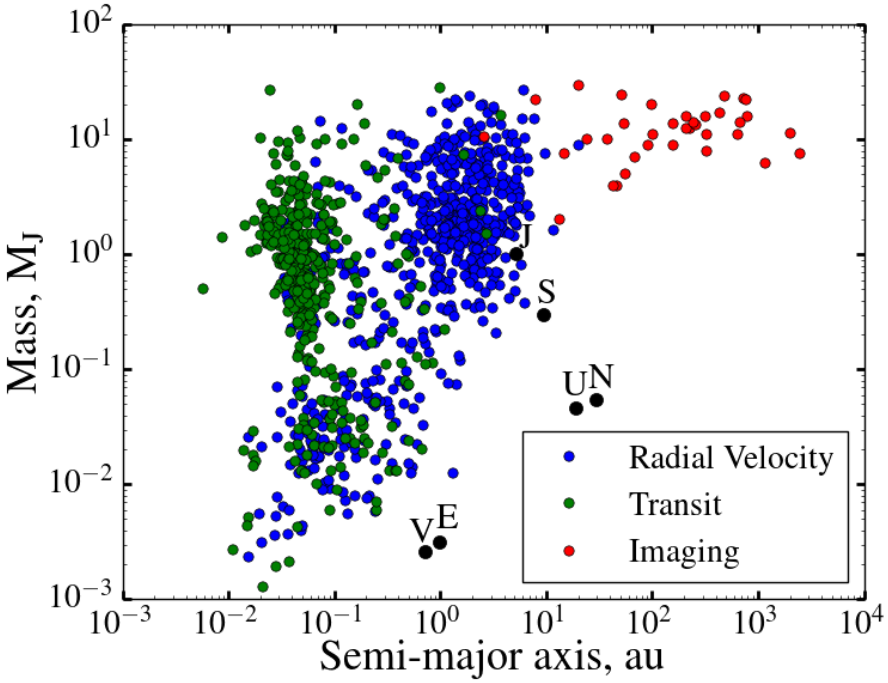

Figure 1.3 The mass and semi-major axis distribution of confirmed planets detected with the radial velocity, transit and imaging methods. Solar System planets from Figure 1.1 are shown for reference.

wards due to dynamical interactions, either with surrounding material or other planets (see Nelson et al. 2017 and references therein). A description of these possible dynamical delivery methods is given later in this section.

A plethora of exoplanets have also been found with radii of $\sim 1-5 M_\oplus$. Surprisingly, these non-Solar System type planets are the most numerous among detected planets (I note that many of these planets are not plotted on Figure 1.3 due to a lack of direct mass estimate, see §1.5.2). Often referred to as 'super Earths', these objects have been detected at a range of distances from the host star, from Hot Jupiter-type distances to 1au and beyond. The composition of these super-Earths is unclear. It is theorized that super-Earths can take different compositional qualities depending on bulk density (see Haghighipour 2013 and references therein), with high-density super-Earths thought to have a terrestrial planet-like composition i.e. rocky with the possibility of a thin atmosphere. For lower bulk densities, super-Earths are expected to be formed of a rocky core surrounded by a gaseous envelope, similar to that of Uranus and Neptune. Thus, these objects are often referred to as 'mini-Neptunes'. Conversely, this bulk density may also be indicative of a dense core surrounded by a thick layer of water type elements in liquid form. Finally, the lowest-density super-Earths, are expected to be comprised of a rocky core surrounded by a thick hydrogen/helium envelope, equivalent to a smaller version of Jupiter or Saturn.

From Figure 1.3 it is clear that super-Earths outside a few au have not been detected.

However this is expected to be due to the limitations of detection techniques rather than due to some physical mechanism. In the next section I describe planet detection techniques and their limitations, focussing on three techniques sensitive to planets at varying separations from the host star.

1.5 Planet Detection Techniques

1.5.1 Radial velocity

All objects in a planetary system, including the host star, orbit the centre of mass of the system. For most planetary systems the centre of mass is within the photosphere of the host star and so the orbital motion of the star is small. However, despite this small orbital motion, it is possible to detect the radial component of this motion as a periodic Doppler shift of the spectrum of the star. If such a shift is observed to be present, this indicates orbital motion of the star and therefore the possible presence of a planetary companion. The Doppler shifting of a star can only be seen radially in the direction towards the observer as illustrated in Figure 1.4, with the amplitude of this 'radial velocity' (RV) being given by

$$K = \left(\frac{2\pi G}{P}\right)^{1/3} \frac{M_p \sin i}{(M_p + M_\star)^{2/3}} \frac{1}{(1-e^2)^{1/2}}, \tag{1.4}$$

where P, M_p and e are the period, mass and eccentricity of the planet respectively, $M_\star$ is the stellar mass and i is the inclination of the orbit of the planet (where $i = 0^\circ$ indicates a face on orbit). As the Doppler shifting of the star can only be observed along the line of sight, the true mass of the planet cannot be determined without knowledge of the inclination, which is seldom known. The quantity $M_p \sin i$ is therefore often described as the *minimum mass* of the planet, since $\sin i$ is always less than 1. The more inclined the orbit of the planet therefore, the larger the true mass relative to the minimum mass. For this reason, it is common for the minimum rather than true mass of RV detected planets to be quoted in the literature. Indeed, the vast majority of confirmed RV detected planets plotted in Figure 1.3 refer to the minimum mass rather than the true mass of the planet. It is also not possible to measure the radius of a planet directly using the radial velocity method. Estimates for the radii of RV detected planets therefore most commonly come from implementing mass to radius relations (e.g. Chen & Kipping, 2017), or preferably from other planet detection techniques of the same object.

As the gravitational interaction between a planet and a star is stronger for more massive planets that are closer to the star, the radial velocity method is more sensitive to de-

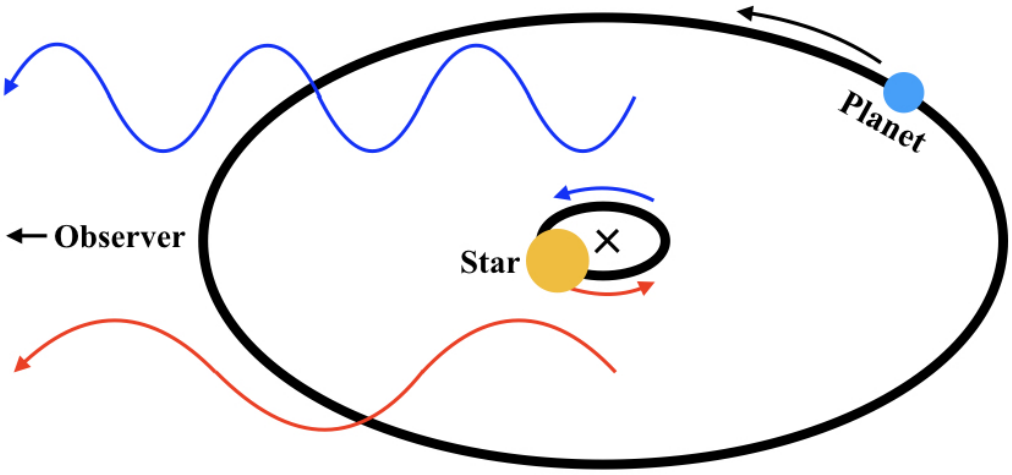

Figure 1.4 Illustration of planet detection by the radial velocity method. An observer measures characteristic Doppler shifting of the stellar spectrum due to motion around the centre of mass of a planetary system.

tecting larger planets on shorter orbits. As an example, the large mass of Jupiter induces a radial velocity motion of $\sim$ 13m/s in the Sun, while for the Earth it is only $\sim$ 0.1m/s (despite Jupiter having a larger separation than Earth from the Sun). Currently, the *HARPS* radial velocity survey is one of the most sensitive to planet detection and can detect radial velocity amplitudes of as little as K $\sim$ 1m/s. This sensitivity limit explains the rough invisible diagonal line on Figure 1.3, below which a dearth of RV detected planets are present. Planets below this limit are either too small or on too wide an orbit to induce a significant radial velocity in the host star. Moreover, Figure 1.3 also highlights that no RV planets have been detected outside of a few au, even for those with large masses. At these separations the timescale of the Doppler shifting becomes longer than the current lifetime of RV surveys and therefore cannot be detected even if the amplitude of the radial velocity of the star is large.

Of the confirmed RV detected planets, many have orbits far inside the equivalent orbit of Mercury at $<$ 0.1au. Moreover, analysis of the number and types of planets detected from RV surveys also suggests that planetary systems are unequivocally common, with occurrence rate estimates suggesting that $\gtrsim$ 50% of solar-type stars harbour at least one planet (Mayor et al., 2011).

As RV studies are only sensitive out to a few au, wide-orbit planets could be present

in these systems without causing a significant radial velocity signature. I investigate the dynamical impact such potential wide-orbit planets could have on inner RV detected systems in Chapter 3. Specifically, I investigate whether long term interactions between inner planets with a wide-orbit object can affect the eccentricity of the inner RV detected planets.

1.5.2 Transits

The transit method detects planets which appear to pass across the face of the host star. Such transit events cause the host star to become periodically dimmed once per orbital period of the planet. The amount of flux blocked by the planet is proportional to the ratio of the areas of the planet and the star, allowing for the radius of the planet to be inferred. However, the mass of the planet cannot be measured directly using this method. Confirmation of transiting planets with radial velocity measurements is especially powerful therefore, as both the mass and radius of the planet can be constrained allowing for estimates of bulk densities to be made. The exact shape of the transit at different wavelengths can also place constraints on atmospheric components of the planet (Winn 2010 and references therein).

The probability of observing a transiting planet can be calculated by considering the band of shadow a planet subtends on a celestial sphere as it orbits the star, as shown in Figure 1.5. The probability of observing a transit is equivalent to the surface area of the band of shadow divided by the total surface area of the celestial sphere. For the simplest case of a planet with radius R_p on a circular orbit with semi-major axis a_p, orbiting a star with radius $R_\star$, the probability of observing a transit P_{tr} is given by

$$P_{tr} = R_\star / a_p, \tag{1.5}$$

for the assumption that $R_p \ll R_\star$ and $R_\star \ll a_p$ (Borucki & Summers, 1984). Planets that are closer to the host star are therefore much more likely to be observed to transit. For example, a planet orbiting at 0.05au around a solar type star has a $\sim$ 10% probability of being observed to transit, however for a planet on an Earth-like orbit this probability drops to $\sim$ 0.5%. Due to the inherently small probabilities of detecting transiting planets, it is necessary to survey many stars to look for transit events. Indeed, the most successful mission in terms of the number of transiting planet detections has been the *Kepler* space telescope which has surveyed over 100,000 stars. The success of this and similar missions has resulted in the transit method being responsible for the largest number of planet detections to date (2789 as of 21/12/17, exoplanetarchive.ipca.caltech.edu). Many detections

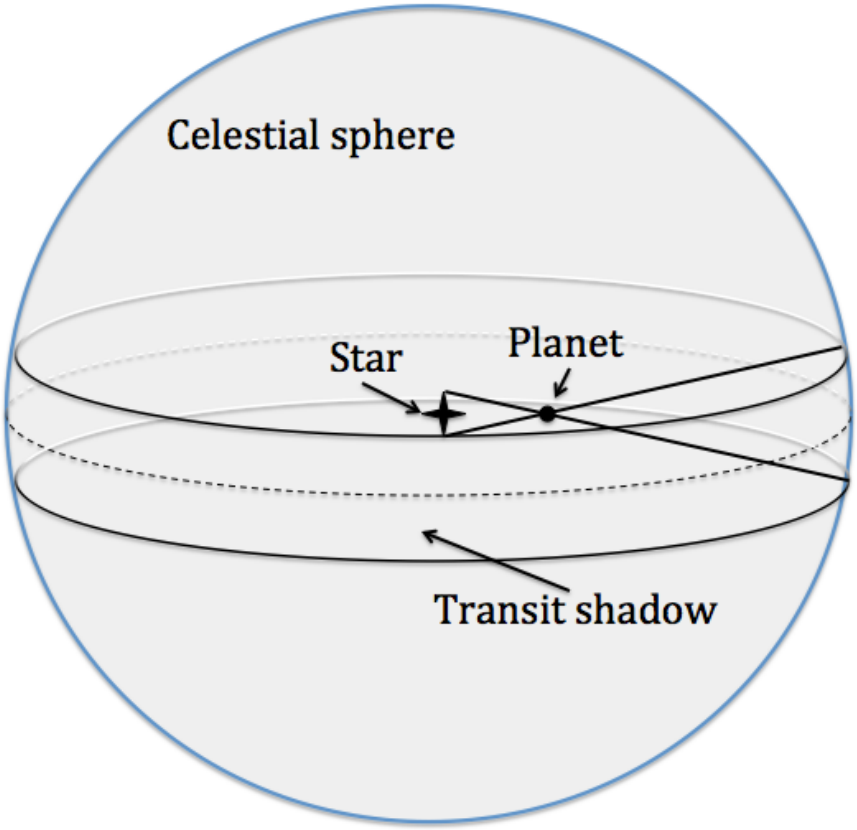

Figure 1.5 A planetary transit on a celestial sphere. The band of shadow subtended by the transit defines the probability that it is observed.

of transiting planets have yet to be followed up with other detection techniques however, such as the RV method. The *Kepler* detected planets are especially challenging to follow up with RV measurements as they are far from Earth, such that the Doppler shifting of the host star is below the current noise threshold for even the most sensitive of RV instruments. Indeed, many *Kepler* planet detections are not plotted in Figure 1.3 as the masses are currently unconstrained.

The most commonly detected planets by the transit method are super-Earth type planets with radii of 1 – 5$R_{\oplus}$, that are within $\sim$ 1au of the host star. Systems with multiple, closely packed transiting planets have also been detected, most notably demonstrated in recent times by the TRAPPIST-1 system, which has been observed to host 7 planets all within 0.059au of the host star (Gillon et al., 2017).

Systems where multiple planets are present can produce unique transit signatures. In these systems, gravitational interactions between the planets themselves can cause the transits of a given planet to occur slightly sooner or later than the previous transit. Moreover, planets that are responsible for changing the transit timing of another planet need not be transiting themselves. Measuring periodic changes in the transit time of a planet

therefore allows for the presence of additional planets to be inferred. This transit timing variation technique (commonly referred to as the TTV method in the literature) has led to the successful detection of many multi-planet systems (e.g. Steffen et al., 2012b). This method can even theoretically detect planets of Earth-like masses if they are present in tightly-packed multi-planet systems (Agol et al., 2005). If the inter-planet gravitational interactions are strong enough in multi-planet transiting systems then even the duration of the transit of a given planet can be affected. Known as the transit duration variation technique (TDV), if this change in transit duration can be measured it can also be used to infer the presence of additional, possibly non-transiting, planets (Agol & Fabrycky, 2017).

Similarly to RV surveys, the transit technique is not sensitive to objects outside of $\sim$ 1au. Wide-orbit planets could therefore be present in these systems and even be on highly inclined orbits without contradicting current observations. This topic is the motivation for Chapter 4, where I investigate the effect that wide-orbit planets on inclined orbits can have on inner transiting planets.

1.5.3 Direct imaging

Detection of planets with direct imaging involves the direct detection of photons emitted from a planet. Flux from the planet itself can be scattered light from the host star or thermal emission generated from the planet itself due to gravitational contraction. Scattered light from a planet is most visible toward optical wavelengths, with the gravitational contraction of the planet producing thermal emission most detectable in the infrared.

The main challenge with detecting planets via direct imaging is not detecting the emission from the planet itself, but nulling the stellar halo such that the emission from the planet can be disentangled from that of the star. It is often preferable to directly image planets in the infrared therefore rather than the optical, as the amount of flux in scattered light from the planet, while large, is drowned out by emission from the star. However, in the infrared, the ratio of the emission from the planet to that of the star is generally greater. As the planet ages the gravitational contraction produces less energy, reducing the amount of thermal emission. Planets therefore become dimmer as they age, making it common for direct imaging surveys to target younger stars, which host younger planets, for planetary detections.

A commonly referred-to quantity in the direct imaging of planets is the contrast. The contrast is defined as the ratio between the planet and stellar flux at a given separation from the star. As stellar emission is reduced at larger distances from the star, it becomes easier to disentangle emission from a planet at larger separations. Contrasts are therefore worse at the shortest separations from the star but can improve dramatically for larger

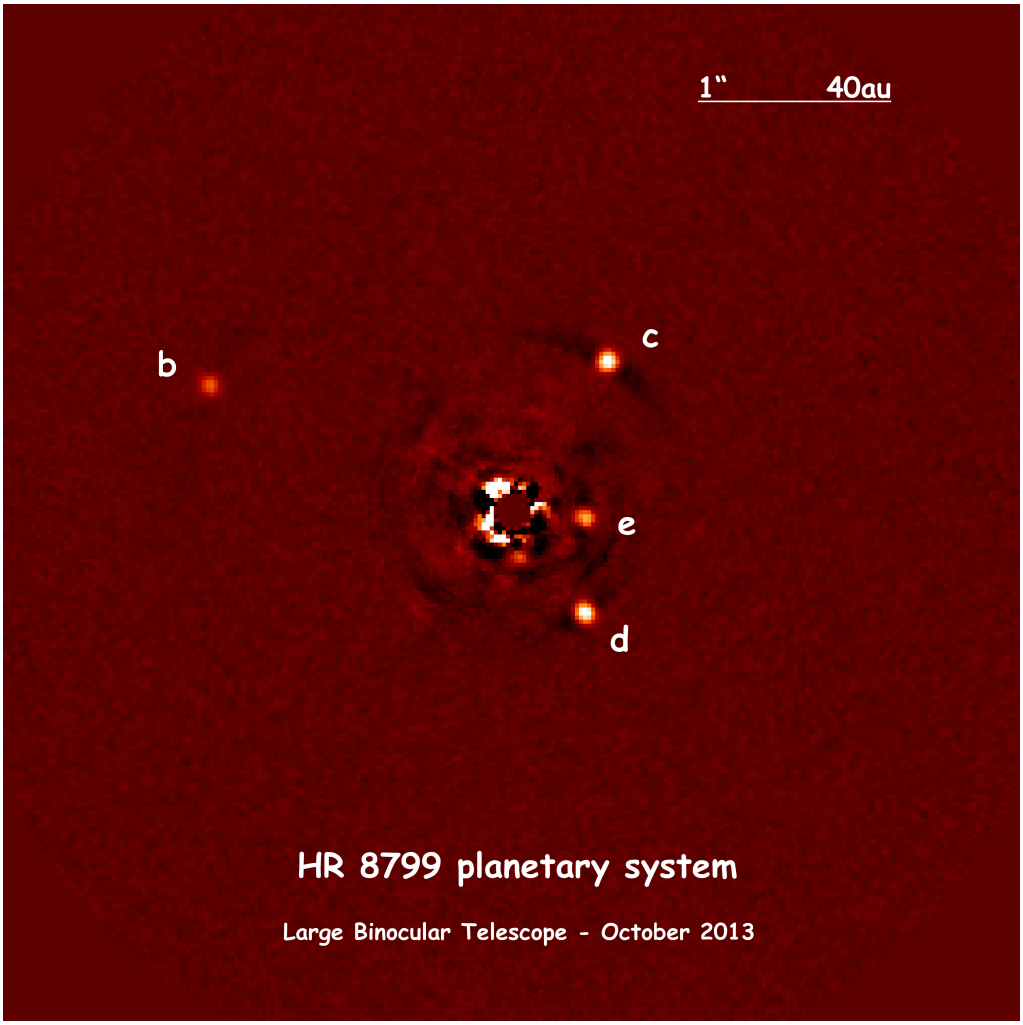

Figure 1.6 The direct image of the HR8799 planetary system, credit: A.-L. Maire / LBTO.

distances (examples of contrast curves are given later in this work in Chapter 6).

Detections of planets from direct imaging only allow for the flux and separation of a planet to be measured. Other physical properties of the planet cannot be measured directly. It is therefore necessary to use planetary evolutionary models to predict the parameters of a planet, most notably the mass. These models typically model the evolution of the luminosity of a planet according to different isochrones (see Allard et al. 2001; Baraffe et al. 2003).

As larger planets emit proportionally more flux, planets detected by direct imaging tend to be large. Moreover, due to the ease of detection, they are also at wider separations, evident in Figure 1.3. For example, the most recent direct imaging instruments are currently sensitive to planets that are at least a few Jupiter masses and outside $\sim$10au (e.g. Beuzit et al. 2008; Hinkley et al. 2011a; Macintosh et al. 2014, see also Hinkley 2012 for a discussion of direct imaging instruments). A benchmark system for directly imaged planets in recent years has been HR8799 (Marois et al., 2008, 2010), which has been found to host

four giant planets, shown in Figure 1.6. This system is especially interesting as it has been observed to host two belts of debris which are internal and external to the giant planets. In Chapter 5 I consider the dynamical effect that the giant planets have on the population of debris external to the planets and whether this can be used to infer the presence of an additional planet in this system.

Direct imaging therefore offers the main way of detecting planets outside of a few au, which is not currently feasible with RV or transit techniques. Currently, no systems with wide-orbit giant planets have been observed to host additional internal planets closer to the host star. However, future direct imaging surveys may offer a tantalising method to detect such systems. In Chapter 6 I describe an on-going survey which is looking to image giant planets in systems with known super-Earths detected with RV measurements. Rather than looking at younger systems, this survey is unique in that it is looking at older systems where the planets are expected to be less self luminous. However, this is balanced by these systems being close enough to Earth that the apparent brightness is sufficiently increased.

1.5.4 Additional planet detection techniques

In addition to the RV, transit and imaging techniques, other methods are used to detect exoplanets around main sequence stars which I summarize here.

Astrometry looks to identify the physical movement of a star on the sky as it orbits the centre of mass of a planetary system. If the 'wobble' of the star as it orbits the centre of mass of the system can be identified, then the presence of a planetary companion can be inferred. This method is capable of detecting planets far from the host star due to the larger displacement of the host star from the centre of mass.

Distant planetary systems can be detected with the aid of an intervening star that lies along the line of sight. The relativistic bending of space-time around the intervening star can act as a lens, magnifying the distant target planetary system. This method is commonly referred to as the 'gravitational microlensing technique'. The apparent brightness of the distant star is increased as the intervening lensing star passes in front of it. If a planet is present around the distant star, emission from the planet itself can also be observed due to the magnification from the lensing star. Similarly to direct imaging, microlensing allows for the separation and indirect estimates of the mass of the planet to be made.

Despite all the different techniques that can be used to detect exoplanets, we are currently not at the stage where the detection of an Earth-like planet at separations of $\sim$ 1au has been made. Indeed, even detecting a Uranus or Neptune-like planet at equal separations to that in the Solar System is currently proving to be difficult with current techno-

logical limits.

1.6 Debris

Much like the Asteroid and Kuiper belts in the Solar System, populations of debris have also been observed in exoplanetary systems. Emission from debris in planetary systems is comprised of scattered light from the host star and stellar re-processed emission. The re-processed emission stems from radiation that is absorbed by dust grains and then re-emitted at a wavelength which can be described by Wein's displacement law

$$\lambda_{peak} = \frac{2800 \mu mK}{T},$$

where λ_{peak} is the peak wavelength of re-emitted emission in μm and T is the temperature of the dust in K. The amount of emission from dust at a given wavelength therefore scales with the temperature of the dust, or how far away it is from the host star.

The typical size of dust grains in exoplanetary systems varies from $\sim \mu$m grains all the way up to km sized bodies (see Wyatt 2008 and references therein). The majority of the mass in debris belts is concentrated in the largest of the bodies, however the surface area of a debris population is dominated by the smallest mm grains. The presence of reprocessed emission from dust can be identified by measuring the Spectral Energy Distribution (SED) of the star, which is the flux of the star as a function of wavelength. When a large population of debris is present, a larger amount of flux is measured at the peak emission wavelength of the dust compared with what would be expected from the star in isolation. This additional emission is commonly referred to in the literature as an 'infrared excess'. As an example, the infrared excess observed in the system HR8799, taken from Marshall et al. 2016, is shown in Figure 1.7. Through modelling of the SED, fundamental parameters describing the debris, such as its position and mass, can be inferred.

Planets and debris are closely entwined, and can have significant interactions. Debris belts represent regions where large planets able to scatter out material have failed to form. The spatial features of debris can therefore be used to infer the presence of surrounding planets. For example, in the Asteroid belt, gaps exist due to debris being dynamically ejected by interactions with Jupiter, with the inner edge of the whole belt being sculpted by dynamical interactions with Saturn. While limited spatial information can be inferred by SED-fitting, imaging provides a better method for robust characterisation of the spatial features of a disk. Through imaging, fundamental parameters of the disk such as the inner and outer edges and therefore the radial extent of the disk can be measured. Moreover, gaps in the disk, which are often attributed to the presence of a planet (e.g. Fung

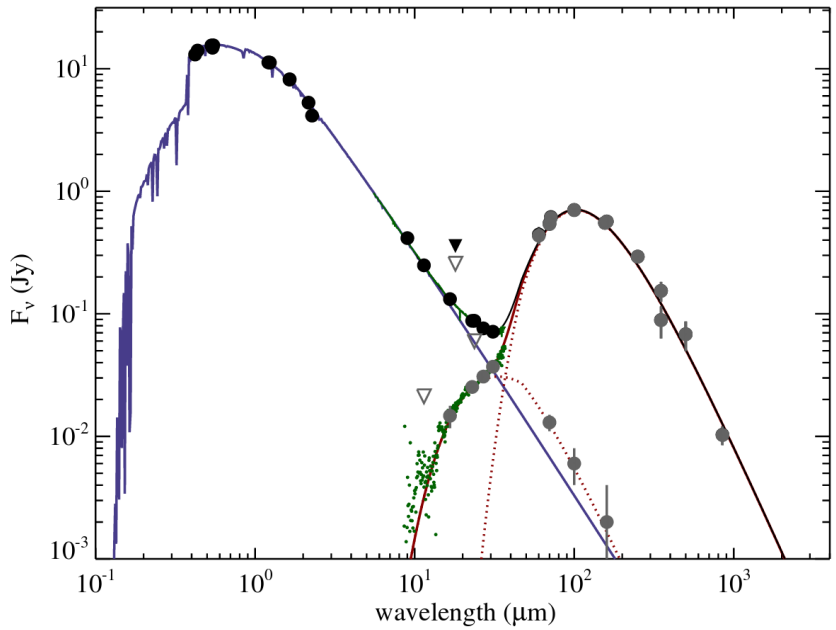

Figure 1.7 Spectral energy distribution of HD8799 taken from Figure 4 of Matthews et al. 2014. Emission at ∼0.1-10μm is dominated by the photosphere of the star, however a peak of emission is also present at ∼100μm. This is due to reprocessed stellar emission from dust grains in a disk present around HR8799.

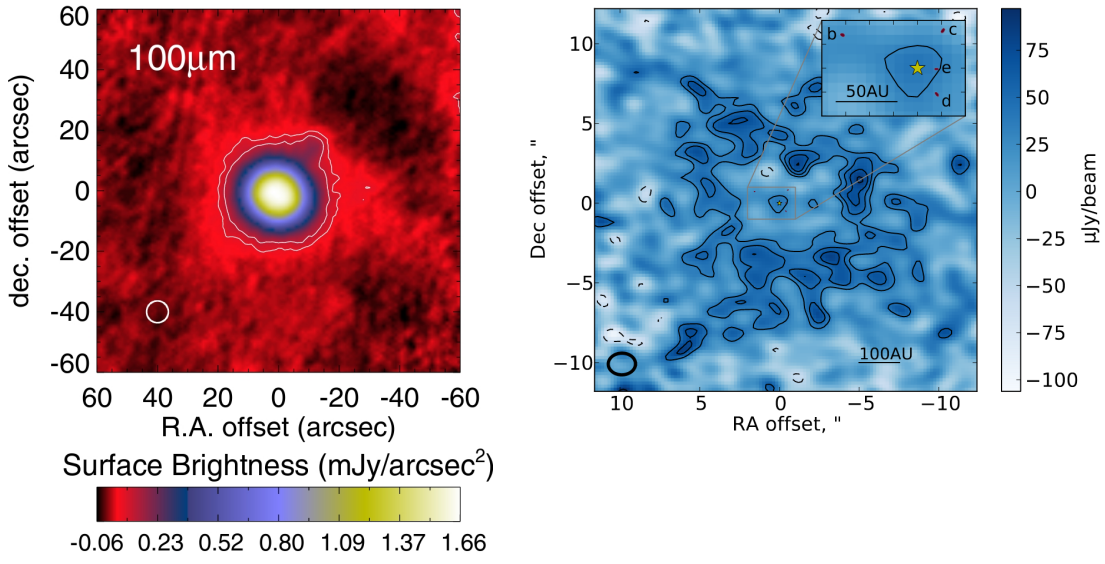

Figure 1.8 Images of HD8799 at: (*left*) 100μm from the *Herschel* space telescope, taken from Figure 1 of Matthews et al. 2014. (*right*) 1.34mm from the *Atacama Large Millimeter Array*, taken from Figure 3 of Booth et al. 2016.

et al., 2014; Malik et al., 2015; Dong & Fung, 2017), can be identified. Asymmetries in the disk can also be observed, including clumps, which may be due to dust interactions with a planet (e.g. β Pic Lagrange et al. 2009) or a giant impact between two bodies (see Wyatt & Jackson, 2016). Warps in a disk, potentially arising from long term interactions with a planet on an inclined orbit, have also been observed through imaging (e.g. Marino et al., 2015).

Combining spectral information from an SED with spatial information from imaging therefore provides a powerful constraint on fundamental parameters of a disk and has implications for potential planets in the system. Images of a disk around HR8799 at 100μm and 1.34mm are shown in the left and right panels of Figure 1.8 respectively. In Chapter 5 I compare simulations of this disk with these observations to predict the presence of a currently undetected planet in the system.

1.7 Dynamical Configuration of Planetary Systems

The bulk parameters of exoplanets and any surrounding debris place strong constraints on planetary formation and evolution models. However, these models must in turn be able to explain the observed orbital parameters of the planets. In Chapter 2 I discuss in detail how planetary orbits are defined. Here, however, I highlight the distribution of two of these orbital parameters: eccentricity and inclination.

1.7.1 Eccentricity and inclination distribution

How closely the orbit of a planet resembles a circle is described by it's eccentricity. An eccentricity of zero describes a circular orbit, while a value of one describes an orbit so eccentric it is unbound. Planets are expected to form on near-circular orbits, as interactions between a planet and surrounding material during formation damps down any large eccentricities (Lissauer, 1993). Indeed, this is the case for the Solar System planets as they are on largely circular orbits. For reference, all the eccentricities of the Solar System planets are shown in Figure 1.9 as blue circles.

The eccentricities of the population of confirmed exoplanets are shown by the black circles in Figure 1.9. Comparing with the eccentricities of the planets in the Solar System, it is clear that exoplanetary systems can be far more eccentric that what might be expected. These large eccentricities are assumed to be due to post-formation dynamical interactions (e.g. Rasio & Ford, 1996; Lin & Ida, 1997; Yu & Tremaine, 2001; Zakamska & Tremaine, 2004; Jurić & Tremaine, 2008; Raymond et al., 2009). In Chapter 2 I describe

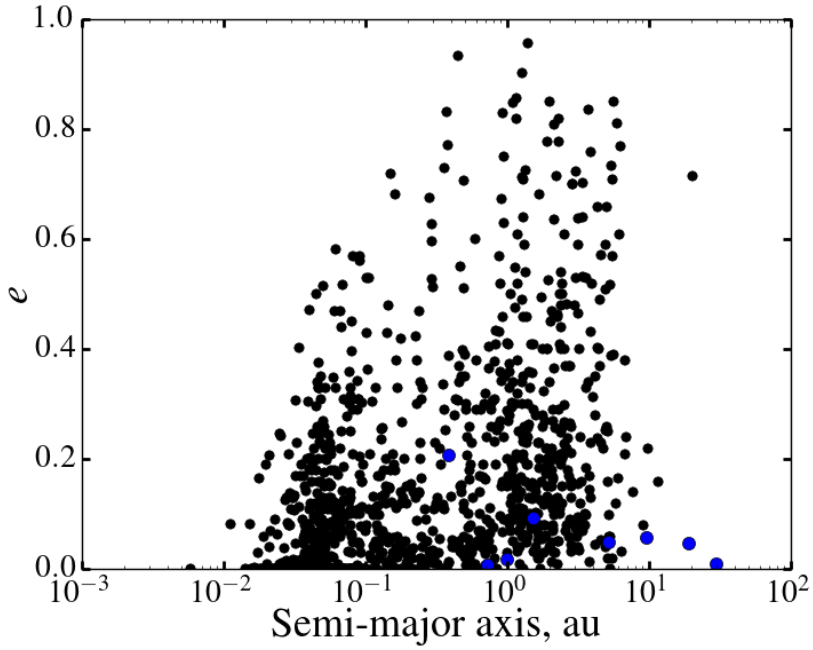

Figure 1.9 Eccentricity distribution of the exoplanet population. Blue dots refer to Solar System planets.

the dynamical interactions that occur in planetary systems in detail, and how these interactions can excite eccentricities directly and/or cause scattering between neighbouring planets, potentially providing some explanation for the observed exoplanet eccentricity distribution (e.g. Ford & Rasio 2008; Read & Wyatt 2016).

The mutual inclinations between planets also gives insight into the dynamical history of planetary systems. Planets in the Solar System have a small dispersion of inclinations, such that all the planets orbit in roughly the same plane. This is perhaps expected from planetary formation models, as the disk around the star in which planets form would promote planet co-planarity. Most exoplanetary systems are observed to have small inclination dispersions of $\lesssim 5^\circ$ (Lissauer et al., 2011; Fang & Margot, 2012; Figueira et al., 2012; Tremaine & Dong, 2012; Marmier et al., 2013; Fabrycky et al., 2014). However it is currently unclear how representative these dispersions are, as current observational methods are biased towards detecting co-planar systems (see §1.5). Exoplanetary systems with large mutual inclinations may therefore exist and be evading current observational surveys. In Chapter 4 I investigate how inclined planets affect the inclinations of other planets in the system, and whether the presence of such inclined planets is consistent with explaining currently observed exoplanetary systems.

1.8 Planet Formation

It is necessary for planetary evolution models to explain all the diverse exoplanetary systems that have been detected rather than only the Solar System. The exact mechanisms and processes responsible for planet formation are unclear, and are currently a particularly active topic of research in Astronomy, with many in-depth reviews present in the literature (e.g. Lissauer 1993; Wuchterl et al. 2000; Papaloizou & Terquem 2006; Matsuo et al. 2007; Morbidelli et al. 2012; Helled et al. 2014; Johansen et al. 2014; Raymond et al. 2014; Morbidelli & Raymond 2016). A basic description of planet formation begins with the disk of material that forms around a star during its formation. This disk is composed of gases and solid dust grains and is referred to as a protoplanetary disk. The gas dominates the mass of a protoplanetary disk, typically representing 99% of the total mass. The motion of dust grains in the disk are therefore thought to be strongly coupled to that of the gas as it moves inward towards the forming star. The turbulence of this motion causes dust grains to collide, resulting in them sticking together due to electrostatic forces. Gradually, repeated collisions between dust grains cause objects of $\sim$cm sizes to form. Collisions between objects of these sizes are of particular interest as rather than sticking together, fragmentation should occur (Weidenschilling, 1977). Often referred to as the 'metre-sized barrier' in the literature, this problematically predicts that object sizes should be limited such that planets would never form. Processes have been suggested to circumvent this barrier in growth however, such as the streaming instability model (Youdin & Goodman, 2005; Johansen et al., 2009; Bai & Stone, 2010), modified collision processes (Boley et al., 2014) and detailed dynamical models of planetesimal-disk interactions (Rafikov, 2013; Rafikov & Silsbee, 2015a,b). Further evolution past $\sim$m size objects is thought to occur according to two competing models: core accretion and gravitational instability.

Core accretion states that solid objects accrete further solid material until a critical mass is reached, upon which gas begins to be accreted and is bound to the object. Objects of this size are now large enough that they can be considered to be planetary embryos, or the cores of future planets. Planets that are formed in this way would be expected to be enriched in heavy elements due to accretion of dust grains with the gas. Indeed, this is consistent with the atmospheres of Jupiter and Saturn, which show heavy element enrichment rather than a solely hydrogen and helium composition. The terrestrial planets in the Solar System have also been hypothesised to form via core accretion. Either the forming planetary embryos reached a mass which is just enough for a small amount of gas to collapse onto them, or they formed in regions largely absent of gas (e.g. Lissauer, 1993; Wuchterl et al., 2000; Papaloizou & Terquem, 2006; Matsuo et al., 2007). Core accretion is therefore consistent with all the types of planets observed in the Solar System.

The role of core accretion in exoplanetary systems is unclear however. This model has difficulty explaining the most massive of the exoplanets detected at $\gtrsim$ 1M$_J$, as the timescale required for enough gas to collapse onto the forming planetary core is on the order of ∼10Myr (see Rafikov 2005, Matsuo et al. 2007, Rafikov 2011 and references therein). Evidence suggests however that protoplanetary disks have lifetimes of roughly ∼ 10Myr before they are dispersed by the star (see Williams & Cieza 2011 and references therein). Therefore, it might be necessary for another formation model to explain these massive exoplanets.

The gravitational instability model states that for massive enough protoplanetary disks, local disk instabilities can cause the fragmentation of material into clumps, which then rapidly accrete surrounding gas (see Williams & Cieza 2011 and references therein). The main benefit of this model is that Jupiter-mass planets can form in the space of hundreds of years, well below the lifetime of the protoplanetary disk. The rapid accretion of gas onto a clump in the disk means that little solid material is also accreted. Planets formed by the gravitational instability model are therefore expected to be mainly comprised of light hydrogen and helium-type elements. This is at odds with the heavier elements observed in the atmospheres of Jupiter and Saturn however. Perhaps then, both core accretion and gravitational instability are important for planet formation, with the characteristics of the protoplanetary disk defining which model is dominant.

Beyond the initial formation of the planet, interactions with the protoplanetary disk can modify the position of its orbit. This is because as planets form, they cause gaps to be carved into the disk. Relative over/under densities of material form on either side of the gap and generate torques which act upon the planet. Depending on the exact nature of the density of material either side of the carved gap, these torques can act to move a planet to wider or smaller orbits. Therefore, planets formed on wide orbits can interact with the disk and migrate closer to the star. Indeed, this mechanism is predicted to form the closely-packed multi-planetary systems observed by *Kepler* (Rein, 2012).

1.9 Introduction Summary

It is clear that detected exoplanetary systems are far more exotic than what would be expected from the Solar System alone. Exoplanets can have a range of sizes and orbits, from massive Jupiter-mass planets that have orbits of a few days to the overwhelming abundance of super-Earth planets which have no Solar System analogue. Large eccentricities also exist in the exoplanet population, indicative of post-formation dynamical processes, which give us an insight into the potentially violent and unpredictable nature of the planet formation process.

Current detection methods are generally only sensitive to planets within a few au of the host star however. Wide-orbit giant planets could therefore exist in many observed exoplanetary systems without contradicting observations. These giant planets may play a crucial role in the formation and evolution of other planets in the system through inter-planet dynamical interactions. This is the motivation for the work that is presented in this thesis, where I focus on investigating how potential wide-orbit planets in exoplanetary systems affect the evolution of detected planets. In Chapter 3 I investigate how an eccentric wide-orbit planet can affect the eccentricity of inner planets through long-term dynamical interactions and how this can be used to place constraints on the types of wide-orbit planets that would be unlikely to be present in RV-detected systems. In Chapter 4 I perform a similar analysis, focussing on how a wide-orbit planet on an inclined orbit can affect the probability that inner planets are observed to transit due to long term interactions. Following this, in Chapter 5 I investigate the effect that wide-orbit planets have on the populations of debris present in the planetary system HR8799 through dynamical interactions. Chapter 6 then goes on to describe a survey that I have been conducting which is looking to directly image giant planets in systems with known RV-detected planets. Detections of wide-orbit planets in these systems provide observational constraints on the dynamical modelling described in previous chapters. Preliminary results are presented for this survey, as observations and analysis are currently on-going. Finally, in Chapter 7 I summarize the main conclusions of the work I have completed during my PhD, before giving a brief overview of the future outlook for this field in the context of upcoming telescope missions.

Before presenting the work completed during my PhD however, I first describe post-formation dynamical interactions that occur in planetary systems and how evidence of such interactions would be imprinted on observations of planetary systems seen today.

2

Theory of Dynamical Interactions

2.1 Orbital Elements

The orbits of objects in planetary systems can be defined by orbital elements. A two dimensional orbit can be described by four orbital elements: semi-major axis, eccentricity, longitude of pericentre and the true anomaly. The semi-major axis, a, describes half the length of the major axis of an orbit. As mentioned previously, the eccentricity, e, defines how much an orbit represents an ellipse and takes values from 0 (circular orbit) to 1 (unbound orbit). Using the semi-major axis and eccentricity, the smallest and largest distance of the orbit away from the centre of mass of the system, known as the pericentre, r_{per}, and apocentre, r_{apo}, respectively can be defined as

$$\begin{aligned} r_{per} &= a(1-e), \\ r_{apo} &= a(1+e). \end{aligned} \tag{2.1}$$

The argument of pericentre, ω, denotes the angle from a fixed reference direction to the pericentre with the true anomaly, f, describing the angle from the pericentre to the position of the object in the orbit. Increasing to a three dimensional orbit requires the addition of two further elements: inclination, i, and longitude of ascending node, Ω. The inclination refers to how inclined an orbit is from a given reference plane. The longitude of ascending node describes the angle from a reference direction to where the orbital plane crosses the $i = 0^\circ$ plane. The orbit of a planet with these orbital elements is shown in Figure 2.1. The argument of pericentre and longitude of ascending node are often represented in a single 'dog leg' style angle known as the longitude of pericentre, $\varpi = \omega + \Omega$.

In addition to the true anomaly, the position of an object in the orbit can also be characterised by the mean anomaly M. This angle is taken from the pericentre to the position of an object in the orbit, for when the orbit is moved to one that is circular, where the orbital speed is constant and the orbital period is unchanged from the original elliptical orbit. Both the orientation of the orbit, captured by ω and Ω, and the position of the object

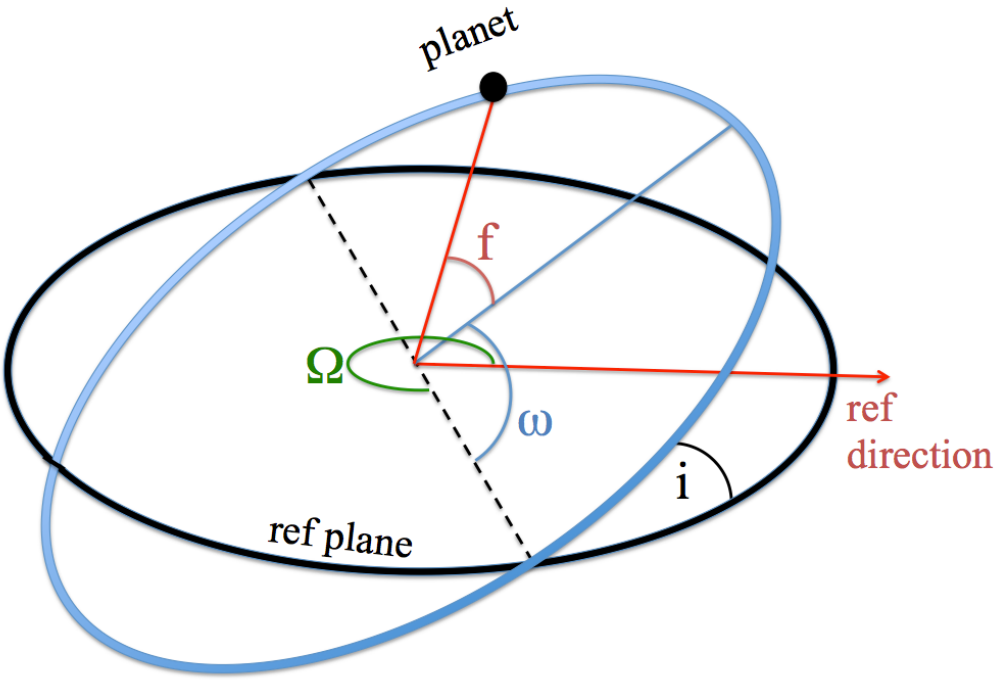

Figure 2.1 Geometry of a planetary orbit.

in the orbit, represented by M, can also be defined by a single quantity known as the mean longitude, $\lambda = \omega + \Omega + M$.

Finally, the orbital velocity of an object is described by the mean motion, n, which is given by

$$n = \frac{2\pi}{P}, \tag{2.2}$$

where P is the orbital period.

2.2 Inclination Reference Planes

The reference plane used to define the inclination varies. Reference planes can include the plane of the line of sight, the projected equator of the observed star, the projected plane of the orbit of the Earth (the ecliptic) etc. A more general reference plane often chosen however is the invariable plane, which refers to the plane that is perpendicular to the total orbital angular momentum vector of a planetary system. Using this reference plane also allows for fundamental parameters describing the orbits of planets to be related.

An example demonstration of the invariable plane being used as a reference plane can be made by considering a star with a mass $M_\star$ orbited by two planets on circular orbits with masses and semi-major axes for the inner and outer planet of m_1, a_1 and m_2, a_2 respectively. The inner and outer planet have a respective orbital angular momentum in

the low eccentricity limit $L_1 = m_1\sqrt{GM_\star a_1}$ and $L_2 = m_2\sqrt{GM_\star a_2}$, where G is the gravitational constant. Each planet will have an inclination and longitude of ascending node (i_1, Ω_1 and i_2, Ω_2 for the inner and outer planet respectively), with respect to the invariable plane. Transforming the planetary orbits into a frame that is perpendicular to the total orbital angular momentum vector (i.e. the invariable plane) is made using the transformation:

$$L_1 \begin{bmatrix} \sin i_1 \sin\Omega_1 \\ -\sin i_1 \cos\Omega_1 \\ \cos i_1 \end{bmatrix} + L_2 \begin{bmatrix} \sin i_2 \sin\Omega_2 \\ -\sin i_2 \cos\Omega_2 \\ \cos i_2 \end{bmatrix} = L_{tot} \begin{bmatrix} \sin i' \sin\Omega' \\ -\sin i' \cos\Omega' \\ \cos i' \end{bmatrix}, \tag{2.3}$$

where i' and Ω' are the inclination and longitude of ascending node of the invariable plane with respect to some reference plane. As the choice of this reference plane is arbitrary, one can simply define $i' = 0$, $\Omega' = 0$. Solving the above transformation under these conditions results in the fundamental parameters of the planets being related through:

$$L_1 \sin i_1 = L_2 \sin i_2$$

$$\Omega_2 - \Omega_1 = \pi.$$

Rather than considering individual inclinations for each of the planets it is perhaps physically more useful to define a mutual inclination between them. In the invariable frame, the mutual inclination is the angle between individual angular momentum vectors, which for the two planet case is equal to $\Delta i = i_1 + i_2$. Assuming that the mutual inclination is small, one finds

$$\begin{aligned} i_1 &= \Delta i \left(1 + L_1/L_2\right)^{-1} \\ i_2 &= \Delta i \left(1 + L_2/L_1\right)^{-1}. \end{aligned} \tag{2.4}$$

Use of the invariable plane to describe planetary orbits is applied in Chapter 4, albeit for planetary systems with three planets. It is relatively simple to calculate inclinations of planets in such systems with respect to the invariable plane, as it is only required to add an additional matrix term in eq. (2.3) for a third planet. Following on from the definition of planetary orbits and reference planes therefore, one can describe how planets dynamically interact which I outline in the following section.

2.3 The Disturbing Function

The dynamical evolution of planetary systems is driven by interweaving planet-planet interactions in addition to the more obvious interactions with the host star. Perturbations

in orbital elements caused by one planet's gravitational interaction with another can be described through the disturbing function. Consider the simplest case of a two planet system with masses m_1 and m_2 respectively, orbiting a host star with a mass $M_\star$, where the respective position vectors of the two planets are given by r_1 and r_2. The associated disturbing functions for each planet, $\mathcal{R}_1$ and $\mathcal{R}_2$ respectively, are given by

$$\mathcal{R}_1 = \frac{Gm_2}{|\, r_2 - r_1 \,|} - Gm_2 \frac{r_1 \cdot r_2}{r_2^3} \quad \text{and} \quad \mathcal{R}_2 = \frac{Gm_1}{|\, r_1 - r_2 \,|} - Gm_1 \frac{r_1 \cdot r_2}{r_1^3}, \tag{2.5}$$

where G is the gravitational constant. The first and second terms in each of the above disturbing functions are referred to as the direct and indirect terms respectively. The indirect terms correspond to the choice of origin for the coordinate system, with these terms disappearing if the origin is taken at the centre of mass (c.f. Ellis & Murray 2000).

To describe how the associated orbital elements of each planet (a_1, a_2, e_1, e_2, ϖ_1, ϖ_2, i_1, i_2, Ω_1, Ω_2) evolve with time, the disturbing function can be expanded as an infinite sum of these elements (c.f. chp6 Murray & Dermott 1999 assuming coordinate origin at the centre of mass of the system):

$$\begin{aligned} \mathcal{R}_1 &= \mu_2 \sum F_1(a_1, a_2, e_1, e_2, i_1, i_2) \cos\varphi, \\ \mathcal{R}_2 &= \mu_1 \sum F_2(a_1, a_2, e_1, e_2, i_1, i_2) \cos\varphi \end{aligned} \tag{2.6}$$

where $\mu_1 = Gm_1$ and $\mu_2 = Gm_2$ respectively and

$$\varphi = j_1\lambda_2 + j_2\lambda_1 + j_3\varpi_2 + j_4\varpi_1 + j_5\Omega_2 + j_6\Omega_1$$

where j_n are integers and λ_1 and λ_2 are the respective mean longitudes of each of the planets.

While this infinite summation seems like a complex way to describe orbital evolution, the number of terms in this summation can be significantly reduced through only considering certain types of dynamical interactions. The full disturbing function describes three types of perturbations: fast, resonant and slow (secular) which I discuss below.

2.4 Fast and Scattering Interactions

Fast interactions in the disturbing function are often assumed to cause rapid changes in orbital elements that average to zero over single periods and therefore associated terms in the disturbing function can be neglected.

In the event of scattering or collisional interactions between two bodies however this

is not the case, with the orbital elements for either of the bodies becoming significantly altered over very small timescales. A rough estimate for when such close encounters can occur can be made by considering whether the bodies approach each other within some number of mutual Hill radii. The Hill radii around an object refers to the radius within which the gravitational interaction is dominated by the object rather than the host star. For an object of mass m_1 and semi-major axis a_1 and a neighbouring object of mass m_2 and semi-major axis a_2 the mutual Hill radii R_H, using the assumption of low eccentricity, is given by

$$R_H = \frac{1}{2}\left(\frac{m_1 + m_2}{3M_\star}\right)^{1/3}(a_1 + a_2), \tag{2.7}$$

where $M_\star$ is the mass of the central star. Defining mutual Hill radii in this way does not properly account for interactions between objects on highly eccentric orbits, for which a modified form of eq (2.7) outlined in Pearce & Wyatt 2014 can be used to express R_H in terms of apocentre/pericentre distances.

2.5 Resonant Effects

Resonant terms in the disturbing function become important when the orbital periods of two bodies (1 and 2) are spaced by an integer ratio. These mean motion resonances (MMRs) occur when the ratio of their semi-major axes is given by

$$\frac{a_2}{a_1} \approx \left(\frac{p}{q}\right)^{2/3}, \tag{2.8}$$

where p and q are integers and $p > q$. The effects of these MMRs can be described by considering a planet on a circular orbit and a planetesimal on an eccentric orbit that is internal to the planet, where both the planet and planetesimal are orbiting in the same direction (see example in chp 8.3 in Murray & Dermott 1999). The point of closest approach between the planet and planetesimal is referred to as the conjunction of the two bodies. If the conjunction occurs when the planetesimal is at pericentre then the tangential force on the planetesimal will be the same both before and after the conjunction, such that the net tangential force on the planetesimal is zero during the conjunction. As a net tangential force causes orbital angular momentum to be exchanged (c.f. chp 2 Murray & Dermott 1999), conjunction at pericentre causes no net change to the orbit of the planetesimal.

Consider now however the case where the conjunction occurs before pericentre. The tangential force on the planetesimal is larger before the conjunction than after. Moreover the relative orbital velocity between the planet and the planetesimal is smaller before con-

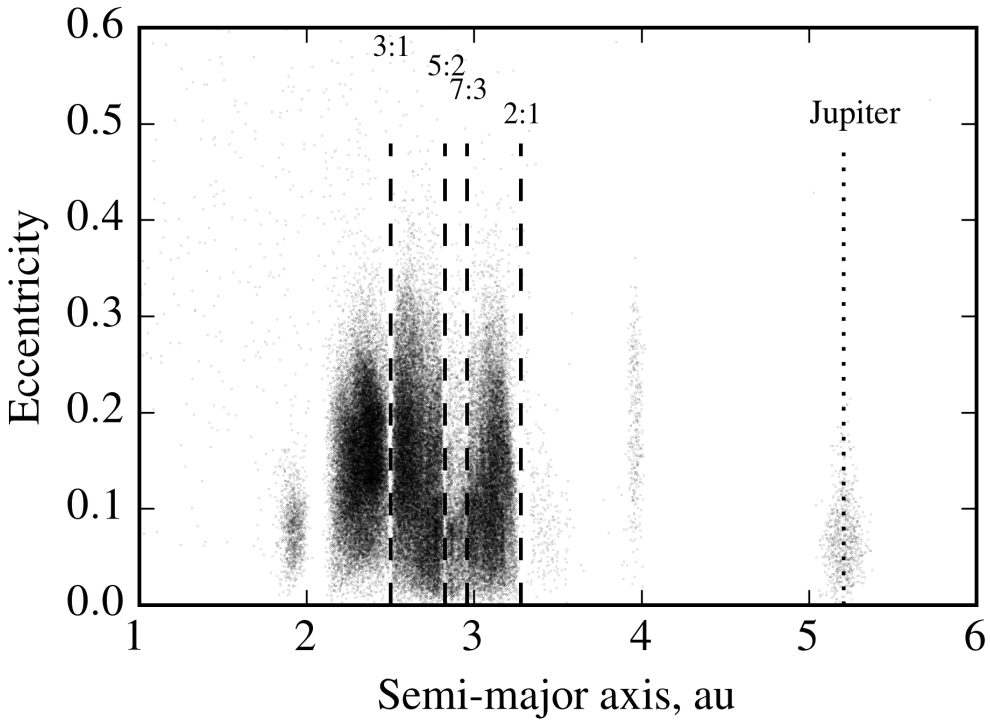

Figure 2.2 The distribution of eccentricities and semi-major axes of objects in the Asteroid belt. Gaps in the distribution refer to objects that have been cleared out by mean motion resonances with Jupiter.

junction rather than after. The larger tangential force, acting for a longer time before conjunction compared with after, therefore causes the planetesimal to gain orbital angular momentum, moving it to a wider orbit with an orbital velocity closer to that of the planet. The next conjunction therefore occurs closer to the pericentre of the planetesimal.

If the conjunction occurs as the planetesimal is approaching apocentre then the net tangential force on the particle will cause a net loss of orbital angular momentum in the opposite sense to that described above. The effect of repeated conjunctions therefore causes the orbit of the planetesimal to naturally evolve to where the conjunction occurs at pericentre. Mean motion resonances can therefore promote orbits where close encounters between objects occur at the largest separation and therefore the most stable position between them.

Repeated conjunctions at the same point in the orbits of bodies can however, cause one of the objects to become unstable if the exchange of angular momentum is large enough. Indeed this is seen in the Asteroid belt, where gaps in the density distribution of asteroids have been carved out at given locations as shown in Figure 2.2. Known as the Kirkwood gaps, these are due to major MMRs from Jupiter (Nesvorný & Morbidelli, 1998;

Ozernoy et al., 2000; Roig et al., 2002; Minton & Malhotra, 2009).

MMRs described by eq. (2.8) have finite widths. For regions close to massive bodies, MMRs become densely packed and can overlap, which causes chaotic motions in less massive bodies that enter this region on timescales of ∼kyr – Myrs (Mustill & Wyatt, 2012; Morrison & Malhotra, 2015). The semi-major axis from the planet, inside which instability is predicted (Δa) is given by

$$\Delta a = 1.5 a \mu^{2/7}, \tag{2.9}$$

where a is the semi-major axis of the planet and μ is equal to the planet to star mass ratio, $m/M_\star$ (Wisdom, 1980; Duncan et al., 1989; Faramaz et al., 2014).

The presence of MMRs has tentatively been observed in exoplanetary systems. Notably, the planetary system HR8799 has been discovered to host four giant planets (Figure 1.6) which is thought to only remain stable due to the planets being in a MMR chain (e.g. Goździewski & Migaszewski, 2009; Reidemeister et al., 2009; Fabrycky & Murray-Clay, 2010; Sudol & Haghighipour, 2012; Goździewski & Migaszewski, 2014; Konopacky et al., 2016; Zurlo et al., 2016).

2.6 Secular Interactions

Secular components of the disturbing function represent long term interactions related to the precession of orbits, with typical timescales being at least the orbital period of a planet over the mass ratio with the star. As orbital periods are negligible over such timescales, secular interactions in the disturbing function are defined as those which are independent of mean longitude, which leads to the semi-major axis and therefore energy remaining constant. That is, secular interactions result in changes to (e, ϖ, i, Ω) and angular momentum being exchanged but not energy. If eccentricities and inclinations remain low then the corresponding evolution of each respective orbital element can be calculated by taking the disturbing function expansion to second order in eccentricity and inclination which is known as Laplace-Lagrange theory (e.g. Murray & Dermott, 1999). Here, one finds that the evolution of e and ϖ is completely decoupled from the evolution of i and Ω. I first discuss the derivation for the evolution of eccentricity and longitude of pericentre.

2.6.1 Eccentricity evolution

Consider a system of N planets in which planet j has an eccentricity and longitude of pericentre e_j and ϖ_j respectively which can be combined to give a complex eccentricity $z_j = e_j \exp(i\varpi_j)$ so that $e_j(t) = \mid z_j(t) \mid$. If $\mathbf{z} = [z_1, z_2, ..., z_N]$ then Laplace-Lagrange theory

gives the time evolution of eccentricities of planets around a star of mass $M_\star$ in the form

$$\dot{\mathbf{z}} = i\mathbf{A}\mathbf{z}, \tag{2.10}$$

where i refers to the imaginary unit here only and $\mathbf{A}$ is a matrix with elements given by

$$A_{ji} = -\frac{1}{4} n_j \frac{m_i}{M_\star + m_j} \alpha_{ji} \tilde{\alpha}_{ji} b^{(2)}_{3/2}(\alpha_{ji}) \quad (j \neq i), \tag{2.11}$$

$$A_{jj} = \frac{1}{4} n_j \sum_{i=1, i\neq j}^{N} \frac{m_i}{M_\star + m_j} \alpha_{ji} \tilde{\alpha}_{ji} b^{(1)}_{3/2}(\alpha_{ji}), \tag{2.12}$$

j and i are integers which refer to corresponding planets, n_j the mean motion where $n_j^2 a_j^3 \approx GM_\star$, $\alpha_{ji} = \tilde{\alpha}_{ji} = a_j/a_i$ for $a_j < a_i$ and $\alpha_{ji} = a_i/a_j$ and $\tilde{\alpha}_{ji} = 1$ for $a_j > a_i$. Laplace coefficients are given by

$$b^{(\nu)}_s(\alpha) = \frac{1}{\pi} \int_0^{2\pi} \frac{\cos(\nu x) dx}{(1 - 2\alpha\cos(x) + \alpha^2)^s}, \quad \alpha < 1. \tag{2.13}$$

As eq (2.10) can be represented by a set of linear differential equations with constant coefficients, it can be solved as an NxN eigenfrequency problem. The solution represents the evolution of $\mathbf{z}$ through a superposition of sinusoids associated with each eigenfrequency g_i of the matrix $\mathbf{A}$

$$z_j(t) = \sum_{i=1}^{N} \mathbf{e}_{ji} e^{i(g_i t + \beta_i)}, \tag{2.14}$$

where $\mathbf{e}_{ji}$ includes the eigenvectors of $\mathbf{A}$ and initial conditions of the system and β_i is an initial phase term. Each planet therefore imposes an eccentricity variation in the other planets on a timescale of $\sim 1/g_i$. To demonstrate this, the evolution of the eccentricities of Jupiter and Saturn due to their secular interaction is shown in Figure 2.3. Here it is clear that the eccentricity of both planets evolve in a sinusoidal type motion, with the maximum eccentricity Saturn experiences almost reaching twice the eccentricity that is observed today.

Description of the secular evolution by Laplace - Lagrange theory begins to break down as eccentricities are increased, specifically above e$\sim$0.2, where it is necessary to include higher order terms in the disturbing function. Beyond e$\sim$0.66 the expansion of the disturbing function no longer converges (known as the Sundman criterion), so it is not clear to what extent the second order eccentricity terms will capture any aspect of the secular interaction, although it may give an approximation. High inclinations also add further complications to the secular solution as the evolution of inclinations starts to be coupled with the evolution of eccentricity, resulting in qualitatively different behaviour.

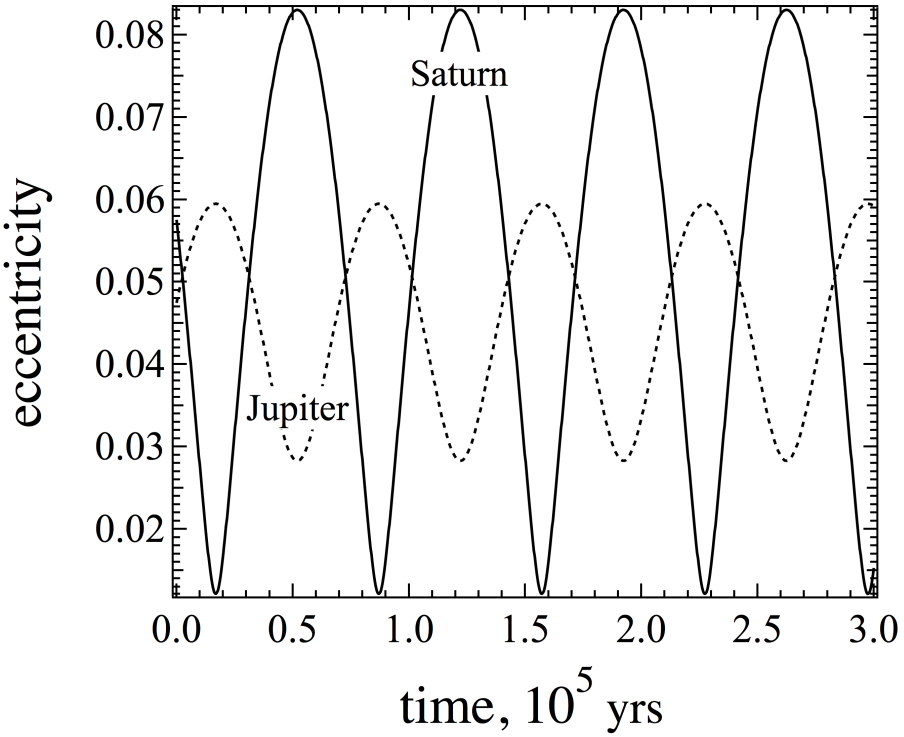

Figure 2.3 Evolution of the eccentricity of Jupiter (dashed line) and Saturn (solid line) due to their secular interaction.

The evolution of a massless test particle can also be fully described within Laplace - Lagrange theory, with the full mathematical derivation given in Murray & Dermott 1999. This finds that the test particle eccentricity precesses in a circle around forced elements that are imposed upon it by the secular solution of the planets. Locations where the particle's rate of precession is equal to one of the eigenfrequencies introduces a singularity into the secular solution, causing forced elements to become infinite. That is, test particles will tend to an infinite eccentricity at discrete positions, known as secular resonances. These resonances are implicit to Laplace-Lagrange theory however, as including higher order terms in the disturbing function allows for resonances to move with time, even to the point where they overlap. Ensuing chaotic motions can subsequently take place on timescales as long as ∼Gyrs (Lithwick & Wu, 2011).

2.6.2 Inclination evolution

The evolution of the inclination from secular interactions can be calculated in a similar way to eccentricities. Consider a system of N secularly interacting planets in which planet j has a semi-major axis a_j and mass m_j. The inclination and longitude of ascending node of planet j are given by I_j and Ω_j respectively, and can be combined into the associated

complex inclination $y_j = I_j e^{i\Omega_j}$. Assuming that the vector involving all the planet's orbital planes is given by $\mathbf{y} = [y_1, y_2, ..y_N]$, the evolution of complex inclinations in the low inclination and eccentricity limit can be given by Laplace - Lagrange theory in the form

$$\dot{\mathbf{y}} = i\mathbf{B}\mathbf{y}, \tag{2.15}$$

(Murray & Dermott, 1999) where i here is the imaginary unit and $\mathbf{B}$ is a matrix with elements given by

$$\begin{aligned} B_{jk} &= \frac{1}{4} n_j \left(\frac{m_k}{M_\star + m_j} \right) \alpha_{jk} \tilde{\alpha}_{jk} b^{(1)}_{3/2}(\alpha_{jk}) \qquad (j \neq k) \\ B_{jj} &= -\sum_{k=1, j\neq k}^{N} B_{jk}, \end{aligned} \tag{2.16}$$

where variables take equivalent values to that described for eq. (2.12), substituting the integer k here for i in eq. (2.12). Eq. (2.15) can be solved to show that the evolution of $\mathbf{y}$ is given by a superposition of eigenmodes associated with each eigenfrequency, f_k, of the matrix $\mathbf{B}$

$$y_j(t) = \sum_{k=1}^{N} I_{jk} e^{i(f_k t + \gamma_k)}, \tag{2.17}$$

where I_{jk} are the eigenvectors of $\mathbf{B}$ scaled to initial boundary conditions and γ_k is an initial phase term. If it is assumed that all objects are spherically symmetric, additional terms in the diagonal elements of $\mathbf{B}$ in eq. (2.16), which relate to stellar oblateness, need not be included. A choice of reference frame for the inclination also becomes arbitrary, leading to one of the eigenfrequencies equalling zero (c.f. Murray & Dermott 1999). This free choice of reference plane results in the invariable plane described in §2.2 often being chosen, with it only being meaningful to describe a mutual inclination between planets (e.g. eq. 2.4). The inclination solution described by eq. (2.17) becomes simplified when the invariable plane is taken as a reference plane as the eigenvector associated with the zero value eigenfrequency reduces to be equal to zero.

In Chapters 3 and 4 I consider planetary systems where eccentricities and inclinations respectively are evolving due to secular interactions. I make use of the theory of secular interactions described above and apply it to a variety of systems in these Chapters, including those with up to three planets.

3

Dynamical Constraints on Outer Planets in Super-Earth Systems

3.1 Chapter Summary

This Chapter considers secular interactions within multi-planet systems. In particular I consider the dynamical evolution of known planetary systems resulting from an additional hypothetical planet on an eccentric orbit. I start with an analytical study of a general two-planet system, showing that a planet on an elliptical orbit transfers all of its eccentricity to a planet on an initially circular orbit if the two planets have comparable orbital angular momenta. Application to the single super-Earth system HD38858 shows that an additional hypothetical planet below current radial velocity (RV) constraints with an *Msini*=3-10$M_\oplus$, semi-major axis of 1-10au and eccentricity of 0.2-0.8 is unlikely to be present from the eccentricity that would be excited in the known planet (albeit cyclically). However, additional planets in proximity to the known planet could stabilise the system against secular perturbations from outer planets. Moreover these additional planets can have an *Msini* below RV sensitivity and still affect their neighbours. For example, application to the two Super-Earth system 61Vir shows that an additional hypothetical planet cannot excite high eccentricities in the known planets, unless its mass and orbit lie in a restricted area of parameter space. Inner planets in HD38858 below RV sensitivity would also modify conclusions above about excluded parameter space. This suggests that it may be possible to infer the presence of additional stabilising planets in systems with an eccentric outer planet and an inner planet on an otherwise suspiciously circular orbit. This reinforces the point that the full complement of planets in a system is needed to assess its dynamical state. The work presented in this Chapter has been published in Read & Wyatt 2016.

Planet	a (au)	*Msini* ($M_\oplus$)	e	Period (days)	ω (degrees)
HD38858b	0.642 ± 0.002	12 ± 2	-	198 ± 1	-
61Vir-b	0.050201 ± 0.000005	5.1 ± 0.5	0.12 ± 0.11	4.22	105 ± 54
61Vir-c	0.2175 ± 0.0001	18.2 ± 1.1	0.14 ± 0.06	38.02	341 ± 38

Table 3.1 Orbital parameters for the planets of HD38858 and 61Vir given in Kennedy et al. 2015 from Marmier et al. in prep and Vogt et al. 2010.

3.2 Chapter Introduction

Since the discovery of the first stellar multi-planetary system ν Andromedae (Butler et al., 1999), the number of current detections stands at 487[1]. Compared with single systems, multiplicity introduces dynamical interactions between planets, leading to an evolution of orbital elements. Whether dynamics can be used to probe the formation mechanisms of exoplanets is an on-going topic of research, however it is possible that evidence of early interactions may be imprinted on the orbital elements of planets in current observations. An often quoted example is the relatively large eccentricities seen across the exoplanet population discussed in §1.7.1 (e.g. Butler et al., 2006; Mayor et al., 2011; Kane et al., 2012) which cannot be explained by migratory formation models alone, as coupling between the planet and protoplanetary disk promotes the circularisation of orbits (Lissauer, 1993). One dynamical process believed to account for this is post-formation gravitational planet-planet scattering brought on by a dynamical instability after the protoplanetary disk has dispersed (Rasio & Ford, 1996; Jurić & Tremaine, 2008; Raymond et al., 2009), with it being likely that secular interactions further evolve eccentricities on long timescales (Rasio & Ford, 1996; Lin & Ida, 1997; Yu & Tremaine, 2001; Zakamska & Tremaine, 2004; Rafikov, 2014).

Our understanding of different scenarios of dynamical interactions in multi-planetary systems during formation and beyond can also have implications for additional planets. For example, a dearth of low mass, close-in orbit planets is expected in areas of Hot-Jupiter migration (Mustill et al., 2015). The spacing of planets has also been attributed to the transfer of angular momentum between inner low mass and outer high mass gas giant planets (Laskar, 1997). The number of Jupiter sized objects scattered out to wide orbits detectable via direct imaging has also been predicted to be related to the number and radial distribution of close in planets (Veras et al., 2010). Thus the presence or absence of additional planets within a given system may give some insight into constraints on evolutionary history.

[1] exoplanet database, exoplanet.eu (Schneider et al., 2011)

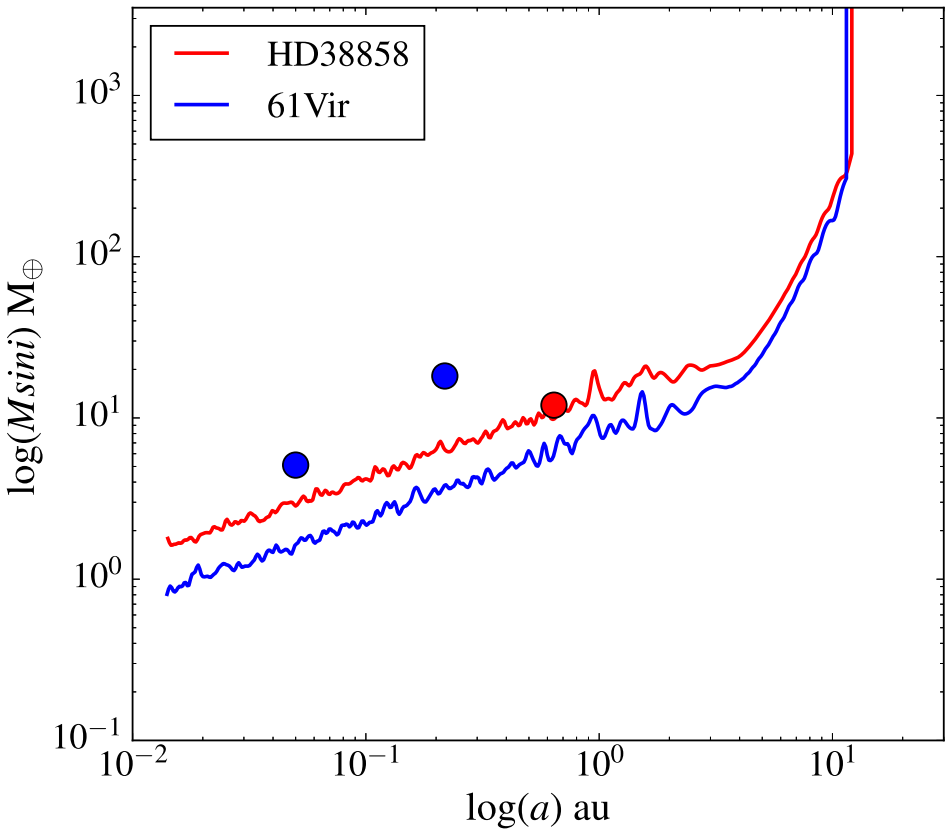

Figure 3.1 Super -Earth systems HD38858 (red) and 61Vir (blue). The respective planets of each system are represented by circles, alongside the current HARPS RV sensitivity. Sensitivity is quantified through identifying whether the signal generated by simulated planets is above the observational threshold, which is approximately that expected for 1m/s which has a semi-major axis dependence of $\sim a^{1/2}$ up to $\sim$8au due to the survey being active for $\sim$10yrs, not long enough to detect full periods from planets on wider orbits.

Our full interpretation of the dynamical state of known exoplanet systems is impeded by the fact that we have only partial knowledge of the planets that are present. As mentioned in §1.5.1, currently the HARPS radial velocity (RV) survey (Mayor et al., 2003) is one of the most sensitive to planet detection, measuring Doppler shifts down to as little as $\sim$1m/s, with detections resulting in an estimate that $\gtrsim$50% of solar-type stars harbour at least one planet (Mayor et al., 2011). The sensitivity of HARPS is shown in Figure 3.1, when applied to the super-Earth systems HD38858 and 61Vir (blue and red lines respectively, (Mayor et al., 2003, 2011; Kennedy et al., 2015). Since these systems are discussed in detail later in this Chapter I summarize the orbital parameters of the contained planets in Table 3.1 (Vogt et al. 2010a; Kennedy et al. 2015; Marmier et al. in prep). HARPS can only detect objects above the RV sensitivity, and provides no information on the existence or otherwise of objects below, as associated Doppler shifting would be too small or the orbital period too long. That is, Earth type planets on close in, $\sim$0.1au, orbits or any sized

object outside of ∼10au could be present in these systems without contradicting current observations.

I aim to understand how the dynamics of exoplanet systems are affected by the presence of extra hypothetical planets. The work in this Chapter focuses on systems currently known to have 1 or 2 planets, and in particular considers the long term secular interactions with an additional planet on an eccentric orbit. I subsequently explore the possibility of placing constraints (in addition to those placed by HARPS) on such hypothetical planets, by identifying where these objects would be expected to induce eccentricities in known planets that are significantly larger than observed values. I also consider whether these eccentricities induced in confirmed planets would be large enough to cause a potential scattering/collisional event between neighbouring planets. I focus application on a general 2 planet system and then to the specific planetary systems HD38858 and 61Vir. The close proximity of HD38858 and 61Vir and associated HARPS RV measurements provides the best chance for future follow-up studies to detect additional planets, for which this work can be used to guide. These systems also each have the benefit of an imaged debris disk at ∼30au (Wyatt et al., 2012; Kennedy et al., 2015), which is assumed to provide an outer constraint on the orbits of hypothetical planets and an estimate for orbital inclination of the planetary system. Understanding the dynamics of these systems may also go some way to explaining the abundance of super-Earths in exoplanetary systems, as it is estimated that as many as 30-50% of G-type stars host such objects (Batalha et al., 2013).

In this Chapter I first apply secular theory of eccentricity evolution outlined in §2.6 to a general 2-body system and then to HD38858b interacting with an additional object in §3.5 to investigate the dynamical evolution of a 2 (planet)-body system subject to secular perturbations and discuss any constraints that can be placed on hypothetical planets. Extension of this analysis to a 3 (planet)-body system is discussed through application to 61Vir secularly interacting with an additional planet in §3.6. I discuss a method of using secular theory to infer the presence of planets in §3.7, before comparing dynamical evolution made using secular theory with N-body simulations in §3.8. A final conclusion of the work in this Chapter is then given in §3.9.

3.3 Application of eccentricity secular theory

For the purpose of the work in this Chapter I assume that eccentricities and inclinations are small, allowing for the direct application of Laplace - Lagrange theory described in §2.6 to measure the eccentricity evolution of secularly interacting planets. I also assume that at high eccentricities this theory can still be applied as an approximation, which I quantify later in this Chapter through comparisons with N-body simulations. Finally, as eccentric-

ities are assumed to be small I treat secular resonances as occurring at fixed locations and ignore any inclusion of secular chaotic interactions. It is possible to include MMRs (§2.5) in secular theory (Malhotra et al., 1989; Christou & Murray, 1999; Agnor & Lin, 2012), however to simplify the discussion I assume that planetary orbits are well spaced and away from MMRs. Thus I note that the results may not capture all of the relevant dynamics when considering planets with semi-major axis ratios defined by eq (2.8). I also assume that motion may be chaotic, and the system is unstable inside the region given in eq (2.9). If the separation of the pericentre and apocentre of neighbouring objects is within a distance of $5R_H$, I also assume a scattering event can occur and the system is unstable. I use R_H in the low eccentricity limit defined by eq (2.7) for simplicity. I note that assumed scattering events are the more stringent constraint on how close planets can orbit when compared with the region of resonant overlap given in eq (2.9), as this is expected to only go out to ∼3 Hill radii (Ida et al., 2000; Kirsh et al., 2009).

3.4 Generalised 2-body Interactions

Initially I consider the eccentricity evolution of two planets interacting via secular perturbations only, with the assumptions stated in §3.3. These planets have masses and semi-major axes of M_1, M_2 and a_1, a_2 respectively, where M_1 is initialised on a circular orbit interior to M_2, which is on an eccentric orbit with an initial eccentricity $e_2(0)$. Both planets orbit a star of mass $M_\star$ and have respective initial longitudes of pericentre of $\varpi_1(0)$ and $\varpi_2(0)$.

I propose various substitutions to the form of eq (2.14) to simplify the secular solution for the evolution of eccentricity. I give the ratio of the Laplace coefficients (eq (2.13)) as the variable $f = b^{(1)}_{3/2}(\alpha) \Big/ b^{(2)}_{3/2}(\alpha)$, where $\alpha = a_1/a_2$ and introduce the variable $L_i = M_i a_i^{1/2}$ for a planet of mass M_i and semi-major axis a_i, which scales with orbital angular momentum for low eccentricity. The eccentricity solution for each planet (z_1, z_2) is then explicitly given by

$$\begin{aligned} z_1(t) &= \left(\frac{e_2(0)}{2y}\right) e^{i\varpi_2(0)} \left[e^{ig_2 t} - e^{ig_1 t}\right], \\ z_2(t) &= \left(\frac{e_2(0)}{2y}\right) e^{i\varpi_2(0)} \left[(y-x)e^{ig_1 t} + (x+y)e^{ig_2 t}\right], \end{aligned} \tag{3.1}$$

where $x = (f/2)(1 - L_1/L_2)$ and $y = \sqrt{x^2 + L_1/L_2}$. The associated eigenfrequencies are given

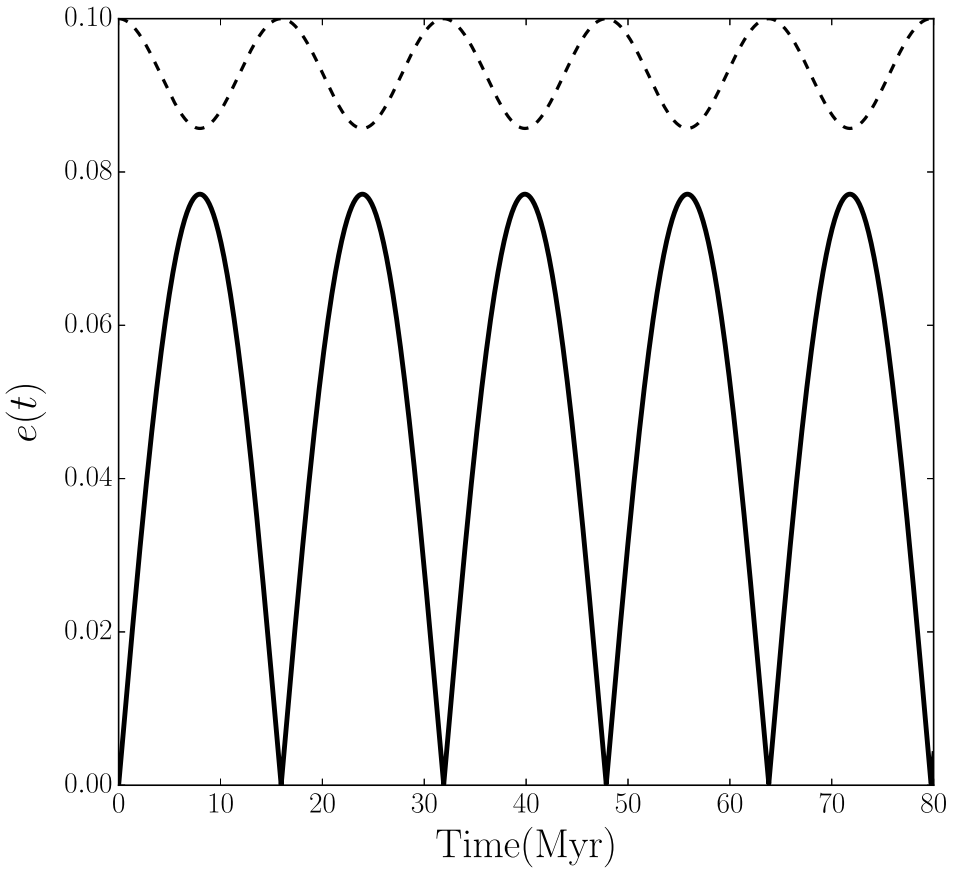

Figure 3.2 The evolution of eccentricity between an inner planet started on a circular orbit, M_1 (solid line) secularly interacting with a planet, M_2 (dotted line) of initial eccentricity $e_2(0) = 0.1$. Each planet has $5M_\oplus$ and placed at 1,5au respectively. The oscillation in the eccentricity of both planets, assuming that both eccentricities and inclinations are small, can be determined through a 2x2 eigenfrequency problem via application of Laplace - Lagrange theory. The timescale of the precession in eccentricity is $2\pi/g_1 - g_2$, where g_1, g_2 are the two eigenfrequencies of the system in radians per year.

by

$$\begin{aligned} g_1 &= -(A^*/2)\left[f(L_1+L_2) + \sqrt{f^2(L_1-L_2)^2 + 4L_1L_2}\right], \\ g_2 &= -(A^*/2)\left[f(L_1+L_2) - \sqrt{f^2(L_1-L_2)^2 + 4L_1L_2}\right], \end{aligned} \tag{3.2}$$

where $A^* = -\left(\pi a_1^{1/2} b_{3/2}^{(2)}(\alpha)\right) / \left(2\sqrt{M_\star} a_2^{5/2}\right)$ in radians per year, for a_1, a_2 and $M_\star$ in units of au and $M_\odot$ respectively. Figure 3.2 shows the oscillation in eccentricity from eq (3.1) for two example planets with M_1, M_2 of $5M_\oplus$ each and a_1, a_2 of 1, 5au respectively with the planet on the initially eccentric orbit being initialised with $e_2(0) = 0.1$. The timescale in years of a single period in this oscillation for both planets is given by $T = 2\pi/\left(g_1 - g_2\right)$.

Another way of visualising the evolution of $z_1(t)$ and $z_2(t)$ is to consider the evolution

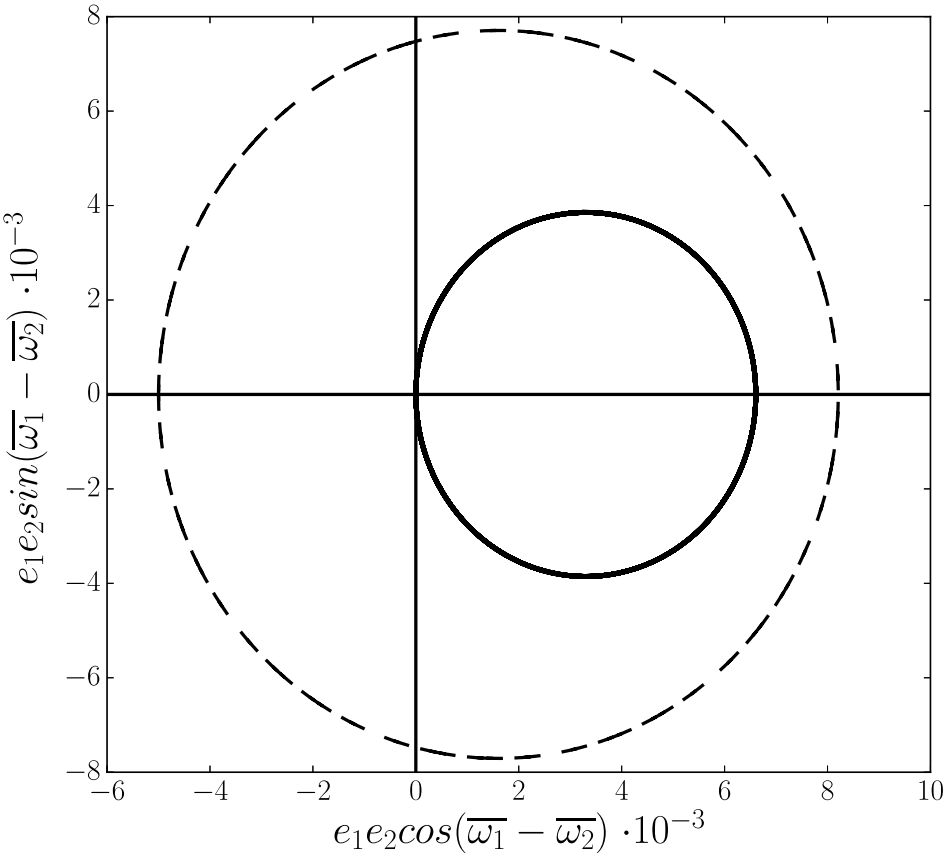

Figure 3.3 Evolution of $z_1 z_2^*$ for the example system shown in Figure 3.2, where both complex eccentricities are given in eq (3.1), and z_2^* is the complex conjugate of z_2. Such evolution for the example planets given in Figure 3.2 precesses around the solid circle. The dotted circle corresponds to when the planet on the initially circular orbit is initialised with an eccentricity of $e_1(0) = 0.05$. The pericentres of the two planets are started 180° apart. Evolution is similar to the previous case, with the effect of the extra initial eccentricity component $e_1(0) \neq 0$ shifting the radius and position of the circle.

of $z_1 z_2^*$ (where z_2^* is the complex conjugate of z_2), which shows precession around a circle in an anti-clockwise direction (see solid circle in Figure 3.3), highlighting the coupling of the secular solution that exists between the two planets.

The maximum in the eccentricity oscillation of the planet on the initially circular orbit, $\max[e_1(t)]$, as a result of the interaction with the planet on the initially eccentric orbit, as a function of its initial eccentricity $e_2(0)$, is given through the associated amplitude of $z_1(t)$ in eq (3.1)

$$\max[e_1(t)/e_2(0)] = \left[\frac{L_1}{L_2} + \frac{1}{4}f^2\left(\frac{L_1}{L_2} - 1\right)^2\right]^{-1/2}. \tag{3.3}$$

Through inspection, it becomes evident that $\max[e_1(t)/e_2(0)]$ equals unity at points of $L_1 = L_2$, implying that the planet on the initially circular orbit will have a maximum ec-

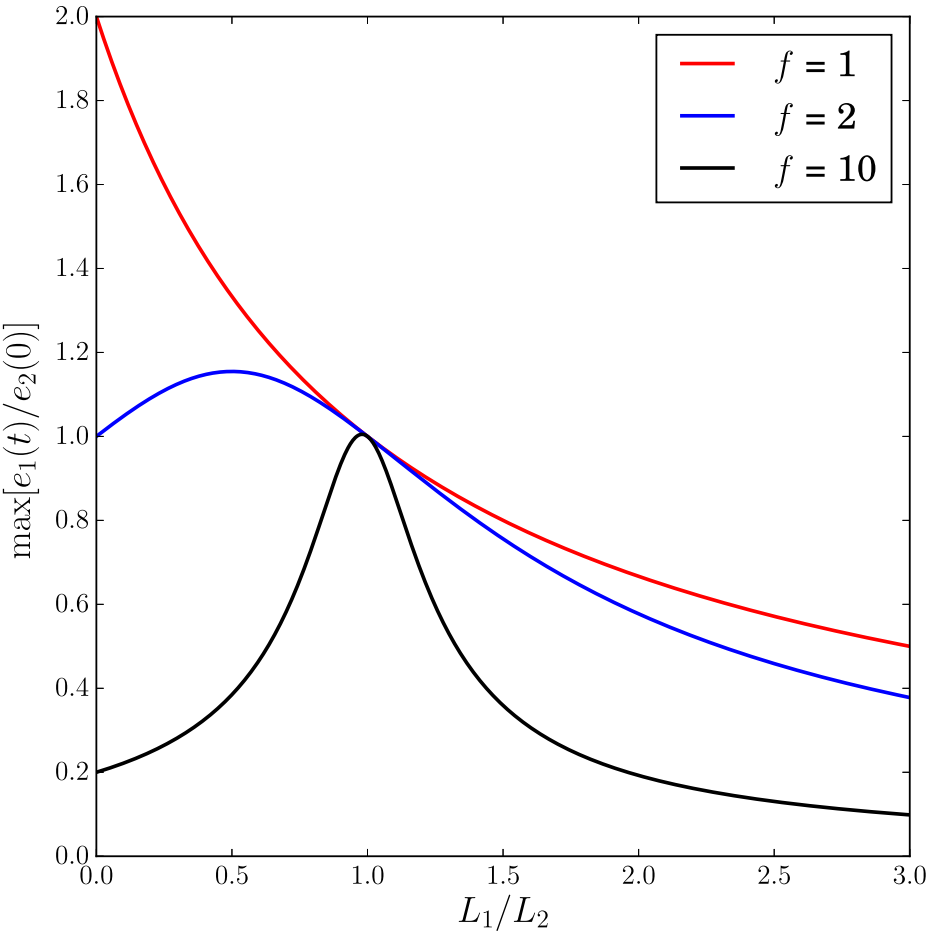

Figure 3.4 Maximum eccentricity of a planet on an initially circular orbit M_1 due to secular perturbations of a planet on an initially eccentric orbit M_2 as a function of L_1/L_2 (which is approximately the ratio of the angular momentum of the two bodies) for planets with different separations characterised by the parameter f. Regimes of equal orbital angular momentum between the two planets (in the low eccentricity limit) causes the maximum of the oscillation in eccentricity for the planet on the initially circular orbit to be equal to the initial eccentricity of the planet on the initially eccentric orbit.

centricity equal to the initial eccentricity of the planet on the initially eccentric orbit. Remembering my definition of L_1, L_2, it suggests that this will occur when the planets share an equal orbital angular momentum in the low eccentricity limit ($L_1 = L_2$). I show this in Figure 3.4, plotting eq (3.3) as a function of L_1/L_2, for various values of f.

The subtlety of varying f becomes important when considering the value of L_1/L_2 that maximises eq (3.3). By taking associated derivatives, one finds this occurs at $L_1/L_2 = 1 - 2/f^2$. For the $f \gg 1$ regime, eq (3.3) is indeed maximised when both bodies share equal orbital angular momentum (in the low eccentricity limit). When considering small f values on the order of unity, eq (3.3) has a maximised value where $e_1(t) > e_2(0)$ such that the maximum eccentricity of the planet on the initially circular orbit is greater than the initial

eccentricity of the planet on the initially eccentric orbit. Realistically such f values tend to limits where planets share small separations ($1.0 > \alpha \gtrsim 0.9$), which would most likely occur in regions where scattering or chaotic interactions can occur. Secular interactions of the most interest can therefore be assumed to be in the $f \gg 1$ regime.

When considering the limits of Figure 3.4 they can be seen to agree with expectations, as for $L_1 \gg L_2$ (implying a case where $M_1 \gg M_2$), the planet on the initially circular orbit is massive enough to be unaffected by the secular perturbations of the planet on the initially eccentric orbit, hence it remains circular such that $e_1(t) \sim 0$. The opposite case of $L_1 \ll L_2$ implies that the planet on the initially circular orbit instead tends to a limit where its behaviour is similar to that of a massless test particle ($M_1 \ll M_2$). One can evoke the well studied problem of a test particle in a secularly interacting system to explain this motion, which was touched upon in §2.6.1 and given in detail in Murray & Dermott 1999. In this case $z_1(t)$ precesses around a circle centred on the forced elements given by $z_2(0)/f$, resulting in an associated maximum eccentricity of $\max[e_1(t)] = 2e_2(0)/f$.

I further demonstrate eq (3.3) by plotting it as a function of both the semi-major axis and mass ratio of both planets, M_2/M_1 and a_2/a_1 respectively, which I show in Figure 3.5. The maximum eccentricity induced in the planet on the initially circular orbit by the planet on the initially eccentric orbit, $\max[e_1(t)/e_2(0)]$, (eq (3.3), also shown by the vertical axis in Figure 3.4) is now represented by the colour scale. Our choice of axis allows for the planet on the initially eccentric orbit to be both interior and exterior to the planet on the initially circular orbit.

It is clear that the maximum in the eccentricity oscillation of the planet on the initially circular orbit is equal to the initial eccentricity of the planet on the initially eccentric orbit ($\max[e_1(t)/e_2(0)] = 1$ in eq (3.3)) at regions of equal angular orbital momentum (in the low eccentricity limit) regardless of the f value. This occurs along a straight line in Figure 3.5, which I denote in black. The low f regime ($f \sim 1$) can also be clearly identified in Figure 3.5 at close separations between the planets ($\alpha \sim 1$). Here the maximum eccentricity of the planet on the initially circular orbit tends to the limit of $\max[e_1(t)] = 2e_2(0)/f$ from eq (3.3). As described before, some form of close encounter instability between the planets would most likely occur in this region. The high f regime ($f \gg 1$) in Figure 3.5, where secular interactions are of most interest, refers to wider separations between the planets. The maximum eccentricity the planet on the initially circular orbit can have in this regime tends to the limit of $e_1(t) = e_2(0)$ from eq (3.3), which is traced by the black line (e.g. where the two planets have comparable orbital angular momentum).

As Figure 3.5 is plotted in terms of ratios, the underlying shape of the maximum eccentricity of the planet on the initially circular orbit (e.g. the colour scale) will never change. This makes it completely generalised for direct application to similar two planet systems,

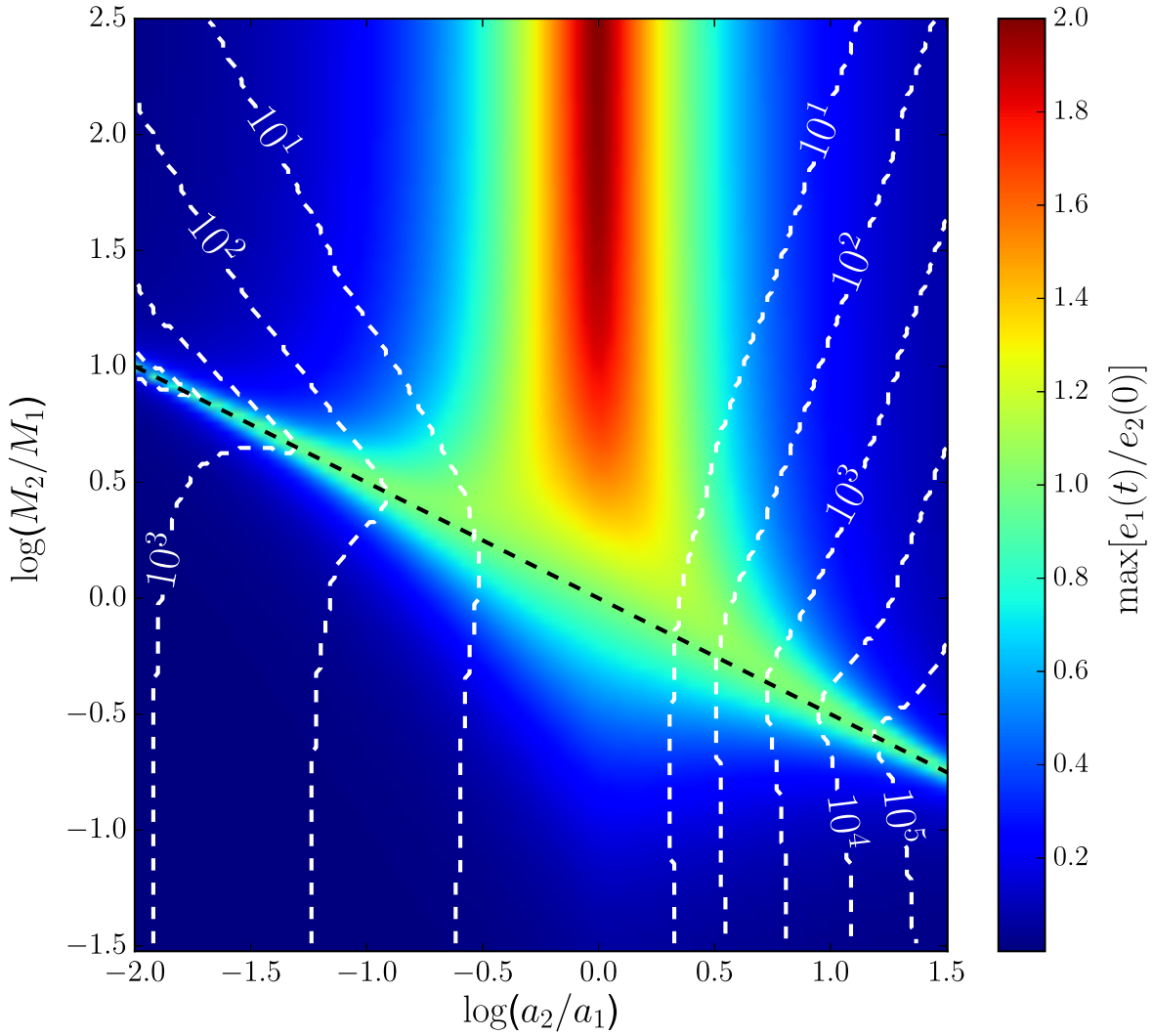

Figure 3.5 Colour scale gives the maximum eccentricity of a planet on an initially circular orbit due to secular perturbations of a planet on an initially eccentric orbit (as a function of its initial eccentricity $e_2(0)$) for a given mass and semi-major axis ratio between the two objects. The region of equal orbital angular momentum (in the low eccentricity limit) between the two planets is given by the black line, showing where the maximum eccentricity of the planet on the initially circular orbit is equal to $e_2(0)$. The white contours are values of K in eq (3.5), which when multiplied by the orbital period of the planet on the initially circular orbit and its mass ratio with the central star ($M_\star/M_1$), give the timescale of a single oscillation period in the eccentricity of both planets.

observational or otherwise.

I note that as the eccentricity of both planets oscillates on a timescale of $T = 2\pi/\left(g_1 - g_2\right)$, the planet on the initially circular orbit will only be at a maximum in its eccentricity for a very small period of time. By substituting in eq (3.2), T in years is explicitly given by

$$T = \frac{4}{b^{(2)}_{3/2}(\alpha)} \left(\frac{a_2}{a_1}\right)^{5/2} \left[f^2 \left(1 - \frac{L_2}{L_1}\right)^2 + 4\frac{L_2}{L_1}\right]^{-1/2} P_1 \frac{M_\star}{M_1}, \tag{3.4}$$

which can be simplified to say that

$$T = K P_1 \frac{M_\star}{M_1} \tag{3.5}$$

where P_1 is the orbital period of the planet on the initially circular orbit. The value K in eq (3.5) is therefore a function of constants and the mass and semi-major axis ratios of the two planets given in eq (3.4). When the planet on the initially eccentric orbit is interior to the planet on the initially circular orbit ($a_2 < a_1$), a substitution can be made to K in eq (3.5) to keep eq (3.4) as a function of $P_1 M_\star/M_1$. This is done by switching a_1 with a_2, M_1 with M_2 and vice versa. The $(a_2/a_1)^{5/2}$ factor is also replaced by $(a_1 M_1/a_2 M_2)$. I show different values of K through the dashed white lines in Figure 3.5.

While I have discussed the case where one of the planets started on an initially circular orbit, the evolution is similar if that planet were started on an eccentric orbit. For example the Figure 3.3 shows the evolution of $z_1 z_2^*$ when the planet previously started on the circular orbit is initialised with an eccentricity $e_1(0)$=0.05 (dotted circle). Evolution is still around a circle but with a shifted centre and radius. The timescale of the interaction given in eq (3.4) remains unchanged, with a dependence purely on mass and semi-major axis. In the $f \gg 1$ regime, maximum transfer of eccentricity still occurs when $L_1 \approx L_2$, though the exact maximum depends on the initial difference in the longitude of pericentres.

Whether the transfer of eccentricity predicted by eq (3.3) occurs in systems with a higher number of planets is unclear as the secular solution becomes more complex (e.g. Zakamska & Tremaine 2004). I first apply this generalised 2-body secular theory to HD38858 by introducing a hypothetical planet into the system. I also now include treatment for how close planets can orbit before an instability may occur, outlined in §3.3. I then see specifically if eq (3.3) is still valid in describing a 3-body problem through application to 61Vir interacting with a hypothetical planet in §3.6.

3.5 2 body application to HD38858

HD38858 is a relatively close, $0.9M_{\odot}$ solar type G4V located in the constellation of Orion at a distance of 15.18 ± 0.09pc (Lawler et al., 2009; Wyatt et al., 2012; Boyajian et al., 2013). Various age estimates exist from 200Myr (Casagrande et al., 2011), to 2.32 – 8.08Gyr (Takeda et al., 2007) and 9.3Gyr (Sousa et al., 2010). Notably, HD38858 is part of a tentative correlation between low mass (sub-Saturn) planets and the presence of a debris disk (Wyatt et al., 2012). As shown in Figure 3.1 the HARPS survey detects a single super -Earth mass planet, HD38858b, with *Msini* = $12.0 \pm 2.0M_{\oplus}$ and semi-major axis of 0.642 ± 0.002au (Kennedy et al. 2015; Marmier et al. in prep). Derivation of further orbital parameters are expected to be presented in Marmier et al. (in prep), as such I simply consider a case where HD38858b has a circular orbit. It should be noted that a HD38858b was first detected with HARPS to have a minimum mass of $\sim 30M_{\oplus}$ and semi-major axis of 1au (Mayor et al., 2011), however this signal has since been identified as stellar activity (see Kennedy et al. 2015 for further discussion). *Herschel* DEBRIS imaging resolves disk structure at 30 – 200au at an inclination of $44 \pm 5^{\circ}$ (Kennedy et al., 2015), supported by inferred structure at 102au from 70μm MIPS infrared excess (Wyatt et al., 2012) and lower resolution *Spitzer* images (Krist et al., 2012). Hereafter I assume this to be the inclination of the planetary system and so consider the mass of HD38858b to be $17M_{\oplus}$.

I introduce a hypothetical planet on an initially eccentric orbit to the system (HD38858c herein) and apply the secular interactions discussed in §3.4. I largely ignore the presence of the disk and any additional interactions it would have with planets, using the inner edge as an outer constraint for the orbit of HD38858c only and assuming it to be coplanar with both planets for all time. HD38858c is therefore initialised with an *Msini*, M_c, of $0.1M_{\oplus}$ – $10M_J$, semi-major axis, a_c, of 0.01 – 30au and eccentricity, $e_c(0)$, of 0.1 - 0.9. I refer to the maximum eccentricity of HD38858b due to its secular interaction with a given HD38858c as e_{bmax}. Due to the wide range of ages that exist for this system I simply calculate the secular interaction out to 1Gyr. I represent the ratio of $e_{bmax}/e_c(0)$ given by eq (3.3) as the colour scale in Figure 3.6. I plot masses in terms of *Msini* to directly include the raw HARPS RV sensitivity of this system, which I give by the red line. I acknowledge Mark Wyatt for an initial script used to calculate the secular interaction, from which my own code is based. The underlying shape of the colour scale is identical to that seen in Figure 3.5 and therefore I make no further discussion of it here. However I note again that when HD38858b and HD38858c share equal orbital momentum (in the low eccentricity limit), the maximum in the eccentricity oscillation of HD38858b is equal to the initial eccentricity of HD38858c. For larger semi-major axes of HD38858c in Figure 3.6, the timescale of the eccentricity oscillation increases according to eq (3.4). If this timescale is greater than

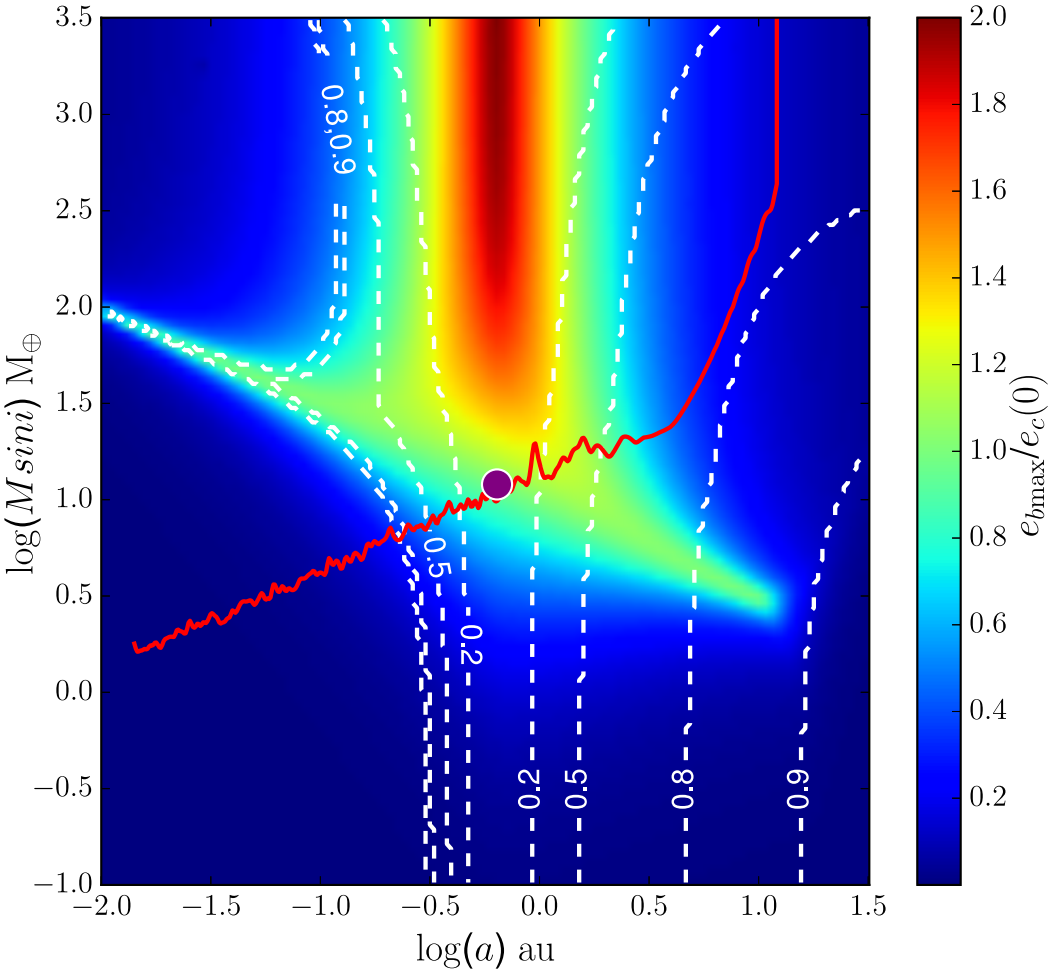

Figure 3.6 The maximum eccentricity of HD38858b (e_{bmax}) as a function of the initial eccentricity of a secularly perturbing hypothetical HD38858c ($e_c(0)$) of given *Msini* and semi-major axis over 1Gyr. HD38858b is given by the purple circle with the HARPS RV sensitivity being given by the red line. White dashed contours enclose areas of assumed close encounters (<5R_H) for varying $e_c(0)$.

1Gyr, HD38858b does not have time to reach a maximum in the oscillation. This causes the difference between the colour scales of Figure 3.5 and Figure 3.6 for a hypothetical HD38858c with a_c >10au.

The maximum eccentricities shown in Figure 3.6 are only valid in regions where the planets are always sufficiently separated for the effects of resonance overlap and close encounters between the planets to be negligible. Figure 3.6 also shows the regions where such close encounters might be expected to occur, that is, when at some point in the secular evolution the planets can possibly come within 5R_H as discussed in §3.3. The regions are outlined by contours representing the cases for different initial eccentricities of HD38858c. As noted in §3.3 this is always a more stringent constraint than the planets being close enough for resonance overlap. The size of this close encounter regime depends

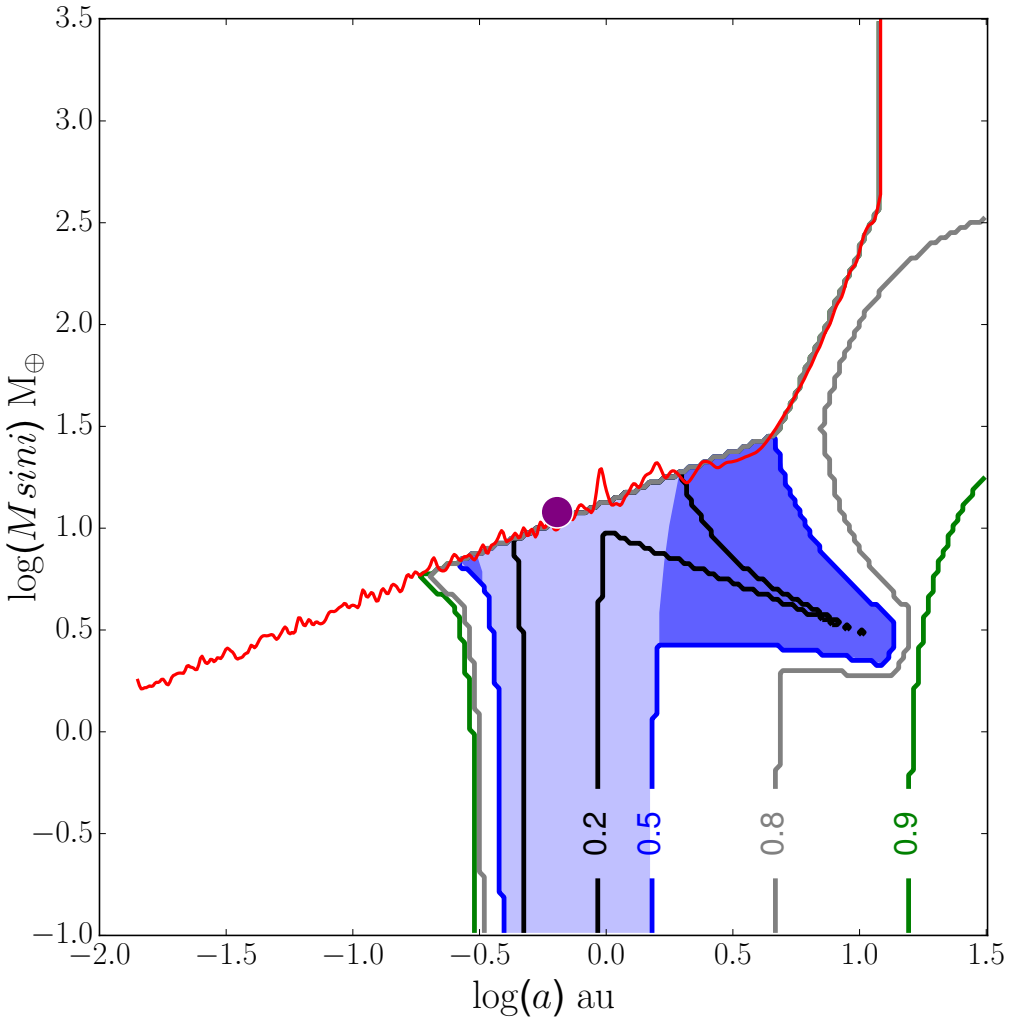

Figure 3.7 Contours represent constraints where a HD38858c with given initial eccentricity ($e_c(0)$) is unlikely to be present below the current HARPS RV sensitivity (red line). This is due to either a close encounter with HD38858b (purple circle) being likely at some point in the secular evolution (light blue shaded region, explicitly for $e_c(0) = 0.5$ for demonstration), or because HD38858b is secularly perturbed onto a significantly non-circular orbit (e_{bmax}>0.2, dark blue shaded region, explicitly for $e_c(0) = 0.5$). Contour labels refer to different values of $e_c(0)$. For clarity, the light/dark blue shaded region is representative of where a HD38858c with an $e_c(0) = 0.5$ would be unlikely to be present in HD38858 only, and is not fully representative of where a HD38858c would be unlikely to be present when $e_c(0)$ is changed.

on the initial eccentricity of HD38858c and it can be assumed that inside this region the 2-planet system is unstable on a short timescale.

By noting the minimum threshold of HARPS sensitivity, a hypothetical HD38858c can exist in HD38858 without contradicting current observations whilst potentially inducing a large eccentricity in the observationally confirmed HD38858b. This becomes interesting when considering possible constraints on hypothetical planets in HD38858 which are not

detectable via current HARPS sensitivity. If HD38858b was indeed measured by Marimer et al. to be on a roughly circular orbit, it would suggest that a hypothetical HD38858c may be unlikely to be present in regions where it induces a significant maximum eccentricity in HD38858b. However this does not mean that a HD38858c cannot be present in such regions, as potential eccentricity oscillations in HD38858b would be sinusoidal, thus its orbit may still appear roughly circular at a given moment in time. Similarly if the timescale of this oscillation is longer than the age of the system, HD38858bs orbit would potentially not have had sufficient time to have been perturbed onto a non-circular orbit. Thus, such an analysis only points to regions where a hypothetical HD38858c is unlikely to exist rather than being strictly ruled out.

In Figure 3.7 I show the regions below the HARPS RV sensitivity where a hypothetical HD38858c is unlikely to exist, either because of a potential close encounter interaction with HD38858b at some point in the secular evolution, or because the secular interaction between the two planets causes HD38858b to have a maximum eccentricity, given by eq (3.3), that is significantly non-circular (judged to be when e_{bmax} >0.2). Each contour corresponds to a different HD38858c initial eccentricity. For clarity, I explicitly shade in blue the region where a HD38858c with an $e_c(0) = 0.5$ below the HARPS RV sensitivity is unlikely to exist for the sake of demonstration. The light blue part of this shaded region refers to where such a HD38858c is unlikely to exist due to a potential close encounter with HD38858b at some point in the secular evolution. The dark blue part of this shaded region shows the further constraint of where such a HD38858c is unlikely to exist solely because the maximum eccentricity it induces in HD38858b from the secular interaction is too large (e_{bmax} >0.2), rather than because the two planets orbit close enough for a potential close encounter at some point in the secular evolution. This second constraint (e.g. the equivalent of the dark blue shaded region in Figure 3.7 for a HD38858c with an $e_c(0) = 0.5$) also exists for a HD38858c with an $0.2 \lesssim e_c(0) \lesssim 0.8$. I note that the shaded light/dark blue region in Figure 3.7 is representative of where a HD38858c that has an eccentricity $e_c(0) = 0.5$ only is unlikely to be present in HD38858. This light/dark blue shaded region is therefore not fully representative of where a HD38858c with a different initial eccentricity ($e_c(0) \neq 0.5$) would be unlikely to be present in HD38858.

While the region where HD38858c is unlikely to exist below the HARPS RV sensitivity, solely due to its secular interactions causing HD38858b to have an e_{bmax} >0.2 only, may be relatively small, it encapsulates an interesting area of the parameter space, namely a HD38858c with a mass between 3-10$M_\oplus$ and semi-major axis between 1-10au. I conclude therefore that it is useful to consider if significant eccentricities are induced between secularly interacting planets, not only in HD38858 but also in other single planetary systems. If this were the case it would add an extra constraint on the regions where a hypothetical

planet is unlikely to be present, in addition to the perhaps more obvious interaction of where the planets may scatter/eject one another.

3.6 3 body application to 61Vir

At 8.55 $\pm$ 0.02pc (van Leeuwen, 2007), 61Virginis (61Vir/HD115617) is the 8th closest G-type star (G5V) to the Sun with a mass of 0.88$M_\odot$ (Cenarro et al., 2007; Sousa et al., 2008). Age estimates place it to be relatively old, in the region of 3 – 11.5Gyr (Valenti & Fischer, 2005; Cenarro et al., 2007; Takeda et al., 2007), with most recent estimates from gyrochronology placing it at 4.6 $\pm$ 0.9Gyr (Wright et al., 2011; Vican, 2012). KECK/HIRES and HARPS RV measurements confirm two super-Earth type planets: 61Vir-b and 61Vir-c, with an *Msini* and semi-major axis of 5.1 $\pm$ 0.5$M_\oplus$, 18.2 $\pm$ 1.1$M_\oplus$ and 0.05au, 0.218au respectively, shown in Figure 3.1 along with the current HARPS sensitivity (Vogt et al., 2010a; Wyatt et al., 2012). The full set of orbital elements for 61Vir-b and 61Vir-c derived by Vogt et al. 2010a are given in Table 3.1. Vogt et al. 2010a also detected a third planet with an *Msini* and semi-major axis of 22.9 $\pm$ 2.6$M_\oplus$ and 0.48au respectively. However much like the original detection of HD38858b, this was identified to be a stellar signal (Wyatt et al., 2012). *Herschel* DEBRIS imaging has identified a debris disk at $\sim$30-100au with an inclination of $\sim$77° (Wyatt et al., 2012). I again assume this to be the inclination of the planetary system and so consider that 61Vir-b and 61Vir-c have a mass of 5.2$M_\oplus$ and 18.7$M_\oplus$ respectively.

I consider the 3-body secular problem of 61Vir-b and 61Vir-c interacting with a hypothetical planet on an eccentric orbit (called 61Vir-d herein). I calculate the maximum eccentricity induced in the outer planet, 61Vir-c, from 61Vir-d which I refer to as e_{cmax} (with the effects on/from 61Vir-b still being included in our calculations). Any deviation from the 2-body interaction described by eq (3.3) is therefore due to the presence of the third body (61Vir-b in this case). For simplicity I initialise 61Vir-b and 61Vir-c on circular orbits, since derived eccentricities are also consistent with $\sim$0 from Table 3.1, and assume all objects to be coplanar with the disk for all time. I also calculate the secular interaction out to 4.6Gyrs. I include 61Vir-d in the same way as HD38858c in §3.5, using the inner edge of the disk (30au) as an outer constraint only, initialising 61Vir-d with an *Msini*, M_d, of 0.1$M_\oplus$ – 10M_J, semi-major axis, a_d, of 0.01 – 30au and eccentricity, e_d, of 0.1 - 0.9.

The colour scale in Figure 3.8 shows the maximum eccentricity induced in 61Vir-c as a function of the initial eccentricity of 61Vir-d ($e_{cmax}/e_d(0)$) that has a given *Msini* and semi-major axis. As the colour scale is a function of $e_{cmax}/e_d(0)$, it is independent of the initial eccentricity of 61Vir-d. Comparing Figures 3.6 and 3.8, there is a clear difference between the 2 and 3-body secular interaction, as the maximum eccentricity of 61Vir-c is not equal to the initial eccentricity of 61Vir-d in regions where they share an equal orbital

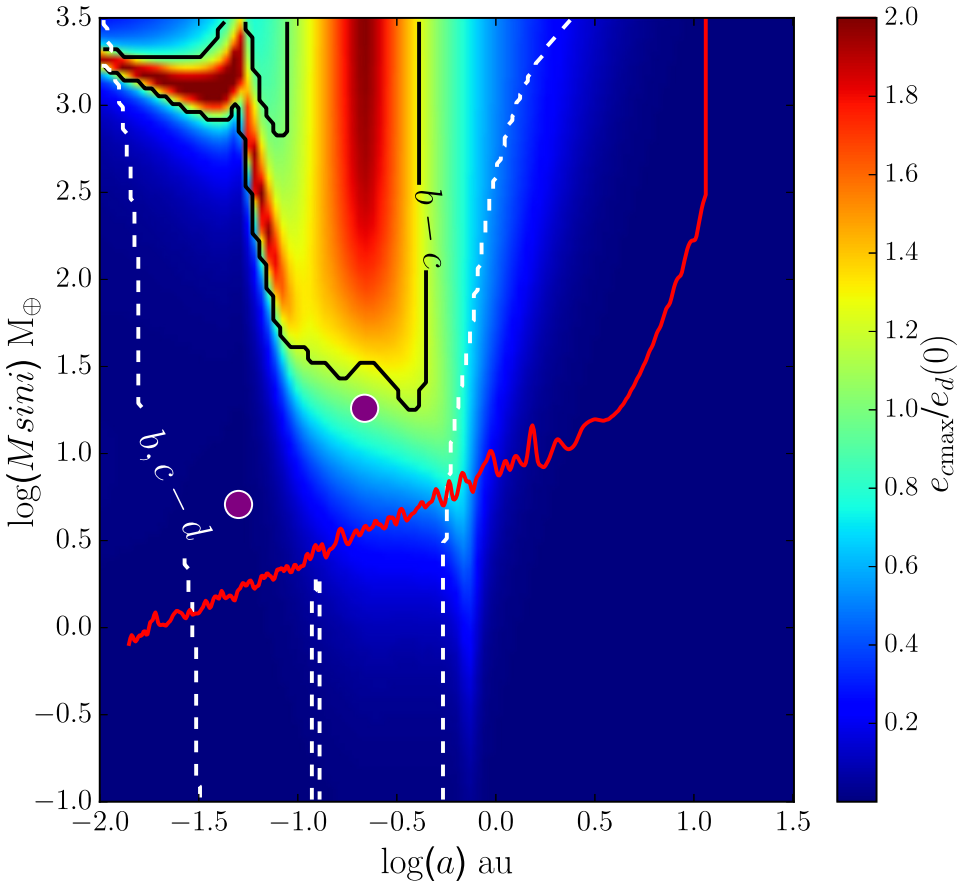

Figure 3.8 The maximum eccentricity of 61Vir-c (e_{cmax}) as a function of the initial eccentricity of a secularly perturbing hypothetical 61Vir-d ($e_d(0)$) of given mass and semi-major axis over 4.6Gyr. 61Vir-b/61Vir-c are given by the respective purple circles with the red line giving HARPS sensitivity. The white contour encloses a region where a close encounter would be likely between 61Vir-d with $e_d(0) = 0.5$ and 61Vir-b or 61Vir-c. The black contour encloses a region inside which a 61Vir-d with $e_d(0) = 0.5$ causes large enough perturbations in the eccentricity of 61Vir-b and 61Vir-c for a close encounter between the latter two bodies to be likely.

angular momentum (in the low eccentricity limit). Moreover outside of ∼1au in Figure 3.8, e_{cmax} becomes very small for all masses of 61Vir-d. As such, eq (3.3) does not describe the maximum eccentricity 61Vir-c will have due to the secular perturbations of 61Vir-d. The presence of 61Vir-b can therefore reduce the effect of the secular perturbations of 61Vir-d on 61Vir-c, even for a 61Vir-d outside of ∼1au that is significantly eccentric and massive. I also note that the eccentricity of 61Vir-d is also unchanged from the interaction with 61Vir-b and 61Vir-c.

This 'stabilising' of 61Vir-c by 61Vir-b can also be inferred from where the parameters of 61Vir-d cause the eccentricities of 61Vir-b and 61Vir-c to become large enough, such that one of the planet pairs come within a distance that may lead to a potential close en-

counter at some point in the secular evolution (<5R_H, outlined in §3.3). In Figure 3.8, I show that 61Vir-d with an $e_d(0) = 0.5$, causes such a potential close encounter specifically between 61Vir-b and 61Vir-c (solid black contour), only when this 61Vir-d itself already has a large enough eccentricity to potentially experience a close encounter with either 61Vir-b or 61Vir-c at some point in the secular evolution (dotted white contour). This behaviour is true regardless of the initial eccentricity of 61Vir-d.

Therefore I conclude that it is not possible for a highly eccentric, very massive 61Vir-d on a wide orbit below the HARPS RV sensitivity to induce a significant eccentricity in the inner planets through secular perturbations, causing them to potentially collide/eject each other at some point in the secular evolution. A caveat exists however that if a greater number of planets are included at much wider semi-major axes than I have considered here ($\sim$ 50-200au), then propagation of eccentricities through the planets may be expected, potentially causing large eccentricities in the inner planets (Zakamska & Tremaine, 2004).

The process that causes 61Vir-b to stabilise 61Vir-c against the secular perturbations of 61Vir-d can be understood by considering the timescales of the interactions between each of the planets. From eq (3.4), 61Vir-b and 61Vir-c secularly interacting in isolation produces an eccentricity oscillation in both planets that varies over $\sim$22kyrs. Adding a 61Vir-d at 10au with 10$M_\oplus$ imposes an additional eccentricity variation on the other planets that occurs on a timescale of $\sim$Gyrs. Any coherent increase in the eccentricity of 61Vir-c caused by the secular perturbations of 61Vir-d would therefore be affected by the shorter period interaction between 61Vir-b and 61Vir-c. I note that it is this effect that has recently been the focus of explaining the dearth of planets around short period ($P \lesssim 7$d) binaries (Hamers et al., 2015a,b; Muñoz & Lai, 2015; Martin et al., 2015). How low mass a '61Vir-b' equivalent object can be and still stabilise the system is considered in further application to HD38858 (§3.7).

As was discussed in §3.5 and shown explicitly for HD38858c in Figure 3.7, constraints can be placed on where 61Vir-d would be unlikely to be present below the HARPS RV sensitivity (below the red line in Figure 3.8). This occurs when a given 61Vir-d orbits within 5R_H of 61Vir-b or 61Vir-c at some point in the secular evolution and is assumed to experience a potential close encounter discussed in §3.3. This also applies where the secular perturbations of a given 61Vir-d causes 61Vir-c to have a maximum eccentricity significantly above the currently derived value such that $e_{cmax} > 0.2$ (Table 3.1 at limit of uncertainty). I show regions where 61Vir-d is unlikely to be present in Figure 3.9. Each contour corresponds to a different initial eccentricity of 61Vir-d. Also in a similar way to what was shown in Figure 3.7, I explicitly shade in blue where a 61Vir-d below the HARPS RV sensitivity with an eccentricity of $e_d(0) = 0.5$ is unlikely to exist for the sake of demonstration. The light blue region is where such a 61Vir-d experiences a potential close encounter with 61Vir-b

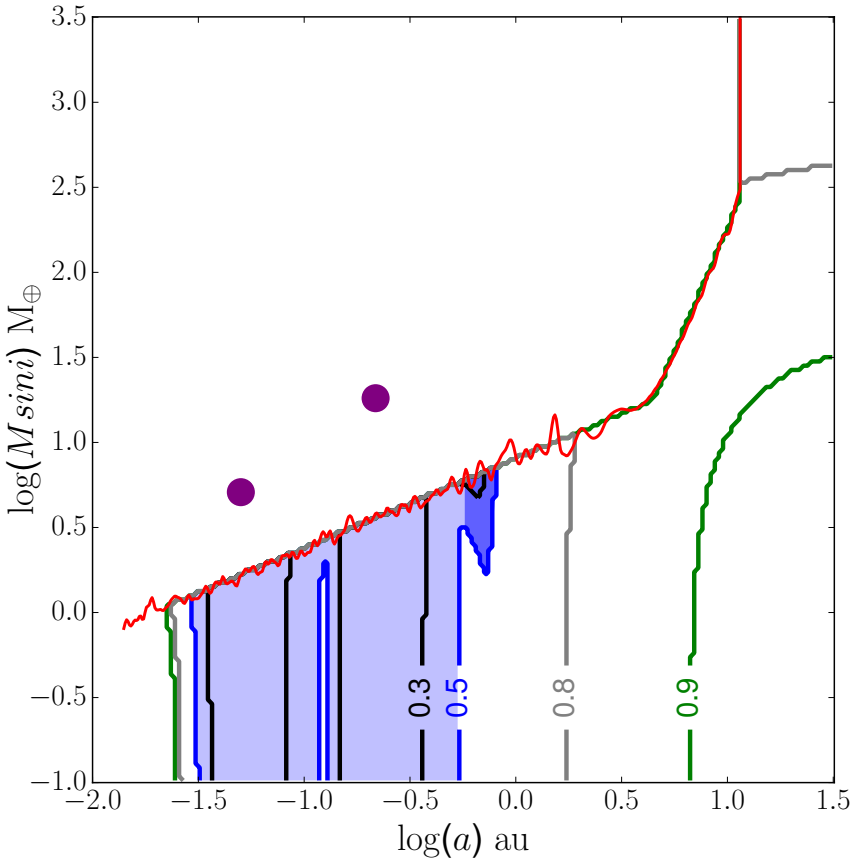

Figure 3.9 Constraints on where a 61Vir-d of a given $e_d(0)$, represented by each contour, is unlikely to be present in 61Vir below the HARPS RV sensitivity (red line). This is either due to a close encounter between 61Vir-d and 61Vir-c or 61Vir-b (purple circles) being likely (light blue shaded region, explicitly for $e_d(0) = 0.5$ for demonstration, or because 61Vir-c has a maximum eccentricity above 0.2 as a result of the secular interaction with 61Vir-d (dark blue shaded region, explicitly for $e_d(0) = 0.5$). Contour labels refer to different values of $e_d(0)$. The light/dark blue shaded region is representative of where a 61Vir-d with an $e_d(0) = 0.5$ would be unlikely to be present in 61Vir only, and is not fully representative of where a 61Vir-d would be unlikely to be present when $e_d(0)$ is changed.

or 61Vir-c at some point in the secular evolution. The dark blue region is where such a 61Vir-d causes 61Vir-c to have a maximum eccentricity $e_{cmax} > 0.2$ only, without the two planets orbiting close enough for a potential close encounter at some point in the secular evolution. As described for Figure 3.7 in §3.5 I note that the shaded light/dark blue region in Figure 3.9 is representative of where a 61Vir-d that has an eccentricity $e_d(0) = 0.5$ only is unlikely to be present in 61Vir, and is included for demonstration. This light/dark blue shaded region is not fully representative of where a 61Vir-d with a different initial eccentricity ($e_d(0) \neq 0.5$) would be unlikely to be present in 61Vir.

Comparing Figures 3.7 and 3.9, it is clear that the excluded parameter space for where a 61Vir-d is unlikely to exist, solely due to the secular interaction causing 61Vir-c to have a

maximum eccentricity $e_{cmax} > 0.2$, is much less than what was seen for the 2-body problem in §3.5 for HD38858c (e.g. comparing the dark blue shaded regions in Figure 3.7 and 3.9). This area of parameter space below the HARPS RV sensitivity only excludes a 61Vir-d with $0.3 \lesssim e_d(0) \lesssim 0.6$, for a mass and semi-major axis of 2-7$M_\oplus$ at ∼0.5au. Why this region is so much smaller than that seen for HD38858c in Figure 3.7 can be understood to be due to 61Vir-b reducing the influence of the secular perturbations of 61Vir-d on 61Vir-c. I conclude therefore that I can only place very limited constraints on where a 61Vir-d of given *Msini*, a_d and $e_d(0)$ would be unlikely to be present in 61Vir, by calculating where it induces a maximum eccentricity in 61Vir-c above its currently derived value of ∼0.2, and is such that it does not orbit close enough to 61Vir-c for a potential close encounter at some point in the secular evolution. I also suggest that this is more generally applicable to other planetary systems with two confirmed planets in close proximity to each other.

To summarize, I conclude that a consideration of secular interactions is unlikely to place significant constraints on an eccentric wide-orbit planet that is secularly interacting with a pair of inner planets on close circular orbits, assuming that the wide-orbit planet is below HARPS RV sensitivity. That is, in order to place constraints on massive planets on wide eccentric orbits in 61Vir and other 2-planet systems, one cannot use the orbits of the known planets. Other than directly detecting a wide-orbit planet, I suggest that investigations into the structure of an outer debris disk would provide the best type of constraints on such wide-orbit planets. Planets on eccentric orbits have been shown to cause unique ring structure (Pearce & Wyatt, 2015), sculpt the inner edge (Mustill & Wyatt, 2012) and define the radial density profile (Pearce & Wyatt, 2014). For example a 61Vir-d would only need to be at $\gtrsim$5au to secularly interact with material at the inner edge of the disk on a timescale less than the age of the system (4.6Gyr).

3.7 Stabilising in HD38858

I discuss a possible application of using the stabilising interaction between planets outlined in §3.6 to infer the presence of additional planets in a 2-body system. As such I return to the example of the known HD38858 planetary system secularly interacting with a hypothetical additional planet on an eccentric orbit (HD38858c) discussed in §3.5. Consider such a HD38858c in Figure 3.6 that causes a significant maximum eccentricity in HD38858b (e_{bmax}>0.2) through secular perturbations described in §3.4. Also assume that the two planets do not orbit within $5R_H$ at any point in the secular evolution and as such, a close encounter event between them is unlikely as outlined in §3.3. Finally consider that this HD38858c is on the threshold of the HARPS RV sensitivity in Figure 3.7 (on the red line), and that it is detected after the addition of further/reanalysis of RV data. For exam-

ple, if this HD38858c had an initial eccentricity of $e_c(0) = 0.5$, then this can be visualised in Figure 3.7 by considering a HD38858c in an area where the HARPS RV sensitivity (red line) and the dark blue shaded region meets.

As HD38858b is assumed to have an eccentricity of zero, the presence of this 'newly detected' HD38858c could infer either of the following: (1) HD38858b is not close to a maximum in eccentricity as a result of the secular interaction with HD38858c at the time of observations. (2) The 'newly detected' HD38858c does not actually have a large enough eccentricity to cause a significant eccentricity in HD38858b through secular perturbations ($e_{bmax} < 0.2$, discussed in §3.5 and shown in eq (3.1)). (3) There is a third object in HD38858 which is currently undetected, but is stabilising HD38858b against the secular perturbations of HD38858c in a way discussed in §3.6. I discuss the case where the last point is true.

I consider how massive and at what semi-major axis a third body (a hypothetical HD38858d) would have to be to reduce the effects of the secular perturbations of a HD38858c on HD38858b. For simplicity I assume that the hypothetical HD38858d is interior to HD38858b, on a circular orbit and is also on the limit of HARPS RV sensitivity. I also assume that a close encounter interaction between HD38858b and the internal hypothetical HD38858d (§3.3) is unlikely at any point in the secular evolution. This represents an ideal scenario where this stabilising inner HD38858d could also be detected upon follow up studies of RV data.

Figure 3.10 represents HD38858b (Table 3.1) as the purple circle along with the HARPS RV sensitivity represented by the red line. I show three different example HD38858ds interior to HD38858b on circular orbits, which are on the limit of HARPS RV sensitivity with an *Msini* and semi-major axes of roughly 2.4, 3.4, 4.8$M_\oplus$ and 0.03, 0.06 and 0.13au, represented by the green, grey and blue circles respectively. I label each HD38858d as d_1, d_2 and d_3 respectively. The respectively coloured contours show where a HD38858c would need to exist to have the maximum eccentricity it induces in HD38858b, divided by its own eccentricity ($e_{bmax}/e_c(0)$), halved due to the presence of the inner HD38858d. At this point I assume that this HD38858d has stabilised HD38858b against the secular perturbations of a HD38858c. For example any HD38858c that lies along the green contour in Figure 3.10 will have the maximum eccentricity it induces in HD38858b divided by its own eccentricity, $e_{bmax}/e_c(0)$, reduced by half, due to the presence of the inner HD38858d located at the green circle (d_1). As the contours are ratios of $e_{bmax}/e_c(0)$ both before and after adding the internal HD38858d they are independent of the initial eccentricity of HD38858c.

Consider for example a 'newly detected' HD38858c with an *Msini* and semi-major axis of 22$M_\oplus$ and 3.2au respectively with an eccentricity of $e_c(0) = 0.5$ (shown by the black circle in Figure 3.10). Figure 3.10 shows that the maximum eccentricity it induces in HD38858b is reduced by half when a HD38858d internal to HD38858b on a circular orbit

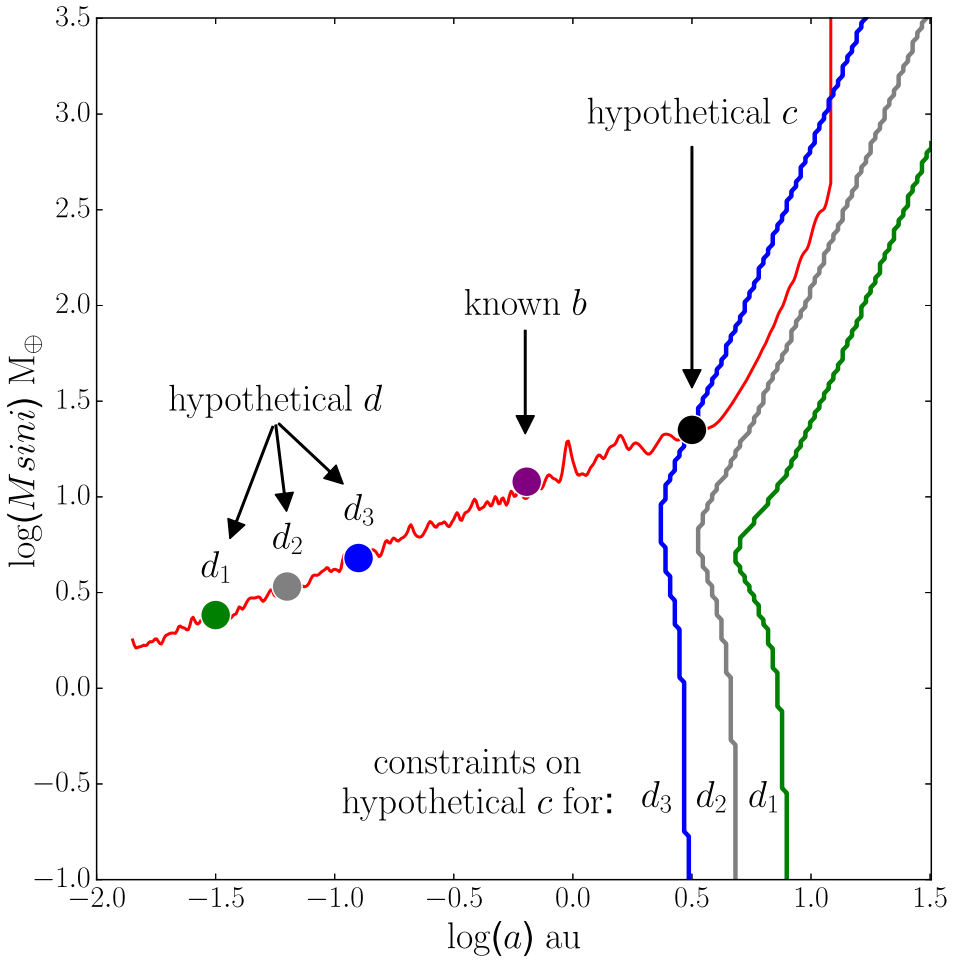

Figure 3.10 HD38858b in the presence of an inner hypothetical planet d. The contours show where an inner d reduces the secular perturbations of an outer hypothetical planet (c) on HD38858b by half. The black circle represents a specific outer hypothetical planet that should induce a large eccentricity in HD38858b from secular perturbations. If this planet were detected, it may infer the presence of planet interior to HD38858b located at the blue circle.

with 4.8$M_\oplus$ at 0.13au is present. Therefore if a HD38858c is detected at the black circle in Figure 3.10 with an eccentricity of $e_d(0) = 0.5$, then as this HD38858c should induce a significant eccentricity in HD38858b (e_{bmax} >0.2, seen in Figure 3.7), this could also infer the presence of an additional planet, possibly located at the blue circle on a circular orbit in Figure 3.10.

This is obviously a very specific example dependant on many considerations. To our knowledge a two planet system where one planet is on a circular orbit and the other is on a significantly eccentric orbit has also yet to be discovered. However if future observations do detect such systems, I predict further planets might be inferred using the above method. I also note that it is possible that any stabilising effect could be due to multiple planets. This technique would still be useful in inferring that *something* is causing a

stabilising effect whether it is a single or many objects.

More generally I conclude that an inner planetary system made up of multiple planets is shielded from dynamical interactions from planets in the outer system. Moreover these inner planets do not need to be massive to have a protective effect on their neighbours. This reinforces the point that the full complement of planets in a system is needed to assess its dynamical state.

3.8 Limitations of Secular Theory

Thus far I have assumed eccentricities are small ($\lesssim 0.2$), allowing for the application of second order Laplace - Lagrange theory (§2.6) to calculate the evolution of eccentricity of secularly interacting planets. Once eccentricities go above $\sim$0.2 this theory begins to break down and higher order terms in the expansion of the disturbing function are required, as discussed in §2.6. Assumptions for this work were also made in §3.3 that the effects of MMRs and long term secular chaotic interactions (e.g. Lithwick & Wu 2011) were negligible. I run N-body simulations to judge the validity of these assumptions, concentrating on application to 61Vir in §3.6, specifically to see if secular interactions are the dominant source of dynamical evolution in 61Vir and whether 61Vir-b actually damps the secular perturbations of a given 61Vir-d on 61Vir-c.

I use the N-body `Mercury6-2` code (Chambers, 1999) and incorporate a hybrid integrator that switches from a more computationally efficient second order mixed symplectic algorithm, to a more detailed Bulirsch-Stoer integration when planets orbit close enough, assumed to be at <5 Hill radii for which the accuracy parameter is set to 10^{-12}. I set the timestep to 0.2 days, which is equal to $\sim$1/20 of the orbital period of 61Vir-b (Table 3.1). I neglect GR effects, however this would be expected to change the precession period of the eccentricity oscillation in eq (2.14) rather than to have a significant effect on the maximum eccentricity (Veras & Armitage, 2007; Campanella et al., 2013).

I run a grid of Mercury simulations for which 61Vir-d has an *Msini* and semi-major axis of 10 – 562$M_\oplus$ and 1.12 – 6.31au respectively. This is assumed to be where the increase in the maximum eccentricity of 61Vir-c as a result of the secular interaction with 61Vir-d is of the most interest (see Figure 3.8). I run this grid twice, initialising 61Vir-d with an eccentricity of $e_d(0) = 0.1$ and $e_d(0) = 0.5$ to represent a low and high eccentricity regime respectively. I also assume that all planets are initially coplanar with the disk as described in §3.6. Each simulation is run to ten times the maximum secular period given by $\max(2\pi/\Delta g_i)$ where Δg_i is the difference between a given pair of eigenfrequencies (implied by eq (2.14)). Specifically this refers to run times of $\sim 10^5$ - 10^6yrs. I also run a subset of simulations out to 3Gyr to look for the possibility of very long term chaotic sec-

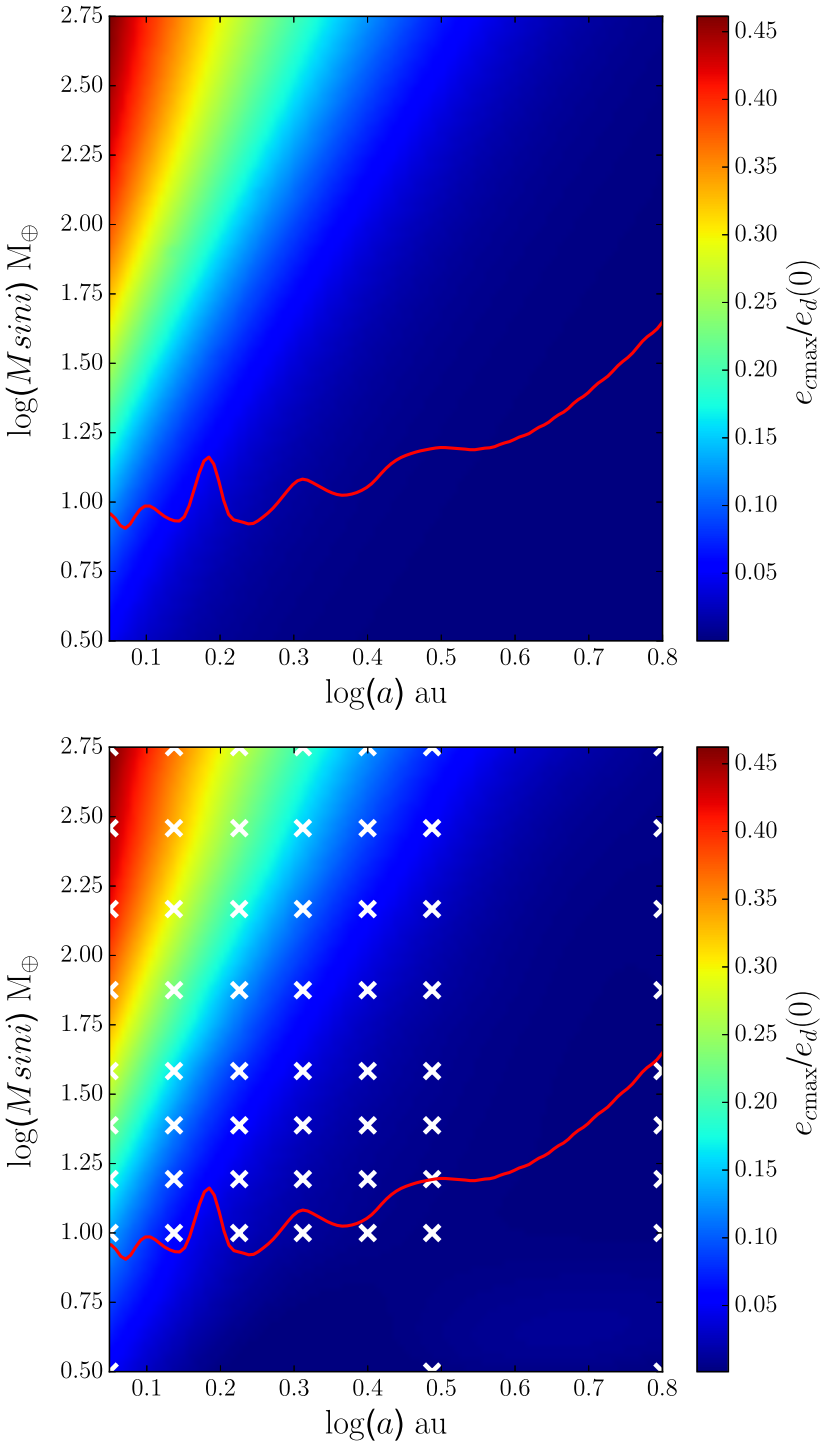

Figure 3.11 *(top)*: The maximum eccentricity induced in 61Vir-c by 61Vir-d, divided by the initial eccentricity of 61Vir-d, (e_{cmax}/e_d) calculated by second order Laplace - Lagrange theory. This is simply a sub-region of Figure 3.8. The red line represents HARPS RV sensitivity. *(bottom)*: e_{cmax}/e_d calculated by N-body simulations. White crosses represent individual simulations for when 61Vir-d is initialised with an eccentricity of $e_d = 0.1$. N-body simulations and second order Laplace - Lagrange theory predict the same e_{cmax}/e_d in the low eccentricity limit as expected.

ular effects (Lithwick & Wu, 2011). For direct comparison with Figure 3.8, the maximum eccentricity of 61Vir-c due to the secular interaction with 61Vir-d, divided by the initial eccentricity of 61Vir-d ($e_{cmax}/e_d(0)$) is calculated for each simulation.

Figure 3.11 shows the comparison between $e_{cmax}/e_d(0)$ (given by the colour scale) for a 61Vir-d with a given *Msini* and semi-major axis and initial eccentricity $e_d(0) = 0.1$, calculated by second order Laplace - Lagrange theory (top panel of Figure 3.11, from §2.6) and by Mercury simulations (bottom panel of Figure 3.11). Each individual simulation in the bottom panel of Figure 3.11 is given by the white crosses, with the colour scale being a cubic interpolation over these points. Whereas, the interpolation was over 200×200 grid in the top panel of Figure 3.11, as were the previous Figures 3.4, 3.6 and 3.8.

The top panel of Figure 3.11 can be thought of a just a sub-region of Figure 3.8. The values of $e_{cmax}/e_d(0)$ calculated by simulations and Laplace - Lagrange theory agree with each other to within a range of 6×10^{-3} (e.g. the maximum difference between values of the colour scale in the top and bottom panels of Figure 3.11 is 6×10^{-3}). This shows that second order Laplace - Lagrange theory is indeed a good predictor of secular evolution in the low eccentricity limit as expected. The bottom panel of Figure 3.11 also shows that the reduced effect of the secular perturbations of 61Vir-d on 61Vir-c due to 61Vir-b described in §3.6 is present in simulations, as a significant eccentricity is not induced in 61Vir-c when it has a similar orbital angular momentum to 61Vir-d.

Figure 3.12 shows the same comparison between $e_{cmax}/e_d(0)$ calculated by second order Laplace - Lagrange theory (top panel of Figure 3.12) and simulations (bottom panel of Figure 3.12), however now setting the initial eccentricity of 61Vir-d to $e_d(0) = 0.5$. The values of $e_{cmax}/e_d(0)$ calculated by simulations and Laplace - Lagrange theory now only agree to within a range of 0.2 (e.g. the maximum difference between the colour scales of the top and bottom panels of Figure 3.12 is 0.2). That is, simulations show that a significantly larger maximum eccentricity is induced in 61Vir-c by 61Vir-d, when compared with what is predicted by Laplace-Lagrange theory. This reflects the fact that higher order terms beyond those included in second order Laplace - Lagrange theory are required for large eccentricities as discussed in §2.6. However as the same relative increase in the maximum eccentricity of 61Vir-c due to the secular interaction with 61Vir-d is seen in both the top and bottom panels of Figure 3.12 (e.g. the gradient of the colour scales are similar), it suggests that 61Vir-b still reduces the effects of the secular perturbations of 61Vir-d on 61Vir-c in the high eccentricity limit. I conclude therefore that second order Laplace - Lagrange theory can be used as an approximation of the secular interaction between planets in 61Vir in the high eccentricity limit.

To highlight how much second order Laplace - Lagrange theory becomes an approximation of secular behaviour in the high eccentricity limit, I take a subset of our simula-

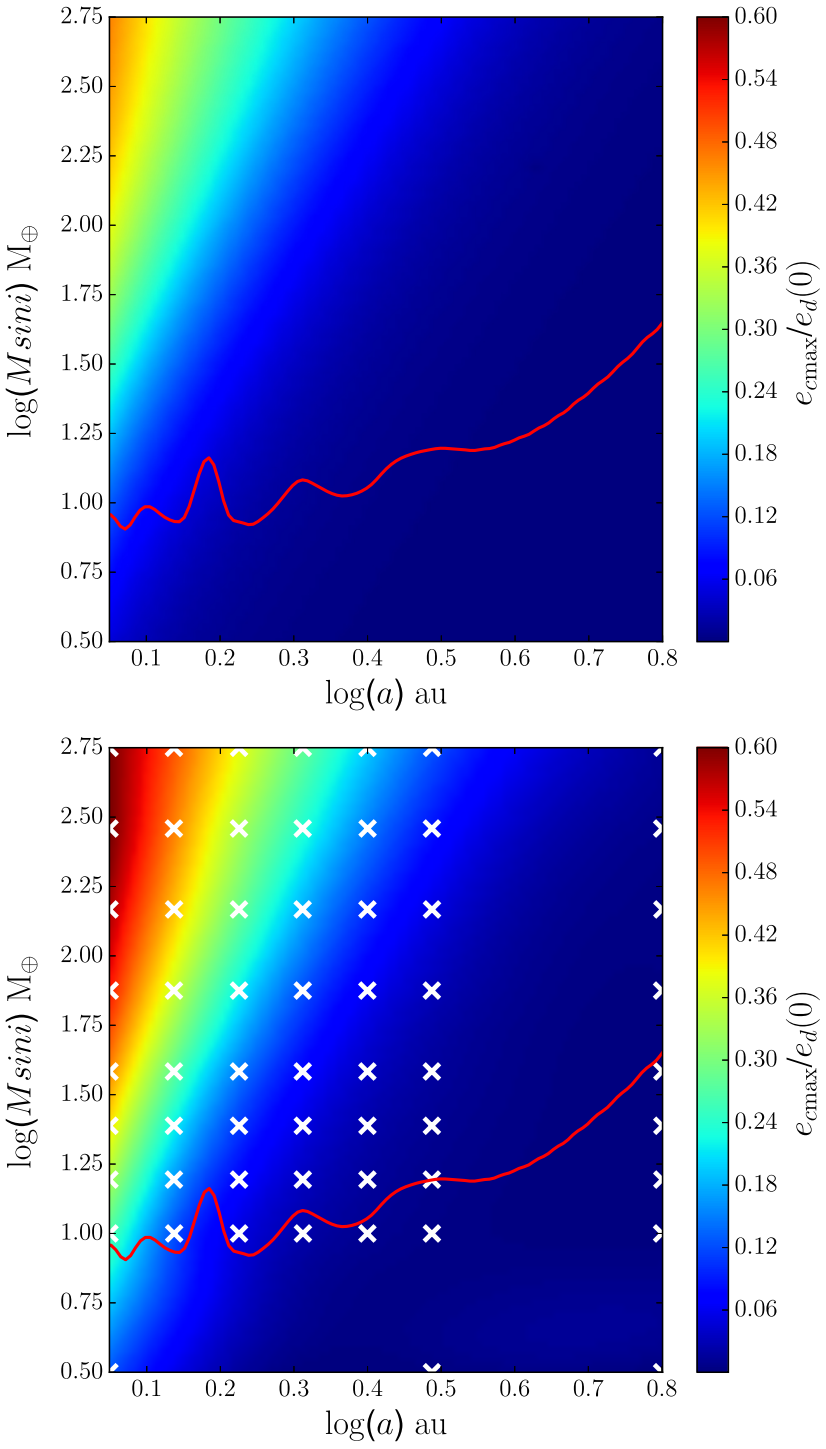

Figure 3.12 *(top)*: e_{cmax}/e_d (see Figure 3.11 caption for definition) calculated by second-order Laplace Lagrange theory (see Figure 3.8). The red line represents the HARPS RV sensitivity. *(bottom)*: e_{cmax}/e_d calculated by N-body simulations where the initial eccentricity of 61Vir-d is $e_d = 0.5$. White crosses represent individual simulations. Comparing with the top panel, second order Laplace - Lagrange theory underestimates the maximum eccentricity that is induced in 61Vir-c by 61Vir-d from secular perturbations in the high eccentricity limit. However 61Vir-b can still be seen in simulations to reduce the effects of the secular perturbations of 61Vir-d on 61Vir-c.

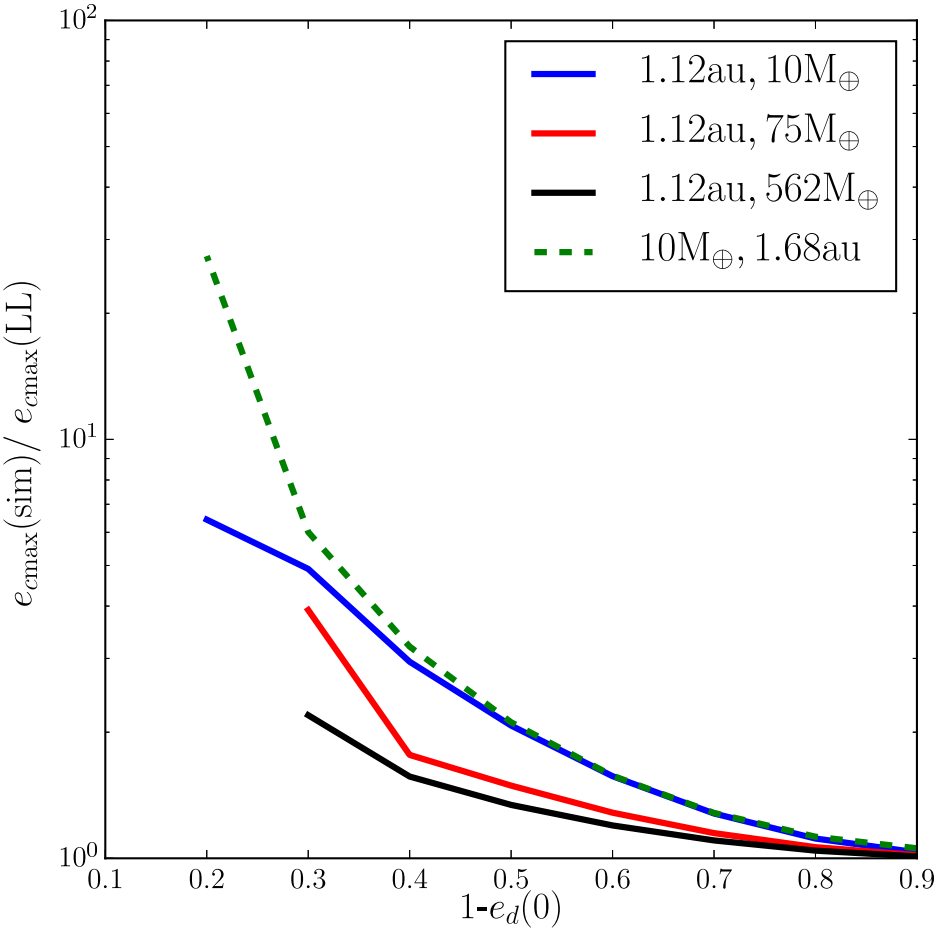

Figure 3.13 The ratio of the maximum eccentricity induced in 61Vir-c by 61Vir-d due to secular interactions, divided by the initial eccentricity of 61Vir-d, e_{cmax}/e_d, calculated by N-body simulations to second order Laplace - Lagrange theory, as a function of the initial eccentricity of 61Vir-d. Eccentricity evolution predicted by second order Laplace - Lagrange theory shares a stronger agreement with simulations in the low eccentricity limit.

tions and initialise 61Vir-d with an eccentricity $e_d(0) = 0.1 - 0.9$. This is done for a 61Vir-d with *Msini* = 10, 75, 562M$_\oplus$ at a semi-major axis a_d = 1.12au and for a_d = 1.68au with *Msini* = 10$_\oplus$. The ratio between the maximum eccentricity induced in 61Vir-c by 61Vir-d, divided by the initial eccentricity of 61Vir-d ($e_{cmax}/e_d(0)$) from simulations to second order Laplace - Lagrange theory is calculated for each of these *Msini* and a_d values of 61Vir-d. That is, a ratio of 1 means that simulations and second order Laplace - Lagrange theory predict an identical $e_{cmax}/e_d(0)$. Figure 3.13 plots this ratio against the initial eccentricity of 61Vir-d. The cut-off in some lines for high eccentricities occurs because a planet was ejected or scattered in our simulations. Figure 3.13 shows as the initial eccentricity of 61Vir-d is increased, $e_{cmax}/e_d(0)$ calculated by simulations becomes increasingly larger than what is predicted by second order Laplace - Lagrange theory, as expected from the discussion in §2.6.

I finally note that for the area of parameter space of 61Vir-d in Figure 3.11 and 3.12, MMRs seem to have a negligible effect, as simulations and second order Laplace - Lagrange theory show the same relative increase in the maximum eccentricity that is induced in 61Vir-c by 61Vir-d. This indicates that secular interactions between planets are the dominant source of dynamical evolution in 61Vir. However I note that a larger number of simulations would be required to confirm this, since our simulations only probed a limited number of semi-major axes and do not cover any significant MMRs. Our sub-set of simulations that were run out to long timescales ($\sim$3Gyr) also show no change in the maximum eccentricity of 61Vir-c as a result of the interaction with 61Vir-d, indicating that the effects of long term secular chaotic interactions are minimal.

3.9 Summary and Conclusions

I investigated how the dynamics of known exoplanet systems are affected by the presence of an extra hypothetical planet. I specifically focused on systems with 1 or 2 currently known planets, and considered the long term secular interaction with an additional hypothetical planet on an eccentric orbit. I subsequently investigated whether any constraints can be placed on such a hypothetical planet (in addition to those placed by HARPS RV measurements) by seeing if it were possible for this object to induce significant eccentricities in confirmed planets. I applied second order Laplace - Lagrange theory to calculate the eccentricity evolution of the planets due to their secular interaction, under the assumption that eccentricities remain small.

I initially considered a generalised 2-planet system, where one planet was on an initially circular orbit and the other initially on an eccentric orbit. I showed that the maximum eccentricity of the planet on the initially circular orbit, due to the secular interaction, is equal to the initial eccentricity of the planet on the initially eccentric orbit, when both planets have a comparable orbital angular momentum.

This generalised 2-planet secular interaction was then applied to the single planet system HD38858 in the presence of a hypothetical planet on an eccentric orbit. I showed that constraints can be placed on where this hypothetical planet would be unlikely to present below the HARPS RV sensitivity, solely due to the secular interaction causing an eccentricity in the known planet significantly above the low value observed. As potential eccentricity oscillations in the known planet would be sinusoidal however, its orbit may appear roughly circular at a given moment in time. Thus, this analysis places constraints on where a hypothetical planet is unlikely, rather than being strictly ruled out. These constraints apply to a hypothetical planet with an *Msini* of 3-10$M_{\oplus}$, a semi-major axis between 1-10au, and an eccentricity in the range 0.2 - 0.8. I concluded therefore that secular interactions

can be used to place significant constraints on hypothetical planets in single planetary systems, in addition to those placed by just considering where planets may scatter/eject one another.

Whether the type of constraint from secular interactions can be applied to a hypothetical planet in a known 2-planet system was investigated through application to the 61Vir system in the presence of an additional hypothetical planet on an eccentric orbit. I showed that the maximum eccentricity of the outer known planet is no longer equal to the initial eccentricity of the hypothetical planet when the two planets have a comparable angular momentum. The inner known planet therefore reduces the effect of the secular perturbations of the hypothetical planet on the outer known planet. Constraints on where a hypothetical planet would be unlikely to be present in 61Vir below the HARPS RV sensitivity, from secular interactions alone causing an eccentricity in the outer known planet above the low value observed are limited. These constraints apply to a hypothetical planet with an $Msini$=2.7$M_{\oplus}$, a semi-major axis of $\sim$0.5au and an eccentricity in the range of 0.3 - 0.6. I concluded therefore that the orbits of known planets cannot be used to place significant constraints on massive planets on wide eccentric orbits in 61Vir and other 2-planet systems. I suggest that the structure of an outer debris disk may provide the best constraints on wide-orbit hypothetical planets.

I investigated whether a hypothetical planet in the single planetary system HD38858, that is interior to the known planet can reduce the effects of the secular perturbations from an outer hypothetical planet. I showed that this can occur for the case where both the inner and the outer hypothetical planets are on the limit of HARPS RV sensitivity. This suggests that it may be possible to infer the presence of additional stabilising planets in systems with an eccentric outer planet and an inner planet on an otherwise suspiciously circular orbit. I concluded that inner planetary systems made up of multiple planets are shielded from dynamical perturbations from planets in the outer system. Moreover these inner planets do not need to be massive to have a protective effect on their neighbours. This reinforces the point that the full complement of planets in a system is needed to assess its dynamical state.

Finally I showed that for the case of the 61Vir system interacting with a hypothetical planet, N-body simulations also show that the inner known planet reduces the effects of the secular perturbations of a hypothetical planet on the outer known planet. I also showed by comparisons with N-body simulations that second order Laplace - Lagrange theory can be used as an approximation of secular interactions in the high eccentricity limit. However in this limit an under prediction of the maximum eccentricities that are induced between secularly interacting planets is expected when calculated by second order Laplace - Lagrange theory.

This Chapter has therefore focussed on the eccentricity perturbations a wide-orbit planet can have on inner planets through secular interactions. In the next Chapter I perform a similar analysis, however I focus on the inclination perturbations a wide-orbit planet can have on inner planets due to secular interactions. Specifically I investigate how these inclination perturbations can affect the probability that the inner planets are observed to transit.

4

Transit Probabilities in Secularly Evolving Planetary Systems

4.1 Chapter Summary

This Chapter considers whether the population of known transiting exoplanets provides evidence for additional outer planets on inclined orbits, due to the perturbing effect of such planets on the orbits of inner planets. As such, I develop a semi-analytical method for calculating the probability that two mutually inclined planets are observed to transit. I subsequently derive a simplified analytical form to describe how the mutual inclination between two planets evolves due to secular interactions with a wide-orbit inclined planet and use this to determine the mean probability that the two inner planets are observed to transit. From application to Kepler-48 and HD-106315 I constrain the inclinations of the outer planets in these systems (known from RV). I also apply this work to the so called Kepler Dichotomy, which describes the excess of single transiting systems observed by Kepler. I find 3 different ways of explaining this dichotomy: some systems could be inherently single, some multi-planet systems could have inherently large mutual inclinations, while some multi-planet systems could cyclically attain large mutual inclinations through interaction with an inclined outer planet. I show how the different mechanisms can be combined to fit the observed populations of Kepler systems with one and two transiting planets. I also show how the distribution of mutual inclinations of transiting two planet systems constrains the fraction of two planet systems that have perturbing outer planets, since such systems should be preferentially discovered by Kepler when the inner planets are coplanar due to an increased transit probability. The work presented in this Chapter has been published in Read et al. 2017.

4.2 Chapter Introduction

Over the past 20 years the number of exoplanet detections has soared most notably due to contributions from the *Kepler space telescope* (Kepler herein), as discussed in §1.5.2. As of January 2018 Kepler has detected 2342 confirmed planets, with 439 existing in multi-planet systems (exoplanet.eu; Schneider et al. 2011). Planet multiplicity provides information on the underlying architecture of planetary systems, such as expected orbital spacing, mutual inclinations and size distributions. For the multi-planet systems observed by Kepler, super Earth/mini Neptune type objects on tightly packed orbits inside of $\sim$200 days are common (Lissauer et al., 2011, 2014; Morton et al., 2016). Moreover such systems are observed to have small inclination dispersions of $\lesssim 5^\circ$ (Lissauer et al., 2011; Fang & Margot, 2012; Figueira et al., 2012; Tremaine & Dong, 2012; Marmier et al., 2013; Fabrycky et al., 2014).

How representative Kepler multi-planet systems are of a common underlying planetary architecture however is impeded by Kepler preferentially detecting objects which orbit closest to the host star. To generalise Kepler systems to an underlying population, it is therefore necessary to account for the inherent probability that transiting systems are observed. Taking into account such probabilities, there appears to be an over-abundance of planetary systems with a single transiting planet (Lissauer et al., 2011; Youdin, 2011; Johansen et al., 2012; Ballard & Johnson, 2016). This is commonly referred to as the 'Kepler Dichotomy' (see also Zhu et al. 2018 who suggest that there is no Kepler Dichotomy, as it can be explained by a distribution of mutual inclinations that depends on the number of planets in a system).

It is currently not known what causes this excess. Statistical and *Spitzer* confirmation studies all suggest that the false positive rate for single transiting objects with $R_p < 4R_\oplus$ is low at $\lesssim$15% (Morton & Johnson, 2011; Fressin et al., 2013; Coughlin et al., 2014; Désert et al., 2015). Perhaps then, there are populations of inherently single planet systems in addition to multi-planet systems which are closely packed and have small inclination dispersions. However there may also be a population of multi-planet systems where the mutual inclination dispersion is large, such that only a single planet is observed to transit.

The presence of an outer planetary companion may drive this potential large spread in mutual inclinations. Recent N-body simulations show that the presence of a wide-orbit planet in multi-planet systems can decrease the number of inner planets that are observed to transit, either through dynamical instability or inclination excitation (Mustill et al., 2016; Hansen, 2017). Beyond a few au, planetary transit probabilities drop to negligible values. It is possible therefore that additional wide-orbit planets could indeed exist in multi-planet systems observed by Kepler. Giant planets at a few au have been detected

around stars in the general stellar population by a number of radial velocity (RV) surveys (Marmier et al., 2013; Rowan et al., 2016; Wittenmyer et al., 2016; Bryan et al., 2016), with suggested occurrence rates ranging from $\sim 10-50\%$ (Cumming et al., 2008; Mayor et al., 2011; Bryan et al., 2016). Moreover, indirect evidence of undetected giant planets has also been suggested through apsidal alignment of inner RV detected planets (Dawson & Chiang, 2014). As RV studies are largely insensitive to planetary inclinations, it is possible that such wide-orbit planets could be on mutually inclined orbits, which may arise from a warp in the disc (Fragner & Nelson, 2010) or due to an excitation by a stellar flyby (Zakamska & Tremaine, 2004; Malmberg et al., 2011).

Calculating transit probabilities of multi-planet systems is complex, often requiring computationally exhaustive numerical methods such as Monte Carlo techniques (e.g. Lissauer et al. 2011; Johansen et al. 2012; Becker & Adams 2016; Mustill et al. 2016; Hansen 2017). However analytical methods can offer a significantly more efficient route for this calculation and allows for coupling with other fundamental analytical theory, such as for the expected dynamical evolution of the system from inter-planet interactions. Despite this however, analytical investigations into the transit probabilities of multi-planet systems for this purpose are relatively sparse (e.g. Ragozzine & Holman, 2010; Brakensiek & Ragozzine, 2016). Recently Brakensiek & Ragozzine 2016 showed how differential geometry techniques can be used to calculate multi-planet transit probabilities by mapping transits onto a celestial sphere. In this Chapter I perform a similar analysis, however I focus on regions where pairs of planets can be observed to transit. I also give an explicit analytical form using simple vector relations to describe the boundaries of such transit regions.

The multi-planet systems observed by Kepler appear to be mostly stable on long timescales (Lissauer et al., 2011; Pu & Wu, 2015). Dynamical interactions with a potential outer planet on an inclined orbit would therefore be expected to occur on secular timescales. Recent analytical work by Lai & Pu 2017 suggests that such interactions can lead to large mutual inclinations in an inner planetary system, assuming that the direction of the angular momentum vector of the outer planet is fixed. I build on this work by deriving analytical relations for the mutual inclination that can be induced in an inner planetary system by a general planetary companion. I then simplify this result specifically for when the companion is on a wide orbit. Combining this result with our robust analytical treatment of transit probabilities, I can then derive a simple relation describing how the presence of an outer planetary companion affects the transit probability of an inner system due to long term interactions.

I also complement recent N-body simulations of Kepler-like systems interacting with an inclined outer planetary companion shown in Mustill et al. 2016 and Hansen 2017 by

using our robust treatment of transit probabilities to consider whether an outer planet with a range of masses, semi-major axes and inclinations can reduce an underlying population of Kepler double transiting systems enough to recover the observed number of single transiting systems through long term interactions only. I also investigate whether the presence of specific wide-orbit planets in multi-planet systems preferentially predicts single transiting planets with a given distribution of radii and semi-major axes.

In §4.3 I overview our semi-analytical method for calculating the transit probability of two mutually inclined planets. In §4.3.3 I derive a simplified form to describe the evolution of the mutual inclination between two planets due to presence of an outer planetary companion. I show how this mutual inclination affects the transit probability of the two inner planets in §4.4. In §4.5 I apply this work to Kepler-56, Kepler-68, HD 106315 and Kepler-48 to place constraints on the inclination of the outer planets in these systems. In §4.6 I investigate whether a wide-orbit planet in Kepler systems can decrease the number of observed two planet transiting systems enough to recover the observed abundances of single transiting systems. I finally discuss this work in §4.7 and conclude in §4.8.

4.3 Semi-analytical Transit Probability

A planet on a circular orbit with a semi-major axis a and radius R_p subtends a band of shadow across the celestial sphere due its orbital motion (see Figure 1.5). I refer to this band of shadow as the *transit region* (Ragozzine & Holman, 2010; Brakensiek & Ragozzine, 2016). The probability that an observer will view an individual transit event of this planet, assuming that the system is viewed for long enough, is equal to the number of viewing vectors that intersect the transit region, divided by the total number of possible viewing vectors. Perhaps more intuitively, this is equivalent to the surface area of the transit region divided by the total surface area of the celestial sphere.

To calculate the area of a transit region on the celestial sphere first consider that the area of a given surface element (S) on a unit sphere is equal to

$$S = \int_0^{\vartheta_0} \int_0^{\varphi_0} \sin\vartheta' d\vartheta' d\varphi' = \left[1 - \cos\vartheta'\right]_0^{\vartheta_0} \left[\varphi'\right]_0^{\varphi_0}, \tag{4.1}$$

where ϑ' is the polar angle and φ' is the azimuthal angle. A given area on the celestial sphere can therefore be represented on a 2d plane of $1 - \cos\vartheta'$ vs. φ', from $0 \rightarrow 2$ and $0 \rightarrow 2\pi$ respectively, such that the 2d plane has a total surface area of 4π. Below I show how the boundaries of a given transit region traverses this 2d plane. This allows for the area contained within these boundaries and therefore the associated transit probability to be

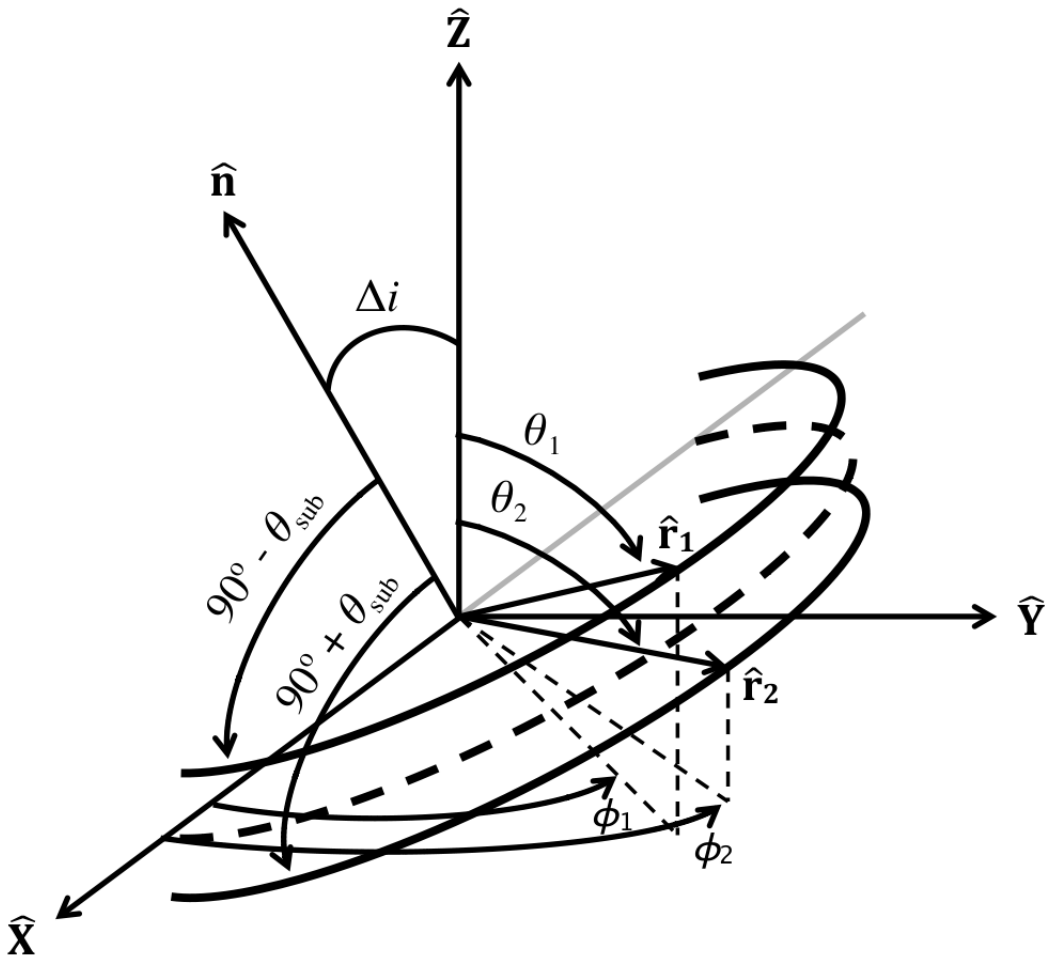

Figure 4.1 The coordinate system used to show how a transit region traverses the surface of a celestial sphere. The dashed line represents an orbital plane inclined to a fixed reference plane by Δi. The direction $\hat{\mathbf{n}}$ is normal to the orbital plane. The directions $\hat{\mathbf{r}}_1$ and $\hat{\mathbf{r}}_2$ trace the upper and lower of a transit region respectively.

calculated.

4.3.1 Single Planet Case

Consider some fixed reference plane where [$\hat{\mathbf{X}}$, $\hat{\mathbf{Y}}$] define a pair of orthogonal directions in this plane, and $\hat{\mathbf{Z}}$ defines a direction orthogonal to this plane as shown in Figure 4.1. The fixed reference frame in Figure 4.1 is assumed to be centred on a host star with radius $R_\star$. The line of sight of an observer is considered to be randomly oriented over the surface of a celestial sphere with respect to this fixed reference plane. Now consider that the orbital plane of a planet with a semi-major axis a and radius R_p, is inclined to the fixed reference plane by Δi, with the intersection between the two planes occurring along the $\hat{\mathbf{X}}$ direction. The direction of the normal of the orbital plane is given by $\hat{\mathbf{n}}$. The position of a planet

in the orbital plane is defined by the direction $\hat{\mathbf{r}}$ which makes the angles ϑ and φ with the $\hat{\mathbf{Z}}$ and $\hat{\mathbf{X}}$ directions respectively. Hence $\hat{\mathbf{r}}$ traces the centre of the transit region with respect to the fixed reference plane. As $\hat{\mathbf{n}} \cdot \hat{\mathbf{r}} = 0$, where $\hat{\mathbf{n}} = [0, \sin\Delta i, \cos\Delta i]$ and $\hat{\mathbf{r}} = [\sin\vartheta\cos\varphi, \sin\vartheta\sin\varphi, \cos\vartheta]$ it follows that

$$-\sin\Delta i \sin\vartheta \sin\varphi + \cos\Delta i \cos\vartheta = 0. \tag{4.2}$$

Hence eq. (4.2) defines how the centre of a transit region inclined to a fixed reference plane by Δi traverses a celestial sphere. This is shown by the dashed lines in Figure 4.2 for different values of Δi, where the surface area of the celestial sphere is shown on a 2d plane defined by eq. (4.1). I note that at the special case where $\Delta i = 90^\circ$, φ can only take values of 0 or π.

Similarly the directions that define the boundaries of the transit region can be given by $\hat{\mathbf{r}}_1$ and $\hat{\mathbf{r}}_2$ which makes the angles ϑ_1, ϑ_2 and φ_1, φ_2 with the $\hat{\mathbf{Z}}$ and $\hat{\mathbf{X}}$ directions respectively, shown in Figure 4.1. The boundaries of the transit region also subtend an angle $\pm\vartheta_{\rm sub}$ from the orbital plane where $\sin\vartheta_{\rm sub} = R_\star/a$ assuming $R_\star \gg R_p$ (Borucki & Summers, 1984). As $\hat{\mathbf{r}}_1 = [\sin\vartheta_1\cos\varphi_1, \sin\vartheta_1\sin\varphi_1, \cos\vartheta_1]$, $\hat{\mathbf{r}}_2 = [\sin\vartheta_2\cos\varphi_2, \sin\vartheta_2\sin\varphi_2, \cos\vartheta_2]$ and $\hat{\mathbf{n}} \cdot \hat{\mathbf{r}}_1 = R_\star/a$ and $\hat{\mathbf{n}} \cdot \hat{\mathbf{r}}_2 = -R_\star/a$, it follows that

$$-\sin\Delta i \sin\vartheta_1 \sin\varphi_1 + \cos\Delta i \cos\vartheta_1 = R_\star/a, \tag{4.3}$$

$$-\sin\Delta i \sin\vartheta_2 \sin\varphi_2 + \cos\Delta i \cos\vartheta_2 = -R_\star/a. \tag{4.4}$$

Hence eq. (4.3) and eq. (4.4) describe how the lower and upper boundaries of the transit region for a planet inclined to a fixed reference plane by Δi traverse a celestial sphere. The solid lines in Figure 4.2 show these boundaries for different values of Δi, where $R_\star/a = 0.25$. This value of $R_\star/a$ might be considered to be unrealistically large and is used for demonstration purposes only. In Appendix A I further discuss how the values of (ϑ_1, φ_1) and (ϑ_2, φ_2) in eq. (4.3) and eq. (4.4) respectively would be expected to change as Δi is increased from $\Delta i = 0 \rightarrow 90^\circ$.

An integration between the upper and lower boundaries of a transit region divided by the total surface area of the celestial sphere gives the associated *single transit probability* of the planet ($R_\star/a$, §1.5.2, Borucki & Summers 1984). All of the transit regions shown in Figure 4.2 for different Δi therefore contain identical areas and hence have identical single transit probabilities equal to 0.25. I note that if the planet has a non-negligible radius then the single transit probability becomes $(R_\star \pm R_p)/a$ for grazing and full transits respectively. Throughout this work however I assume that $R_p \ll R_\star$.

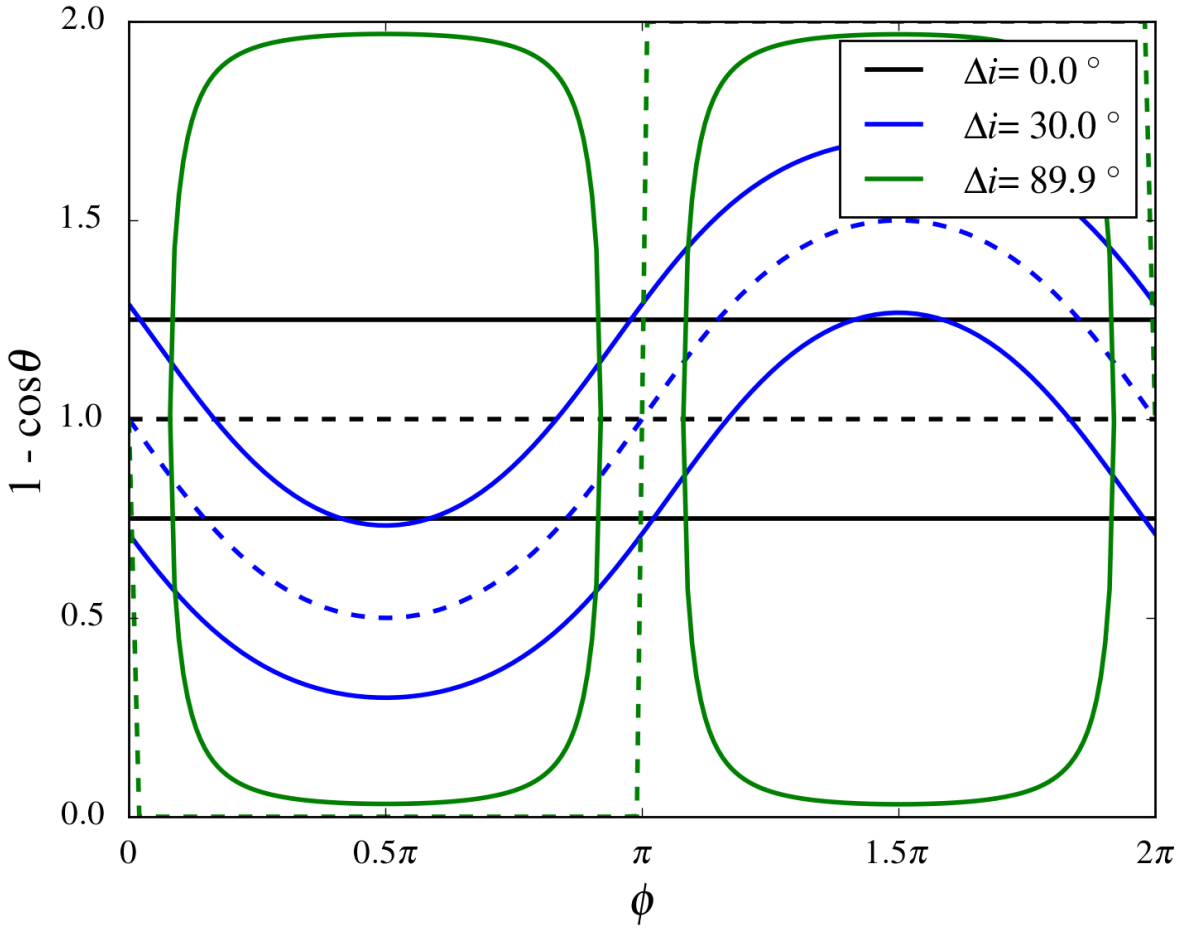

Figure 4.2 The surface of a celestial sphere represented on a 2d plane. The dotted lines represent the centre of a transit region for a planet inclined to a fixed reference plane by Δi. The solid lines refer to the boundaries of such transit regions for when $R_\star/a = 0.25$. The area within these transit regions are identical, giving an identical single transit probability equal to 0.25.

4.3.2 Two Planet Case

Consider now a system containing two planets, both of which are on circular orbits with semi-major axes and radii of a_1, a_2 and R_{p_1}, R_{p_2} respectively, where $a_1 < a_2$ and the orbital planes are mutually inclined by Δi (an exact definition for mutual inclination was given in §2.2). The probability that a randomly oriented observer will view both planets to transit (assuming the system is observed for long enough) is equal to the overlap area between the transit regions of both planets, divided by the total area of the celestial sphere. I refer to this probability as the *double transit probability*.

Therefore, using eq. (4.3) and eq. (4.4) to find where the boundaries of the transit regions of each planet intersect, an outline of the overlap between the transit regions can be determined. The area of this overlap can subsequently be calculated by an appropriate

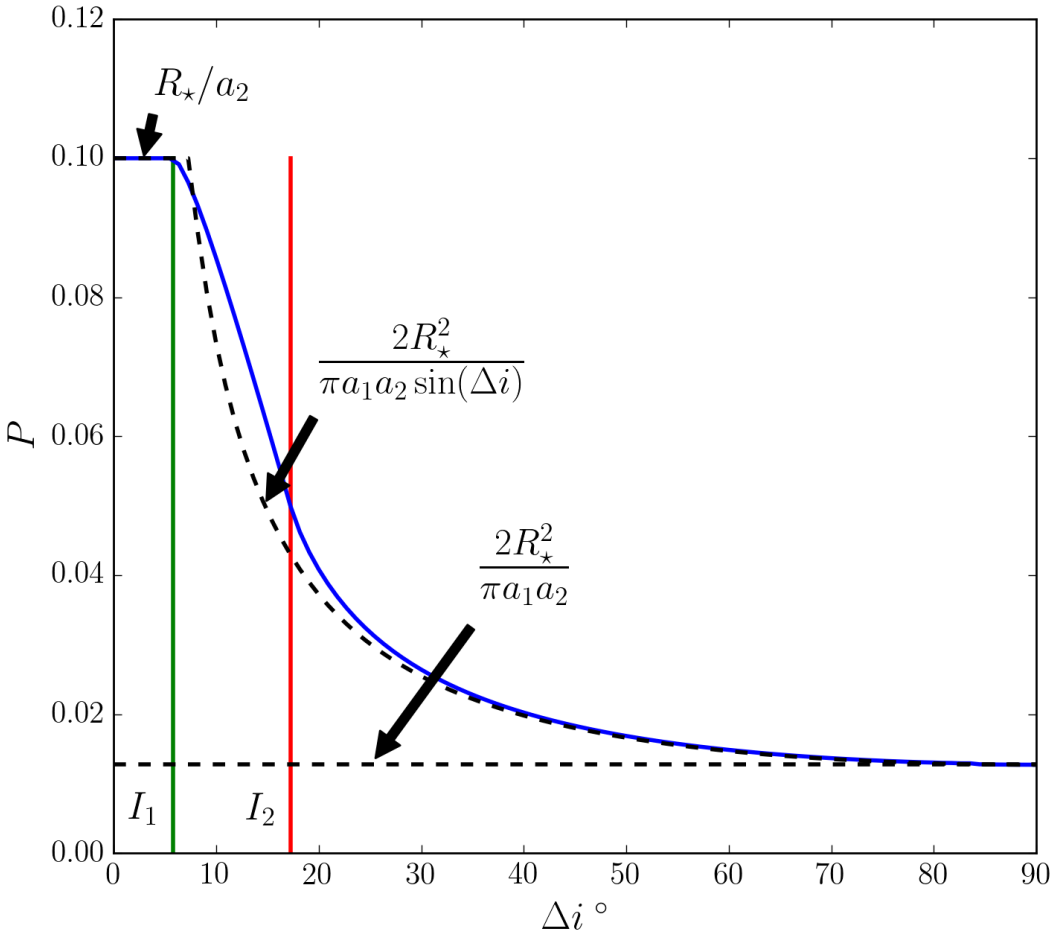

Figure 4.3 The double transit probability as a function of mutual inclination between two planets from our method (blue line) for when $R_\star/a_1 = 0.2$ and $R_\star/a_2 = 0.1$. The dashed black lines represent the associated analytical estimate given by eq. (4.7). The green and red lines represent which inclination cause the double transit probability to go from regime 1 to 2 and regime 2 to 3, with the regimes being defined in §4.3.2.

integration, which when divided by 4π gives the double transit probability. How the double transit probability changes as a function of Δi is shown by the blue line in Figure 4.3, for when $R_\star/a_1 = 0.2$ and $R_\star/a_2 = 0.1$. I note that this result is consistent regardless of the choice of reference plane and the orientation of the orbital planes of both planets with respect to this reference plane (see Ragozzine & Holman 2010 for a further discussion). That is, the double transit probability depends on the mutual inclination between the two planets only (in addition to the physical size of the respective transit regions).

Depending on the value of Δi, the double transit probability (P herein) can be split into three regimes (also discussed in Ragozzine & Holman 2010; Brakensiek & Ragozzine 2016).

(1) For low values of Δi, the transit region of the outer planet is enclosed within that of the inner planet. The double transit probability is therefore equal to $R_\star/a_2$.

(2) Δi is large enough that the transit region of one planet is no longer fully enclosed inside the other, however there is still partial overlap for all azimuthal angles on the celestial sphere. The transition to this regime occurs for a value of $\Delta i = I_1$, which causes ϑ_1 in eq. (4.3) for both planets to be equal at $\varphi_1 = \pi/2$. Evaluating eq. (4.3) at this point gives

$$\sin I_1 = -\varkappa_2(1-\varkappa_1^2)^{1/2} + \varkappa_1(1-\varkappa_2^2)^{1/2}, \tag{4.5}$$

where $\varkappa_1 = R_\star/a_1$ and $\varkappa_2 = R_\star/a_2$ for simplicity. I note that determining the overlap area of the two transit regions with an exact analytical expression in this regime is difficult and is commonly calculated by Monte Carlo techniques (e.g. Ragozzine & Holman, 2010; Johansen et al., 2012; Becker & Adams, 2016; Mustill et al., 2016; Hansen, 2017).

(3) For large Δi, the transit regions only overlap at the intersection of the two orbital planes. The transition to this regime occurs when $\Delta i = I_2$, where ϑ_1 for the inner planet is equal to ϑ_2 for the outer planet at $\varphi_1 = \varphi_2 = \pi/2$. Evaluating eq. (4.3) and (4.4) here gives

$$\sin I_2 = \varkappa_2(1-\varkappa_1^2)^{1/2} + \varkappa_1(1-\varkappa_2^2)^{1/2}. \tag{4.6}$$

The values of I_1 and I_2 are shown by the green and red lines respectively in Figure 4.3. If it is assumed that the transit region overlap in regime 3 can be represented as a 2d parallelogram, Ragozzine & Holman 2010 showed the double transit probability can be approximated by[1]

$$P = \frac{2R_\star^2}{\pi a_1 a_2 \sin \Delta i}. \tag{4.7}$$

For large Δi therefore, the double transit probability predicted by eq. (4.7) tends to a value of $2R_\star^2/\pi a_1 a_2$. I show eq. (4.7) as the black dashed line in Figure 4.3. I note that in Ragozzine & Holman 2010 it was assumed that the double transit probability transitions straight from regime (1) to (3) at $\Delta i = \arcsin\left(\frac{2}{\pi} \cdot \min(R_\star/a_1, R_\star/a_2)\right)$[1].

For $\Delta i > I_2$ our method predicts a double transit probability that agrees well with the analytical estimate from Ragozzine & Holman 2010. However there is a clear discrepancy for $I_1 < \Delta i < I_2$, for when there is partial overlap between the transit regions at all azimuthal angles. This highlights the need for semi-analytical methods like the one suggested here over purely analytical relations, to robustly calculate double transit probabilities at all values of Δi. I note that our method also agrees well with the Monte Carlo treatment of double transit probabilities shown in Ragozzine & Holman 2010.

Calculating transit probabilities using the method outlined here is significantly more computationally efficient than equivalent Monte Carlo methods, as it is only necessary to

[1] For greater accuracy, I include a $2/\pi$ factor here that is not included in Ragozzine & Holman 2010.

solve combinations of eq. (4.3) and (4.4) for different planets to find where transit regions overlap. From integrating around this overlap, the associated double transit probability is also exact and not subject to Monte Carlo noise effects from under-sampling the total number of line of sight vectors.

4.3.3 Two planet system with an inclined companion

Consider the same general two planet system from §4.3.2. Assume that the two planets are initially coplanar. Consider now a third planet on an external circular orbit, with a mass and semi-major axis of m_3 and a_3 respectively such that $a_3 > a_2$. The orbital plane of this external planet is initially mutually inclined to the inner planets by Δi. I assume that each of the planets interact through secular interactions only and that inclinations and eccentricities remain small, allowing for the application of Laplace - Lagrange theory outlined in §2.6. Assuming that the invariable plane (§2.2) is taken as a fixed reference plane, the initial inclination of the third planet i_3 is given by

$$i_3 = \arctan\left[\frac{(L_1 + L_2)\sin\Delta i}{L_3 + (L_1 + L_2)\cos\Delta i}\right]$$

where $L_j = m_j a_j^{1/2}$ and is proportional to the angular momentum in the low eccentricity limit. The initial inclination of the inner planets with respect to the invariable plane is therefore $i_1 = \Delta i - i_3$.

From eq. (2.17) the complex inclination of each of the inner two planets with respect to the invariable plane evolves in the form of

$$\begin{aligned} y_1 &= I_{11}e^{i(f_1 t+\gamma_1)} + I_{12}e^{i(f_2 t+\gamma_2)} \\ y_2 &= I_{21}e^{i(f_1 t+\gamma_1)} + I_{22}e^{i(f_2 t+\gamma_2)}, \end{aligned} \tag{4.8}$$

where y_1 and y_2 are the complex inclinations of the innermost and second innermost planet respectively. The evolution of the mutual inclination between the inner pair of planets is hence given by

$$y_1 - y_2 = (I_{11} - I_{21})e^{i(f_1 t+\gamma_1)} + (I_{12} - I_{22})e^{i(f_2 t+\gamma_2)}. \tag{4.9}$$

The $t = 0$ boundary conditions give $\gamma_1 = \pi$ and $\gamma_2 = 0$. Also as $y_1(t = 0) = y_2(t = 0) = i_1$, it follows from eq. (4.8) that $I_{11} - I_{21} = I_{12} - I_{22}$. The evolution of the mutual inclination from eq. (4.9) is therefore is equivalent to

$$y_1 - y_2 = (I_{12} - I_{22})\left(e^{i(f_1 t+\pi)} + e^{if_2 t}\right). \tag{4.10}$$

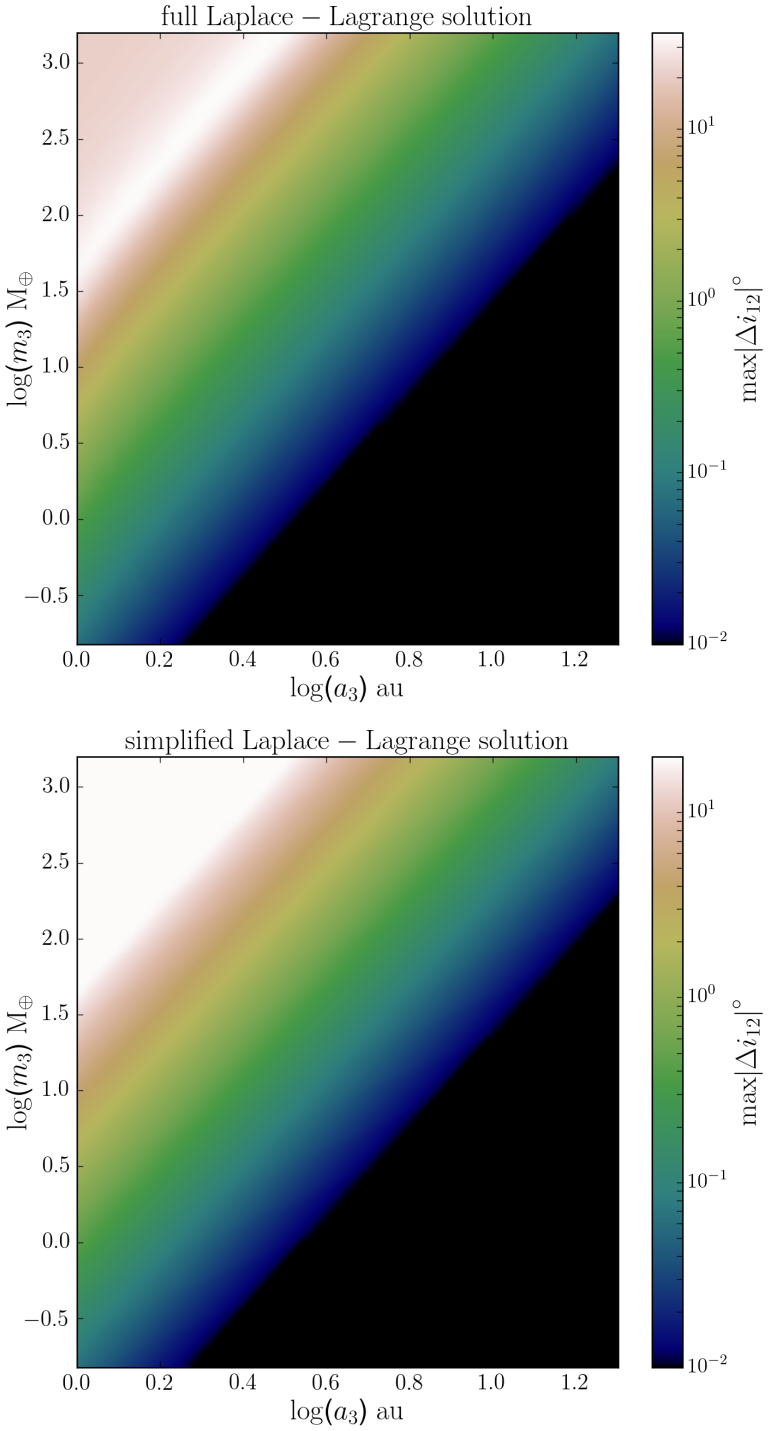

Figure 4.4 The maximum mutual inclination, max$|\Delta i_{12}|$, between two planets on circular, initially coplanar orbits with semi-major axis of 0.2, 0.5au and masses of $10M_\oplus$ respectively, from the secular interaction with an outer third planet. The value of max$|\Delta i_{12}|$ calculated by the full Laplace-Lagrange solution from eq. (4.11) is given by the colour scale on the top panel. The bottom panel colour scales give max$|\Delta i_{12}|$ calculated by the simplified Laplace-Lagrange solution for when $a_3 \gg a_1, a_2$, given by eq. (4.12) and eq. (4.13). For this Figure $\Delta i = 10°$. It is important to note that the assumptions of Laplace-Lagrange theory break down when $\Delta i \gg 20°$. Larger inclinations are only included in this Figure to aid comparison between max$|\Delta i_{12}|$ predicted by the full and simplified Laplace-Lagrange theory solutions.

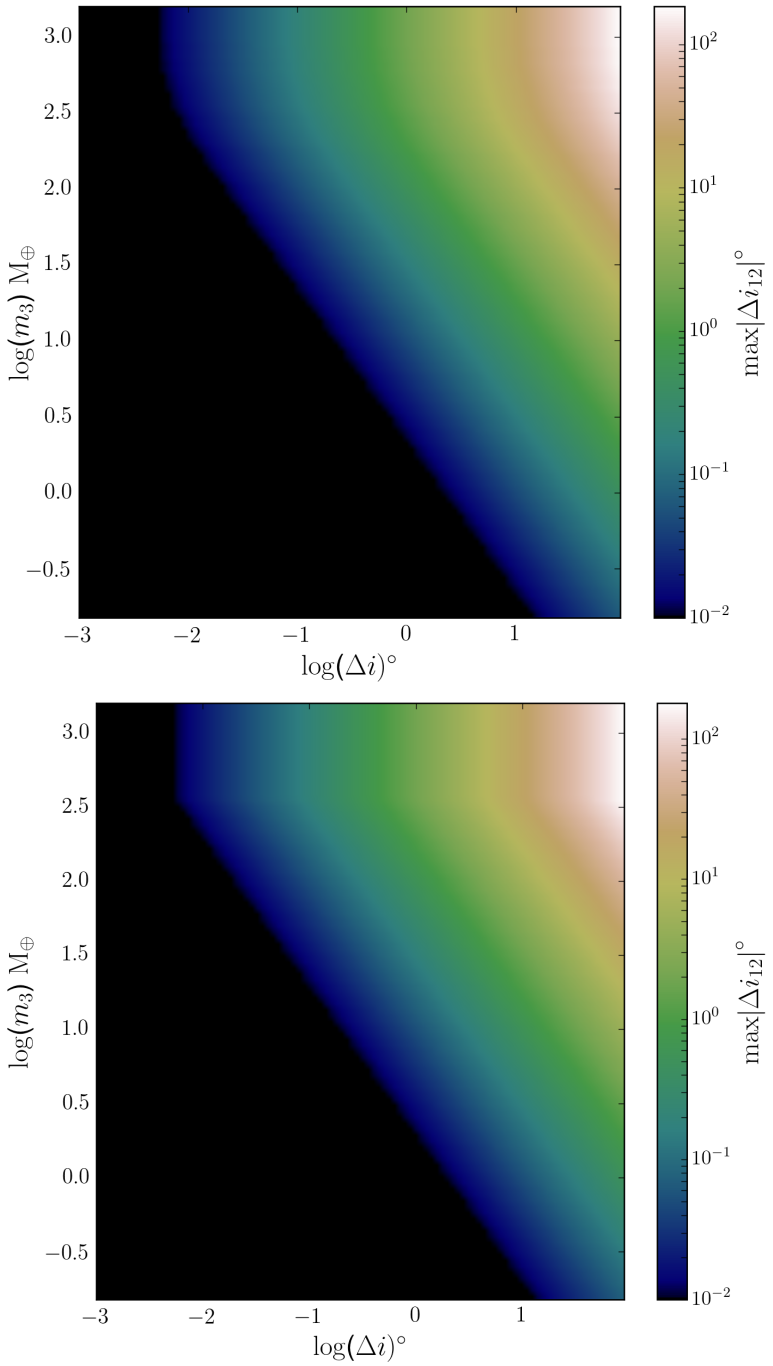

Figure 4.5 Same as Figure 4.4 but with a third planet with a range of masses and inclinations for when a_3= 2au.

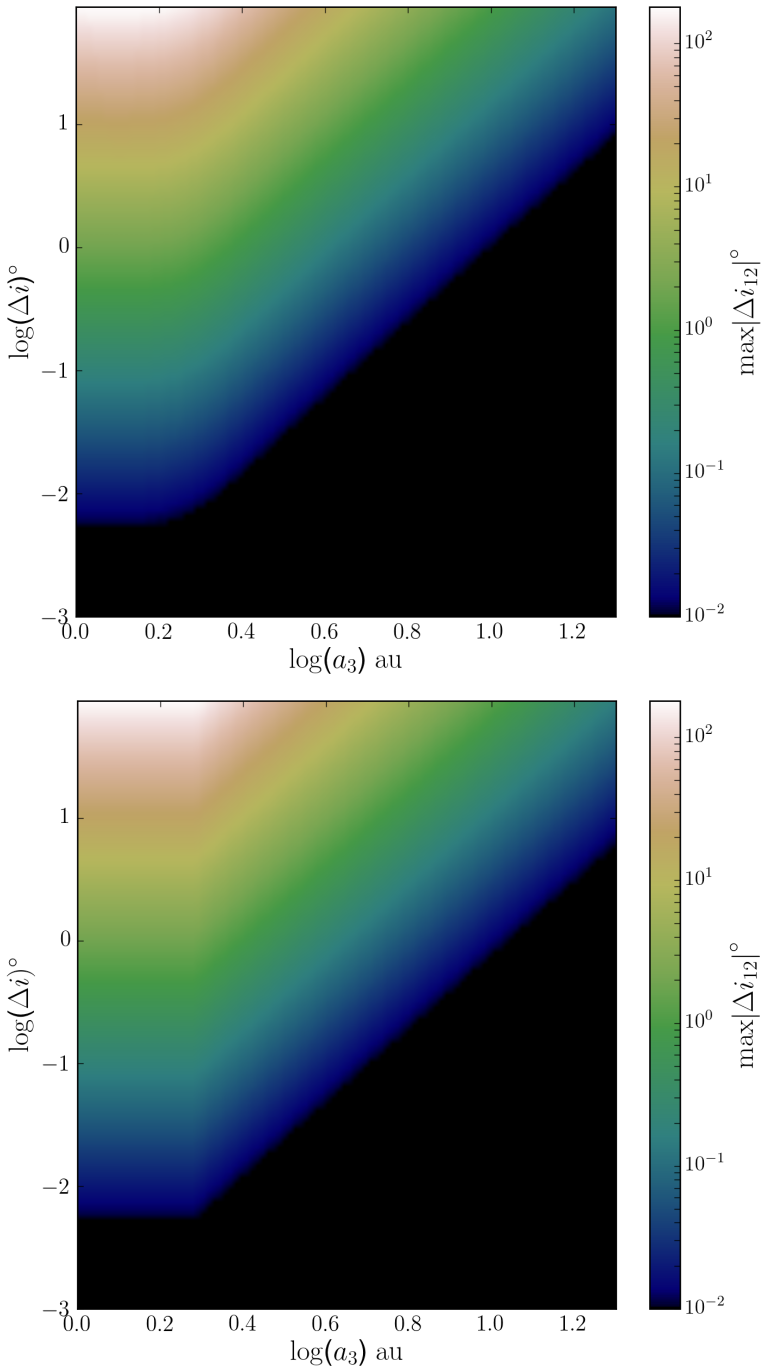

Figure 4.6 Same as Figure 4.4 but with a third planet with a range of masses and inclinations for when $m_3 = 1M_J$.

Hence the evolution of the instantaneous mutual inclination between the inner pair of planets, $\Delta i_{12} = |y_1 - y_2|$, can be calculated if the first and second elements of the eigenvector associated with the f_2 eigenfrequency are known. In Appendix B I fully solve eq. (2.15) to give I_{12} and I_{22} in terms of physical variables. Here I simply say that

$$y_1 - y_2 = \Delta i K \left[e^{i(f_1 t + \pi)} + e^{i f_2 t} \right], \tag{4.11}$$

where K is dependant on the masses and semi-major axes of the three planets, shown explicitly in Appendix B. I note that the maximum value of $K \approx 1$, implying that the maximum value of the mutual inclination between the inner pair of planets from eq. (4.10) is twice the initial mutual inclination with the external third planet i.e. $\max|\Delta i_{12}| = 2\Delta i$. For given values of masses and semi-major axes of the inner pair of planets therefore, the evolution of the mutual inclination between them is dependant on three quantities, a_3, m_3 and Δi.

The top panels of Figures 4.4, 4.5 and 4.6 show how $\max|\Delta i_{12}|$ changes as a function of different combinations of a_3, m_3 and Δi in eq. (4.11) for an example system where a_1, $a_2 = 0.2, 0.5$au and m_1, $m_2 = 10 M_\oplus$ respectively. I note that the assumptions of Laplace-Lagrange theory are expected to break down when $\Delta i \gg 20^\circ$. Larger inclinations are included for demonstration purposes only. It is evident that as the third planet tends to a limit where it is on a wide orbit, with a low mass and low initial mutual inclination, the maximum mutual inclination between the inner pair of planets becomes small as one might expect.

4.3.4 Companion wide-orbit approximation

In §4.4 I look to investigate how the evolving mutual inclination between the inner pair of planets affects the associated double transit probability, for the specific case where the external third planet is assumed to be on a wide orbit. For $a_3 \gg a_1, a_2$, certain individual and combinations of **B** matrix elements from eq. (2.16) become small and I find that eq. (4.11) can be simplified to

$$y_1 - y_2 \approx \Delta i K_{\rm simp} \left[e^{i(f_1 t + \pi)} + e^{i f_2 t} \right], \tag{4.12}$$

where

$$K_{\rm simp} = \frac{3 m_3 a_2^{7/2}}{m_2 a_1^{1/2} a_3^3} \frac{1}{b^1_{3/2}\left(\frac{a_1}{a_2}\right)\left(1 + (L_1/L_2)\right)}. \tag{4.13}$$

Here it is assumed that as $a_3 \gg a_1, a_2$, certain Laplace coefficients from the **B** matrix elements can be simplified, specifically $b^1_{3/2}(\alpha) \approx 3(\alpha)$ (Murray & Dermott, 1999). Similar simplifications can be made to each of the eigenfrequencies, for which

$$\begin{aligned} f_1 &\approx -\frac{\pi m_2 a_1^{1/2}}{2M_\star^{1/2} a_2^2} b^1_{3/2}\left(\frac{a_1}{a_2}\right)\left(1 + L_1/L_2\right), \\ f_2 &\approx -\frac{3\pi m_3 a_2^{3/2}}{2M_\star^{1/2} a_3^3}\frac{1}{1 + L_1/L_2}. \end{aligned} \tag{4.14}$$

As eq. (4.11) shows that the maximum value of the mutual inclination between the inner pair of planets cannot be larger than twice the initial mutual inclination with the wide-orbit planet ($\max|\Delta i_{12}| \not> 2\Delta i$) I assume that the maximum value of the mutual inclination between the inner two planets predicted by eq. (4.12) is

$$\begin{aligned} \max|\Delta i_{12}| &\approx 2\Delta i K_{simp} && \text{for } K_{simp} < 1, \\ &\approx 2\Delta i && \text{otherwise.} \end{aligned} \tag{4.15}$$

The bottom panels of Figures 4.4, 4.5 and 4.6 show $\max|\Delta i_{12}|$ predicted by eq. (4.15) and eq. (4.13) using the same planet parameters as shown in the top panels. I find that when $a_3 \gtrsim$1.25au, the simplified form for $\max|\Delta i_{12}|$ from eq. (4.15) and eq. (4.13) agrees with the full Laplace - Lagrange solution to within $\sim$ 25% for all values of m_3 and Δi. For $a_3 \sim$1au, the simplified form of $\max|\Delta i_{12}|$ begins to break down and eq. (4.15) can underestimate $\max|\Delta i_{12}|$ from the full Laplace - Lagrange solution by up to a factor of 2.

This estimate is similar to the result derived by Lai & Pu 2017, who assumed that the angular momentum vector direction of the outer inclined planet is fixed in time. They find that the maximum mutual inclination that can be induced in an inner pair of planets depends on the strength of the coupling between them (parametrized by ε_{12} in their eq. 12). Assuming inclinations are small I find eq. (4.15) agrees with the equivalent prediction of $\max|\Delta i_{12}|$ from Lai & Pu 2017 if $K_{simp} = \varepsilon_{12}$. Indeed, K_{simp} and ε_{12} are almost identical despite the different derivation techniques (e.g. I derive the full Laplace- Lagrange solution and then simplified assuming $a_3 \gg a_1, a_2$), apart from K_{simp} contains an additional factor of $a_1^{1/2} a_2^{3/2}$ whereas ε_{12} contains a factor of $(a_2^2 - a_1^2)$. By considering different combinations of a_1 and a_2 and comparing to the value of $\max|\Delta i_{12}|$ given by the full solution in Appendix B, I find that neither eq. (4.15) and (4.13) or the equivalent equation from Lai & Pu 2017 is favoured as a more accurate approximation, since which is closer to the full solution depends on the exact parameters.

4.4 Combining Transit Probabilities with Secular Theory

Considering two inner, initially coplanar planets and an outer inclined planetary companion, I combine the analysis of transit probabilities from §4.3 with secular interactions from §2.6 in two main ways. First in §4.4.1, I assume that the outer planet is not necessarily on a wide orbit. The evolution of the mutual inclination between the inner planets is therefore assumed to be given by the full Laplace-Lagrange solution derived in eq. (4.11). The double transit probability of the inner two planets during this evolution is then calculated through the method outlined in §4.3. This provides the most accurate prediction for how the double transit probability of two inner planets evolves (in the low inclination limit) considering a given outer planetary companion. I make use of this method for a detailed discussion of how an outer planet affects an inner population of Kepler systems in §4.6.

Second, in §4.4.2 I assume that the outer planetary companion is on a significantly wide orbit. The evolution of the mutual inclination between the inner two planets is therefore given by eq. (4.12) and eq. (4.13). Here I look to give a simple analytical form to describe the double transit probability of two inner planets, due to secular interactions with a given outer planetary companion. I make use therefore of simple analytical relations such as eq. (4.7) to describe double transit probabilities. Comparing with the work in §4.4.1 allows for the accuracy of these approximations to be judged. I demonstrate in §4.5 how simple constraints can be placed on the inclination of an outer companion in specific systems using this method.

4.4.1 Two planet system with an inclined companion

From Figure 4.3 it is clear that if the amplitude of the mutual inclination between the inner two planets is large, then the associated double transit probability, P, will only be at a maximum value for a small proportion of the secular evolution. The presence of an outer inclined planet may therefore result in a significant reduction in the mean double transit probability $\langle P \rangle$ on long timescales. Figure 4.7 shows how both the mutual inclination and the double transit probability evolve with time for two inner planets from Figure 4.4, which are perturbed by an outer planetary companion with a semi-major axis, mass and inclination of $a_3 = 2$au and $m_3 = 1 M_J$ and $\Delta i = 5^\circ$ respectively. Indeed, P is only at a maximum value for a small proportion of the secular evolution leading to a significant reduction in $\langle P \rangle$ compared with if the outer planet were not present.

Furthermore, the left panels of Figure 4.8 show how $\langle P \rangle$ changes due to perturbations from an outer planet with the same range of parameters considered in Figures 4.4, 4.5 and

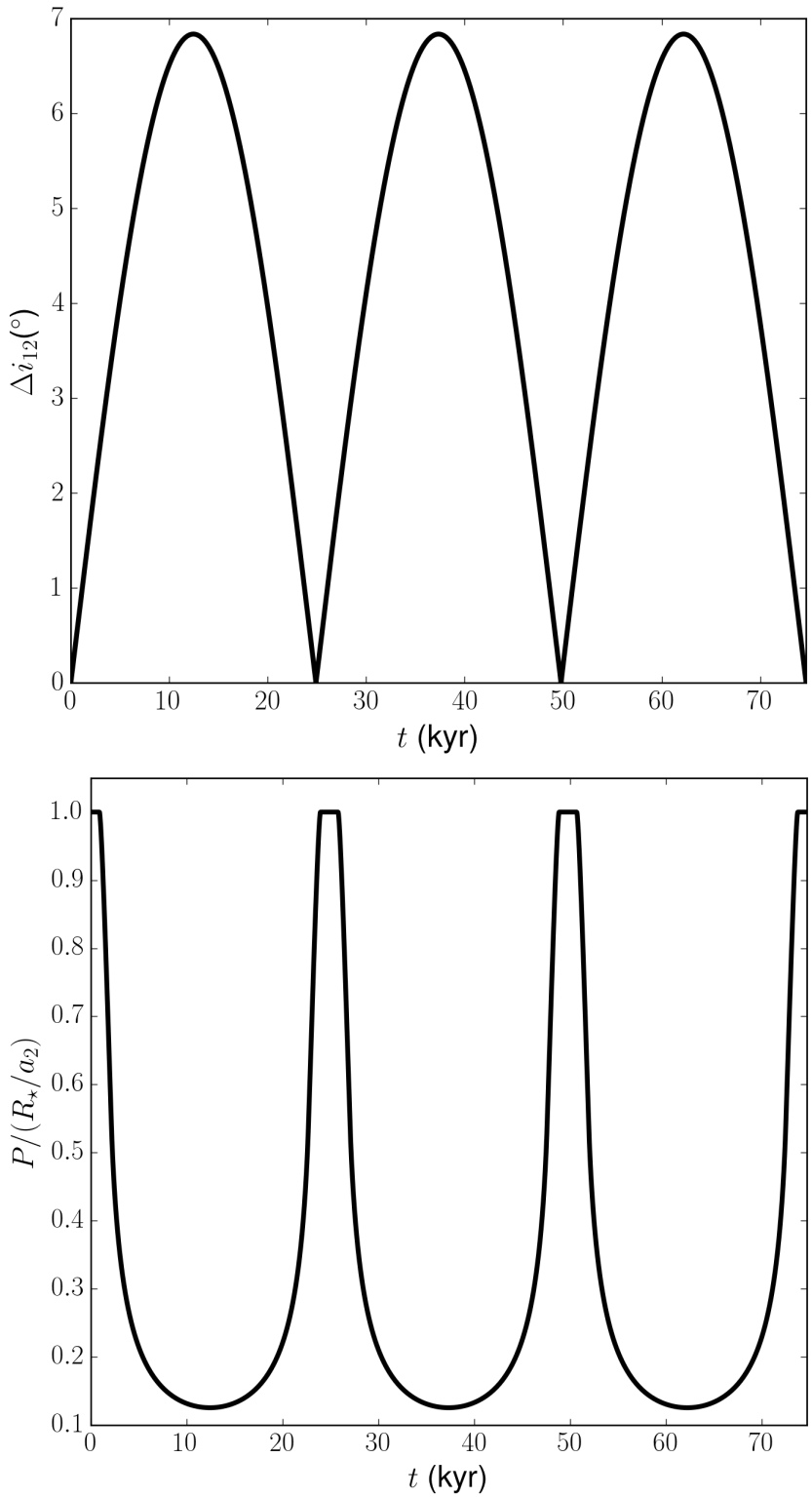

Figure 4.7 (*top*): The evolution of the mutual inclination of the two inner planets considered in Figure 4.4 due to secular interactions with a third planet with $a_3 = 2$au, $m_3 = 1M_J$ and $\Delta i = 5°$. (*bottom*): The associated evolution of the double transit probability.

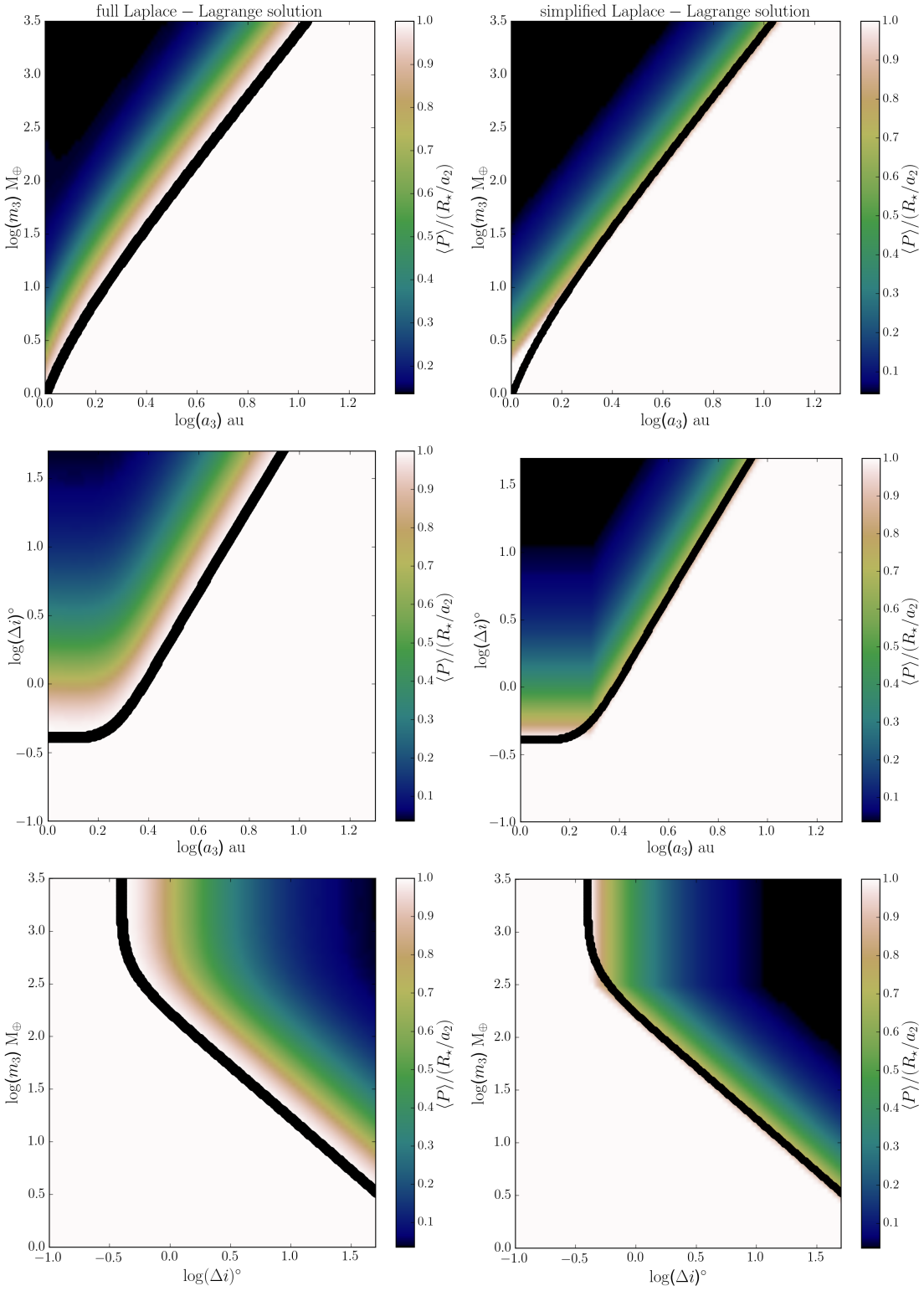

Figure 4.8 The mean double transit probability of two planets $\langle P \rangle$ from Figure 4.5, which are being secularly perturbed by a third planet on a mutually inclined orbit according to the full Laplace - Lagrange solution (left panels) and the simplified Laplace-Lagrange solution for when the third planet is assumed to be on a wide orbit (right panels). The black lines show the boundary where the maximum mutual inclination between the inner planets exceeds I_1 from eq. (4.5) and $\langle P \rangle$ is assumed to be significantly reduced. Laplace - Lagrange theory is expected to break down for $\Delta i \gg 20^\circ$ and is included here for demonstration purposes only.

4.6. As one may expect, through comparing Figures 4.4, 4.5 and 4.6 with the left panels of Figure 4.8, an outer planet which induces a large value of $\max|\Delta i_{12}|$ also causes a significant reduction in the mean double transit probability of the inner two planets and vice versa for small values of $\max|\Delta i_{12}|$.

The left panels of Figure 4.8 also suggest a clear boundary of a_3, m_3 and Δi, above which the outer planet causes $\langle P \rangle$ to be significantly reduced and below which $\langle P \rangle$ is unchanged. From Figure 4.3, the double transit probability of the two inner planets can be considered to be significantly reduced when $\Delta i_{12} > I_1$, where I_1 is given by eq. (4.5). I assume therefore that the boundary where $\langle P \rangle$ is significantly reduced occurs when $\max|\Delta i_{12}| \approx I_1$. The values of a_3, m_3 and Δi which give this boundary are shown by the black lines in the left panels of Figure 4.8.

4.4.2 Companion wide-orbit approximation

Considering the simplified evolution of the mutual inclination from eq. (4.12) and (4.13) for when $a_3 \gg a_1, a_2$, here I estimate the value of the mean double transit probability itself. I assume that $\langle P \rangle$ is dominated by the maximum or minimum value of the double transit probability, P_{max} and P_{min} respectively, depending on whether $\max|\Delta i_{12}|$ is greater than I_1. I assume that $I_1 \approx R_\star/a_1 - R_\star/a_2$ from eq. (4.5) for $R_\star/a_1$, $R_\star/a_2 \ll 1$. From Figure 4.3, the value of $P_{max} = R_\star/a_2$, however a value of P_{min} is more difficult as no specific analytical estimate exists. I therefore assume P_{min} can be given by the estimate from Ragozzine & Holman 2010 shown by eq. (4.7). I note that this approximation for P_{min} would be expected to break down if $\max|\Delta i_{12}|$ predicts partial overlap between the transit regions of the inner planets for all azimuthal angles (see Figure 4.3). Assuming that the masses and semi-major axes of all the planets are known, in addition to the inclination of the outer planet and that $\max|\Delta i_{12}|$ is given by the simplified Laplace - Lagrange solution from eq. (4.15), $\langle P \rangle$ can be estimated by

$$\begin{aligned} \langle P \rangle &\approx R_\star/a_2 && \text{for } \max|\Delta i_{12}| < R_\star/a_1 - R_\star/a_2 \\ &\approx \frac{2R_\star^2}{\pi a_1 a_2 \sin(\max|\Delta i_{12}|)} && \text{otherwise,} \end{aligned} \tag{4.16}$$

The right panels of Figure 4.8 show the value of $\langle P \rangle$ predicted by eq. (4.16), using the same planet parameters as those in the left panels. The black lines are identical to those in the left panels of Figure 4.8 and are included to aid comparison between both sides of the Figure.

The above assumptions bias the double transit probability toward spending a greater proportion of the secular evolution at P_{min}. As such, eq. (4.16) can under predict $\langle P \rangle$, by a

factor of up to 4 when comparing the left and right panels of Figure 4.8. I suggest therefore that eq. (4.16) should be used as a first order approximation of $\langle P \rangle$ only.

4.5 Application to specific systems

Here I consider real systems observed to have both transiting planets and an additional outer, non-transiting planet. Due to the inherent faintness of Kepler stars, follow up observations to detect non-transiting planets, namely by RV studies, are challenging. Thus the number of systems observed with such architectures are relatively sparse. I consider three of these systems: Kepler-56, Kepler-68 and Kepler-48 in addition to HD 106315. As RV surveys are largely insensitive to planetary inclinations, I apply eq. (4.16) with eq. (4.13) to place constraints on the inclination of the non-transiting planets in these systems.

Assume that, as the transiting planets are indeed transiting, the mean double transit probability is at a maximum. Rearranging eq. (4.16) one finds

$$\begin{aligned} \Delta i_{crit} &\approx \frac{R_\star/a_1 - R_\star/a_2}{2K_{simp}} && \text{for } K_{simp} < 1 \\ &\approx \frac{R_\star/a_1 - R_\star/a_2}{2} && \text{otherwise,} \end{aligned} \tag{4.17}$$

where Δi_{crit} is the inclination of the non-transiting planet required to significantly reduce the mean probability that the inner planets are observed to transit due to secular interactions. I note that eq. (4.17) assumes that the transiting planets are initially coplanar. However if these planets were initially mutually inclined by a small amount, a smaller secular perturbation from the outer planet would be required to significantly reduce the mean probability that the inner planets are observed to transit. In this case, i_{crit} from eq. (4.17) would be reduced.

4.5.1 Kepler-56

Kepler-56 is a red giant star with a mass and radius of $M_\star = 1.32 \pm 0.13\ M_\odot$ and $R_\star = 4.23 \pm 0.15 R_\odot$ respectively (Huber et al., 2013), which is observed to host three planets. Interestingly, Kepler-56 represents one of the few red giant stars observed to host a planetary system (Lillo-Box et al., 2014; Ciceri et al., 2015; Quinn et al., 2015; Pepper et al., 2016). The two inner planets (b, c) are observed to transit with periods of 10.5 and 21.4 days respectively (Borucki et al., 2011; Steffen et al., 2013; Huber et al., 2013; Hadden & Lithwick, 2014; Holczer et al., 2016; Morton et al., 2016) and have masses of $22.1^{+3.9}_{-3.6} M_\oplus$ and $181^{+21}_{-19} M_\oplus$ respectively (Huber et al., 2013). Keck/HIRES and HARPS-North observations have re-

vealed a non-transiting giant planet (d) with a period of 1002±5 days and minimum mass of 5.62±0.38M_J (Huber et al., 2013; Otor et al., 2016). An interesting quirk of this system is that the transiting planets, while being roughly coplanar, are misaligned to the stellar spin axis by ∼40° (Huber et al., 2013). It is unclear if this large obliquity is caused by long term dynamical interactions with a highly inclined companion, such as Kepler-56d, or from the star being inherently tilted to the disk from which the planets formed (Li et al., 2014).

Applying eq. (4.17), I find that $i_{crit} = 704°$. This unphysically large value means that, regardless of how Kepler-56d is inclined in this system, the mean double transit probability of the inner two transiting planets cannot be significantly reduced. That is, I suggest that the transiting planets in Kepler-56 are not strongly affected by the secular perturbations of Kepler-56d, regardless of its mutual inclination. This is a similar result to that found in Lai & Pu 2017 who also find that the inner planets are strongly coupled against external secular interactions. I therefore cannot place any constraint on the inclination of Kepler-56d using this method. I note however that this does not preclude that the 40° misalignment from the stellar spin axis comes from an inclined outer companion, since both inner planets could be inclined together without significant mutual inclination.

4.5.2 Kepler-68

Kepler-68 is a roughly solar type star with a mass and radius of 1.08±0.05$M_\odot$ and 1.24±0.02$R_\odot$ respectively (Gilliland et al., 2013; Marcy et al., 2014). It hosts two transiting planets (b, c) with periods of 5.4 and 9.6 days respectively (Gilliland et al., 2013; Marcy et al., 2014; Van Eylen & Albrecht, 2015; Holczer et al., 2016; Morton et al., 2016) and fitted masses of 5.97±1.70 and 2.18±3.5$M_\oplus$ respectively (Marcy et al., 2014). Keck/HIRES RV follow up of this system detected a non-transiting planet (d) with a period of 625±16 days with a fitted mass of 267±16$M_\oplus$ (Marcy et al., 2014).

Applying eq. (4.17) I find $i_{crit} = 244°$. Similar to Kepler-56 therefore, regardless of the mutual inclination of Kepler-68d, the mean double transit probability of the inner two transiting planets cannot be significantly reduced by secular perturbations. I therefore cannot place a constraint on the inclination of Kepler-68d using this method. I note that Kepler-68d can indeed have a large inclination without affecting the overall stability of the system according to a suite of N-body simulations, which suggest that Kepler-68d is inclined by $\Delta i < 85°$ (Kane, 2015).

4.5.3 HD 106315

HD 106315 is a bright F dwarf star at a distance d = 107.3 ± 3.9pc (Gaia Collaboration et al., 2016) with mass and radius of 1.07±0.03$M_\odot$ and 1.18±0.11$R_\odot$ respectively (Morton, 2012; Petigura, 2015; Crossfield et al., 2017). Recent *K2* observations detect two transiting planets (b, c) with periods of 9.55 and 21.06 days respectively and radii of $2.23^{+0.30}_{-0.25}$ and $3.95^{+0.42}_{-0.39}R_\oplus$ respectively (Crossfield et al., 2017; Rodriguez et al., 2017). Mass-radius relationships suggest these planets have masses of 8 and 20$M_\oplus$ respectively (Weiss et al., 2016; Wolfgang et al., 2016; Crossfield et al., 2017). Further Keck/HIRES RV observations also indicate the presence of a third outer companion planet (d) with a period of $P_d \gtrsim 80$ days, which has a mass of $m_d \gtrsim 1M_J$ (Crossfield et al., 2017). As the exact period of this outer planet is unknown I consider two possibilities where the outer planet has a period of $P_d = 80$ days and $P_d = 365$ days respectively. Assuming $P_d = 80$ days implies a mass of $m_d = 1M_J$ (Winn et al., 2009; Crossfield et al., 2017). Applying eq. (4.17) with this outer planet gives $i_{crit} = 1.1°$. This suggests that if the outer planet had a period of $P_d = 80$ days, it must have an inclination of $\Delta i \lesssim 1.1°$, otherwise the mean probability of observing the inner two planets to transit would be significantly reduced due to the secular interaction. Conversely, if the outer planet is assumed to be further out with $P_d = 365$ days, implying a mass of ∼7M_J, eq. (4.17) suggests that $i_{crit} = 2.4°$. That is, if the outer planet has a period of $P_d = 365$ days, it must have an inclination of $\Delta i \lesssim 2.4°$, otherwise the secular interaction would significantly reduce the mean probability that the inner planets are observed to transit.

The mutual inclination of the outer planet might also be constrained through astrometric observations of HD 106315 with ESA's *Gaia* mission (Perryman et al., 2001; Casertano et al., 2008; Sozzetti et al., 2014; Perryman et al., 2014; Sahlmann et al., 2015). The astrometric displacement of the host star due to the presence of a planet is defined by

$$\alpha = \left(\frac{m_p}{M_\star}\right)\left(\frac{a_p}{1au}\right)\left(\frac{d}{1pc}\right)^{-1} \text{arcsec}, \tag{4.18}$$

with the astrometric signal-to-noise equal to $S/N = \alpha\sqrt{N_{obs}}/\sigma$, where N_{obs} is the scheduled number of astrometric measurements ($N_{obs} = 36$ for HD 106315[2]) with typical uncertainties of $\sigma = 40$mas (de Bruijne, 2012). If $S/N > 20$, the orbital inclination can be constrained to a precision of $< 10°$ (Sahlmann et al., 2015). I find that for the example periods and masses considered above for HD 106315d that $S/N < 10$. I therefore expect that the inclination of the above examples of HD 106315d cannot be constrained using *Gaia* astrometry. However if HD 106315d is outside of ∼1.3au, (implying a mass of $\gtrsim 12M_J$)

[2] http://gaia.esac.esa.int/gost/

eq. (4.18) suggests that S/N > 20 such that the inclination of HD 106315d should be constrained by *Gaia* astrometry. Further RV follow-up of this system will allow for greater constraints to be placed on the mass and the orbit of HD 106315d, which in turn allow for greater constraints to be placed on the inclination, either through potential astrometry measurements or through our model represented by eq. (4.17).

4.5.4 Systems with three transiting planets and a wide-orbit companion

Here I generalise the effect a wide-orbit planet has on the transit probabilities of three inner transiting planets. Consider Kepler-48 as an example of such a system. Kepler-48 has a mass and radius of $M_\star = 0.88 \pm 0.06 M_\odot$ and $R_\star = 0.89 \pm 0.05 R_\odot$ respectively. It hosts three transiting planets (b,c,d) with periods of 4.78, 9.67 and 42.9 days and fitted masses of 3.94 ± 2.10, 14.61 ± 2.30 and $7.93 \pm 4.6 M_\oplus$ respectively (Steffen et al., 2013; Marcy et al., 2014; Hadden & Lithwick, 2014; Holczer et al., 2016; Morton et al., 2016). Keck/HIRES RV analysis also detects a non-transiting planet (e) with a period and fitted mass of 982 ± 8 days and $657 \pm 25 M_\oplus$ respectively (Marcy et al., 2014).

Returning to the derivation of the secular interaction in §4.3.3, the initial inclination of the non-transiting planet, i_e, with respect to the invariable plane can be generalised to

$$i_e = \arctan\left(\frac{\sin\Delta i\left(\sum_{n=1}^{3} L_n\right)}{L_e + \cos\Delta i\left(\sum_{n=1}^{3} L_n\right)}\right), \tag{4.19}$$

where $L_e = m_e a_e^{1/2}$ and is proportional to the angular momentum of Kepler-48e in the low eccentricity limit and $L_n = m_n a_n^{1/2}$ for either Kepler-48b, c, or d. The initial inclination of the transiting planets is therefore equal to $\Delta i - i_e$.

As the strength of the secular interaction between planets largely depends on their separation (e.g. eq. (4.15)) I assume that Kepler-48d will be affected most by perturbations from the non-transiting planet. I demonstrate this in Figure 4.9, which shows how the mutual inclination between each of the transiting planets evolves assuming Laplace - Lagrange theory (eq. (2.17)) and that Kepler-48e is initially mutually inclined by $\Delta i = 10^\circ$. The red line shows the mutual inclination between Kepler-48b and c (Δi_{bc}), the green between b and d (Δi_{bd}), and the blue between c and d (Δi_{cd}). The mutual inclination between Kepler-48b and c is largely unchanged and they remain roughly coplanar. Conversely the mutual inclination between b and d and c and d is significant and roughly equal

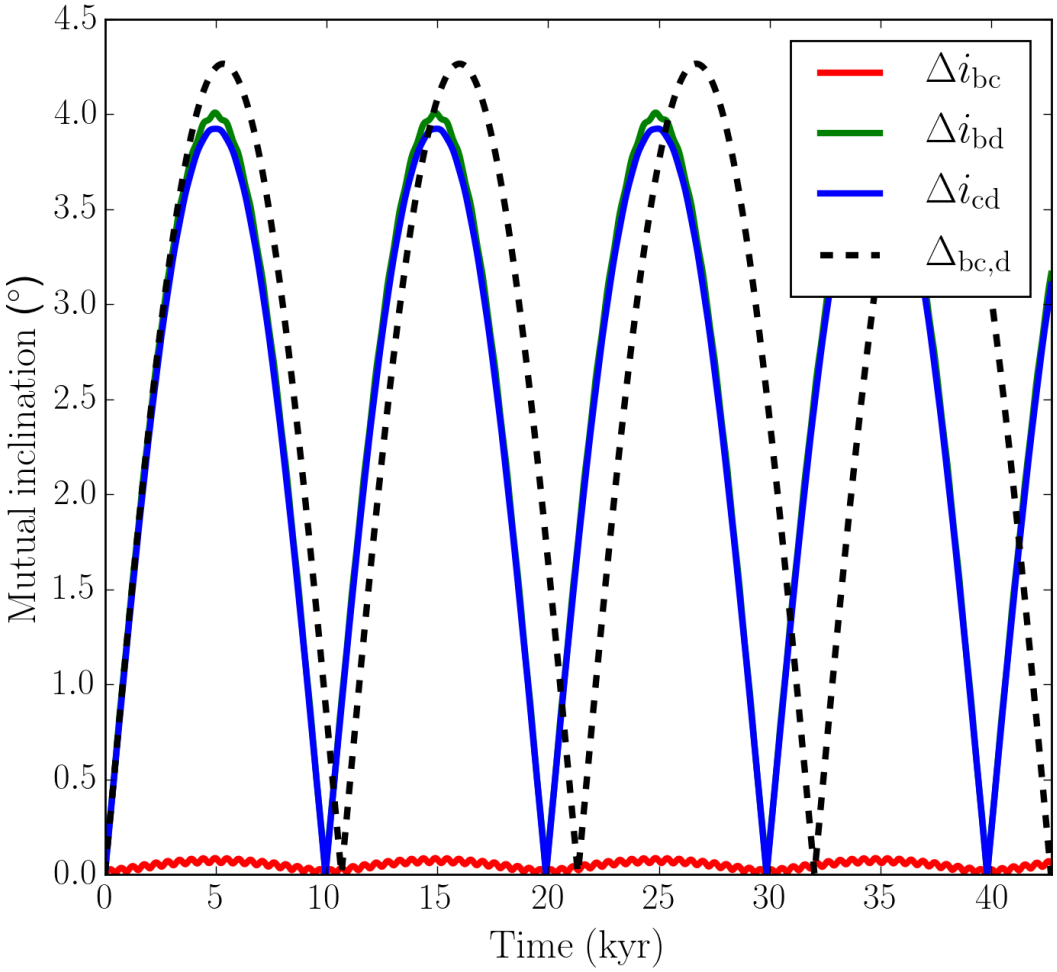

Figure 4.9 The mutual inclination between the respective planets in Kepler-48, when the non-transiting planet, Kepler-48e is initially mutually inclined by $\Delta i = 10^\circ$. The black dashed line shows the evolution of the mutual inclination between the inner two transiting planets with the outer transiting planet, for when the inner two planets are treated as a single body with an equal orbital angular momentum.

throughout the secular evolution. It can be assumed for Kepler-48 therefore that the inner two transiting planets are largely unaffected by the secular perturbations of Kepler-48e, but both can become significantly mutually inclined to the outer transiting planet.

As such, I assume that Kepler-48b and c can be treated as a single body whose angular momentum is the sum of Kepler48-b and c, reducing the system to a total of three planets. With this approximation, the evolution of the mutual inclination between Kepler-48b and c with d ($\Delta i_{\rm bc,d}$) is shown by the dashed black line in Figure 4.9. It can be seen that this way of treating Kepler-48b and c as a single body gives a good approximation for the evolution of the mutual inclination between Kepler-48b, c with d.

The initial mutual inclination of Kepler-48e which causes a significant reduction in the mean probability of the inner planets transiting, $\Delta i_{\rm crit}$, can therefore be approximated by

eq. (4.17), where the value of K_{simp} becomes

$$K_{simp} = \frac{3m_e a_d^{7/2}}{m_d a_{bc}^{1/2} a_e^3} \frac{1}{b_{3/2}^1 \left(\frac{a_{bc}}{a_d}\right) \left(1 + (L_{bc}/L_d)\right)}, \tag{4.20}$$

with the subscripts referring to a respective planet and the subscript 'bc' to the planet which has the same total angular momentum as Kepler-48b and c.

I find that $\Delta i_{crit} = 3.7^\circ$. This suggests therefore that the inclination of Kepler-48e $\Delta i \lesssim 3.7^\circ$, otherwise the secular interaction would cause a significant reduction in the mean probability that all three inner planets are observed to transit. Under the simpler assumption that $\max|\Delta i_{bc,d}| \lesssim R_\star/a_d$, Lai & Pu 2017 also find that the inclination of Kepler-48e, considering secular interactions only, must also be small with $\Delta i \lesssim 2.3^\circ$.

4.6 Application to the Kepler Dichotomy

As discussed in §5.2, Kepler has observed an excess of single transiting systems which cannot be explained by geometric effects alone, commonly referred to as the Kepler dichotomy (Lissauer et al., 2011; Youdin, 2011; Johansen et al., 2012; Ballard & Johnson, 2016). This may suggest that there is a population of inherently single transiting systems in addition to a population of multi-planet systems with small inclination dispersions. However there may also be a population of multi-planet systems where the mutual inclination dispersion is large, increasing the probability that only a single planet is observed to transit. Here I investigate whether both these types of multi-planet systems can significantly contribute to the abundance of systems observed by Kepler to have one and two transiting planets respectively.

The Kepler systems I consider are discussed in §4.6.1. A method for debiasing Kepler systems to a general population of planetary systems is described in §4.6.2. I consider the scenario where planets share some inherently fixed mutual inclination in §4.6.3, before considering when this mutual inclination is evolving due to the presence of an outer inclined planetary companion in §4.6.4. I note from the outset that I do not consider Kepler systems observed to have more than two planets. Instead I look to explore what effects an outer planet might have on observables of a subset of Kepler like systems, rather than observables of the whole Kepler population. I discuss this assumption further in §4.7.6.

4.6.1 Kepler Candidate Sample

I select planet candidates from the cumulative Kepler objects of interest (KOI) table from the NASA exoplanet archive[3], accessed on 13/09/16. The vast majority of the KOIs ($\sim$ 97%) that survive our cuts detailed below, to make it into our final sample are listed as being taken from the most recent Q1-17 DR24 data release. This data release is of particular note as it incorporates an automated processing of all KOIs (Coughlin et al., 2016).

Out of the initial 8826 KOIs I consider those which orbit solar type stars, with surface temperatures and surface gravities between 4200K < T < 7000K and 4.0 < log(g) < 4.9 respectively. This reduces the total number of KOIs to 7446. I also find the total number of unique Kepler stars within this range (discussed in §4.7) is 164966 from the 'Kepler Stellar data' table. I next remove false positives, which refer to KOI light curves that are indicative of either an eclipsing binary, having significant contamination from a background eclipsing binary, showing significant stellar variability which mimics a planetary transit or where instrument artefacts have produced a transit like signal (see Coughlin et al. 2014; Rowe et al. 2014; Rowe & Thompson 2015; Seader et al. 2015; Coughlin et al. 2016). This reduces our sample of KOIs (candidates herein) to 4072 objects. I subsequently remove non planetary-like objects with radii >22.4$R_\oplus$ (Borucki et al., 2011), leaving 3757 objects, after which I remove candidates with a SNR < 10 reducing the possibility that a transit signal is caused by systematic background noise (Morton et al., 2016), leaving 3327 objects. Finally I remove candidates listed as not having a satisfactory fit to the transit signal (Rowe et al., 2014; Rowe & Thompson, 2015). This gives our final sample of 3255 objects. I note that our choice of cuts means that KOI systems can become reduced in multiplicity. I find that our final sample includes systems which contain 1-6 candidates with N_i = (1, 2, 3, 4, 5, 6) = (1951, 341, 117, 43, 15, 4) e.g. 1951 systems with a single candidate, 341 systems with two candidates etc. Herein, I consider the 1951 systems observed by Kepler to have a single transiting planet and the 341 systems observed to have two.

The smoothed distribution of the semi-major axis and planetary radii for the single and double planet transiting systems are shown in Figure 4.10. Comparing the top and bottom panels of Figure 4.10, there are types of planets which are only present in single transiting systems. I briefly discuss these differences here for future reference. Large planets with short periods i.e. Hot Jupiters, are not present in Kepler systems with two transiting planets. Indeed, investigations into the formation processes of Hot Jupiters predict a lack of close companions (Wright et al. 2009; Steffen et al. 2012a; Mustill et al. 2015; Huang et al. 2016, see WASP-47 for an exception, Becker et al. 2015; Almenara et al. 2016). Long period planets are also more abundant in the population of single transiting systems. This may

[3] exoplanetarchive.ipac.caltech.edu

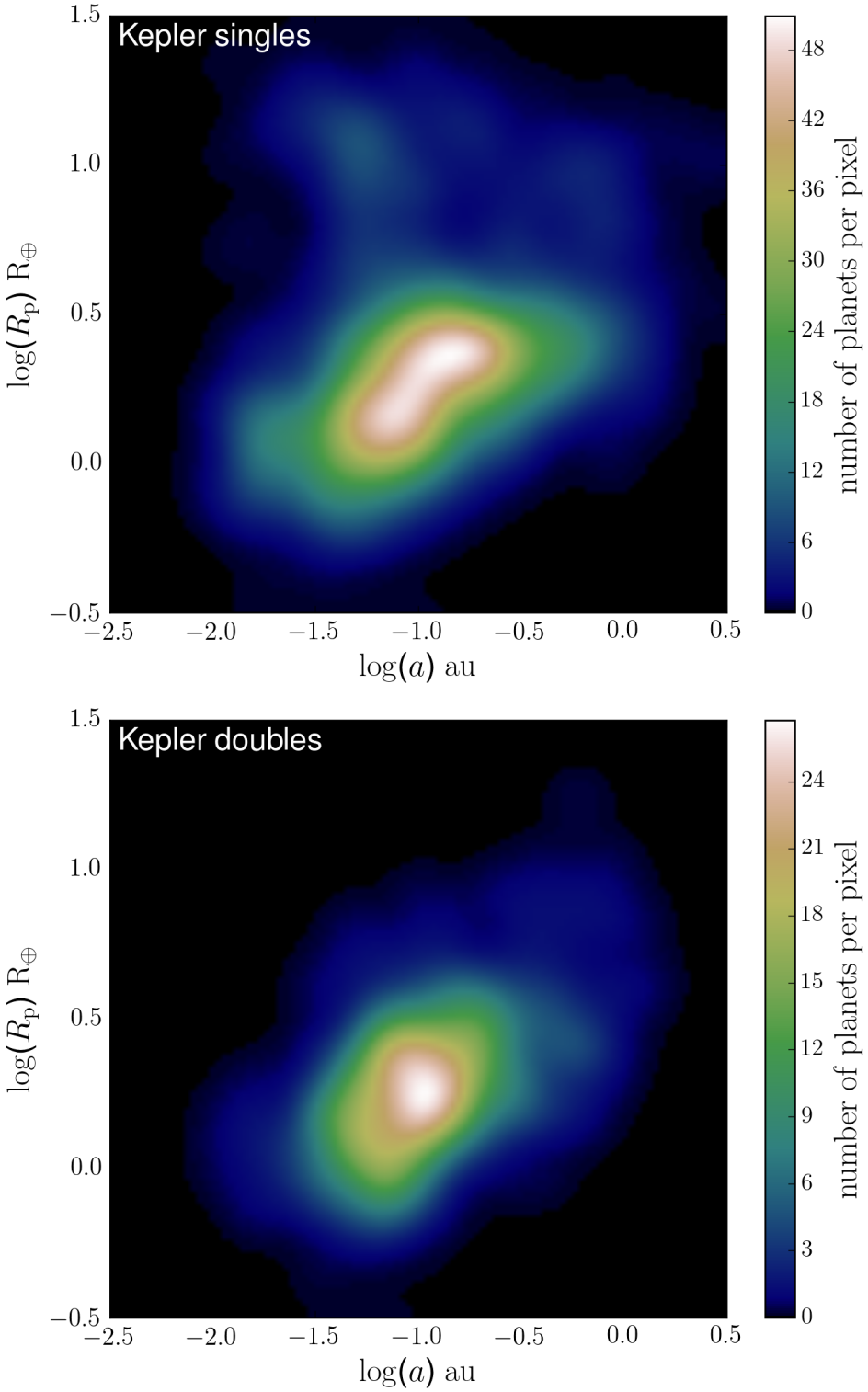

Figure 4.10 The smoothed distribution of the radii and the semi-major axes of planets observed by Kepler to be in systems with a single transiting planet (*top*) and in systems with two transiting planets (*bottom*). Pixel sizes are log(a) = 0.15 by log(R_p) = 0.1.

not necessarily indicate that long period planets inherently favour being in single transiting systems, but instead they might be the inner planet of a higher multiplicity system where the outer planets are on too long a period to produce a significant transit signal.

Finally there appears to be an over abundance in the population of single transiting systems for planets with $R_p \lesssim 2R_\oplus$ at periods P < 10 days ($\lesssim$ 0.03au) (see Lissauer et al. 2011; Johansen et al. 2012; Steffen & Coughlin 2016; Lopez & Rice 2016). The formation processes which lead to these types of planets are unclear. It is also unknown if these objects are inherently rocky planets, or are the cores of Neptune sized planets whose envelopes have been irradiated (Dressing & Charbonneau, 2015; Rogers, 2015; Lopez & Rice, 2016). If these outlying systems are largely ignored, the question remains of whether the remaining planets in single transiting systems are part of the same underlying distribution of higher order planetary systems; i.e. could these single transiting systems contain similar planets which are not observed to transit?

For our dynamical analysis it is not the radii of these planets which is of relevance, rather their masses. I estimate the masses of planets according to the following mass-radius relations. For radii less than $1.5R_\oplus$ I use the rocky planet mass-radius relation from Weiss & Marcy 2014, where density (ρ_p) is related to radii (R_p) through $\rho_p = 2.43 + 3.39(R_p/R_\oplus)\text{gcm}^{-3}$. For radii $1.5 \leq R_p \leq 4R_\oplus$, I use the deterministic version of the probabilistic mass-radius relation for sub-Neptune objects from Wolfgang et al. 2016, where mass (M_p) is given by $M_p/M_\oplus = 2.7(R_p/R_\oplus)^{1.3}$. Once radii become $R_p \gtrsim 4R_\oplus$ deterministic mass-radius relations become uncertain due to the onset of planetary contraction under self-gravity (see Chen & Kipping 2017). From the mass-radius relations detailed in Chen & Kipping 2017, I find their 'Neptunian worlds' deterministic relation of $M_p/M_\oplus = (1.23R_p/R_\oplus)^{1.7}$ gives the most sensible masses for all planets with $R_p > 4R_\oplus$.

4.6.2 De-biasing the Kepler population

As previously alluded to, Kepler only observes planetary systems that have their orbital planes aligned with our line of sight. It is therefore sensible to suggest that there is a much larger, underlying population of planetary systems within which only some are observed to transit. I refer to this underlying population of planetary systems as the *model population*. Conversely, I refer to the population of planetary systems actually observed by Kepler as the *Kepler population*. I assume that Kepler systems are representative of planetary systems in the model population once geometrical biases have been taken into account.

To construct an underlying model population, our primary goal is for this to predict the correct number and planet parameter distribution seen in the Kepler population for systems with two transiting planets (Figure 4.10 bottom). To achieve this I first assume

that all stars either have two or zero planets. Any system which hosts two planets is assumed to be identical to one of the 341 double transiting systems observed by Kepler. I assume the abundance of a specific Kepler-like system in the model population is equal to the inverse of the mean of the double transit probability calculated by the method outlined in §4.3. Systems with inherently low mean double transit probabilities, are therefore probabilistically assumed to be more numerous in the model population. By definition therefore, each unique system in the model population would be expected to be observed with both planets transiting exactly once and so the model population predicts the correct distribution shown in the bottom panel of Figure 4.10. I note that a model population generated in this way is similar to the method described in Johansen et al. 2012, albeit with their work predicting the correct number and planet parameter distribution seen in the Kepler population for systems with three transiting planets.

The sum of the inversed mean double transit probabilities of all the 341 double transiting systems gives the total number of planetary systems in the model population. If I assume that all of the two planet systems are coplanar, I find the model population includes 16517 systems (the remaining 148449 systems observed by Kepler are assumed to have no planets).

Each system in the model population can be observed to have a single transiting planet, depending on the viewing angle. The sum of the mean single transit probabilities for each of the 16517 systems in the coplanar model population gives the total number of single transiting planets, N_{sing}, that would be expected to be observed. Here the mean single transit probability for a given system is equal to $R_\star/a_1 - R_\star/a_2$, where a_1, a_2 are the semi-major axes of each planet when $a_2 > a_1$ and $R_\star$ is the radius of the host star. I find $N_{sing} = 589$, which clearly underestimates the 1951 single transiting systems in the observed Kepler population, by a factor of ~ 3. This is the Kepler dichotomy discussed in §4.2. I show the smoothed distribution of the semi-major axes and planet radii for these 589 predicted single transiting planets in the top left panel of Figure 4.11, which when compared with the top panel of Figure 4.10 clearly shows an under-prediction of the single transiting planets observed by Kepler.

4.6.3 Inherently inclined multi-planet systems

From transit duration variation (TDV) studies, the mutual inclinations of planets in multi-transiting systems are small at $\lesssim 2-3^\circ$ (Fang & Margot, 2012; Fabrycky et al., 2014). I note that this mutual inclination also best fits the distribution of impact parameters in the Kepler population. Perhaps then, if two planets are assumed to be inherently mutually inclined by a small amount, this may account for the abundance of single transiting planets

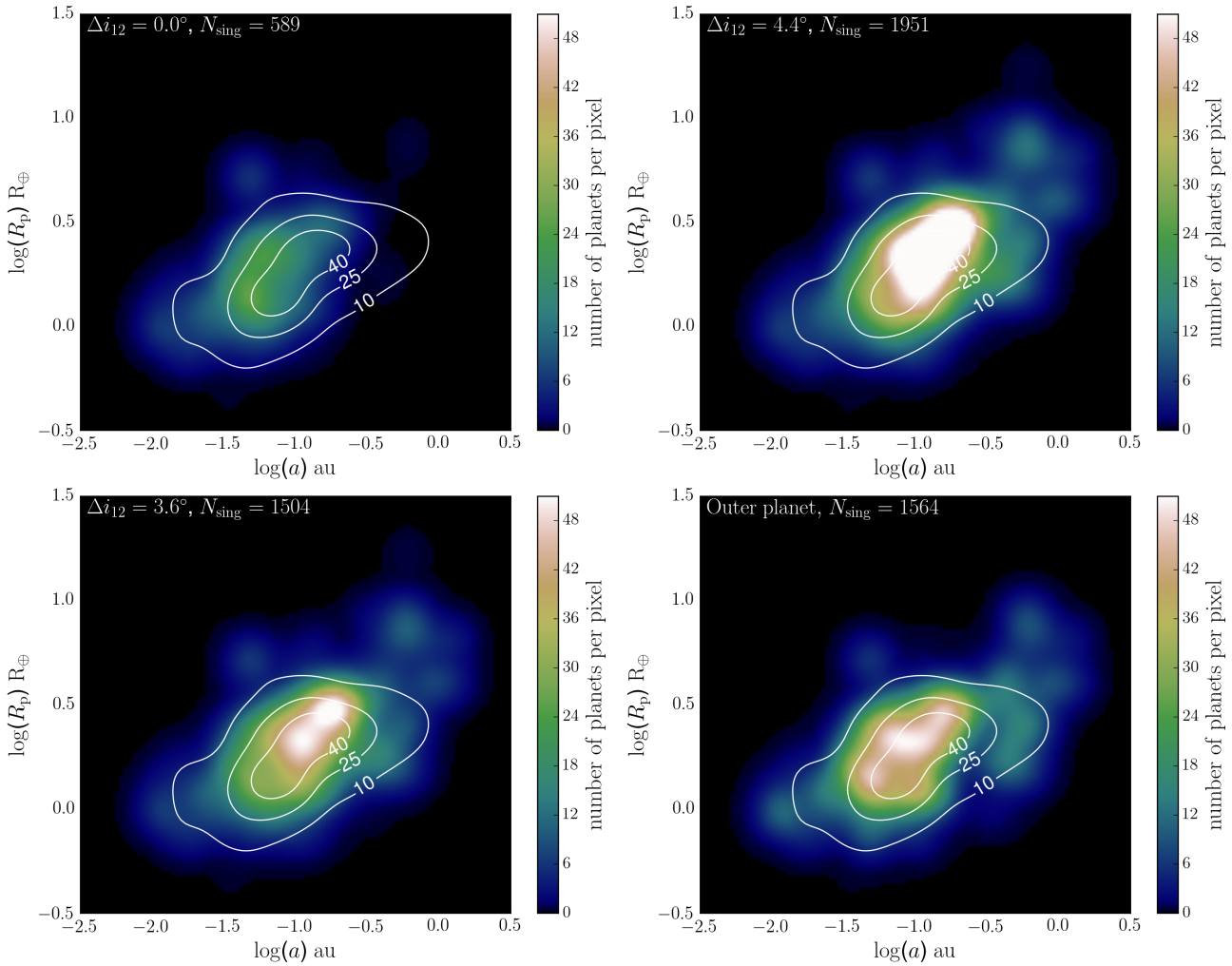

Figure 4.11 The distribution of the radii and semi-major axis of single transiting planets observed from the model population with: (*top left*) no third planet with coplanar two planet systems. (*top right*) Two planet systems inherently mutually inclined by 4.4°. The total number of single transiting planets predicted by the model population is equal to that observed by Kepler. The colour scale for this panel is saturated for ease of comparison. (*bottom left*) Two planet systems inherently mutually inclined by 3.6°. The distribution of single planet systems more strongly agrees with that observed by Kepler. (*bottom right*) A third planet with $m_3 = 24M_\oplus$, $a_3 = 1.07$au and $\Delta i = 10°$. I find the 1564 single transiting planets predicted here are a best fit to those observed by Kepler (left panel of Figure 4.10). The contours show the distribution of single transiting planets from the Kepler population. Pixel sizes are log(a) = 0.15 by $\log(R_p) = 0.1$.

in the Kepler population. Consider a fixed mutual inclination Δi_{12} between the two planets in each of the 341 double transiting systems. The mean single transit probability for each planet from a given system, $P_{sing,1}$ and $P_{sing,2}$ respectively where $P_{sing,1} > P_{sing,2}$, is now given by

$$\begin{aligned} P_{sing,1} &= \frac{R_\star}{a_1} - P \\ P_{sing,2} &= \frac{R_\star}{a_2} - P, \end{aligned} \tag{4.21}$$

where P is the mean double transit probability and $P_{sing,1} + P_{sing,2}$ is the total mean single transit probability for this system. As Δi_{12} increases, the mean double transit probability decreases (Figure 4.3). Therefore for a fixed population of double transiting systems considered here, the expected abundance of single transiting systems increases. Figure 4.12 shows how N_{sing} increases with Δi_{12} for when the number of double transiting systems is kept constant at 341 systems. If $\Delta i_{12} = 4.4^\circ$, I find $N_{sing} = 1951$, i.e. the number of single transiting planets expected to be observed from the model population is equal to the number in the observed Kepler population. This suggests that mutual inclinations in Kepler systems observed with two planets must be less than 4.4°, or the number of single planet systems observed by Kepler would be too large relative to the number of doubles.

I show the distribution of the semi-major axes and radii of the expected single transiting planets for when $\Delta i = 4.4^\circ$ in the top right panel of Figure 4.11. Comparing with the top panel of Figure 4.10, there is an over abundance of predicted single transiting planets with radii of $\sim 2.5 R_\oplus$ and semi-major axes of $\sim$0.15au. This is due to the model population compensating for not being able to reproduce all types of single transiting planets in the Kepler population (e.g. Hot Jupiters discussed in §4.6.1). Herein therefore when discussing how well a model population predicts the Kepler population of single transiting planets I refer to how well the *types* of planets from each population compare, rather than the total number. That is, I look to find which value of Δi_{12} causes the associated version of the top right panel of Figure 4.11 to be most like the top panel of Figure 4.10.

I judge the success of this comparison using a modified χ^2 minimisation test, in which I simply sum the square of the difference between the number of singles with a given radius and semi-major axis expected from the model population, with that of the observed Kepler population. Varying Δi_{12} I therefore look to identify a minimum in the modified χ^2 space without caring for the modified χ^2 value itself. I show this in the bottom panel of Figure 4.12, with the modified χ^2 minimum occurring for $\Delta i_{12} = 3.6^\circ$. The distribution of the single transiting planets expected from the model population for this mutual inclination is shown in the bottom left panel of Figure 4.11. Comparing with the top panel of Figure 4.10, these single transiting planets share a stronger agreement with those in the Kepler

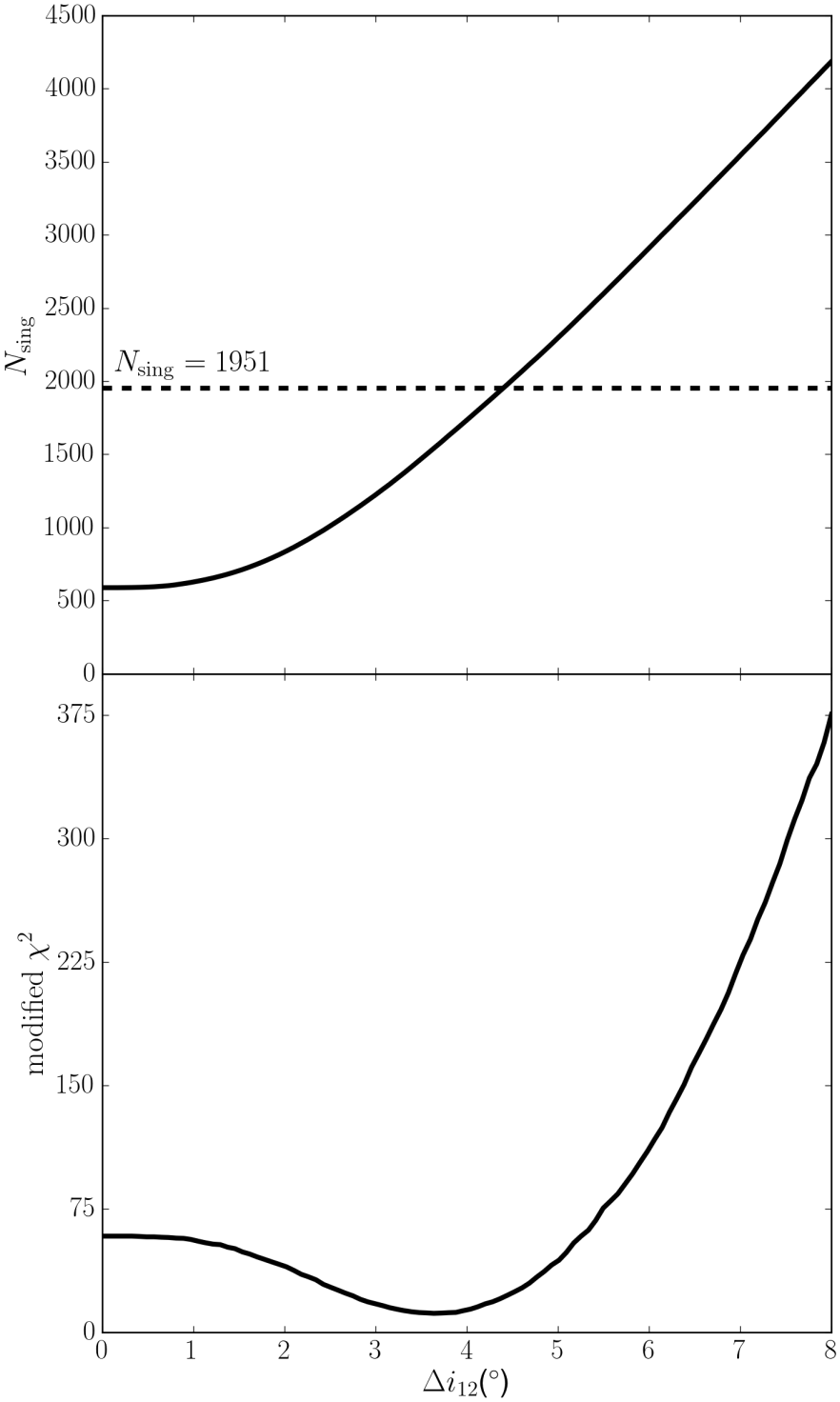

Figure 4.12 (*top*) The expected number of single transiting planets observed from a model population generated from Kepler systems with two planets that are mutually inclined by Δi_{12}. The number of double transiting systems predicted by the model population is constant with 341 systems. (*bottom*) The associated modified χ^2 comparing types of single transiting planets predicted by the model population with the Kepler population. The minimum modified χ^2 value corresponds to $\Delta i_{12} = 3.6^\circ$.

population, compared with when the outer planet predicted $N_{sing} = 1951$ (e.g. top right panel of Figure 4.11). I note that the total number of single transiting planets expected from the model population for $\Delta i_{12} = 3.6^\circ$ is 1504. I assume therefore that the remaining 1951-1504 = 447 single transiting transiting planets in the Kepler population not fit by this model population are *inherently single planet systems*.

Despite the model population for $\Delta i_{12} = 3.6^\circ$ giving the lowest modified χ^2 value, this mutual inclination is perhaps larger than that suggested by TDV studies. I note however that mutual inclination estimates from TDV studies consider a range of planet multiplicities. For example Fang & Margot 2012 consider a model population of planetary systems with 1-7+ planets and predict that ∼50% of observed planetary systems should contain a single planet, with the remaining systems containing multiple planets with mutual inclinations of $\lesssim 3^\circ$. In order to properly predict the inherent mutual inclination in the multi-planet systems considered in this work therefore, it would be necessary to simultaneously model the TDV data directly. I consider such an analysis as part of future work. Instead in §4.6.4 I consider the possibility that Kepler planets form coplanar, but end up mutually inclined due to perturbations from an outer planetary companion on an inclined orbit. This may provide another way to predict the correct abundance of single transiting systems observed by Kepler, and also result in a low mutual inclination for those systems with two transiting planets.

4.6.4 Including an inclined planetary companion

I now consider the effects of a hypothetical outer planet in each of the systems in the model population. I first amend the assumption from §4.6.2 and assume that all stars either host three or zero planets. Any system which hosts three planets is assumed to be identical to one of the 341 double transiting systems from the Kepler population plus an additional outer planet. The outer planet is assumed to have the same mass and semi-major axis in all systems and starts on an inclination to the inner planets when these are coplanar, causing the mutual inclination between the inner planets to evolve according to eq. (4.11). I assume that the outer planet satisfies the Hill stability criterion of $\Delta = 2\sqrt{3}$ (Chambers, 1999) with the outer of the inner two planets for all 341 considered systems, where $\Delta = (a_3 - a_2)/R_H$ and

$$R_H = \left(\frac{m_2 + m_3}{3M_\star}\right)^{1/3} \left(\frac{a_2 + a_3}{2}\right),$$

where $M_\star$ is the stellar mass. If this criterion is not satisfied, I move the outer planet for this specific system until it is. For example, when the outer planet is assumed to have a semi-major axis and mass of 1au and $1M_\oplus$ respectively, I find 6 of the 341 systems do

not satisfy this stability criterion and the outer planet needs to be moved to a mean semi-major axis of 1.2au. When the outer planet has a semi-major axis and mass of 1au and $10M_J$ respectively I find 22 of the 341 systems do not satisfy the stability criterion and the outer planet needs to be moved to a mean semi-major axis of 1.4au.

Each one of the 341 systems is again replicated enough times in the model population to be expected to be observed exactly once. That is, the inverse of the mean double transit probability of the inner two planets, gives the abundance of each of the 341 systems in the model population. The associated mean single transit probabilities for each of the inner two planets is of the same form as eq. (4.21). The sum of the mean single transit probabilities for every system in the model population therefore again gives the abundance of a given single transiting planet that would be expected to be observed from the model population that also fits the number of double transiting systems.

Similarly to the modelling approach in §4.6.3, I look to identify which mass (m_3), semi-major axis (a_3) and initial inclination (Δi) of the outer planet causes the types of single transiting systems expected from the associated model population to be most like those in the observed Kepler population. For a given combination of a_3, m_3 and Δi I therefore calculate a modified χ^2 value described in §4.6.3. I show these modified χ^2 values in Figure 4.13 for an outer planet with $\Delta i = 10^\circ$ (top panel), $m_3 = 1M_J$ (bottom left panel) and $a_3 = 2$au (bottom right panel). Inclinations of $\Delta i \gg 20^\circ$ where eq. (4.11) is expected to break down are included for completeness.

From the top panel in Figure 4.13, it is clear that there is a 'valley' of semi-major axes and masses of the outer planet which causes a significantly lower modified χ^2 value. It can be assumed therefore that such an additional planet predicts single transiting systems whose radii and semi-major axes better fit those in the Kepler population. However there is also a distinct minimum in the modified χ^2 space when the outer planet has a semi-major axis of $\sim$1au for a mass of $\sim 30M_\oplus$. Similarly in the other panels of Figure 4.13 there appear to be distinct minima. For the bottom left panel this occurs for an outer planet (of $m_3 = 1M_J$) with a semi-major axis of 1.38au, initially inclined to the inner planets by $\Delta i = 5.7^\circ$. Finally for the bottom right panel, this minimum occurs for a mass of $\sim 6M_J$ and inclination of 6° (where $a_3 = 2$au). Generally, I find the distribution of single transiting planets expected from the model population is more representative of those in the Kepler population for $3 \lesssim \Delta i \lesssim 10^\circ$.

The bottom right panel of Figure 4.11 gives the distribution of single transiting planets expected from the model population when the outer planet exists in a minimum of the modified χ^2 space with $a_3 = 1.07$au, $m_3 = 24M_\oplus$ and $\Delta i = 10^\circ$ (white circle in the top panel of Figure 4.13). I note that the total number of single transiting planets expected from this model population is 1564. The outer planet parameters which predict $N_{sing} = 1564$ are

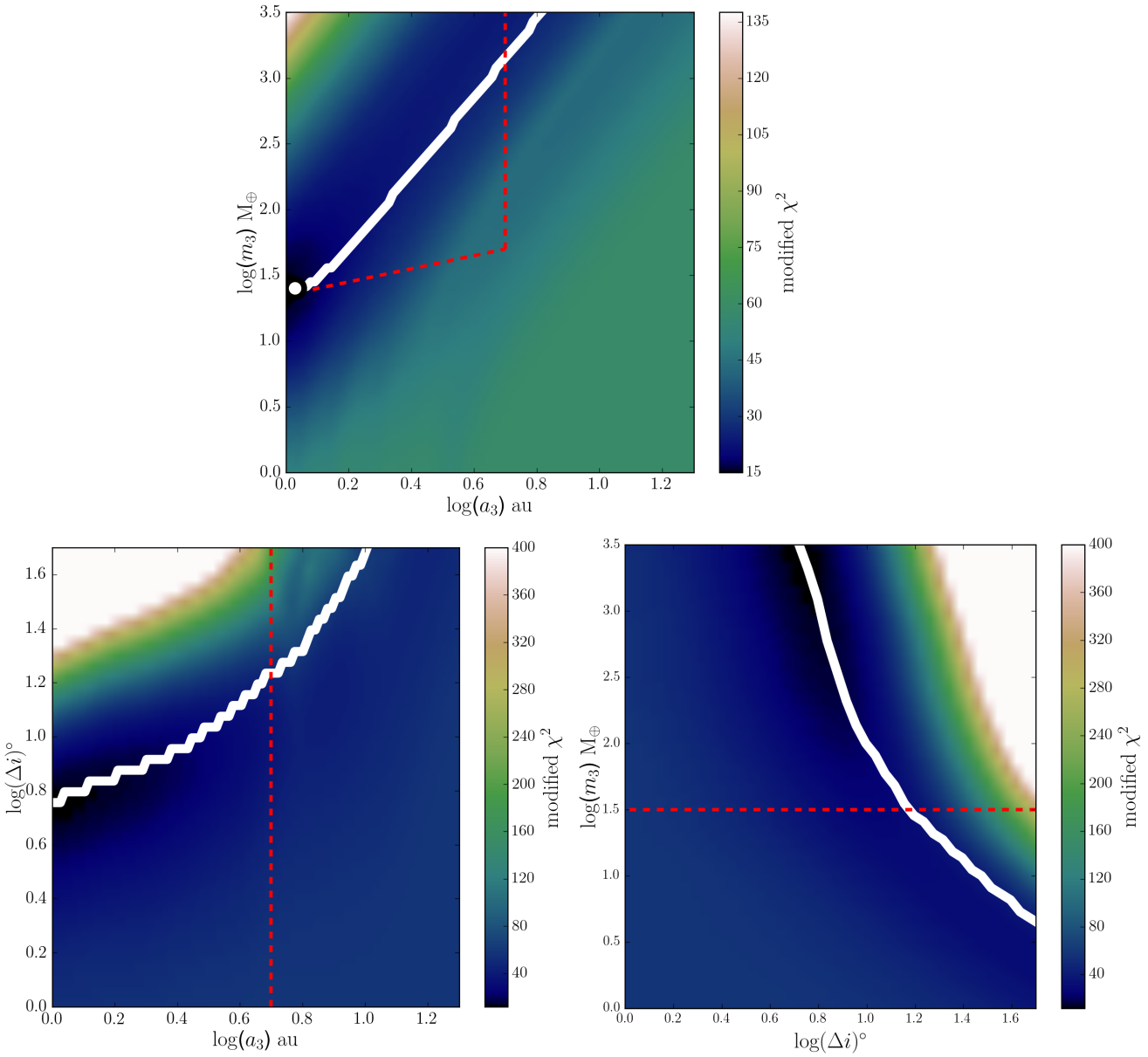

Figure 4.13 Modified χ^2 value comparing types of single transiting planets predicted by the model with Kepler population. For the top panel Δi = 10°, for the bottom left panel $m_3 = 1M_J$ and for the bottom right panel $a_3 = 2$au. Laplace-Lagrange theory is expected to break down for $\Delta i \gg 20°$. The red dashed line refers to a rough RV detection threshold. The white line shows where the model population predicts $N_{sing} = 1564$. The white circle gives the third planet parameters used to produce the bottom right panel of Figure 4.11.

shown by the white lines in Figure 4.13. This line highlights that while many outer planet parameters can predict $N_{sing} = 1564$, some predict single transiting planets which are more representative of those in the Kepler population. I note that N_{sing} predicted by the same range of outer planet parameters from Figure 4.13 is shown in Appendix C.

4.7 Discussion

4.7.1 Combining inherently mutually inclined and outer planet populations

In reality it is likely that the total number of single planet transiting systems observed by Kepler ($N_{sing,Kep} = 1951$) is contributed to by different populations of planetary systems. These may include a number of inherently single planet systems ($N_{sing,inh}$) in addition to a number of single transiting planets observed from a population of two planet systems which have a fixed mutual inclination of Δi_{12} ($N_{sing,Di_{12}}$). They may also include a number of single transiting planets which are observed from a population of initially coplanar two planet systems interacting with an inclined planetary companion ($N_{sing,planet}$). Hence in general, it can be considered that

$$N_{sing,Kep} = N_{sing,inh} + N_{sing,\Delta i_{12}} + N_{sing,planet}. \tag{4.22}$$

Here I make the assumption that the total number of double transiting systems observed by Kepler ($N_{doub,Kep} = 341$) is made up of a fraction f that are two planet systems with an inherent mutual inclination and a fraction (1-f) that are two planet systems with an inclined outer companion. I can thus rewrite eq. (4.22) as

$$\begin{aligned} N_{sing,Kep} = N_{sing,inh} &+ f(N_{sing,Ndoub=341})_{\Delta i_{12}} \\ &+ (1-f)(N_{sing,Ndoub=341})_{planet}, \end{aligned} \tag{4.23}$$

where $(N_{sing,Ndoub=341})_{\Delta i_{12}}$ is the number of singles that would have been produced from the population of two planet systems with a fixed mutual inclination of Δi_{12}, had it been numerous enough to reproduce the 341 double transiting Kepler systems (which is shown in Figure 4.12 as a function of Δi_{12}). Conversely $(N_{sing,Ndoub=341})_{planet}$ is the number of singles that would have been produced from the population of two planet systems which are perturbed by an outer companion, had it been numerous enough to reproduce the 341 double transiting systems. I estimate the number of inherently single planet systems

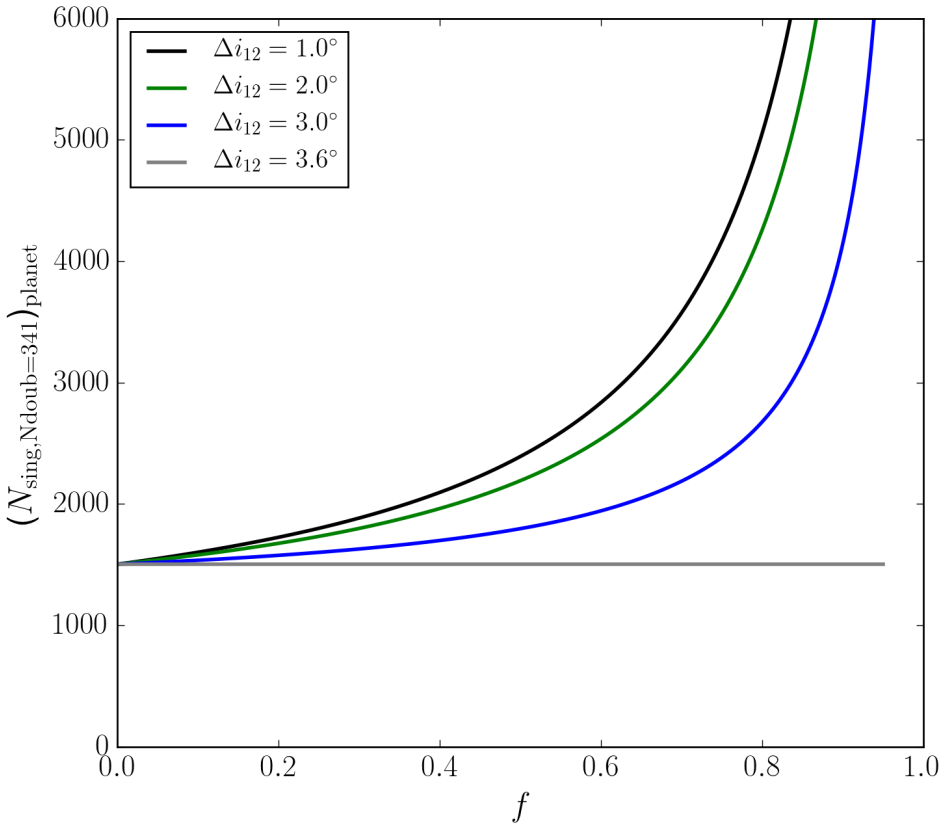

Figure 4.14 The number of single transiting planets needed to be predicted by a population of two planet systems with an outer planetary companion, assuming that (1 – f) of observed Kepler systems host such systems. The remaining fraction of observed Kepler systems are assumed to be two planet systems inherently mutually inclined by Δi_{12}.

to be $N_{sing,inh}$ = 447 from §4.6.3. I note that $N_{sing,inh}$ will change for different values of Δi_{12}, however for simplicity I keep it constant at 447.

For the assumed $N_{sing,inh}$ and an assumed fixed mutual inclination for the fraction of the double transiting systems that are inherently inclined (f), eq. (4.23) means that the number of single transiting systems observed by Kepler can be reproduced by specific combination with the fraction of double transiting systems that have an outer planet (1 – f) and the properties of these planetary systems which determine the ratio of single to double transiting systems from this population (i.e. $(N_{sing,Ndoub=341})_{planet}$). This combination is plotted in Figure 4.14, which can be read alongside Figure C.1 to determine the outer planet parameters required to reproduce the required $(N_{sing,Ndoub=341})_{planet}$. For example, for f = 0.2 and $\Delta i_{12} = 2°$, $(N_{sing,Ndoub=341})_{planet}$ = 1676 from Figure 4.14, which from Figure C.1 would be reproduced by an outer planet with a_3 = 2au, $m_3 = 132 M_\oplus$ and $\Delta i = 10°$. For f = 0.5, $(N_{sing,Ndoub=341})_{planet}$ is increased to 2192 requiring the mass of this outer planet to be increased to $m_3 = 955 M_\oplus$ (for a_3 = 2au and $\Delta i = 10°$). The outer planet parameters required to produce $(N_{sing,Ndoub=341})_{planet}$ are therefore extremely sensitive

to the value of f. However, increasing the value of Δi_{12} for a given value of f increases the value of $(N_{sing,Ndoub=341})_{\Delta i_{12}}$ and hence decreases $(N_{sing,Ndoub=341})_{planet}$ as seen in Figure 4.14, requiring an outer planet which is a weaker perturber of the inner planets.

It should be noted that f and 1 – f are not equivalent to the underlying fraction of stars that host a two planet system with a fixed mutual inclination, or a two planet system with an outer companion respectively. However if f is known, such fractions for the underlying population of stars can be estimated through occurrence rate calculations. I discuss such calculations of occurrence rates in §4.7.3, however it is first necessary to estimate a value for f, which I discuss below.

4.7.2 Comparing inherently mutually inclined and outer planet populations

From §4.6.3 a sole population of two planet systems which are inherently mutually inclined by $\Delta i = 3.6^\circ$ (i.e. when $f = 1$) can reproduce a population of single and double transiting systems representative of those observed by Kepler (Figure 4.11). However from §4.6.4 a sole population of two planet systems with an outer planet (i.e. $f = 0$) can also reproduce a population of single and double transiting systems representative of those observed by Kepler (Figure 4.13). Here I look to differentiate between these two models by considering the predicted distribution of mutual inclinations that would be observed in the two planet populations for each model. I note that combining these two models in a way described in §4.7.1 (i.e. when $0 < f < 1$) would then give some intermediate distribution of mutual inclinations between the overall two planet population.

For the model in which the two planets have an inherent mutual inclination of $\Delta i = 3.6^\circ$, that distribution is narrowly peaked at 3.6° (see Figure 4.15). In contrast, for the model in which two planets are perturbed by an inclined outer planet, the distribution of mutual inclinations is biased toward coplanar systems. This is because, while the outer planet induces a significant mutual inclination between the inner planets, as required to reproduce the correct ratio of single to double transiting systems, the inclination is not always large (see Figure 4.7) and the probability of witnessing a double transit system is much higher when their mutual inclination is low. Consider an outer companion with $m_3 = 24M_\oplus$, $a_3 = 1.07$au and $\Delta i = 10^\circ$, which was in a minimum of the modified χ^2 space (white circle, Figure 4.13 top). Weighting the secularly evolving mutual inclinations between the inner two planets in the 341 considered systems by the associated double transit probability gives the predicted distribution of mutual inclinations which are most likely to be observed. This distribution is shown by the black line in Figure 4.15. It is clear that the most likely observed mutual inclination is when the inner two planets are copla-

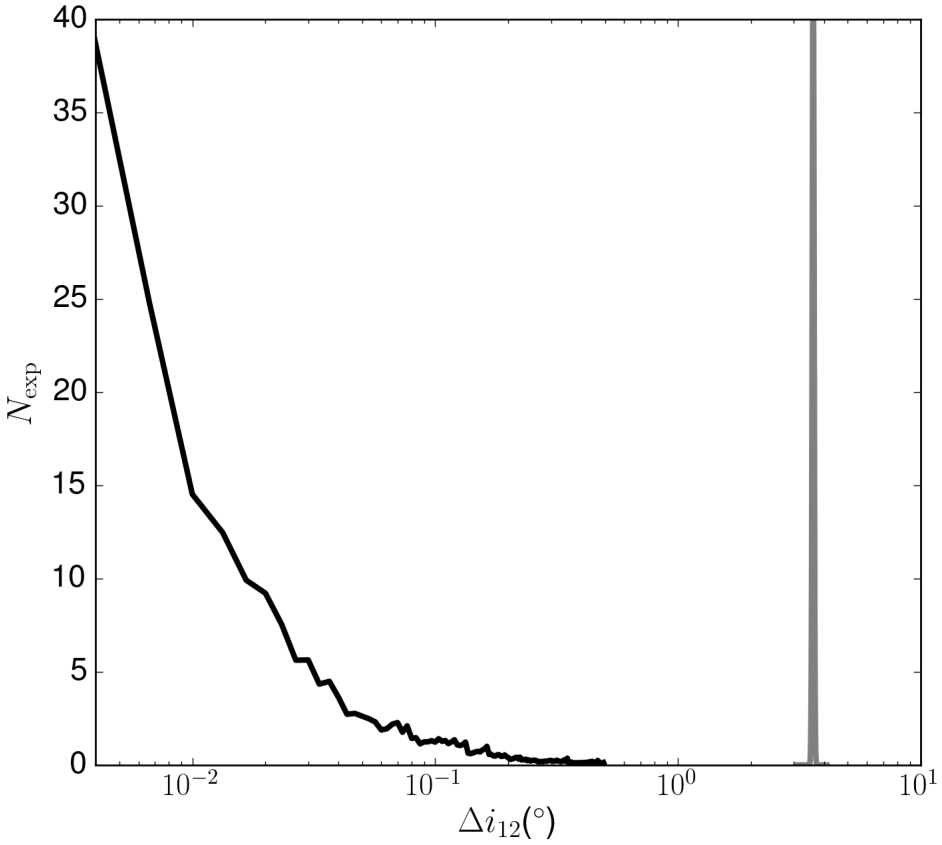

Figure 4.15 Predicted distribution of mutual inclinations between the two planets in the observed Kepler double transit population for different model populations that both produce the correct number of double and single transiting systems. The grey line refers to the model where the two planet are inherently inclined by Δi_{12}=3.6°. The black line refers to the model where two planets are secularly perturbed by a outer companion with m_3 = 24$M_\oplus$, Δi = 10° and a_3=1.07au.

nar. Moreover the number of systems expected to be observed with mutual inclinations beyond 0.5° drops to negligible values.

From transit duration variation studies, the distribution of mutual inclinations between planets in multi-planet Kepler systems is peaked at $\sim$ 2° (Fang & Margot, 2012; Fabrycky et al., 2014), noting however that these works consider different planet populations to those considered here as discussed in §4.6.3. Combining the two above models to produce a similar distribution in mutual inclinations may therefore allow for f to be determined. I look to combine the two models in such a way to predict a value of f, as well as modelling the TDVs of the planetary systems considered in this work directly to predict the distribution of inherent mutual inclinations, as part of future work. For example if a fraction of two planet systems observed by Kepler are considered to have a fixed mutual inclination of Δi_{12} = 4°, then in order to reproduce a distribution of mutual inclinations that peaks at $\sim$2° from modelling of TDVs, it might be expected that f $\sim$ 0.5.

An additional method to estimate f might be to consider whether hypothetical outer planets considered in this work would have been detectable by other means. It is expected that RV studies would be most sensitive to such outer planetary companions. On Figure 4.13 I plot a rough constraint from RV studies, shown by the red dashed lines, assuming a detection threshold of $\sim$2m/s. Outside of 5au I assume RV studies are not sensitive to planets due to long periods. Planets above or to the left of these lines would therefore be detectable with this level of RV precision. This detection threshold suggests that a wide-orbit planet located in the minima of the modified χ^2 values in Figure 4.13 (white circle) should be just detectable by RV studies. This would assume however that all Kepler systems with two planets host this outer companion i.e. $f = 0$. From Figure 4.14 and highlighted in §4.7.1, if $f > 0$ a planet with a larger mass, shorter period or larger inclination is required to reproduce the total number of single transiting systems observed by Kepler. Such outer planets should be readily detectable by RV surveys. For example, for the values of $f = 0.2$ and $f = 0.5$ for $\Delta i_{12} = 2^\circ$ considered in §4.7.1, both of the outer planets in these cases would be expected to be detectable by RV surveys. Due to the inherent faintness of Kepler stars, few have been extensively studied for wide-orbit planets. I suggest therefore that detailed follow-up RV studies of Kepler systems would allow for f to be constrained. Generally for example, a low yield of outer planets in RV studies would suggest that f is low and vice versa.

4.7.3 Occurrence Rates

Similar to that discussed specifically for Kepler systems in §4.7.1, consider that the underlying population of planetary systems contains three possible types of planetary systems. These include inherently single planet systems, two planet systems which have a fixed mutual inclination of Δi_{12} and two planet systems which are being perturbed by an inclined outer planet. In §4.7.1 it was shown that combining these systems with a free parameter f, which describes the fraction of the observed double transiting population that are two planet systems with a fixed mutual inclination, recovers the total number of single and double transiting systems observed by Kepler.

However this value of f is not the same as the fraction of the underlying population of stars that have two planets that are inherently mutually inclined. Here I define the occurrence rate of a given population to be the fraction of stars which would be expected to host such systems. Occurrence rates in this work can be estimated by taking the ratio of the number of systems in a given model population (N_{mod}) to the total number of stars observed by Kepler (N_{Kep}). The individual occurrence rates for the inherently single planet systems is therefore given by $(N_{mod}/N_{Kep})_{inh}$, for the two planet systems with the

fixed mutual inclination of Δi_{12} by $(N_{mod}/N_{Kep})_{\Delta i_{12}}$ and for the two planet systems being perturbed by an inclined outer planet by $(N_{mod}/N_{Kep})_{planet}$. For example, for the population of two planet systems which were inherently mutually inclined by 3.6° (for when f = 1), i.e. those which predicted a population of single transiting planets representative of those observed by Kepler (§4.6.3), the number of systems in the model population was equal to 43807. From §4.6.1 the total number of Kepler stars was 164966. Therefore the occurrence rate for this type of system, $(N_{mod}/N_{Kep})_{\Delta i_{12}} = 27\%$. Conversely, considering the population of two planet systems which were perturbed by an outer companion with $m_3 = 24M_\oplus$, $a_3 = 1.07$au and $\Delta i = 10°$ (white circle Figure 4.13 top) for when f = 0, predicted 42733 systems in the associated model population. Therefore the associated occurrence rate of this type of system $(N_{mod}/N_{Kep})_{planet} = 26\%$.

The calculation of the occurrence rate for the population of inherently single planet systems is slightly different to that described above. From §4.6.3, assume that there are 447 inherently single planet systems (noting that this is subject to the value of Δi_{12}). The distribution of the semi-major axes of these 447 planets is equal to the difference between the distributions of semi-major axes for the single transiting systems observed by Kepler and those predicted by the population of two planet systems with a fixed mutual inclination of $\Delta i_{12} = 3.6°$, i.e. the difference between the top panel of Figure 4.10 and the bottom left panel of Figure 4.11. The number of inherently single planet systems in a model population is then the sum of the inverse of the single transit probabilities $(R_\star/a)$ of all these 447 planets. I find this model population contains 15852 systems, predicting an occurrence rate of inherently single planet systems of 9.6%. This is large compared with the occurrence rate of Hot Jupiters ($\sim$ 1 – 2% e.g. Marcy et al. 2005; Cumming et al. 2008; Mayor et al. 2011; Wright et al. 2012; Santerne et al. 2016). I therefore expect that our population of inherently single planet systems is dominated by a different population, such as those described in §4.6.1 which are poorly constrained.

In a similar way to that described for eq. (4.23), the total occurrence rate of assumed planetary systems in the underlying population of planetary systems can be estimated to be

$$\left(\frac{N_{mod}}{N_{Kep}}\right)_{tot} = \left(\frac{N_{mod}}{N_{Kep}}\right)_{inh} + f\left(\frac{N_{mod}}{N_{Kep}}\right)_{\Delta i_{12}} + (1-f)\left(\frac{N_{mod}}{N_{Kep}}\right)_{planet}. \tag{4.24}$$

Consider the example combination of systems from §4.7.2 for when f = 0.2, $\Delta i_{12} = 2°$ and the outer planet parameters are $a_3 = 2$au, $m_3 = 132M_\oplus$ and $\Delta i = 10°$. Here $f(N_{mod}/N_{Kep})_{\Delta i_{12}}$ $\sim 3\%$ and $(1–f)(N_{mod}/N_{Kep})_{planet}$ $\sim 21\%$. I note that $f(N_{mod}/N_{Kep})_{\Delta i_{12}}/(1–f)(N_{mod}/N_{Kep})_{planet}$ = 3/21 = 14%. This highlights that the occurrence rate of stars which have two planet systems with an inherent mutual inclination is similar to, but not the same as the parameter

f.

Combining with the occurrence rate of inherently single planet systems estimated above, the total occurrence rate of planetary systems becomes 34%. This is similar to occurrence rates of $\sim$ 25%–30% for Kepler like planets derived from injection and recovery analysis of planet candidates from the Kepler pipeline (Petigura et al., 2013; Christiansen et al., 2015).

Estimates of occurrence rates for planets similar to the outer planets considered in this work exist from RV studies. Cumming et al. 2008 suggest an occurrence rate of 7.0 $\pm$ 1.4% for planets with masses and semi-major axes of m_p = 1-10M_J and $\sim$1-5au respectively. Extrapolating this occurrence rate also predicts that 17-20% of stars have gas giants within 20au. Similarly Mayor et al. 2011 suggest an occurrence rate of 13.9 $\pm$ 1.7% for planets with masses and periods of $m_p > 50M_\oplus$ and P < 10yrs respectively. More recently Bryan et al. 2016 suggest that for systems with 1 or 2 RV planets, the occurrence rate of an additional companion with a mass and semi-major axis of 1-20M_J and 5-20au respectively is as high as 52 $\pm$ 5%. The above example occurrence rate for the systems with an outer planet, i.e. $(1-f)(N_{mod}/N_{Kep})_{planet}$ $\sim$21%, is then therefore not contradicted by these studies. However, this example assumed an estimated value of f. In addition to the methods described in §4.7.2, observationally estimated occurrence rates for outer planets may also be able to constrain the value of f. For example if it is assumed that the occurrence rate of the types of outer planets considered in this work is 13.9% (Mayor et al., 2011), then it can be estimated that $(1-f)(N_{mod}/N_{Kep})_{planet} \sim 13.9\%$. As $(N_{mod}/N_{Kep})_{planet} \not> 1$ (i.e. it is unphysical that there are more stars in the model population than the number actually observed by Kepler), this results in an upper limit of $f \leq 0.86$. I suggest therefore that combining this method of placing constraints on f with those described in §4.7.2 might provide a strong constraint on the percentage of planetary systems which may share a fixed mutual inclination compared with systems that may host an outer inclined planet.

4.7.4 Comparing with similar works

Whether an outer planet can reduce the multiplicity of expected transiting planets in an inner planetary system in the context of N-body simulations has recently been investigated by Hansen 2017. A notable example they include is the effect of a companion with a mass of 1M_J at 1au, which is inclined to an inner population of planetary systems with a variety of multiplicities by 10°. They find the ratio of the total number of double to single transiting systems that Kepler would be expected to observe is 0.184 (i.e. $\sim$5 times more expected single than double transiting systems). I find an identical outer planetary companion in our work gives this ratio to be 0.14. I suggest this difference is caused by the population of inner planetary systems used. Hansen 2017 incorporate 50 model inner

planetary systems with a range of multiplicities (the vast majority contained 3-6 planets at the end of their simulations), rather than the two planet Kepler systems considered in this work. Higher multiplicities increases the number of competing secular modes in the system, which can stabilise inner planets against the secular perturbations of an outer companion as shown in Chapter 3 (e.g. Read & Wyatt, 2016). Such an example was also shown in this Chapter in §4.5 for application to Kepler-48. Perhaps then, mutual inclinations are more easily induced between inner planets in this work, increasing the predicted number of single transiting planets that Kepler would be expected to observe, relative to a fixed population of planetary systems.

Moreover compared with N-body simulations, our work does not allow for dynamical instability. If inclinations are large then they couple with eccentricity (Murray & Dermott, 1999), potentially causing orbital crossings between neighbouring planets leading to dynamical instabilities on short, non-secular timescales. Indeed Hansen 2017 find for the above mentioned outer planetary companion that roughly half of the 50 systems they consider lose at least one planet. Moreover Pu & Wu 2015 suggest that the abundance of single and double transiting systems might be the remains of higher order planetary systems that were once tightly packed and have since undergone dynamical instability. A detailed discussion on how dynamical stability would be expected to affect our results is difficult. Our choice that all planets must be initially Hill stable is by no means a robust constraint on the long term stability of all the planetary systems I consider during the secular interaction.

The effects of dynamical instability in tightly packed planet systems interacting with a wide-orbit companion planet was also shown by Mustill et al. 2015. They find that an outer giant planet undergoing Kozai-Lidov interactions with a stellar binary (Kozai, 1962; Lidov, 1962) can have an eccentricity which takes its orbit within the inner planets, leading to a significant reduction in planet multiplicity. Moreover more recent work in Mustill et al. 2016 suggests that these same interactions can cause $\sim$50% of Kepler like systems to lose a planet, either through collisions or ejections. If inclination is not completely decoupled with eccentricity then, these works suggest that dynamical instability plays a significant role in sculpting an inner planetary system.

4.7.5 Metallicity Distribution

The fraction of stars with gas giants increases with higher metal content (e.g. Gonzalez, 1996; Thorngren et al., 2016). However it is unclear if this relation extends to smaller planets with $R_p \lesssim 4R_\oplus$ (Mayor et al., 2011; Zhu et al., 2016). If single transiting planets are in systems which contain an outer giant companion similar to that considered in this work,

then the transiting planet should follow a similar metallicity relation as the giant planet. If there is an inherent population of single planet systems with $R_p \lesssim 4R_\oplus$, in addition to a population of inherently mutually inclined double transiting systems, then these systems will follow a different metallicity relation. Therefore the population of single and double transiting systems observed by Kepler may contain a mixture of metallicity relations. If a distinction can be made between these different relations then this may place constraints on the presence of additional planets in Kepler systems with a single transiting planet.

4.7.6 Assumptions of this work

Throughout this work I have considered mutual inclinations evolve between two planets due to secular interactions with an outer planet. As stated above, increasing the multiplicity of planetary systems complicates the evolution of mutual inclinations. For application to the Kepler dichotomy, including higher multiplicity systems may cause proportionally fewer to be observed as single transiting systems. I look to investigate this as part of future work. Moreover higher multiplicity systems also allow for investigation into whether the presence of an outer planetary companion can explain the number of higher order systems observed by Kepler. This is of particular interest as Johansen et al. 2012 find that generating a model population which predicts the number of systems observed by Kepler with three transiting planets (with small inherent mutual inclinations and no outer companion) cannot simultaneously predict the number of systems with a single and two transiting planets observed by Kepler.

I have also assumed that the inner transiting planets interacting with an outer companion were initially coplanar. However these transiting planets would most likely also have a small inherent mutual inclination (e.g. Fang & Margot, 2012; Fabrycky et al., 2014) which in turn may affect the mean double transit probability.

4.8 Summary and Conclusions

In summary, during the first part of this work I developed a semi-analytical method for the calculation of transit probabilities by considering the area a transiting planet subtends on a celestial sphere (§4.3). Applying this method to a general two planet system, I showed how the probability that both planets are observed to transit changes as they become mutually inclined.

In §4.3.3 I discussed how the mutual inclination between two initially coplanar planets evolves due to secular interactions with an external mutually inclined planetary compan-

ion. I derived the full solution describing this evolution assuming that the mutual inclination remains small, before simplifying it under the assumption that the external planet was on a wide orbit. I found that the maximum mutual inclination between the inner two planets is approximately equal to twice the initial mutual inclination with the external planet. Below this, the maximum mutual inclination between the inner two planets scales according to the mass, semi-major axis and inclination of the external planet by $\propto \Delta i m_3 / a_3^3$.

How the secular interaction causes the double transit probability of the inner two planets to evolve was shown in §4.4. Assuming that this double transit probability is significantly reduced when the maximum mutual inclination exceeds $\approx (R_\star/a_1) + (R_\star/a_2)$ I derived an expression for the mean of the double transit probability considering a given external planetary companion. This expression was applied to Kepler-56, Kepler-68, and Kepler-48 to place constraints on the inclination of the outer RV detected planets in these systems in §4.5. I found that the inner two transiting planets in Kepler-56 and Kepler-68 are not significantly secularly perturbed by the outer planets, regardless of their inclination. For HD 106315 I find that an outer planet inferred from recent RV analysis can cause a significant perturbation to the mutual inclination of two internal transiting planets. Moreover, I find that if the outer planet is present within $\sim$1au, its inclination must be no more than 2.4°, otherwise the probability of observing both the inner planets to transit is significantly reduced. I also found that the RV detected planet in Kepler-48 needs to be inclined with respect to the inner planets by $\lesssim 3.7°$, otherwise the probability that all the inner planets are observed to transit is significantly reduced. I conclude therefore that using the expression for the mean transit probability between inner planets from eq. (4.16) and (4.13) can be used to place significant constraints on the inclinations of RV detected planets, whose host systems also contain transiting planets.

I further applied our method of calculating transit probabilities to the Kepler population in §4.6. I found that relative to a fixed population of transiting systems with two planets on initially coplanar orbits, the expected number of single transiting systems can be significantly increased both by inherently inclining the two planets and by introducing an outer planetary companion. I found that an inherent mutual inclination of $\Delta i_{12} = 3.6°$ predicts a population of single transiting planets most representative of those in the Kepler population. Moreover, I found that outer planets initially inclined by $\sim 3 - 10°$ to the inner planets also predict a representative population of single transiting systems. These outer planets should be detectable by RV studies.

However it is likely that planetary systems observed by Kepler may include a combination of systems which include inherently single planet systems, two planet systems which have some fixed mutual inclination and two planet systems interacting with an inclined

outer planet. For two planet systems which are perturbed by an outer planet, the distribution of the mutual inclinations between the inner planets of such systems is biased toward coplanar systems. This is due to an increased probability of observing inner planets when coplanar compared with when mutual inclinations are larger. I suggest that combining populations of inherently mutually inclined two planet systems with two planet systems which are interacting with an outer planet may be able to reproduce the observed distribution of mutual inclinations between Kepler planets. In doing so, this may provide constraints on the presence of outer planets in the Kepler population. I suggest also that detailed follow-up of RV studies in Kepler systems will provide a more direct constraints on the presence of outer planets. There should also be a dichotomy in the number of transiting systems observed by the upcoming *TESS* mission (Ricker et al., 2014), however for these systems astrometry and RV techniques will be able to be used to verify the presence and influence of outer planets.

From both Chapters 3 and 4, I have shown therefore that wide-orbit planets can have a significant effect on inner planets through long term dynamical interactions. However, as described in §1.6 planetary systems can also contain populations of debris in addition to planets. In Chapter 5 I investigate how a wide-orbit planet interacts with such a population of debris in the planetary system HR8799. Specifically, I investigate whether the presence of a wide-orbit planet can explain the population of debris currently observed in this system.

5

Shaping HR8799's outer dust belt with an unseen planet

5.1 Chapter Summary

HR8799 is a benchmark system for direct imaging studies. It hosts two debris belts, which lie internally and externally to four giant planets. This Chapter considers how the four known planets and a possible fifth planet, interact with the external population of debris through N-body simulations. I find that when only the known planets are included, the inner edge of the outer belt predicted by my simulations is much closer to the outermost planet than recent ALMA observations suggest. I subsequently include a fifth planet in my simulations with a range of masses and semi-major axes, which is external to the outermost known planet. I find that a fifth planet with a mass and semi-major axis of $0.1 M_J$ and 138au predicts an outer belt that agrees well with ALMA observations, whilst remaining stable for the lifetime of HR8799 and lying below current direct imaging detection thresholds. I also consider whether inward scattering of material from the outer belt can input a significant amount of mass into the inner belt. I find that for the current age of HR8799, only $\sim$1% of the mass loss rate of the inner disk can be replenished by inward scattering. However I find that the higher rate of inward scattering during the first $\sim$10Myr of HR8799 would be expected to cause warm dust emission at a level similar to that currently observed, which may provide an explanation for such bright emission in other systems at $\sim$ 10Myr ages. The work presented in this Chapter has been published in Read et al. 2018.

5.2 Chapter Introduction

The vast number of exoplanets that have been observed in recent years has revolutionised planet formation and evolution theories. However, as discussed in §1.5, the vast majority of these planets have been detected using transit or radial velocity techniques, which are

only sensitive to planets within a few au (at best) of the host star (e.g. Mayor et al., 2003; Lissauer et al., 2011; Mayor et al., 2011; Marmier et al., 2013; Lissauer et al., 2014; Morton et al., 2016; Rowan et al., 2016; Wittenmyer et al., 2016). Currently direct imaging offers the best option for detecting planets outside this limiting distance. However, due to the complexities in nulling the stellar halo with extreme precision, most direct imaging studies are only sensitive to planets above a few Jupiter masses (e.g. Vigan et al., 2016; Chauvin et al., 2017). Nevertheless, the detection of wide-orbit giant planets can place stringent constraints on the architecture of the inner planets (e.g. Becker & Adams, 2016; Read & Wyatt, 2016; Mustill et al., 2016; Hansen, 2017; Lai & Pu, 2017; Read et al., 2017), and the existence of unseen planets invoked to explain structure observed in debris belts (e.g. β Pic Lagrange et al. 2009).

HR8799 is one of the most well known directly imaged systems, which has been observed to host four giant planets that are a few times the mass of Jupiter (Marois et al., 2008, 2010). Debris belts, both internal and external to the planets have also been detected (e.g. Chen et al., 2006; Rhee et al., 2007; Su et al., 2009; Hughes et al., 2011; Patience et al., 2011; Matthews et al., 2014; Booth et al., 2016). As such, HR8799 is an ideal test system for planet formation and evolution theories, as interactions between planets themselves and with debris can be investigated. Moreover, HR8799 is perhaps currently one of the most promising systems for understanding the formation of the Solar System, as both harbour four giant planets in addition to internal and external populations of debris.

The outer belt around HR8799 has recently been subject to observations with the *Atacama Large Millimeter Array* (ALMA) (Booth et al., 2016). These observations provide the highest resolution images of the outer belt to date and suggest that the position of the inner edge of the belt is too far out to be carved by dynamical interactions with the outermost known planet. Booth et al. 2016 postulate therefore that an additional planet might be present around HR8799, external to the outermost known planet and below current detection thresholds, which is responsible for the structure of the outer planetesimal belt. In this Chapter I therefore investigate whether a fifth planet around HR8799 indeed provides a better explanation for the ALMA observations of the outer disk, compared with the four known planets in their currently observed configuration.

In §5.3 I give specific details of the HR8799 system including the planets and debris belts. In §5.4 I use N-body simulations to model how the four known planets interact with the outer planetesimal belt and how well this predicts the ALMA observations. In §5.5 I include an additional planet in my simulations, which is external to the outermost known planet, to investigate whether the predicted outer belt agrees more strongly with the ALMA observations. In §5.6 I consider whether this additional planet can replenish the mass of the inner belt, through inward scattering of material from the outer planetesimal

belt, before finally summarizing and concluding in §5.7.

5.3 HR8799

5.3.1 Stellar properties

HR8799 is an A type star (Gray et al., 2003) at a distance of 39.4pc (van Leeuwen, 2007). Characteristic pulsations in luminosity and an unusual deficiency in iron peak elements compared with similar type stars place it as a γ-Doradus and λ-Bootis type star respectively (Venn & Lambert, 1990; Gray & Kaye, 1999; Kaye et al., 1999; Handler, 1999). The mass, radius and luminosity estimates of HR8799 most commonly referenced in the literature are $\sim$1.5$M_\odot$, 1.44$R_\odot$ and 5.05$L_\odot$ respectively (Marois et al., 2008, 2010; Baines et al., 2012). While consensus has largely been reached on these fundamental stellar parameters, the age of the system, especially since the discovery of the giant planets, remains a topic of much debate. The age of HR8799 is of vital importance in determining the mass and therefore the nature of the planets, as planetary evolution models predict planets to cool and therefore significantly dim over time. A younger age estimate for HR8799 therefore predicts less massive planets and vice versa. Most studies agree that HR8799 is unequivocally young at < 100Myr, however estimates of $\sim$Gyrs do exist (Moya et al., 2010a). A summary of age estimates from a variety of different techniques can be found in Table 1. of Baines et al. 2012.

In the discovery papers of the directly imaged planets (Marois et al., 2008, 2010), the age of HR8799 was assumed to be 60^{+100}_{-30}Myr due to: 1) the galactic space motion of HR8799 placing it as a likely member of the Columba moving group which contains stars with ages between $\sim$30-40Myr (Torres et al., 2008; Zuckerman et al., 2011; Bell et al., 2016). 2) The position of HR8799 on a Hertzsprung-Russell diagram is similar to stars with ages of $\sim$ 50 – 70Myr (Zuckerman, 2001). 3) The fact that γ-Doradus and λ-Bootis type stars are typically young with ages of $\sim$100Myr (Krisciunas et al., 1995; Gray & Corbally, 2002). 4) The probability of detecting a debris disk decreases with age, suggesting that HR8799 is indeed young (Spangler et al., 2001; Decin et al., 2003; Rieke et al., 2005; Rhee et al., 2007). I note that both support and doubt of this reasoning has been cast by a variety of authors (e.g. Moya et al., 2010a,b; Moro-Martín et al., 2010; Hinz et al., 2010; Zuckerman et al., 2011; Currie et al., 2011; Baines et al., 2012). Notably, support for the young age of HR8799 is given by measurements of the luminosity and radius of the star using the CHARA Array Interferometer, which places the age at $33^{+7.0}_{-13.2}$Myr, assuming that HR8799 is contracting toward the zero-age main sequence (Baines et al., 2012). Moreover, the probability that

Planet	M (M_J)	a (au)	e	I (deg)	Ω (deg)	ϖ (deg)	M_A (deg)
e	9 ± 2	15.4 ± 0.2	0.13 ± 0.03	25 ± 3	64 ± 3	176 ± 6	326 ± 5
d	9 ± 3	25.4 ± 0.3	0.12 ± 0.02			91 ± 3	58 ± 3
c	9 ± 3	39.4 ± 0.3	0.05 ± 0.02			151 ± 6	148 ± 6
b	7 ± 2	69.1 ± 0.2	0.020 ± 0.003			95 ± 10	321 ± 10

Table 5.1 Masses and stellocentric orbital elements of the planets around HR8799 from Goździewski & Migaszewski 2014. The orbital elements refer to semi-major axis, eccentricity, inclination, longitude of ascending node, longitude of pericentre and mean anomaly respectively. The planets were predicted to be coplanar with $I = 25 \pm 3^\circ$ and $\Omega = 64 \pm 3^\circ$.

HR8799 is a member of the Columba association using the Banyan II online tool detailed in Gagné et al. 2014 is 75%, assuming weighted priors and that the star is younger than 1Gyr. Studies have cast some doubt on the Columba membership of HR8799 however, notably by Hinz et al. 2010 who suggest that HR8799 is too far from the centroid of Columba to be a likely member. However, Columba association members are mainly southern hemisphere targets, such that a northern hemisphere target like HR8799 is likely to be significantly separated from these objects. Indeed, since Hinz et al. 2010, more members of the Columba association have been identified, with relative positions closer to HR8799 (e.g. Zuckerman et al., 2011; Rodriguez et al., 2013).

5.3.2 Planets

For an assumed age of 60^{+100}_{-30}Myr, the masses of the four planets around HR8799 from the discovery papers were predicted to be 7^{+4}_{-2}, 10 ± 3, 10 ± 3, 10 ± 3 M_J for planets b, c, d, e respectively (Marois et al., 2008, 2010), where b is the outermost planet and e the innermost. That is, the planets are indeed planetary objects rather than brown dwarfs. As these planets have such large masses, many authors have investigated the dynamical stability of such a planet configuration (e.g. Goździewski & Migaszewski, 2009; Reidemeister et al., 2009; Fabrycky & Murray-Clay, 2010; Soummer et al., 2011; Currie et al., 2012; Sudol & Haghighipour, 2012; Esposito et al., 2013; Goździewski & Migaszewski, 2014). Indeed, the dynamical stability of the planets can place an additional constraint on the age of the system. Many independent studies agree that stability is maintained between the planets for the lifetime of the system likely due to the planets being in a 1b:2c:4d:8e mean motion resonant chain (e.g. Goździewski & Migaszewski 2009; Reidemeister et al. 2009; Fabrycky & Murray-Clay 2010; Sudol & Haghighipour 2012; Goździewski & Migaszewski 2014; Konopacky et al. 2016; Zurlo et al. 2016, see Pueyo et al. 2015; Götberg et al. 2016 for studies which show that stability can be maintained without resonances however). That is, for

every 1 orbit of b, c orbits twice etc. Such a configuration is supported by recent work from Goździewski & Migaszewski 2014 who consider a suite of masses and orbital elements for the planets to see which simultaneously remain stable and best reproduce the astrometric observations of the planets. I show the masses and stellocentric orbital elements for each of the planets from the best fitting model from Goździewski & Migaszewski 2014 in Table 5.1 (equivalent to Table 1. in Goździewski & Migaszewski 2014). This model predicted the planets to be coplanar with an inclination and longitude of ascending node of I = $25 \pm 3^{\circ}$ and $64 \pm 3^{\circ}$ respectively. I note however that it is unclear whether the planets are indeed coplanar, as two independent studies find that at least planet d may not be co-planar with the other planets (Currie et al. 2012; Pueyo et al. 2015). Co-planarity of the planets is supported by recent fitting of astrometric data detailed in Konopacky et al. 2016, however here some astrometry points considered by earlier works are omitted. The presence of additional giant planets interior to the innermost known planet is unlikely according to *Keck* L'-band aperture masking observations, which place upper limits to planetary mass companions of 80, 60 and $11 M_J$ at projected separations of 0.8, 1 and 3-10au respectively (Hinkley et al., 2011b).

5.3.3 Disk Structure

Belts of material have also been observed around HR8799, both internal and external to the known planets (e.g. Chen et al., 2006; Rhee et al., 2007; Su et al., 2009; Hughes et al., 2011; Patience et al., 2011; Matthews et al., 2014; Booth et al., 2016). *Spitzer* and *Herschel* observations find an unresolved belt of warm ($\sim$150K) dust internal to the known planets between $\sim 6-15$au, with a mass of $1.1 \times 10^{-6} M_{\oplus}$ in small grains between 1.5-4.5mm (Su et al., 2009; Matthews et al., 2014). External to the known planets far-infrared and mm observations resolve a cold ($\sim$45K) planetesimal belt between $\sim 100-300$au (e.g. Su et al., 2009; Hughes et al., 2011; Patience et al., 2011; Matthews et al., 2014) with a mass in 10-1000mm dust grains of $1.2 \times 10^{-1} M_{\oplus}$ (Su et al., 2009). Further outside the planetesimal belt, a halo of small grains has also been observed to extend out to $\sim$ 1000au (e.g. Su et al., 2009; Matthews et al., 2014).

Recent ALMA observations of the outer planetesimal belt resolve it to be between $\sim$145-429au. I defer the reader to Booth et al. 2016 for a detailed description of the ALMA observations and modelling of this outer belt, however I highlight the main points here. Figure 1 in Booth et al. 2016 shows the dirty image (referring to the inverse Fourier transform of the visibilities) of the continuum emission of HR8799 at 1.34mm and the dirty beam, which had a beam size of 1.7×1.3 arcsec^2 in RA and DEC respectively for a position angle of 89° (taken anti-clockwise from North). From this dirty image, it is clear that there is a ring

of emission at ∼5.5arcsec from the star, indicating the presence of an outer planetesimal disk around HR8799.

In order to estimate parameters of this outer disk, Booth et al. 2016 modelled the disk emission in the image space using 6 parameters: (1) the radius of the inner (R_{in}) and (2) outer (R_{out}) edges, (3) a value Γ which defines how the optical depth varies as r^{Γ}, (4) the inclination of the disk from face on (I_{disk}), (5) a position angle measured anti-clockwise from North (ϑ) and (6) the total flux density of the disk at 1.34mm.

From running a MCMC minimisation procedure, the 6 parameters which produced a model disk which most closely represented the dirty image of HR8799 are given in Table 2 in Booth et al. 2016, with $R_{in} = 145^{+12}_{-12}$au, $R_{out} = 429^{+37}_{-32}$au, $\Gamma = -1.0^{+0.4}_{-0.4}$, $I_{disk} = 40^{+5}_{-6}{}^{\circ}$ and $\vartheta = 51^{+8}_{-8}{}^{\circ}$. The azimuthally averaged intensity profile of a model disk with these best fitting parameters in units of mJy beam^{-1}, is shown by the orange line in Figure 5.1 (Booth priv comm). I acknowledge and thank Mark Booth for providing ALMA data for HR8799 shown in this Figure. Herein I simply refer to this intensity profile as the observed intensity profile for the outer planetesimal belt around HR8799, noting that this profile is actually the profile of the best fitting model image from Booth et al. 2016 convolved with the ALMA beam with the residuals added on top, rather than from the dirty image of HR8799 itself. The shaded regions around the intensity profile refer to the 1σ rms of the noise per beam at a given radial location (extracted using a method described in Marino et al. 2016). I acknowledge Sebastian Marino for providing this 1σ rms of the noise per beam shown in Figure 5.1.

Notably, Booth et al. 2016 suggest the position of the inner edge of the outer belt cannot be explained by dynamical interactions with planet b in its current configuration and therefore, this might be indicative of an additional, yet to be detected planet which is external to planet b.

5.4 Outer disk interaction with the four known planets

5.4.1 Simulations

I first model how an outer planetesimal belt around HR8799 would interact with the four known planets. I assume masses and stellocentric orbital elements of the planets equal to those derived in Goździewski & Migaszewski 2014, as shown in Table 5.1. I also assume the same stellar mass and radius of HR8799 used in Goździewski & Migaszewski 2014 of 1.56$M_{\odot}$ and 1.44$R_{\odot}$ respectively (Marois et al., 2010; Baines et al., 2012). I represent the outer disk as a population of 50,000 non-interacting massless particles which are initially

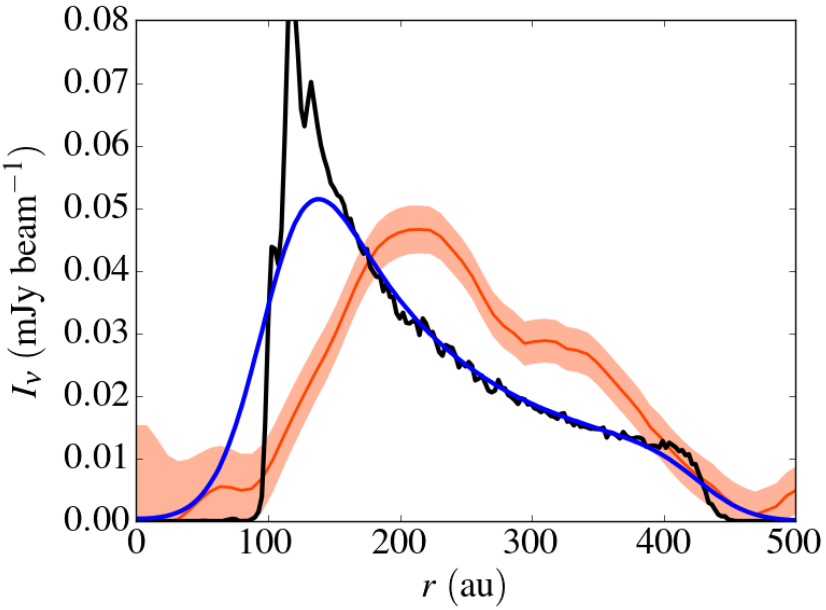

Figure 5.1 Intensity profile of outer disk around HR8799 from ALMA observations, shown by the orange line with the shaded region referring to the 1σ rms of the noise per beam. The black line gives the intensity profile of the outer disk predicted by my simulations from the four known planets interacting with a population of test particles. The blue line shows this profile once the simulated image of the outer belt has been convolved with the beam of ALMA. It is clear that the profile predicted by the four planets in isolation is not a good fit to the ALMA observed profile.

distributed evenly between the semi-major axis of HR8799b (69.1au) and the outer edge of the disk derived from ALMA observations (429au Booth et al. 2016). The particles are initialised with respect to the centre of mass of the system and the orbital plane of the planets, with eccentricities and inclinations randomly sampled between 0-0.05 and 0-0.05radians respectively. The remaining angular orbital elements are initialised randomly between 0-2π. For the radii of the four known planets I use the 'Jovian Worlds' mass to radius relation from Chen & Kipping 2017, valid for $0.414 M_J < M < 0.08 M_\odot$[1]:

$$\frac{R}{R_\oplus} = 17.74 \left(\frac{M}{M_\oplus}\right)^{-0.044} . \tag{5.1}$$

This gives a radii of $1.11 R_J$ for c, d, e and $1.12 R_J$ for b respectively (I note however that the choice of planet radii has little effect on the results of this work).

To model the gravitational interaction between all bodies, I use the N-body integrator REBOUND (Rein & Liu, 2012), using a hybrid integrator (HERMES) which switches from a fixed, to a variable time-step integrator (Rein & Spiegel, 2015; Rein & Tamayo, 2015) when a pair of objects orbit within a given distance. This allows for computational efficiency

[1] I use the deterministic version of the probabilistic mass to radius relation from Chen & Kipping 2017.

when bodies are widely spaced and for close encounters to be followed accurately. For the fixed time-step integrator I use a time-step of 2.4yrs (5% of the period of HR8799e) and switch to the variable time-step integrator when particles orbit within 8 Hill radii of one of the planets or within 50 stellar radii of the star. I integrate the system for 60Myr, noting the orbital elements of all bodies at intervals of 0.6Myr. Particles are removed if they are ejected from the system, which is defined as reaching a distance of 10,000au from the center of mass, or have a physical collision with any of the planets or the star. During a collision, the time and the orbital elements of the particle are noted.

5.4.2 Results

The eccentricity of particles against semi-major axis out to 200au at four different epochs is shown in Figure 5.2. Close to HR8799b, overlapping first-order resonances induce chaotic motions in particles and they are quickly removed from the simulation. The chaotic zone around a planet extends to an approximate distance of $\Delta a = 1.5 a \mu^{2/7}$ where a is the semi-major axis of the planet and μ is the planet to star mass ratio, $M/M_\star$, where M and $M_\star$ are the planet and star mass respectively (e.g. Wisdom, 1980; Duncan et al., 1989). For HR8799b, the width of the chaotic zone extends out to $\sim$ 90au, which is shown by the grey shaded region in Figure 5.2. Particles are also perturbed at the mean motion resonances (MMR) of HR8799b (red dashed lines), with the positions of these resonances given by $a = a_b(p/q)^{2/3}$, where p and q are integers, $p > q$ and a_b is the semi-major axis of HR8799b. I note that the same evolution is also seen in the inclinations of the particles, with the maximum inclination after 60Myr for non-scattered particles reaching $\sim 10^\circ$ at the 2:1b MMR. Beyond 150au, I find particles do not significantly evolve over 60Myr. Secular interactions at these distances are not significant, with particles being perturbed by negligibly small forced eccentricities and inclinations.

To investigate the presence of any smaller scale resonant structure in the surface density of the particles, I plot the de-projected x and y positions of particles in the top panel of Figure 5.3. As few particles undergo scattering interactions with the planets after $\sim$30Myr (see Figure 5.2), I take output from the last 16 intervals of the simulation (from 51-60Myr) and combine them, by choosing a frame co-rotating with HR8799b. This substantially boosts the signal to noise of the image, as the number of particles considered increases from 5×10^4 to 8×10^5. The white cross gives the position of HR8799b for reference. This image highlights that no significant structure is seen external to the inner edge, other than a small dip caused by the 2:1b MMR.

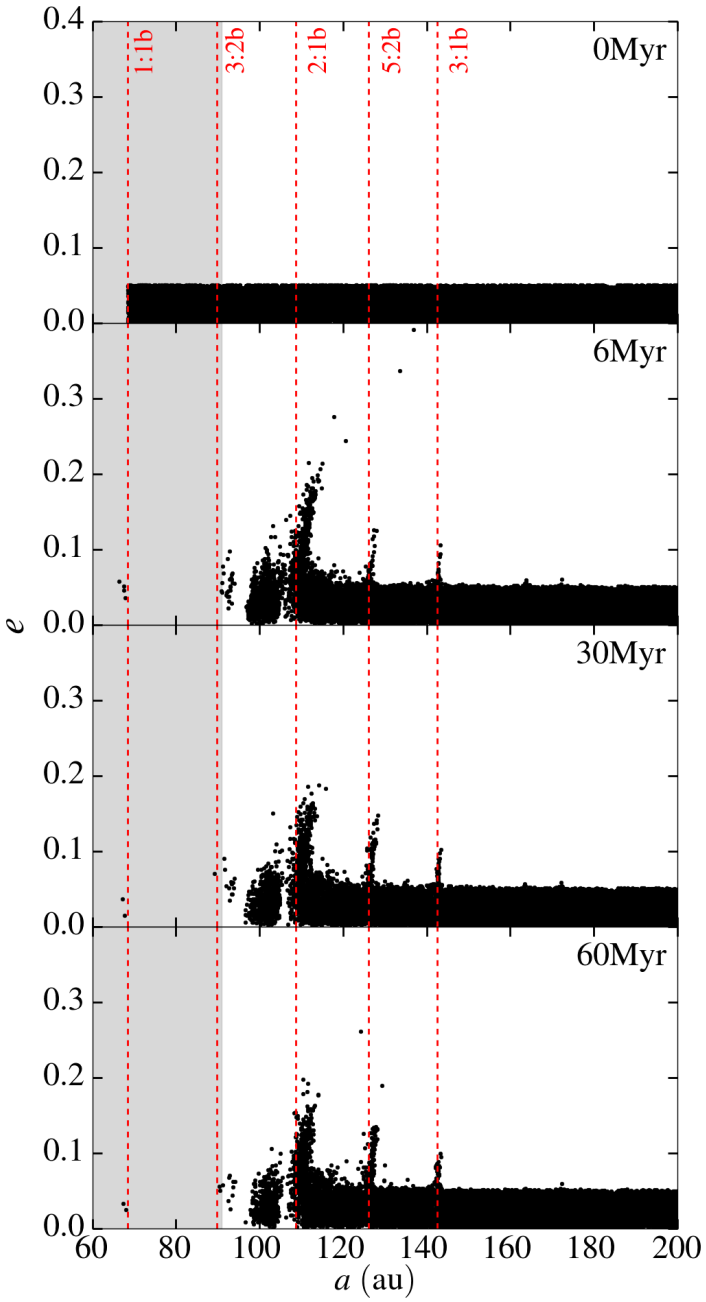

Figure 5.2 Semi-major axis vs. eccentricity of particles evolving due to dynamical interactions with the four known planets around HR8799. The grey shaded area refers to the classical chaotic zone around HR8799b. The red dashed lines refer to the mean motion resonances of HR8799b.

5.4.3 Comparing outer disk with ALMA observations

It is clear therefore from Figure 5.2 that the four known planets carve an inner edge of the planetesimal belt at ∼100au. However, as discussed in §5.3.3, ALMA observations of HR8799 suggest that the inner edge is much further out at 145au (Booth et al. 2016, Figure 5.1). To see how well my simulations predict the overall structure of the disk observed by ALMA, rather than just the inner edge, I compare my simulations directly with the ALMA observations.

To compare my simulated surface density image of HR8799 (e.g. top panel of Figure 5.3) with the ALMA data, I must convert it to an intensity image, with the disk inclined from face on by $I = 40^\circ$ and a position angle (anti-clockwise from North) of $\vartheta = 51^\circ$ (§5.3.3, Booth et al. 2016). I assume that the intensity of the disk is given by:

$$I_\nu(r) \propto \Sigma(r) B_\nu(T) \varkappa_\nu,$$

where $\Sigma(r)$ is the surface density of the disk at a radial position r, $B_\nu(T)$ is the Planck function at temperature T and $\varkappa_\nu$ is the opacity. I assume that the opacity is a fixed quantity and that planetesimals that are emitting at 1.3mm absorb and emit like blackbodies ($T \propto r^{-1/2}$), allowing the Planck function to be approximated in the Rayleigh Jeans limit, resulting in

$$I_\nu = K\Sigma(r) r^{-1/2}, \tag{5.2}$$

where K is a scaling factor. I therefore take the simulated image of HR8799 from the top panel of Figure 5.3, scale it by a factor of $r^{-1/2}$ to convert it to intensity, incline it (from face on) by $I = 40^\circ$ and rotate it to have a position angle (anti-clockwise from North) of $\vartheta = 51^\circ$.

For the simulated intensity image to have the same resolution expected from ALMA, it is necessary to convolve it with the beam of ALMA. I assume that the beam can be approximated by an elliptical Gaussian with a FWHM in x and y of 1.7 and 1.3arcsec respectively (equal to size of the beam in RA and DEC respectively from Booth et al. 2016), and to 67.0 and 51.2au respectively at the distance of HR8799. The bottom panel of Figure 5.3 shows the simulated surface density image from the top panel once it has been scaled to intensity, inclined, rotated and convolved with the beam of ALMA. The beam is shown by the white ellipse for reference. An azimuthally averaged radial profile of the bottom panel of Figure 5.3, which is calculated by using a series of commonly aligned elliptical apertures with an equivalent inclination and position angle of $I = 40^\circ$ and $\vartheta = 51^\circ$ respectively, therefore gives an intensity profile which can be compared with the ALMA observed profile (orange line in Figure 5.1).

I also consider different initial radial profiles for the surface density of the particles.

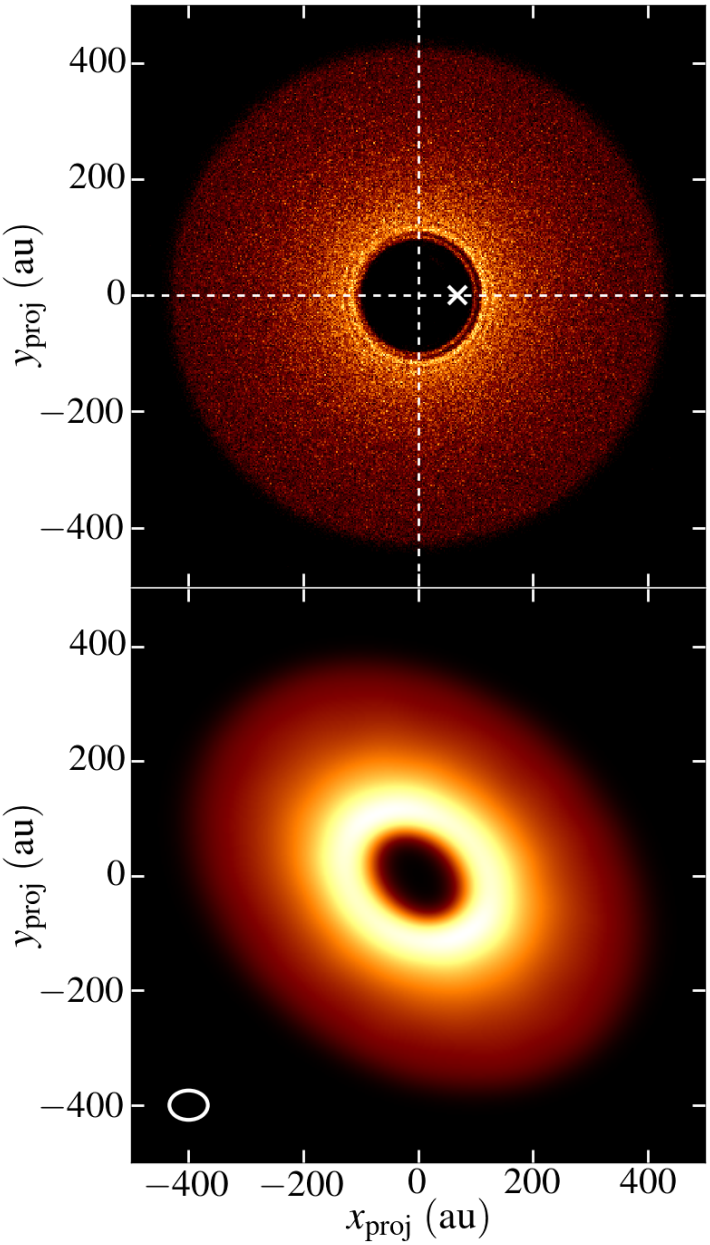

Figure 5.3 (*top*) Surface density image of particles after 60Myr due to interactions with the four known planets. Particles from 16 epochs between 51-60Myr are stacked together in a frame co-rotating with HR8799b (white cross). (*bottom*) Top panel scaled from surface density to intensity, which is inclined by and given a position angle of 40° and 51° respectively, which is then convolved with the beam size of ALMA (1.7×1.3 arcsec^2, white ellipse, Booth et al. 2016).

Thus far, the particles were initially uniformly distributed in semi-major axis, equivalent to an initial surface density proportional to r^{-1}. I consider whether changing this initial distribution of particles improves the agreement between the simulated and observed intensity profiles. To do this, I weight the contribution of a particle in the simulated intensity image by $a_{ini}^{-\gamma}$, where a_{ini} is the initial semi-major axis of the particle and γ is a scaling factor. A zero value of γ would therefore be equivalent to the particles being initially uniformly distributed in semi-major axis, giving an initial surface density proportional to r^{-1}.

I subsequently conduct a simultaneous χ^2 minimisation over a range of values of γ and the vertical scaling factor (K from eq. (5.2)) to find the combination of these two parameters which causes the strongest agreement between the simulated intensity profile and the one observed by ALMA. Each χ^2 value in this minimisation takes the standard value of

$$\chi^2 = \frac{N_{ind}}{N} \sum_{1}^{N} \frac{(O(r) - M(r))^2}{\sigma(r)^2},$$

where O(r) and M(r) are the values of the observed and simulated intensity profiles respectively at a radial position r, $\sigma(r)$ is the 1σ rms of the noise per beam at a given radial location for the observed profile (orange shaded region, Figure 5.1), $N_{ind} \sim 7$ is the number of ALMA beams that fit within my image size and N = 64 is the number of points in the observed profile (orange line Figure 5.1). This minimisation gives $\gamma = 0$, i.e. that the best fitting simulated intensity profile is one where particles are initially uniformly distributed in semi-major axis. The simulated intensity profile for $\gamma = 0$ (with the associated best fitting value of K), both with and without convolving my simulated intensity image with the beam of ALMA are given by the blue and black curves respectively in Figure 5.1.

It is clear that the intensity profile from the simulation does not fit well with that observed by ALMA. This therefore supports the conclusion in Booth et al. 2016 that the four planets in their current configuration cannot shape an outer disk consistent with the one observed by ALMA, in particular the position of the inner edge.

5.5 Including an additional fifth planet

5.5.1 Stability of an additional planet

I therefore consider whether a fifth undetected planet around HR8799, external to the known planets, predicts an outer disk with an intensity profile that more closely represents the one observed by ALMA. I consider a fifth planet with masses of 0.01, 0.016, 0.025, 0.04, 0.063, 0.1, 0.16, 0.25, 0.4, 0.63, 1.0, 1.6, 2.5, 4.0, 6.3M_J (linear in log space) and semi-

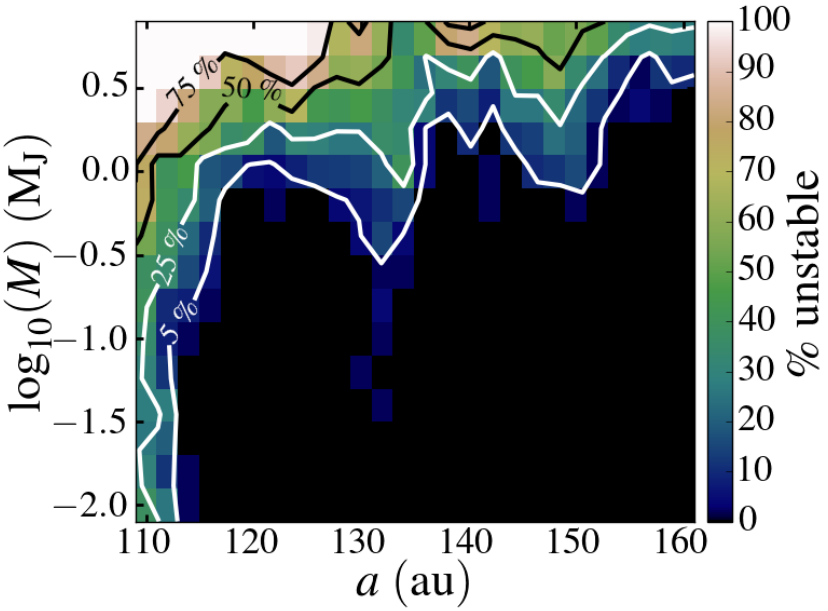

Figure 5.4 Percentage of 50 simulations that went unstable when including an additional fifth planet with a given mass and semi-major axis to HR8799. The angular orbital elements for a given fifth planet were randomly sampled for each of the 50 simulations. Contours refer to specific percentages.

major axes ranging from 110 to 160au with a spacing of 2au. This planet is initialised on a circular orbit with respect to the star (for consistency with the initial orbital elements of the known planets, Table 5.1) and is coplanar with the orbits of the 4 known planets.

Due to the large masses of the known planets around HR8799, one must consider how stable an additional planet would be if it were present. Indeed the known planets are likely stable due to the complex resonant structure of their orbits, which might be disrupted by an additional planet. For each mass and semi-major axis of the fifth planet, I run 50 simulations where the initial true anomaly and longitude of pericentre of the fifth planet are randomized between 0-2π. I note that randomizing the longitude of pericentre is necessary to account for the small initial eccentricity of the fifth planet with respect to the barycentre of the system. The parameters of the simulation are identical to that described in §5.4.1, however for computational efficiency I do not include the population of massless particles.

The percentage of the 50 simulations which went unstable for each fifth planet is shown in Figure 5.4, with contours highlighting specific percentages. Systems are defined to be unstable if the semi-major axis of any of the planets exceeds 10% of its initial value during the simulation. I find that simulations go unstable due to multiple planets being scattered from their original orbits rather than just a single planet. This is perhaps expected, as the known planets orbit on the edge of stability in a resonant chain, such that if this chain is

disrupted by the scattering of a single planet, it will likely affect all the other planets in the resonant chain as well. As might also be expected, Figure 5.4 shows that a more massive planet closer to HR8799b results in a system that is more likely to go unstable. Moreover a fifth planet is more likely to cause an instability in the system if it approaches the 2:1b, 5:2b, 3:1b MMRs of HR8799b at ∼110, 130 and 145au respectively.

I note that due to the resolution of my grid, the fifth planets I consider do not exactly lie on the major MMRs of HR8799b. I therefore do not also sample whether a fifth planet would be stable (in addition to those shown in Figure 5.4) as part of a resonant chain with the known planets. Indeed it is not unreasonable to think that the process which caused the known planets to be caught in a resonant chain might also extend to an additional planet. I leave the topic of whether expanding the resonant chain of the known planets produces stability zones for additional planets to future work.

5.5.2 Simulations

I now consider the effect each of the stable fifth planets has on the population of particles initially described in §5.4.1. Fifth planets close to HR8799b, with a high enough mass for all of the 50 stability simulations in Figure 5.4 to go unstable were disregarded from further study. For each fifth planet I select a true anomaly and longitude of pericentre that produced a stable configuration from Figure 5.4 and initialise it with a population of test particles as described in §5.4.1. The radii of each of the fifth planets are given by the mass to radius relation from eq. (5.1) for $0.414 M_J < M < 0.08 M_\odot$. For $2.04 M_\oplus < M < 0.414 M_J$, I use the 'Neptunian Worlds' relation from Chen & Kipping 2017[1]:

$$\frac{R}{R_\oplus} = 0.81 \left(\frac{M}{M_\oplus}\right)^{0.589}. \tag{5.3}$$

For each fifth planet I followed the same prescription discussed in §5.4.1, running simulations to compare the intensity profile of the disk from my simulations with the profile observed by ALMA. For computational efficiency however, I first considered whether the number of particles could be reduced from 50,000 without degrading the quality of a given intensity profile at the end of my simulations. I took 9 of the considered fifth planets, which sampled the overall range of masses and semi-major axes and ran these simulations to 60Myr with 50,000 particles. I then artificially removed particles to reduce the quality of the intensity profile. I found that 10,000 particles could be used without significantly degrading the final intensity profile for the 9 considered fifth planets. For the remainder of the simulations for all the fifth planet masses and semi-major axes described in §5.5.1 I therefore include 10,000 particles.

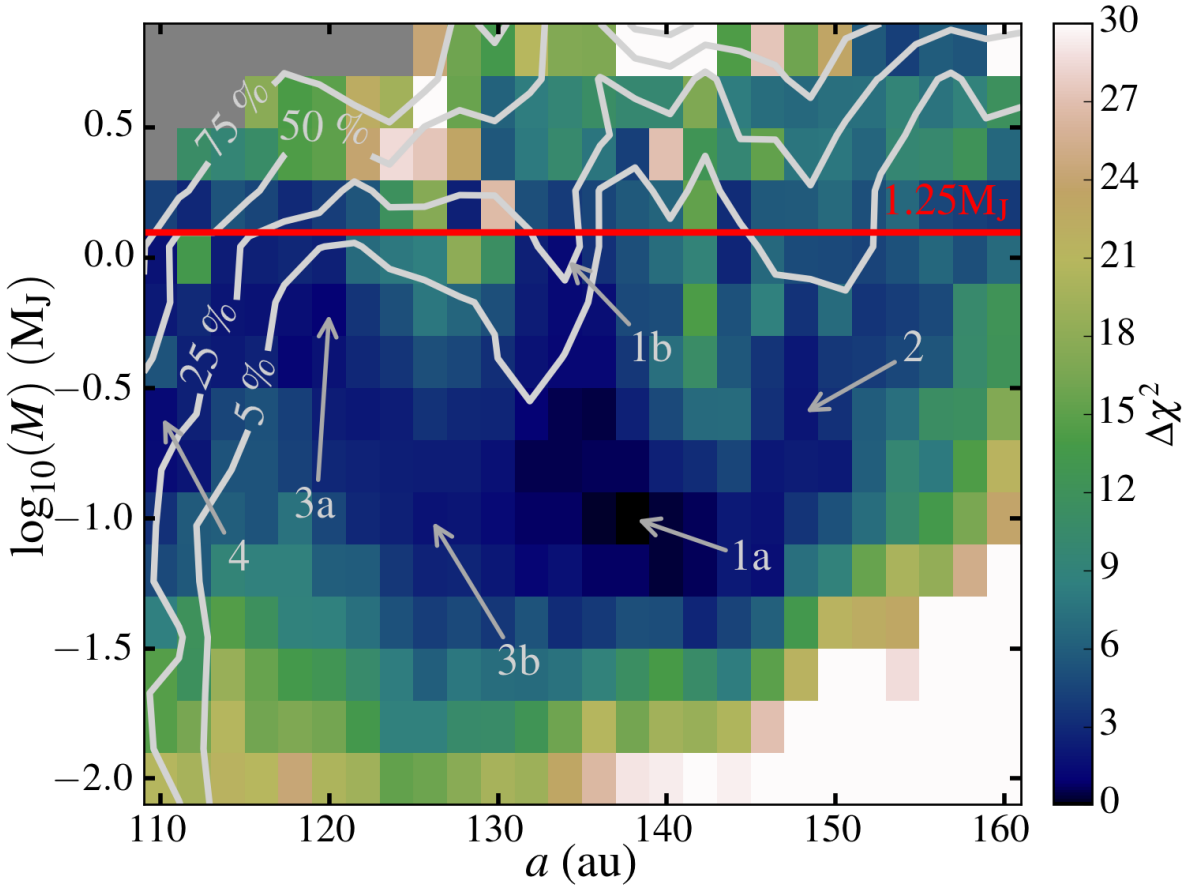

Figure 5.5 How well intensity profiles of the outer disk of HR8799 from my simulations with an additional fifth planet with given mass and semi-major axis agree with the observed intensity profile from ALMA. The colour scale gives the χ^2 value of the fit between the simulated and observed profiles relative to the χ^2 value of the profile that best fit the observed profile. The light grey contours are the stability contours shown in Figure 5.4, with the red line giving the direct imaging threshold for planet detection. The greyed out region refers to fifth planets where 100% of the simulations from Figure 5.4 were unstable. Intensity profiles of individual annotations are shown in Figure 5.6.

To off-set any reduction in the signal to noise of the simulated images generated by each fifth planet from reducing the number of particles, at the end of my simulations I sample each particle 1000 times around its orbit. I note that this approximation is only valid if there is no asymmetric disk structure arising from correlated particle true anomalies, as this structure would become smoothed out. I discuss the validity of this approximation in §5.5.5.

5.5.3 Comparing simulations with ALMA observations

After generating an intensity profile for each fifth planet simulation, I perform a simultaneous χ^2 minimization procedure over the scaling factors γ and K in the exact same way discussed in §5.4.3. That is, finding the optimal scaling factor, γ (which weights particles in the simulated intensity image according to their initial semi-major axis) and the optimal vertical scaling factor, K from eq. (5.2), which cause the intensity profile from the ALMA convolved simulated intensity image to best fit the observed intensity profile. I note the lowest χ^2 value from this minimisation for each fifth planet considered.

I find that of all my simulations a fifth planet with a mass of $0.1M_J$ and a semi-major axis of 138au predicts an intensity profile that most strongly agrees with the one observed by ALMA. Figure 5.5 shows the minimum χ^2 value of all the other fifth planet parameters relative to this overall χ^2 minimum. I refer to this relative χ^2 value as $\Delta\chi^2$. I include the stability contours from Figure 5.4 for reference. I also plot the current upper mass limit for detection of planets around HR8799 from direct imaging, equivalent to $\sim$1.25M_J (see Figure 2 of Maire et al. 2015), with the red line. I note that the upper mass limit for detection presented in Maire et al. 2015 only goes out to $\sim$ 80au, whereas the total field of view for the instrument used in their work included separations out to $\sim$ 275au. Outside of $\sim$ 80au however, their contrast sensitivity is limited by thermal background and not by stellar speckles, such that the $\sim$1.25M_J detection limit is roughly constant for separations > 80au (Maire priv comm). The greyed out region refers to fifth planets which were 100% unstable from Figure 5.4.

5.5.4 Results

The minima in the $\Delta\chi^2$ values in Figure 5.5 can be compartmentalised into four main regions, which are annotated by specific example planets discussed below in Figure 5.5:

1) Fifth planets with a mass and semi-major axis around $0.1M_J$ and 138au respectively. The intensity profile of a fifth planet with exactly this mass and semi-major axis (1a in Figure 5.5) is shown in the top left panel of Figure 5.6. The grey and black lines refer to the intensity profile before and after the simulated intensity image is convolved with the beam of ALMA respectively. The orange line shows the observed ALMA intensity profile with the shaded region giving the 1σ rms of the noise per beam (§5.4.3). The black dashed line shows the semi-major axis of the fifth planet. This fifth planet sculpts an inner edge in the disk at $\sim$160au. However there is also a significant proportion of particles caught in co-rotation with the planet. This results in an intensity profile, which when convolved with the beam of ALMA, is in good agreement with the observed profile.

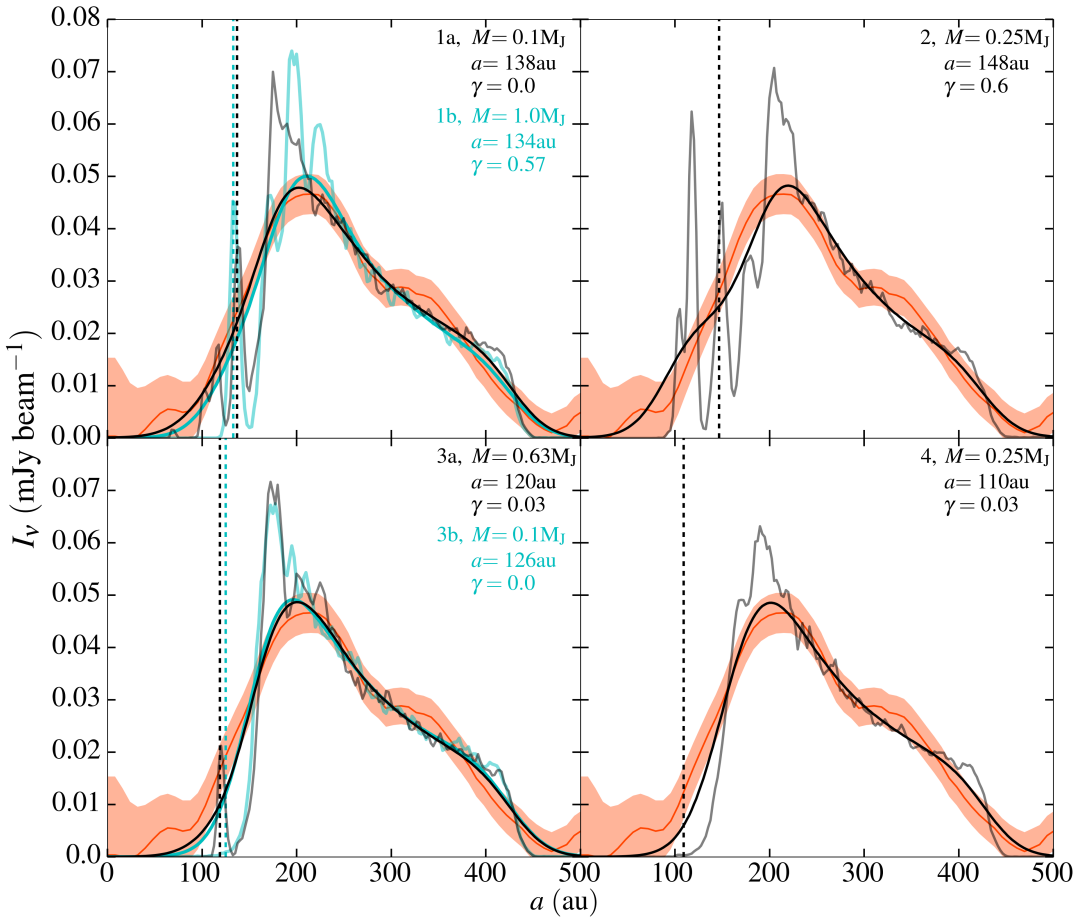

Figure 5.6 Comparison of intensity profiles generated by selected fifth planets from Figure 5.5 with and without convolving with the beam of ALMA (black and grey lines respectively, also solid and lighter blue lines in the top and bottom left panels), with the profile observed by ALMA (orange line). The orange shaded region gives the 1σ rms of the noise per beam. The dashed vertical lines give the position of the fifth planet considered. The values of γ refer to the initial scaling of the surface density of particles such that $\Sigma(r) \propto r^{-1} a_{ini}^{-\gamma}$. All profiles fit the observed profile significantly better compared with the four known planets in isolation.

2) Fifth planets with semi-major axes between 140-160au, for increasing masses between 0.04-1M_J. The intensity profile for one such fifth planet with a mass and semi-major axis of 0.25M_J and 148au respectively (2 in Figure 5.5) is shown in the top right panel of Figure 5.6. The lines refer to the same quantities as the top left panel. This planet carves a gap with an outer edge at $\sim$ 200au, with a significant number of particles surviving internal to the orbit of the fifth planet. A population of particles is also present in co-rotation with the planet. Once the simulated intensity image is convolved with the beam of ALMA, these different particle populations produce a profile that has an overall good agreement with that observed by ALMA. However the inner edge is not fit as well as fifth planets from region (1).

3) Fifth planets between $\sim$ 115 – 130au with decreasing masses between 1-0.04M_J. An example intensity profile is shown in the bottom left panel of Figure 5.6 for a fifth planet with a mass and semi-major axis of 0.63M_J and 120au respectively (3a in Figure 5.5). No particles survive on an orbit internal to this fifth planet, however as with the previous examples, a population of particles (albeit smaller) is present in co-rotation with the fifth planet. The outer edge of the gap carved by the fifth planet therefore defines the position of the inner edge of the disk. While this fifth planet produces an intensity profile that shares a reasonable agreement with the observed profile, the slope of the inner edge is perhaps sharper than what would be expected from the observed intensity profile. For fifth planets in this region with lower masses, the gravitational potential bounding particles in co-rotation is weaker. Particles are therefore more prone to being scattered by interactions with HR8799b. I highlight this with another example fifth planet in this $\Delta\chi^2$ minimum region, with a mass and semi-major axis of 0.1M_J and 126au respectively (3b in Figure 5.5). The intensity profile of this planet, with and without convolution with the beam of ALMA, are shown by the solid and lighter blue lines in the bottom left panel of Figure 5.6. Here it is clear that no particles are present in co-rotation and the inner edge of the disk is defined purely by the outer edge of the chaotic zone of the planet.

4) Fifth planets with a mass and semi-major axis around 0.25M_J and 110au respectively. The intensity profile of this fifth planet (4 in Figure 5.5) is shown in the bottom right panel of Figure 5.6. Here all particles are cleared internal to the orbit of the fifth planet. Moreover, strong interactions with HR8799b result in no particles being caught in co-rotation. The inner edge of the disk is therefore only defined by the outer edge of the chaotic zone of the planet. Similarly to region (3), the intensity profile from the simulation is sloped steeper at the inner edge than what is expected by the observed profile. It is also worth noting that a non-negligible percentage ($\sim$ 40%) of the fifth planets in this region were found to cause an instability in the system in §5.5.1.

Smaller mass planets in Figure 5.5 clear smaller gaps (see discussion in §5.4.2) and take longer to do so (e.g. Morrison & Malhotra, 2015; Shannon et al., 2016). Indeed, for the lowest mass fifth planet in Figure 5.5 (0.01M_J) the timescale to reach 50% of the final surviving material fraction within the gap, from eq. (8) of Morrison & Malhotra 2015 (assuming the scattering dominated regime) is $\sim$Gyr, far longer than the lifetime of HR8799. Very low mass fifth planets would therefore tend to a regime where no significant amount of material is scattered from its chaotic zone and the resulting intensity profile would be equivalent to the profile for the four known planets in isolation (Figure 5.1). Such fifth planets could therefore exist and be embedded in the outer disk around HR8799 without carving a noticeable gap.

5.5.5 Discussion of Results

From Figure 5.5 it is clear that fifth planets in the 4 regions discussed above predict intensity profiles that agree, with different degrees of success, with the profile observed by ALMA. The profiles predicted by all these fifth planets also fit the observed profile much better compared with the four known planets in isolation, i.e. comparing Figures 5.1 and 5.6. Indeed if the $\Delta\chi^2$ value for how well the intensity profile from the four known planets (Figure 5.1) matched the observed profile was to be plotted in Figure 5.5, it would have a value of $\Delta\chi^2 = 60$. It would be expected therefore that the $\Delta\chi^2$ values from even lower mass planets than those simulated in Figure 5.5 would tend to this value, as they would not have a noticeable effect on the disk structure

All the fifth planets from the four discussed regions in Figure 5.5 are also below current direct imaging detection thresholds and their presence would therefore not contradict any observations. Following the original postulation from Booth et al. 2016 therefore, I conclude that *the presence of a fifth planet around HR8799 predicts an intensity profile which fits the observed profile significantly better compared with the profile predicted by the four known planets in isolation, assuming their current configuration.* Moreover I find that a fifth planet with a mass and semi-major axis of $0.1M_J$ and 138au respectively predicts an intensity profile which best fits the profile observed by ALMA.

This best fitting intensity profile contained a significant population of particles in co-rotation with the fifth planet. I therefore also consider the possibility that no particles trapped in co-rotation with the fifth planet. Indeed, the capture of material in co-rotation would depend on how the fifth planet formed, and how material was initially distributed around it. To do this, I take each of my fifth planet simulations after 60Myr and remove all particles that had a semi-major axis within 10% of the fifth planet. Of these particles I do not remove those with eccentricities larger than 0.1. This helps stop particles being removed that are actually being scattered and happen to have a semi-major axis close to the fifth planet rather than being bound on a co-rotational orbit with the planet.

I then repeat the procedure used to create Figure 5.5 (e.g. performing a simultaneous χ^2 minimisation over γ and K values discussed in §5.5.3) to show which fifth planet now predicts an intensity profile most like the one observed by ALMA. I show this in Figure 5.7, with the colour scale again referring to χ^2 minimum values relative to the overall χ^2 minimum, denoted by the variable $\Delta\chi^2$.

It is clear that a fifth planet outside ∼150au (region (2) from §5.5.4) no longer fits the intensity profile observed by ALMA. This is perhaps expected from the top right panel of Figure 5.6, as without particles in co-rotation, the gap carved by the planet is too wide such that there is not a smooth transition in the intensity profile between the edges of

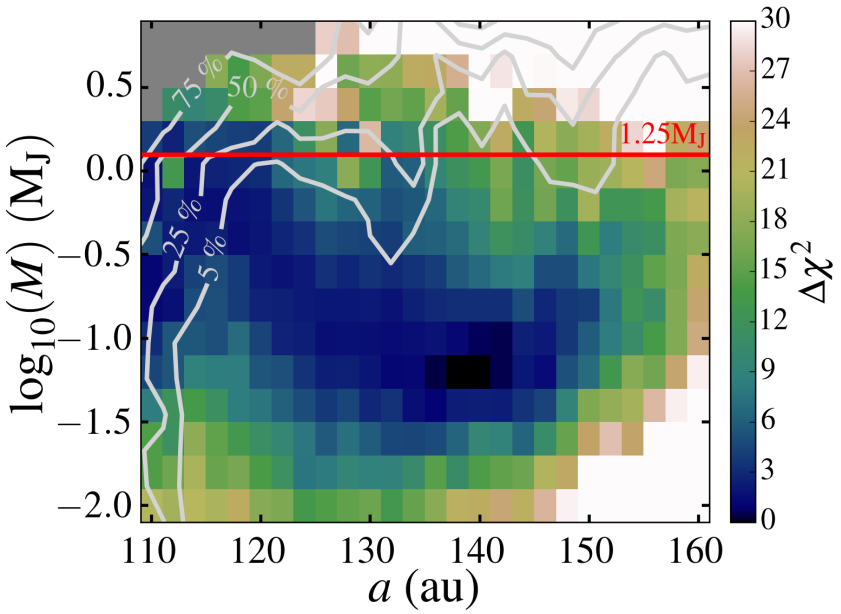

Figure 5.7 Identical plot to Figure 5.5, however here I remove particles at the end of my simulations that have a semi-major axis within 10% of the fifth planet and eccentricity below 0.1.

the gap. The $\Delta\chi^2$ values of fifth planets that were inside $\sim$ 130au (e.g. region (3) from §5.5.4) are largely unchanged from values seen in Figure 5.5 as these did not initially show a significantly population of particles in co-rotation with the fifth planet.

Perhaps surprisingly, a fifth planet with a mass and semi-major axis of 0.063M$_J$ and 140au respectively (e.g. similar to the planets in region (1) discussed in §5.5.4) predict an intensity profile that best fits the one observed by ALMA. This shows that contributions to the predicted intensity profile from particles caught in co-rotation here are small. I note that the absolute value of the χ^2 minimum does not significantly change between Figures 5.5 and 5.7. I conclude therefore that fifth planets with a mass and semi-major axis around 0.1M$_J$ and 138au respectively (region (1) from §5.5.4) predict an intensity profile of the outer disk around HR8799 which closely agrees with the profile observed by ALMA, regardless of whether there is a significant population of material co-orbiting with the planet or not. While such fifth planets are below current direct imaging detection sensitivities ($\sim$ 1.25M$_J$, Maire et al. 2015) and therefore do not contradict current observations, future instruments such as the near infrared imager NIRCam available on the *James Webb Space Telescope* might be able to detect such objects. Indeed, at 4.3μm NIRCam would be expected to achieve a contrast of 10^{-6} – 10^{-7} for separations from the star $\gtrsim 3''$ (Beichman et al., 2010), equivalent to $\gtrsim$ 110au for HR8799. For a 0.5M$_J$ planet at an age of 60Myr, evolutionary models (AMES-Cond models, Allard et al. 2001; Baraffe et al. 2003) suggest a planet-star contrast of 2.5×10^{-6} with the F430M NIRCam filter, highlighting that low mass

planets in HR8799 would be detectable with a high SNR outside of 110au.

If a significant population of particles is present in co-rotation with a fifth planet, I consider whether emission from such a population would be detectable by ALMA. I first consider the best-fit fifth planet ($0.1M_J$ and 138au, top left panel of Figure 5.6), for which the value of γ for this best fit was $\gamma = 0.0$. The left panels of Figure 5.8 show the simulated intensity image including this fifth planet, without (top panel) and with (bottom panel) convolution with the ALMA beam. For consistency with the ALMA observation of the outer disk from Booth et al. 2016, I incline the disk in the bottom panel by I = 40° (from face on) with a position angle of 51° (anti-clockwise from North) before the beam convolution. Here, for this specific planet, I do not smooth each particle 1000 times around its orbit, allowing for asymmetric structure to be preserved. I find that steady state evolution is reached before 60Myr and I therefore combine the last 16 intervals from these simulations in a frame co-rotating with the fifth planet (white cross) to increase the signal to noise of the image. Particles in co-rotation with the planet librate around both the L_4 and L_5 Lagrange points in horseshoe like orbits (see Murray & Dermott 1999). A noticeable asymmetry in the disk caused by particles co-rotating with the fifth planet, both in the images with and without convolving with the beam of ALMA, is therefore not present.

As a fifth planet becomes more massive, it would be expected that the gravitational potential bounding the L_4 and L_5 points would become deeper. For a sufficiently massive fifth planet therefore, particles in co-rotation would be expected to librate around the L_4 or L_5 points only in trojan like tadpole orbits. To highlight this, I consider a fifth planet that is similarly placed in the $\Delta\chi^2$ minimum in Figure 5.5 as the $0.1M_J$, 138au fifth planet. I choose this planet to have a mass and semi-major axis of $1M_J$ and 134au respectively (1b in Figure 5.5). For reference, the intensity profile for this planet which best fit the ALMA profile is shown in the top left panel of Figure 5.6. The profiles with and without convolving the associated intensity images with the beam of ALMA are shown by the solid and lighter blue lines respectively. The best fitting value of γ for this planet was also equal to $\gamma = 0.57$. The intensity image itself for this fifth planet without and with convolving with the ALMA beam is shown by the top and bottom right panels in Figure 5.8 respectively.

The top right panel of Figure 5.8 indeed shows that particles in co-rotation with the fifth planet are localised to the L_4 and L_5 points in trojan like orbits. However, from the bottom right panel of Figure 5.8 it can be seen that, the asymmetry in the ALMA convolved intensity image caused by these trojan like particles is small. Moreover if noise at the level of the ALMA observations were added to this image it would not be detectable (see Figure 1 in Booth et al. 2016). I conclude therefore that a significant population of particles in co-rotation with an undetected fifth planet is not ruled out by current ALMA observations. Furthermore, I conclude that my assumption of smoothing particles 1000 times

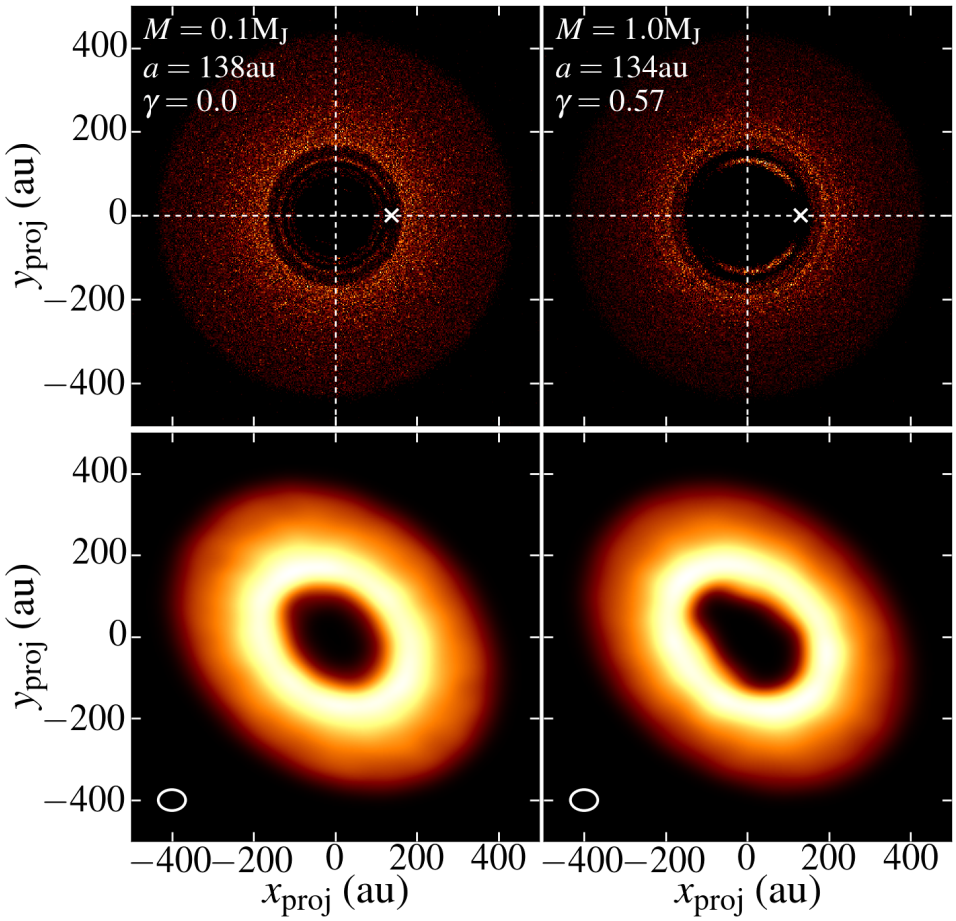

Figure 5.8 Intensity image of outer disk from two example fifth planet simulations without (*top*) and with (*bottom*) convolving with the beam size of ALMA (white ellipse). The bottom panels have an inclination and position angle derived from the ALMA observations. The last 16 intervals of the simulations were de-rotated to a frame co-rotating with the fifth planet (white cross) and stacked. The asymmetry caused by trojan particles is small and would not be expected to be detected.

around their orbit to produce Figure 5.5 is valid, as any asymmetric structure that would be removed in an image from using this technique would not be currently detectable by ALMA.

I note that upcoming ALMA observations will provide higher resolution images of the outer disk, due to an expected beam size of 1×1arcsec^2 (ALMA cycle 5 prog ID 2017.1.01315.S), rather than 1.7×1.3arcsec^2 from Booth et al. 2016. These higher resolution images may be able to begin to disentangle the presence of material co-rotating with an additional planet, however this would depend on the overall sensitivity of the imaging. Moreover, recent imaging with outer belt with the *Submillimeter Array*, which, when independently combined with ALMA data, suggests that the inner edge of the outer belt is much further in than that suggested by Booth et al. 2016 (Wilner et al., 2018). Future ALMA observations will therefore be a vital aspect in constraining the position of the outer belt and the role of

any additional planets in this system.

As discussed in §5.3, the age of HR8799 is unclear. Based on interfermetric data (Baines et al., 2012) and the probable membership of the Columba association (e.g. Gagné et al., 2014), a likely age of HR8799 is $\sim$ 30 – 40Myr. A younger age estimate than the 60Myr I consider during this work means that planets have less time to remove material through dynamical interactions, which may cause different populations of material to be present after 30Myr compared with 60Myr. In Appendix D, I show however that assuming HR8799 is 30Myr old rather than 60Myr has no significant effect on the results presented above.

During this work I have also assumed orbital properties of the known planets in HR8799 calculated from the work presented in Goździewski & Migaszewski 2014, notably that the masses of the four known planets are 9, 9, 9, 7M_J for planets e, d, c, b respectively. However, lower mass estimates also exist, with respective planet masses of, 7, 7, 7, 5M_J, for an assumed age of 30Myr for the star (e.g. Marois et al., 2010; Currie et al., 2011). Lowering the mass of planet b from 7 to 5M_J has a negligible effect on how far out the chaotic zone of this planet extends to ($\sim$90au). Lowering the mass of the known planets would therefore not be expected to produce significantly different intensity profiles to the ones shown in this work, even after a fifth planet is introduced. Hence I would not expect this mass change to affect the conclusions from this work. I note however that lowering the mass of the known planets may affect the overall stability of some systems once a given fifth planet is introduced, though this would also depend on the initial orbital elements of the planets considered.

5.5.6 Surface density profiles

As discussed in §5.5.3, I weight the contribution of each of the particles after 60Myr in each of the fifth planet intensity images by the initial semi-major axis through the parameter γ. Larger γ values result in particles at smaller initial semi-major axes contributing more and vice versa. I show the values of γ which resulted in an intensity profile for each fifth planet that best fit the observed profile in Figure 5.9. It is clear that the more massive fifth planets, the larger the best fitting value of γ. This is due to the chaotic zone around higher mass planets being larger (§5.4.2) and therefore clearing a wider gap by the end of the simulation. With few particles surviving on orbits inwards of $\sim$150au, the ones that do survive need to be heavily weighted to significantly contribute to where the inner edge of the disk is observed to be from ALMA.

Values of γ perhaps place constraints on the likelihood of the presence of a fifth planet, as Booth et al. 2016 predict that the optical depth of the outer disk from the ALMA observations of HR8799 follows a 1/r distribution (see §5.3.3). As the initial particle surface

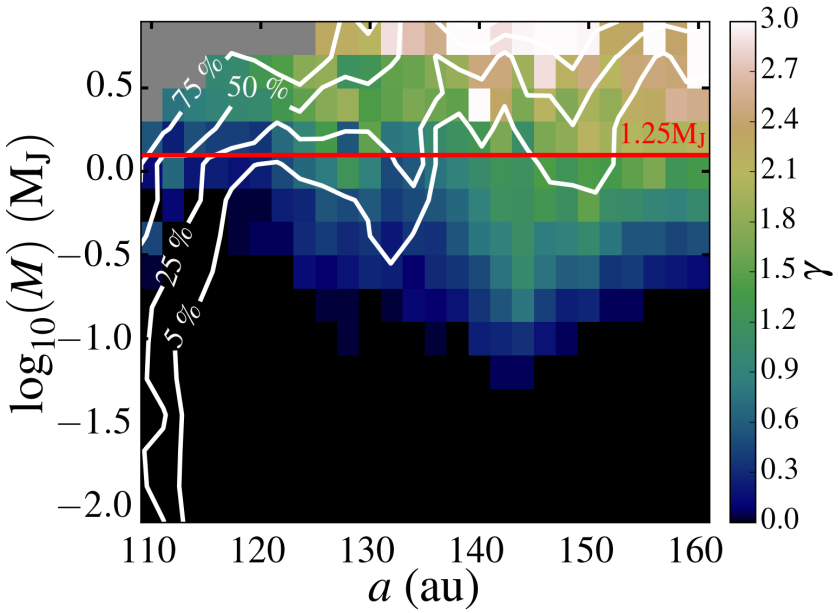

Figure 5.9 The values of γ used for the intensity profiles of the outer disk for each fifth planet simulation that best fit the observed ALMA intensity profile. The initial surface density of particles in a given simulation scales with $\Sigma(r) \propto r^{-1}a_{ini}^{-\gamma}$. Contours and lines are equivalent to those in Figure 5.5.

density in my simulations scales roughly proportional to $1/r^{1+\gamma}$, where r is the radial distance, γ values equal to roughly zero in Figure 5.9 would therefore be expected to be more consistent with the ALMA observations.

5.6 Inward delivery of particles

For all of the simulations considered in this work, I find that the most common reason particles are removed from a given simulation is due to ejection rather than collisions with any of the massive bodies. Such a result is predicted in Wyatt et al. 2017, as large mass planets, like those around HR8799, are significantly more likely to eject particles rather than accrete them. If ejection is the dominant final outcome, I consider whether, at some point in their evolution, particles can be scattered inwards through all the planets to where the inner warm belt of material is known to be around HR8799 (∼6-15au). If so, this may suggest that the inner and outer belts around HR8799 contain shared, rather than distinct populations of material.

The inner belt around HR8799 is known to have a mass of 1.1×10^{-6}M$_\oplus$ in small grains (∼1.5-4.5μm, Su et al. 2009). The total mass however, could be significantly larger once grains of larger sizes are included. Collisional evolution between large grains creates a characteristic size distribution, with the smallest grains being ejected from the system due

to radiation pressure. Assuming a characteristic size distribution that scales as $n(D) \propto D^{2-3q}$, where $q = 11/6$ (e.g. Wyatt et al., 2007a,b), the mass loss rate in $M_\oplus$/yr due to the ejection of small particles can be estimated by

$$\frac{dM_{loss}}{dt} = 1700 f_{obs}^2 r_{disk}^{0.5} L_\star M_\star^{-0.5} \left(\frac{r_{disk}}{dr_{disk}} \right), \tag{5.4}$$

where f_{obs} is the fractional luminosity of the disk, r_{disk} is the radial position of the disk in au, dr_{disk} is the radial width of the disk in au, $L_\star$ is the luminosity of the star in $L_\odot$ and $M_\star$ is the mass of the star in $M_\odot$ (see eq. (29) in Wyatt et al. 2007a). I note that this mass loss rate is not dependent on the maximum grain size and therefore mass of the disk. For the inner disk around HR8799, $f_{obs} = 2.2 \times 10^{-5}$, $r_{disk} = 10$au and $dr_{disk} = 9$au (Su et al., 2009), giving a mass loss rate from eq. (5.4) of $dM_{loss}/dt = 1.2 \times 10^{-5} M_\oplus$/Myr.

Mass input into the inner disk can come from embedded bodies with sufficiently large sizes that they take longer than the lifetime of the system to collide (i.e. an Asteroid belt). However, here I consider that mass may also be replenished due to input from an external source, that is, planetesimals that are scattered inward from the outer belt.

I consider the five previously described simulations from §5.5.4, which contained a fifth planet around HR8799 which produced intensity curves that agreed well with the curve observed by ALMA. That is, the fifth planets with masses and semi-major axes of $0.1 M_J$ at 138au, $0.25 M_J$ at 148au, $0.63 M_J$ at 120au, $0.1 M_J$ at 126au and $0.25 M_J$ at 110au respectively (I note that I do not consider the fifth planet with $1 M_J$ at 134au discussed in §5.5.5). I repeated these simulations, but this time removed the massless particles from the simulations as soon as any part of their orbit reached within 10au. This represents the distance where I deemed particles to have 'joined' the inner disk. Over a given time in these simulations therefore, the rate at which particles join the inner disk could be obtained.

To convert this inward flux of particles into a rate of inward delivery of mass, each particle was assigned mass by scaling to the current mass of the outer belt around HR8799 in 10-1000μm grain sizes of $1.2 \times 10^{-1} M_\oplus$ (Su et al., 2009). Since there are likely also objects larger than 1mm in the disk I assume that the largest objects (in both the disk and in the scattered material) have a size D_{max} resulting in a total mass input rate from a given simulation, $\dot{M}$, during successive 10Myr epochs, as shown in Figure 5.10, where this mass input scales with the square root of the maximum grain size, D_{max} (see eq. (3) in Wyatt et al. 2007a).

Figure 5.10 shows that despite the different masses and semi-major axes of the fifth planet considered, the mass input to the inner disk from the outer disk for all epochs is largely unchanged. The mass input during the final 10Myr of the simulations implies

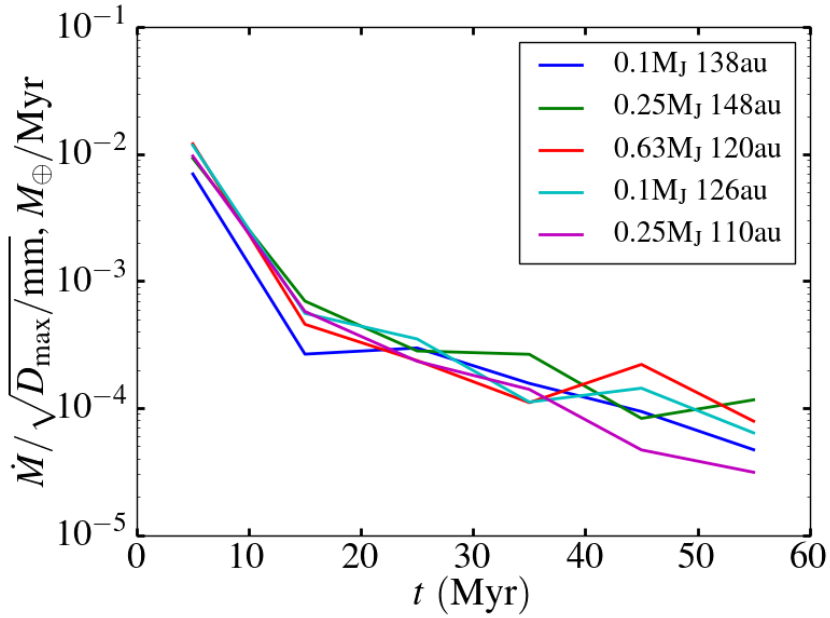

Figure 5.10 Rate at which mass reaches the inner disk due to inward scattering of particles from the outer disk by the planets. Bin sizes for time are 10Myr. To get the mass input rate into the inner disk, it is required to multiply by an efficiency factor discussed in text. D_{max} is the maximum grain size considered in mm. The rate at which mass reaches the inner disk does not significantly change for different fifth planet masses and semi-major axes.

an input rate of $5\times10^{-6}(D_{max}/mm)^{1/2}M_\oplus/Myr$. For $D_{max} \sim$ 1mm this mass input rate is roughly equivalent to the mass loss rate calculated from eq. (5.4), suggesting that the mass loss rate from the inner disk can be replenished by 10-1000μm grains scattered inward from the outer belt. However, first I must consider whether all the grains that are scattered in from the outer belt and reach 10au actually get incorporated into the inner disk or whether they simply pass through the belt to get ejected at a later time.

If I assume that it is collisions that allow material to be incorporated into the inner disk, then the efficiency of mass input rate into the inner disk can be estimated by comparing the timescale for which grains would be expected to mutually collide, t_{col}, with the timescale for which grains would be expected to be ejected by interactions with the innermost known planet HR8799e, t_{scat}. That is, the efficiency is equivalent to

$$\eta_{|eff} = \frac{t_{scat}}{t_{col}}. \tag{5.5}$$

The ejection timescale, t_{scat} is given by eq. (2) in Wyatt et al. 2017

$$t_{scat} = 10^9 \left(\frac{M_\star^{3/4} a^{3/4}}{M}\right)^2, \tag{5.6}$$

in yr, where a and M are the semi-major axis and mass of a planet in au and $M_\oplus$ respectively and $M_\star$ is the mass of the star in $M_\odot$. For HR8799e, t_{scat} is equal to 14kyr. Combining eq. (6), (13) and (25) from Wyatt et al. 2007a, the collisional timescale of objects of size D_{max} in mm at the inner disk is

$$t_{col}(D_{max}) = 0.04 r_{disk}^{1.5} \left(\frac{dr_{disk}}{r_{disk}}\right) \frac{1}{f_{obs}} \left(\frac{10^3 D_{max}}{0.8 L_\star \left(\frac{2700}{\rho}\right)}\right)^{1/2}, \quad (5.7)$$

where ρ is the density of particles in kg m^{-3}. Therefore, I infer an efficiency of mass input rate that scales as $\eta_{|eff} \propto D_{max}^{-1/2}$. Since the rate at which mass reaches the inner disk shown in Figure 5.10 scales $\propto D_{max}^{1/2}$, I find that the rate at which mass is incorporated into the inner disk is insensitive to the largest particle size. That is, while larger maximum grain sizes increase the amount of mass that is scattered inward to reach the inner disk, the collisional timescale for these grains also increases, such that the amount of mass that is actually incorporated into the inner disk remains constant.

For an assumed grain density of 2700kg m^{-3}, I find the mass input rate into the inner disk from inward scattering from the outer disk, including the efficiency factor given by eq. (5.5), to be $8.8\times10^{-8} M_\oplus$/Myr, equal to $\sim$ 1% of the mass loss rate. I conclude therefore that the mass loss from the inner belt cannot be replenished by inward scattering of material from the outer disk for the current age of HR8799, with this conclusion being independent of the maximum grain size of inward scattered material. The inner belt around HR8799 is therefore more likely to be a distinct population of material, akin to the Asteroid belt in the Solar System, rather than containing a significant amount of material from the outer belt.

I note however that the mass input rate is $\sim$100 times larger in Figure 5.10 during the first 10Myr. This suggests that if HR8799 were observed in the first 10Myr of its lifetime, the warm dust emission from the inner belt due to material being scattered inwards from the outer belt would be comparable in brightness to that observed towards HR8799 today. This perhaps has implications for other young systems which have been observed to host belts of particularly hot and warm dust (e.g. η Telescopii, HD95086, Smith et al. 2009; Su et al. 2015), as brighter than expected emission from an inner belt could be an indication of inward scattering of material from outer planets interacting with an outer belt of material (Bonsor & Wyatt 2012; Bonsor et al. 2012; Marino et al. submitted).

5.7 Summary and Conclusions

I simulated how an outer population of material interacts with the four known planets around HR8799. I found that the intensity profile of the outer disk that is formed in my simulations does not agree with the equivalent intensity profile observed by recent ALMA observations (Booth et al., 2016). Notably the inner edge of the disk from my simulations was much further in than that suggested by ALMA. I therefore support the postulation in Booth et al. 2016 that the four known planets in their current configuration do not sculpt an outer disk that is consistent with the one that is currently observed.

I subsequently added an additional fifth planet with a range of masses and semi-major axes in my simulations that was external to the outermost known planet. I found that a fifth planet with a mass and semi-major axis around $0.1M_J$ and 138au respectively produced an outer disk in my simulations with an intensity curve that best fit the curve observed by ALMA. However, fifth planets with semi-major axes between 140-160au for increasing masses between 0.04-$1M_J$, between 115-130au with decreasing masses between 1-$0.04M_J$ and fifth planets with a mass and semi-major axis around $0.25M_J$ and 110au respectively also predict an intensity curve for the outer disk that agrees well with the one observed with ALMA. Moreover, I found that these fifth planets can remain dynamically stable with the known planets for the lifetime of the system and are below the current sensitivity threshold for detection via direct imaging surveys. I conclude therefore that the presence of a fifth planet around HR8799 that is external to the outermost known planet, predicts an intensity profile that fits the one observed significantly better compared with the profile predicted by the four known planets in isolation, assuming their current configuration.

In order for many of the simulated fifth planets to produce a well fitting intensity profile for the outer disk, material needed to be present in co-rotation with the fifth planet. However, after artificially removing material in co-rotation with the fifth planet, I found that a fifth planet with a mass and semi-major axis around $0.1M_J$ and 138au respectively still predicted an intensity profile that best fit the profile observed with ALMA. I therefore concluded that, regardless of whether material in co-rotation with a fifth planet is considered or not, the predicted intensity profile fits the observed profile much better than the profile predicted by the four known planets in isolation. Moreover, I found that any asymmetric structure in the outer disk indicative of material in co-rotation with a fifth planet would not be detectable in the current ALMA observations.

I also considered whether a significant amount of material could be passed from the outer disk around HR8799 through the known planets and an additional fifth planet to the inner disk. That is, whether mass loss of the smallest grains in the size distribution

of the inner disk, due to radiation pressure, could be replenished by inward scattering of material from the outer belt. I found that the amount of material that is scattered through the planets from the outer to the inner belts does not significantly change for different masses and semi-major axes of the additional fifth planet. I assumed that the efficiency of mass input into the inner disk from inward scattering is equal to the ratio between the timescale for inwardly scattered material to collide at the inner belt and the timescale for their ejection by interactions with HR8799e. I found that only $\sim$ 1% of the mass loss rate of the inner disk can be replenished by inward scattering of material from the outer belt. This result is independent of the considered grain size of inward scattered material. I conclude therefore that the inner disk around HR8799 is most likely a distinct population of material akin to the Asteroid belt in the Solar System. However I find that if HR8799 were observed in the first 10Myr of its lifetime, the emission from the hot dust at the inner belt would be expected to be similar in brightness to the hot dust seen around HR8799 today, due to a larger amount of material being scattered inwards from the outer belt. This perhaps has implications for young systems with particularly bright populations of hot and warm dust (e.g. η Telescopii, Smith et al. 2009), as this may be indicative of the inward scattering of material from an outer disk by planetary objects.

From Chapters 3, 4 and 5 I have shown that wide-orbit planets not only can have a significant effect on an inner planetary systems but also debris. Moreover, the presence of wide-orbit planets may be able to explain current observations such as some suspiciously eccentric planets, at least partially explaining the Kepler dichotomy and the population of debris in HR8799. While these studies provide predictions for the presence of wide-orbit planets in planetary systems, confirmation of such planets can only be made if they are actually observed. In the next Chapter I outline an on-going survey that is looking to directly image wide-orbit planets in known planetary systems, allowing for planet formation and evolution processes, like the ones described in this work to be tested in the future.

6

A direct imaging search for giant exoplanets to test formation scenarios in super-Earth planetary systems

6.1 Chapter Summary

One of the running themes throughout this work has been that exoplanetary systems are observed to be far more diverse than what is expected from the Solar System. Specifically, super-Earths on close-in orbits have been found to be common (Figure 1.3, §1.4) and therefore must be explained by theories of planet formation. How important wide-orbit giant planets are in the formation and evolution of these super-Earths is unknown. Three possible formation scenarios of super-Earths, which are consistent with observations, include: 1) super-Earths form in-situ, roughly in their currently observed orbits at <1au. 2) They form further out and are delivered inwards, due to interactions with a giant planet at a fixed orbital radius. 3) They form further out and, independently of a giant planet, move inwards to their currently observed orbits. For each of these 3 scenarios, the presence of a giant planet in the super-Earth system would be irrelevant, expected and unexpected, respectively. As discussed in §1.5, planet detection techniques are largely biased towards detecting objects inwards of a few au. Direct imaging therefore offers the only way to detect planets at separations of $\gtrsim$ 5au. In this Chapter, I describe an on-going survey using the SPHERE imager to investigate the presence of giant planets around all G-, K- and M-type super-Earth hosting stars within 20pc of Earth. The aim of this survey is to detect 0.5-50 M_J companions, and therefore to constrain the likelihood of the three aforementioned super-Earth formation scenarios. Work on this survey began towards the

end of my PhD and the observations are currently ongoing. In this Chapter I therefore only highlight the main points related to the survey and preliminary results.

6.2 Chapter Introduction

The population of observed super-Earths has posed many questions for planet formation and evolution models (see Haghighipour 2013). Super-Earths which orbit within ∼1au have been found to be common (see Figure 1.3). It is unclear whether these objects formed in-situ at their currently observed orbits or further out in the protoplanetary disk, before being delivered to the inner part of the system at a later time. Such inward delivery could be the result of migration due to interactions with the protoplanetary disk (e.g. Kennedy et al., 2006; Kennedy & Kenyon, 2008) and/or scattering from other forming planets (e.g. Terquem & Papaloizou, 2007).

The formation of observed super-Earths is also important in the context of other objects in a system. For example, a population of *giant* planets has begun to be detected out at a few au (e.g. Mayor et al., 2011; Bowler, 2016), with some studies suggesting that as many as ∼50% of RV-detected planetary systems could host a giant planet in the range of 5-20au (Bryan et al., 2016). Many systems have also been observed to have populations of debris, which are typically outside of $\sim$ 30au (Wyatt et al., 2012; Lestrade et al., 2012; Kennedy et al., 2015). The gap between inner super-Earths at $\sim$ 1au and debris at $\sim$ 30au suggests the presence of additional undetected planets that may be sculpting the inner edge of the debris, akin to that shown in Chapter 5.

How important giant planets at $\sim$ 1 – 30au are for the formation of super-Earths is unknown. Giant planets can exist at these separations without causing an instability in close-in super-Earths, as shown in Chapter 3. Moreover, the presence of a wide-orbit giant planet may explain the ratio between the number of *Kepler* systems with 1 transiting planet and, the number of *Kepler* systems with 2 transiting planets, as shown in Chapter 4. The presence of giant planets with separations of ∼1-30au is therefore important in understanding not only the formation of super-Earths but also their currently observed system architectures.

The formation of super-Earths could be affected by outer giant planets in the following ways:

1. Super-Earths form in-situ at their currently observed separations of $\lesssim$ 1au (e.g. Schlaufman, 2014). The presence of a giant planet at $\sim$ 1 – 30au is therefore *not required* for super-Earth formation.

2. The cores of super-Earths form at wide orbits and either get scattered inwards, or

have inwards migration induced by, a **static** giant planet. The cores are then circularized at $\lesssim$ 1au by tidal interactions with the star (Kennedy & Kenyon, 2008). Super-Earth cores may also be caught in the secular resonances of a static giant planet, which move inwards as the protoplanetary disk dissipates. A wide-orbit giant planet is therefore *required* for super-Earth formation.

3. The cores of super-Earths form in the outer parts of a system and migrate inwards independently of a giant planet. If a giant planet is present however, this could block the forming super-Earth from migrating inward any further (Izidoro et al., 2015). The presence of a wide-orbit giant planet therefore forbids the formation of close-in super-Earths and would *not be expected* in super-Earth systems.

A fourth potential formation mechanism is that one of the forming super-Earths grows into a giant planet and migrates inwards. Other forming super-Earths may get caught in, for example, the mean motion resonances of the giant planet and also move inwards (e.g. Raymond et al., 2008; Fogg & Nelson, 2009). Giant planets would therefore be expected to be present where close-in super-Earths are observed. However, this mechanism is *unlikely*, as RV surveys detect a lack of giant planets in super-Earth systems inside of $\sim$ 5au.

The ability to distinguish between the aforementioned formation mechanisms of super-Earths is limited by RV and transit studies only being sensitive to planets inside $\sim$ 5au. Direct imaging offers the only way to detect giant planets outside of this limiting separation and is therefore the only way to constrain the super-Earth formation mechanisms described above. I therefore conducted a direct imaging survey using the European high-contrast imager SPHERE at the *Very Large Telescope* (VLT), to investigate the presence of giant planets in the $\sim$5-30au region of super-Earth systems. I am the principal investigator of this survey and responsible for all the analysis/results presented in this Chapter. I acknowledge my collaborators of this survey: L. Mátra, M.C. Wyatt, J. Milli and G.M. Kennedy, and describe any contributions they had to the work in this Chapter in text or in the declaration of originality section at the beginning of this Thesis. In §6.3 I describe the targets used for this survey. In §6.4 I describe the observations of these targets using the SPHERE imager. I briefly discuss the data reduction process in §6.5, before presenting and discussing preliminary results in §6.6 and summarizing in §6.7.

6.3 Sample

The survey aimed to search for giant planets around the current total of 29 G-, K- and M-type stars that simultaneously fulfil the criterion of hosting super-Earths, being within 20pc and being observable from the southern hemisphere. A super-Earth hosting system

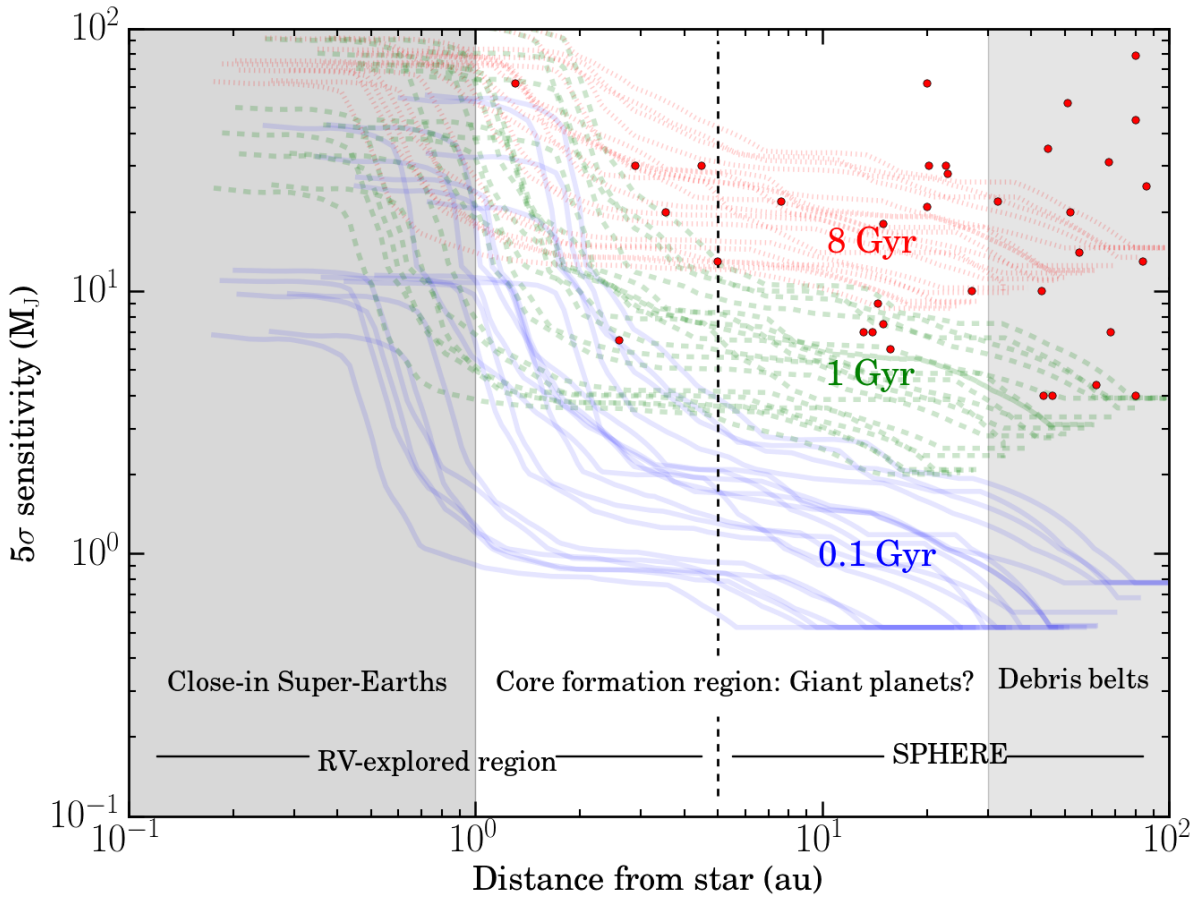

Figure 6.1 Theoretical detection threshold for planets with SPHERE imager. Each curve refers to each of the 19 systems in our final sample for different ages. Red dots are all the planets detected by direct imaging. Figure generated using script from collaborator on project, L. Mátra.

was defined as being observed to contain one or more planets with masses between 1-95$M_\oplus$ only, which are detected using the radial velocity method. Out of the 29 systems two were disregarded from them being GTO reserved targets (Proxima and GJ785). From the remaining 27 systems, 8 were not observable from the VLT during the initial observing run (P99, April-September 2017), giving the final selection of 19 targets which I summarize in Table 6.1. I note that a caveat with this sample is that the stars are those known to host super-Earths, whereas in reality there are likely many more close by systems with super-Earths that have yet to be detected.

The ages of the 19 sample targets are largely uncertain (see Table 6.1), with some stars being possibly as young as $\sim$ 100Myr or as old as $\sim$ 10Gyr. For some survey targets, gyrochronology, which estimates the ages of stars from their rotation periods, predicts estimates as good as $\sim$ 10 – 20% (e.g. Wright et al., 2011). For other survey targets however, the ages are not currently well known. As all the survey targets are field stars, they are likely to be old, though their ages would be difficult to constrain (Soderblom, 2010). As

noted in §1.5.3, direct imaging surveys typically observe young stars, as planetary evolution models predict giant planet companions to dim over time as they cool. This survey is largely unique therefore, in that it is targeting older systems. However, as the target stars are low mass, they are intrinsically fainter, which when combined with the close proximity to Earth, predicts favourable detection thresholds for potential planetary companions.

I highlight this in Figure 6.1 which shows the expected 5σ mass detection threshold of companions as a function of separation from the star for each of the 19 targets. I note this Figure was generated using a script from my collaborator on this survey, L. Mátra. The expected detection thresholds are calculated using the SPHERE exposure time calculator (ETC), with each target being represented by a single line for a given age estimate in Figure 6.1. Due to the uncertain ages of the sample targets, detection thresholds are calculated assuming ages of 0.1, 1 and 8Gyrs, given by the blue, green and red lines respectively. For reference all the known planets detected via direct imaging are plotted with the red dots. It is clear from Figure 6.1 that the survey could detect planets as low as $2M_J$, assuming an age estimate of $\sim$1Gyr, in the 5-30au region that is of vital importance for constraining the formation mechanisms of super-Earth systems described in §6.2.

6.4 Observations

Our targets were observed using the SPHERE imager at the VLT located in Paranal Chile, for the program ID 099.C-0255. For each target the IRDIFS, pupil-stabilised mode using the 185mas diameter apodized-Lyot coronagraph was used (Carbillet et al., 2011; Guerri et al., 2011). The IRDIFS mode observes each target simultaneously with two different instruments, the integral field spectrograph (IFS) (Claudi et al., 2006) and the IRDIS camera (Dohlen et al., 2008).

The SPHERE IFS splits incoming emission across 39 different wavelength channels between the Y and J bands (0.95-1.35μm), allowing for detailed spectral information of potential companions to be observed. The field of view of the IFS extends out to 1.73×1.73arcsec^2, equivalent to a maximum separation from the host star for most of the targets in the survey of $\lesssim$ 5au. Potential giant planets which orbit outside of this separation from the host star will therefore lie outside the field of view of the IFS and be undetectable with this instrument. For this reason, each target in the survey is also observed with the IRDIS camera installed on SPHERE.

The IRDIS camera is used in dual band imaging mode (Vigan et al., 2010), which splits incoming emission between two filters with H2 and H3 wavelengths ($\lambda_{H2} = 1.593\pm0.055\mu$m, $\lambda_{H3} = 1.667 \pm 0.056\mu$m). The field of view of IRDIS is significantly larger than that of the IFS, extending out to 11×12.5arcsec^2. For most targets in our survey this corresponds to a

Target/Field	Type	Age (Gyr)	δ_{Gal} (deg)	μ_α (arcsec/yr)	μ_δ (arcsec/yr)	Mass ($M_\odot$)	d (pc)
61Vir	G7	$6.3^{+3.3}_{-3.1}$ [1]	44.09	-1.07	-1.06	0.94±0.03[2]	8.52±0.05 [17]
HD 102365	G2	9±3 [2]	20.70	-1.53	0.40	0.89±0.03 [1]	9.24±0.06 [18]
HD 136352	G4	$10.36^{+2.32}_{-2.28}$ [2]	7.38	-1.62	-0.28	0.91±0.03[2]	14.56±0.17 [18]
HD 189567	G2	$9.76^{+2.08}_{-2.12}$ [2]	-31.99	0.84	-0.67	0.92±0.03[2]	17.72±0.23 [18]
HD 20794	G8	5.76±0.66 [3,4]	-56.08	3.04	0.73	0.85±0.01[2]	6.06±0.02 [18]
GJ 3998	M1	N/A	26.15	-0.14	-0.35	0.5 ± 0.05 [11]	17.79±0.72 [19]
GJ 422	M3.5	N/A	2.98	-2.47	1.18	0.35 [12]	$12.55^{+0.43}_{-0.46}$ [18]
GJ 433	M1.5	N/A	27.65	-0.07	-0.85	0.48 [13]	$9.04^{+0.14}_{-0.15}$ [18]
GJ 581	M3	4.3[5]	40.02	-1.2	-0.10	0.31±0.02 [5,14]	6.27±0.09 [18]
GJ 649	M2	<0.44 [2]	35.37	-0.12	-0.51	0.54±0.05 [15]	10.32±0.16 [18]
GJ 667C	M1.5	∼ 5 [6]	1.41	1.16	-0.21	0.33±0.02	6.8 [19]
GJ 674	M3	0.1-1 [7,8]	-6.78	0.57	-0.88	0.35 [7]	4.54 ± 0.03 [18]
GJ 682	M3.5	N/A	-6.63	-0.71	-0.94	0.27 [12]	5.04±0.06 [18]
GJ 832	M2.5	9.24 [9]	-46.35	-0.05	-0.82	0.45±0.05 [16]	4.94 ± 0.03 [18]
Wolf 1061	M3	N/A	23.68	-0.09	-1.18	0.294 [14]	4.31±0.01 [20]
HD 154088	K0	$12.48_{-5.00}$ [2]	7.67	0.08	-0.27	$0.92^{+0.09}_{-0.04}$ [2]	$18.08^{+0.29}_{-0.30}$ [18]
HD 3651	K0	>11.80 [2]	-41.53	-0.46	-0.37	$0.88^{+0.03}_{-0.02}$ [2]	11.11±0.09 [18]
HD 85512	K6	5.61±0.61 [3,4]	8.16	0.46	-0.47	$0.71^{+0.01}_{-0.03}$ [2]	11.15±0.10 [18]
HD 99492	K3	4.8±4.1[10]	58.51	-0.73	0.19	0.85±0.02 [10]	18.22±0.09 [20]

Table 6.1 SPHERE survey sample. Variables δ_{Gal}, μ_α, μ_δ and d refer to the galactic latitude, proper motion in right ascension, in declination and distance respectively. Parameters shown to a maximum of two decimal places. References: [1](Valenti & Fischer, 2005), [2](Takeda et al., 2007), [3](Pepe et al., 2011), [4](Sousa et al., 2008), [5](Vogt et al., 2010b), [6](Anglada-Escudé et al., 2012), [7](Bonfils et al., 2007), [8](Leggett, 1992), [9](Sanz-Forcada et al., 2010), [10](Kane et al., 2016), [11](Maldonado et al., 2015),[12](Zechmeister et al., 2009), [13](Delfosse et al., 2013), [14](Delfosse et al., 2000), [15](Johnson et al., 2010), [16](Bailey et al., 2009), [17](Perryman et al., 1997), [18](ESA, 1997), [19](van Leeuwen, 2007), [20](Gaia Collaboration et al., 2016)

maximum separation around the host star of $\lesssim$ 30 – 50au. The H2 and H3 band filters are of importance for this survey as planets are generally brighter in the near-IR due to their thermal emission. The narrow IRDIS bands are also on top of and outside of a prominent methane feature commonly present in old giant planets, like those which may be detected by this survey. Observing target stars with both the IFS and IRDIS camera installed on SPHERE (i.e. the IRDIFS mode) therefore allows for both:

- detailed spectral information to be observed for companion detections that have separations of $\lesssim$ 5au from the host star.
- detections of companions which have separations from the host star out to $\sim$ 30 – 50au.

In pupil stabilised mode, the coronagraph is centred on the target star throughout an observation, such that the field of view rotates with respect to the star allowing for classical angular differential imaging (CADI) to be used (see Marois et al. 2006 for a detailed description of CADI). CADI involves taking images at different times during an observation referring to different amounts of field rotation. Taking a selected number of these images allows for a reference point spread function (PSF) of the star to be generated. This PSF is subtracted off all other images taken during observations to nullify the stellar halo and remove quasi-static noise. Each of these subsequent images are then commonly aligned and combined to produce a final science image used for analysis. For the targets in the survey, 1 hour on source per target allowed for enough field rotation for CADI to be used. Typically, the effects of speckle noise that is roughly static in the stellar PSF can be reduced by a factor of $\sim$ 5 using the CADI technique (Marois et al., 2006). Weather constraints were set by requiring that all observations were taken in conditions where the seeing was below 1arcsec, equivalent to median conditions. A typical observational cycle for each target proceeded as follows:

1. A non-saturated PSF, taken off centre from the star with a neutral density filter was observed, allowing for a reference PSF of the star to be generated.
2. An image centred on the star with modulations in the deformable mirror being used to generate four spots in the image, which allowed for calibration of the position of the star behind the coronagraph required for the common centring of science images.
3. Science images.
4. An additional centring image.

5. An observation of a nearby uniform field, which was used for astrometric calibration of the science images.

6.5 Calibration and Reduction

Standard astrometric calibrations (dark frame subtraction and flat field division) were performed on all science images with the ESOReflex pipeline (Freudling et al., 2013) for IRDIS images and the pipeline outlined in Vigan et al. 2015 for IFS images. Calibrated science images were then reduced for analysis with the VIP pipeline detailed in Gomez Gonzalez et al. 2017. I acknowledge additional code routines provided by J. Milli which extracted data (rotation angle, position of North etc.) from science images which were required for the VIP pipeline to be used. This reduction procedure first identified individual science images for significant signs of contamination. The most common cause of contamination was due to images being taken in high wind conditions, causing stellar emission to become smeared across the coronagraph in the direction of the wind. Images were analysed for contamination by measuring the flux within a common annulus outside of the coronagraph. Images where the flux within this annulus exceeded 2σ of the median value from all the images were disregarded from further use.

The remaining images were then derotated to a common alignment and then combined. For the preliminary results presented in this thesis, images were combined using principal component analysis. Principal component analysis (PCA) reduces a large dimensional parameter space to a few parameters, known as *principal components*, which describe the majority of the variation in a data set (see Soummer et al. 2012 for a mathematical description of PCA). This procedure can be thought of fitting an ellipsoid to an n-dimensional parameter space, where the individual axes of the ellipsoid (or principal components) refer to an axis in the large parameter space where there is the most variance in the data (e.g. Campbell & Atchley, 1981). The use of PCA allows for the reduction of noise in the combined image, as components in the observed images with a small variance are suppressed. This image combination was done for IRDIS observations taken with both the H2 and H3 filters individually (assuming 5 principal components) to produce two final IRDIS images. For IFS observations, to increase the signal to noise of potential companions in the field of view, images taken at different epochs were summed over all wavelength channels before being combined (assuming 10 principal components) to produce a single final IFS image. I note that on-going analysis aims to optimize the number of principal components used for both IRDIS and IFS images to maximise the signal to noise in regions of interest.

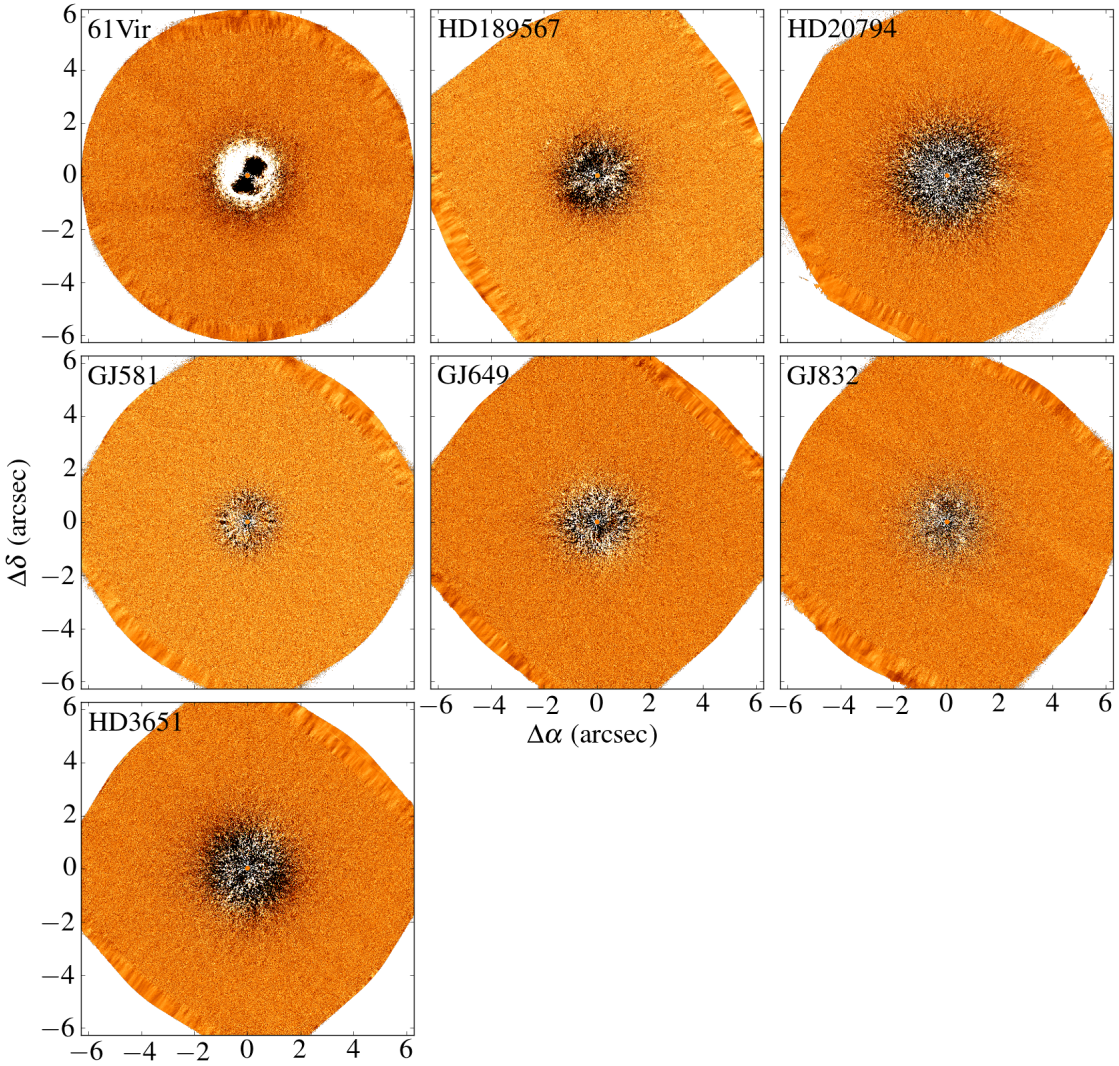

Figure 6.2 IRDIS H2 band filter images of systems from the SPHERE survey with no companion detections. High levels of noise at the centre of the images refer to residual stellar emission.

6.6 Results

Out of the 19 targets in our survey, poor weather meant that 5 systems did not pass the 1arcsec seeing constraint during the P99 period and will be reobserved as part of the observing period P101 (April-September 2018). Of the remaining 14 systems, preliminary reduction of images indicates that 7 show no evidence for a companion. The remaining 7 however contain any number of potential companion detections. Below I split the discussion of results between systems with and without potential companion detections. I note that a more in-depth analysis of all 14 systems is on-going and due to be published as part of future work. Here I summarize the preliminary results only.

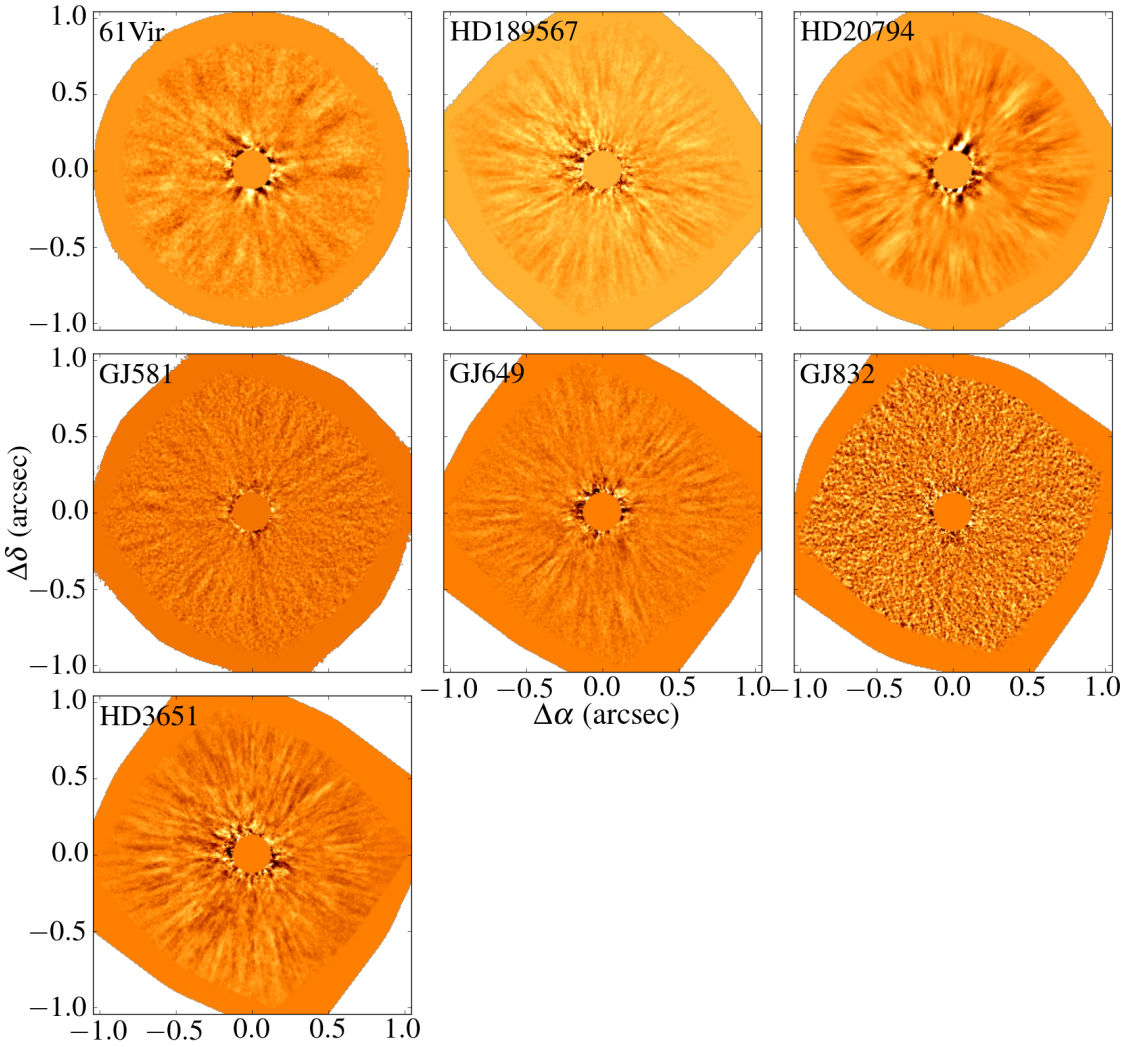

Figure 6.3 IFS images of systems from the SPHERE survey with no companion detections. Images have been averaged across the 39 wavelength channels.

6.6.1 Non-detections

The following systems do not have a companion detection with either IFS or IRDIS: 61Vir, HD 189567, HD 20794, GJ 581, GJ 649, GJ 832 and HD 3651. The IRDIS images for each of these targets in the H2 band are shown in Figure 6.2. The central 8 pixels in each image are masked to represent the coronagraph. For each target, residual emission from the stellar halo is visible out to $\sim$ 1.5arcsec, with flux outside this region reducing to the background level. It is clear from Figure 6.2 that no companions with emission above the background level are present outside of $\sim$ 1.5arcsec for these targets.

The central $\sim$ 1.5arcsec of the IRDIS images is probed with the IFS images, which are shown in Figure 6.3. Again the central regions of these images are masked to represent the coronagraph. No companion with emission above the background level is detected

in any of the IFS images. A preliminary conclusion for these targets therefore is that no companions are detected in these systems with SPHERE out to $\sim$ 12arcsec.

Whilst no companions are detected in these systems, upper limits can be placed on the detection threshold for planets in the form of contrast curves. Contrast curves describe the relative planet-star flux a telescope can observe at a given separation from the host star (§1.5.3). To calculate contrast curves for each of the 7 targets, fake companions were injected into the final IRDIS and IFS images at a given separation from the star, with the contrast of the companions then being retrieved. Figure 6.4 shows the contrast curves calculated in this way for all the 7 systems for IFS (top panel) and IRDIS (bottom panel). The vertical axis in Figure 6.4 refers to what contrast a companion would need to have in order to be detected with a 5σ certainty. Contrasts are calculated for both the H2 and H3 IRDIS filters, with the mean being shown by the solid lines in the bottom panel of Figure 6.4 and the shaded region referring to the limiting contrasts from either filter. For small separations in the IRDIS images, the contrast is heavily influenced by the residual stellar speckle emission which explains the greater deviations of the contrast between the H2 and H3 filters inside of $\sim$ 0.1arcsec.

From the contrast curves shown in Figure 6.4, I calculate the expected planet masses that would be detectable with a 5σ certainty with both IRDIS and IFS at a given separation from the host star. I acknowledge the script to do this conversion was provided by my collaborator on this survey J. Milli. I use the AMES-Cond planetary evolutionary model (Allard et al., 2001; Baraffe et al., 2003) which estimates the mass of a planet for a given flux and age. Due to the uncertain ages for all the systems in the survey, I assume the age estimates at the limits of the uncertainty range from Table 6.1. For systems with no age uncertainty, I assume one of $\pm$2Gyr up to 12Gyr, which is the limiting age of the AMES-Cond models. The 5σ companion mass detection threshold for both IRDIS and IFS for each of the 7 systems is given by the solid and dashed lines in Figure 6.5 respectively. For the IRDIS curves, the mean contrast between the H2 and H3 filters from Figure 6.4 was used. For reference, I plot the known super-Earths in each of these systems with the purple dots and any known populations of debris with a grey shaded region. I also plot a general mass detection limit from RV studies with a red line. It is worth noting that the mass contrasts from Figure 6.5 agree with those expected from Figure 6.1 for the (largely older) ages of these systems.

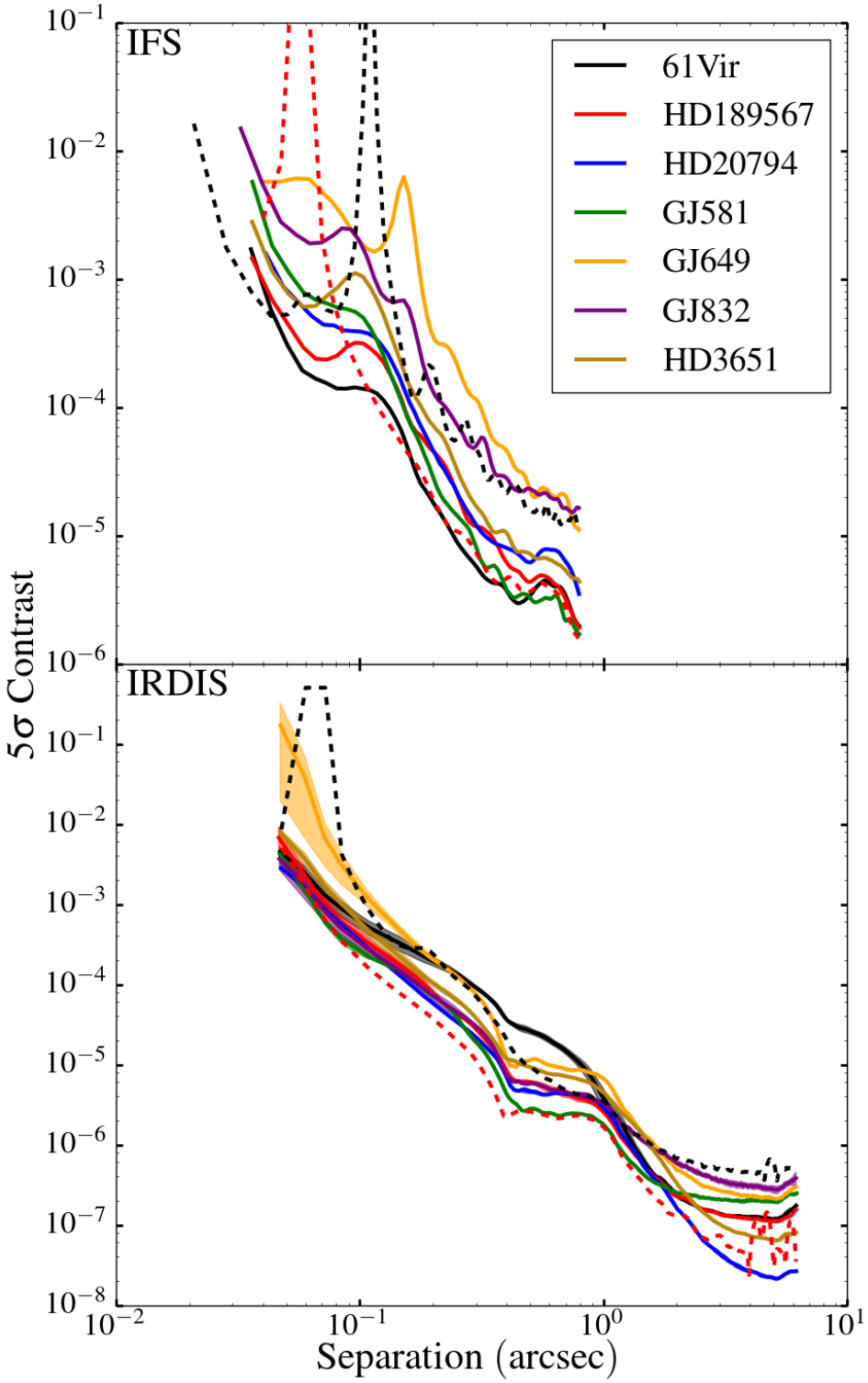

Figure 6.4 Contrast curves for each system with no detections with IFS (top panel) and IRDIS (bottom panel). For the IRDIS contrast curves, the solid line gives average contrast between the H2 and H3 filters, with the shaded region giving the range around the average. The dashed lines show contrast curves from two of the systems where detections were present. It is clear that systems with detections do not have a higher sensitivity than those without.

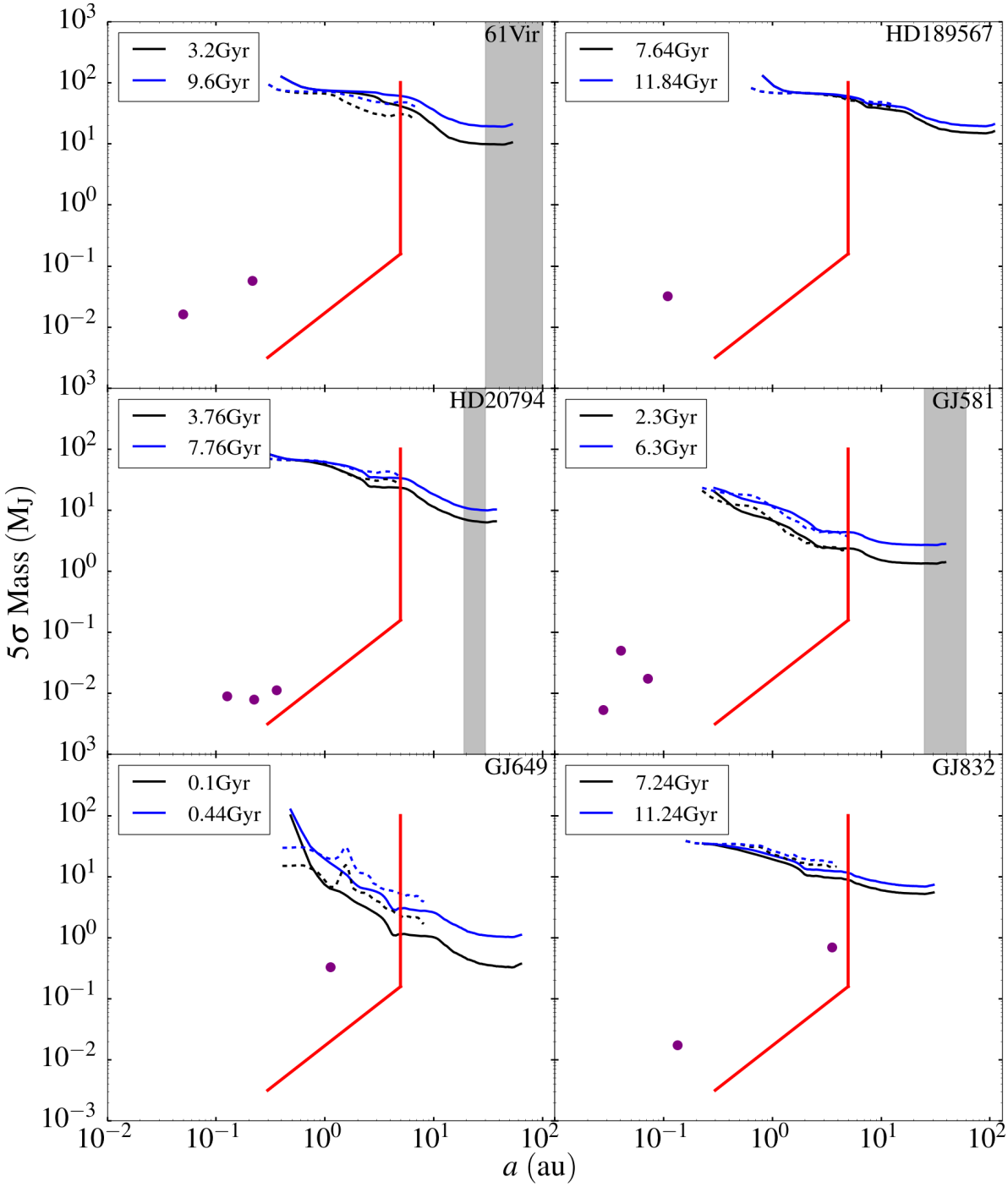

Figure 6.5 Mass contrast curves from the contrast curves shown in Figure 6.4 for a given age. The solid and dashed lines refer to the IFS and IRDIS contrast respectively. Known planets in these systems are given by the purple dots, with grey shaded regions describing the position of any known debris. An approximate RV detection threshold is shown by the red line. References for planet parameters and debris where appropriate: 61Vir (Vogt et al., 2010a; Wyatt et al., 2012), HD 189567 (Mayor et al., 2011), HD 20794 (Kennedy et al., 2015; Feng et al., 2017), GJ 581 (Lestrade et al., 2012; Trifonov et al., 2018), GJ 649 (Johnson et al., 2010), GJ 832 (Wittenmyer et al., 2014).

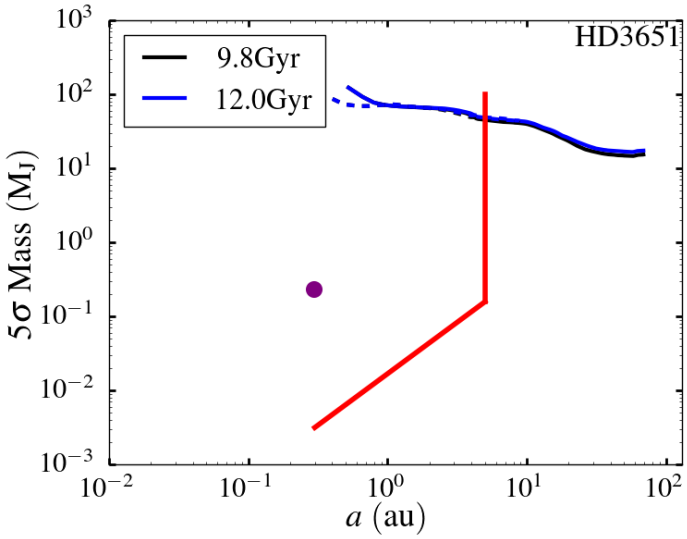

Figure 6.6 Extension of Figure 6.5. Reference for planet (Wittenmyer et al., 2009).

6.6.2 Detections

Of the remaining observed systems, 7 show evidence for one or more potential companions. Due to the on-going analysis of these systems, I do not name them explicitly here. However, I show the detections in the IRDIS field of view in the H2 band for these systems in Figure 6.7, where the bright point sources refer to a detection. A tentative detection is shown in the bottom left panel of Figure 6.7, highlighted by a blue circle. Whether this detection is real or an artefact of the reduction process is unclear and is part of on-going analysis.

The IFS images for these systems are also shown in Figure 6.8. No companion detections have been found in the IFS field of view for any of the targets. To check if this lack of detections was due to some problem arising in the IFS reduction pipeline, I considered a system not in this survey that has a known detection in the IFS field of view (Milli priv comm). Due to on-going analysis of this additional system by the corresponding authors, I do not name it here. I find that the IFS pipeline used for this survey recovers the detection in this additional system, with a separation and flux that agrees with that obtained by the authors analysing this additional system (Milli priv comm). I postulate therefore that the lack of detections in the IFS field of view for this survey may be due to a combination of the small field of view of the IFS, combined with contamination from residual stellar emission not blocked out by the coronagraph. On-going work is looking to reduce this possible stellar contamination to confirm whether no detections are indeed present in the IFS field of view for all the systems in this survey.

Before confirmation can be made of the detected companions in the IRDIS field of

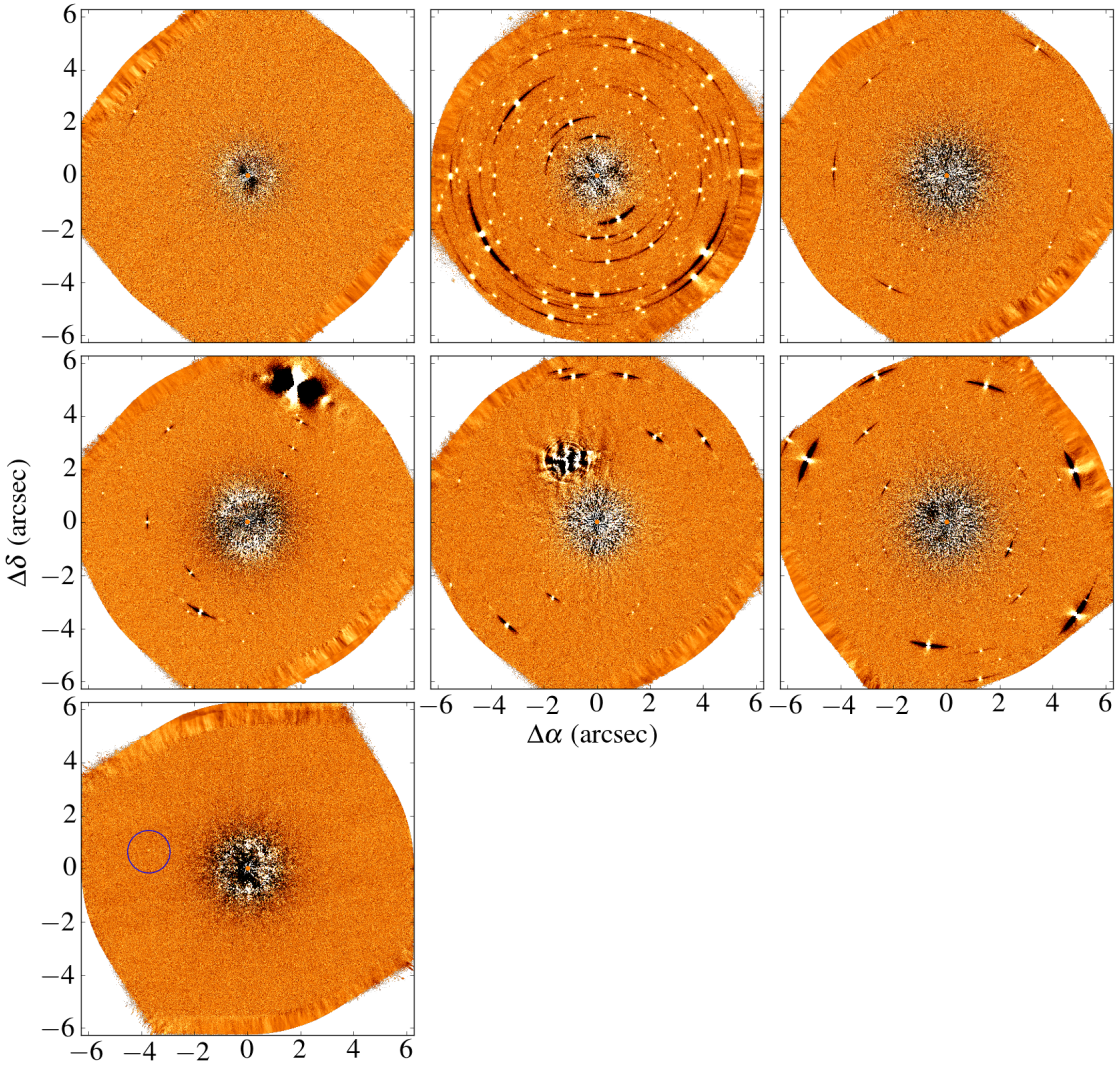

Figure 6.7 IRDIS images of systems with potential companion detections. Due to the ongoing nature of the analysis of these systems they are not named here. The circle in the bottom left panel highlights a tentative detection in this system.

view, it must be investigated whether they are an object that is actually bound to the star or a background object seen in projection. The proper motion of a given star means that it will move across the sky at a different rate compared with distant objects. The most rigorous way of confirming a companion detection with direct imaging is to therefore observe the target star again at a later date. Background objects would have stayed still and so moved with respect to the star, which is placed at the centre of the image. Any companion would have moved with the star, although there may be orbital motion of the companion to consider. Due to the survey observing the closest planetary systems, the relative proper motions of all the targets are high (see Table 6.1), with some in excess of 1arcsec/year. Re-observing any of the targets in the survey in the subsequent observing period (i.e. a year later) would therefore be enough time for any of the target stars to have significantly

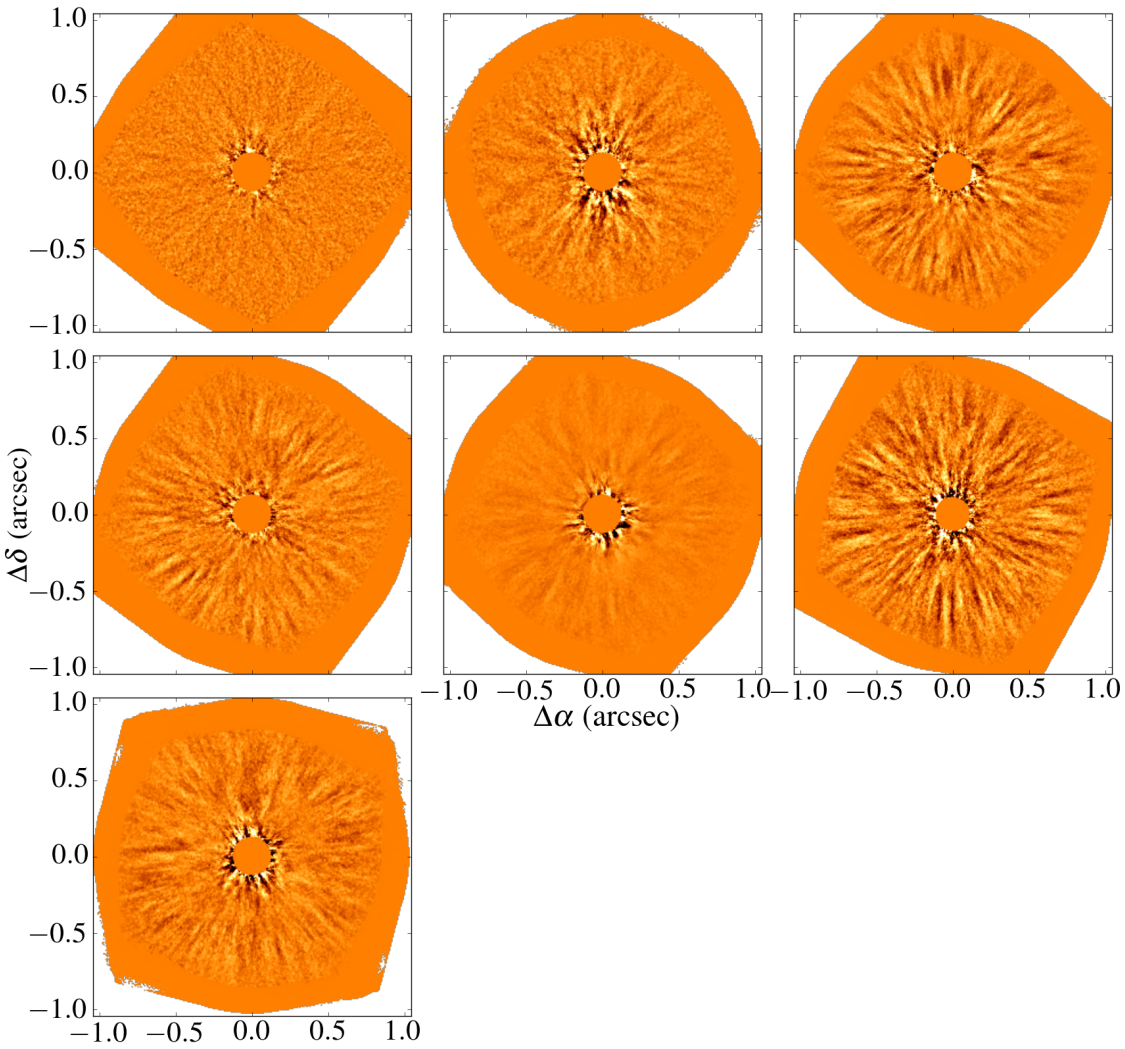

Figure 6.8 IFS images of systems that have potential companion detections with the IRDIS camera. No detections are present in the IFS images for these systems.

moved with respect to background objects. If a detection is present in the second observation with roughly the same separation from the host star as in the first image (allowing for any orbital motion), then it is most likely a bound companion to the star. Currently it is planned to re-observe the most promising of the targets from the survey in this way to confirm potential companion detections.

In lieu of re-observing targets, other methods can also be used to infer the probability of whether a detection is a companion or a background object. One can consider models of the distribution of stars in the Milky Way and use this to work out the probable number of stars that would be observed in a given patch of sky. The number density of stars in the Milky Way falls off significantly for larger galactic latitudes (Drimmel & Spergel, 2001). Target stars with high latitudes would therefore be less likely to have a background star in the IRDIS field of view and vice versa (I note that the galactic latitude, δ_{Gal}, of all targets in

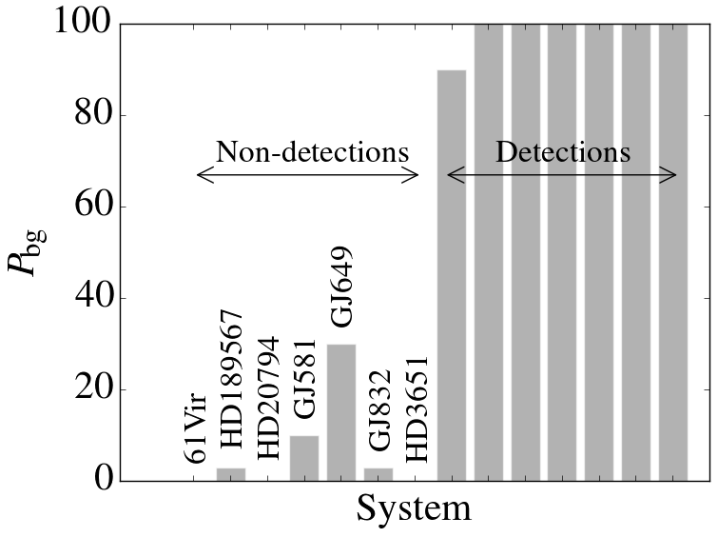

Figure 6.9 Probability of observing at least one background source in the IRDIS field of view according to the *Galaxia* model for the distribution of stars in the galaxy. Systems with potential detections are not named.

this survey are shown in Table 6.1). To work out the probable number of background stars in the field of view for each of the survey target stars, I consider the *Galaxia* model for the distribution of stars in the galaxy (Robin et al., 2003). Defining a galactic longitude and latitude, this model returns the number of stars that would be expected to be observed within a given field of view. For the targets where a potential companion was detected, the probability of there being at least one background object in the field of view (denoted as P_{bg}) is shown in Figure 6.9. For comparison this probability is also shown for targets where no detections were present (§6.6.1). From this figure, it is clear that the probability of background contamination is much larger for systems in the survey where detections have been observed. I conclude therefore that most of the detections shown in Figure 6.7 are likely to be background objects, however this can only be confirmed through a second epoch of observations for these systems.

Insights into the likeliness of the planetary nature of detections can also be investigated through spectral analysis. For detections in the IRDIS field of view the H2 and H3 band fluxes can be compared, as these filters lie of top of and outside a prominent methane feature expected to be present in giant planets. Differences in the flux of the detection between these two images would therefore suggest a planetary type object rather than a background star. Moreover, for any future detections in the IFS field of view, spectra is available in the Y-J band, which when comparing with model spectra allow for a planet, dust-surrounded planet or a background object to be discerned between. Spectral analysis of detections from the survey is on-going and will be presented in future work and as such I make no further mention of it here.

Whether the sensitivity of the observations was better for systems where detections were present can be investigated by considering the associated contrast curves for these systems. I show two of these contrast curves in Figure 6.4, denoted by the dashed lines. These two curves correspond to the approximate range of contrast curves for all the systems where detections are present. From Figure 6.4 I conclude therefore that the sensitivity of observations for systems with detections is not better than those without. Moreover, systems with detections are not inherently younger than those without. I also conclude therefore that the mass sensitivity for systems with detections would not be significantly higher than those without.

6.7 Summary and Outlook

This Chapter has described an on-going survey looking to directly image giant planets on wide orbits in close-by systems with known super-Earths, using the SPHERE imager at the VLT. Out of a total of 19 proposed targets, 14 were observed during the observing period between April-September 2017, with the remaining 5 systems due to be observed during the April-September 2018 period. Of the 14 observed systems, 7 were found to have no companion detections. Upper mass limits for planets in these systems were subsequently presented and represent the best limits to date in the region of $\sim 5-50$au.

The remaining 7 systems were found to have evidence for at least one companion detection. Analysis of these detections is on-going to determine their planetary nature or whether they are background sources observed in projection. The most promising companion detections will be proposed for re-observation to fully confirm whether they are indeed a planetary object bound to the host star. Due to the on-going nature of the survey, the final results including targets with and without companion detections will be fully presented as part of future work.

Once this survey is complete, the results will look to constrain which of the three formation scenarios of super-Earths discussed in §6.2 is the most likely. That is, whether observed super-Earths are most likely to form in-situ (#1 from §6.2), or further out with dynamical interactions with or without a static giant planet (#2 or #3 from §6.2 respectively) causing the super-Earth to move inwards. A large number of companion detections would suggest that giant planets are required for super-Earth formation, pointing toward scenario #2 from §6.2. If few/no companions are detected, this suggests that giant planets are either not needed for, or halt super-Earth formation, suggesting scenarios #1 and #3 from §6.2. I note that these two latter scenarios could be distinguished between by observing the structure of any debris, as scenario #1 would imply limited clearing of debris and vice versa for scenario #3 (e.g. in a way described in Chapter 5).

From the initial analysis of observations from the survey, half of the 14 currently observed systems have detected candidate objects. However it is likely that the majority of these detections are projected background objects. A preliminary conclusion from this survey therefore is that wide-orbit giant planets are not common in systems with close in super-Earths, suggesting that super-Earths form in-situ or through inward migration (#1 and #3 in §6.2). However, it is of course possible that many of the detections presented here could be planetary companions, which would support the conclusion that wide-orbit giant planets are of vital importance in forming observed super-Earth systems (e.g. formation scenario #2 in §6.2).

7

Summary and Conclusions

Since the discovery of the first exoplanet more than 20 years ago, it has become clear that planetary systems can be far more diverse than what would be expected from the example of the Solar System. Exoplanets can have a range of sizes, separations from the host star and bulk characteristics. The orbital properties are also just as diverse, with large eccentricities and small mutual inclinations between planets being observed. However, how representative observed exoplanetary systems are of the wider population is unclear. Current detection techniques are largely bias toward detecting planets on orbits within a few au of the host star and along the line of sight to the Earth. In many of the observed exoplanetary systems therefore it is possible that additional planets on wide orbits could be present which are evading detection. Insight into the possibility that such a population of planets is present can only be investigated by considering the dynamical impact they would have on known planets. This rationale provided the motivation for all the work presented in this thesis.

In Chapter 3 I investigated the long term dynamical evolution of known planetary systems due to the presence of a hypothetical planet on an eccentric orbit. Specifically I investigated how the eccentricity of the hypothetical planet can be transferred to known planets through secular perturbations. From an analytical study of a general two planet system I showed that a planet on an elliptical orbit transfers all of its eccentricity to a planet on an initially circular orbit over long timescales if the two planets have comparable orbital angular momenta. From application to HD38858, I showed for what combinations of masses, semi-major axes and eccentricities a hypothetical planet would need to have in order for it to be unlikely to be present in this system. I also showed that additional planets in proximity to known planets can provide a stabilising effect to long term perturbations from a wide-orbit planet. Moreover, these additional planets can still provide this stabilisation and be below current radial velocity detection thresholds. I showed this effect through application to the two super-Earth system 61Vir. I found that unless an additional planet in this system had a mass, semi-major axis and eccentricity within a restricted area of parameter space, it could not induce a significant eccentricity in the known planets.

This suggests therefore that for systems with two detected planets where one is observed to have an eccentric orbit and the other an otherwise suspiciously circular orbit that the presence of additional stabilising planets in the system could be inferred.

Chapter 3 mainly considered planetary systems in the context of those detected by radial velocity. However, the Kepler space telescope is currently responsible for the largest number of planet detections. As these planets are detected via the transit method, only those with orbits that lie along the line of sight can be observed. It is possible therefore that additional planets on inclined orbits can exist in systems with transiting planets without being detected. In Chapter 4 I considered whether the population of known transiting planets contains evidence for additional planets on inclined orbits which are not observed to transit. Specifically I considered the secular perturbations from these additional planets on the known planets. I developed a simple analytical model to describe the inclinations that get induced in the known planets from secular interactions with an outer planet on an inclined orbit. I then coupled this model with a semi-analytical method for calculating transit probabilities to simply calculate how the secular perturbations cause the transit probability of known planets to evolve. Demonstration of this model was made through application to Kepler-48 and HD-106315 allowing for the inclinations of the outer planets in these systems (which are known from radial velocity measurements) to be constrained.

I also applied the work in this Chapter to the so called 'Kepler Dichotomy' which describes the apparent excess of single transiting systems compared with multi-planet systems observed by Kepler. I found three different ways of explaining this dichotomy, which included 1) that some systems are just inherently single planet systems. 2) some multi-planet systems have inherently large mutual inclinations such that only a single planet is observed to transit. 3) some multi-planet systems could cyclically attain large mutual inclinations through secular interactions with an inclined outer planet. I showed how these three different mechanisms can be combined to fit the properties of Kepler systems observed to have one and two transiting planets. I also showed how the observed mutual inclination distribution of systems with two transiting planets constrains the fraction of two planet systems that have outer perturbing planets. This is because two planet systems observed by Kepler, where the planets are being perturbed by an outer inclined planet, should preferentially be detected when the two planets are co-planar due to the increased transit probability. I showed therefore that the presence of wide-orbit inclined planets in Kepler systems does not contradict the small inclination dispersion of planets currently observed.

Wide-orbit planets in planetary systems not only dynamically interact with other planets but also with any populations of debris. Observations of debris can therefore place constraints on undetected planets in planetary systems. An example of this was shown

in Chapter 5 where I considered the system HR8799, which is observed to host four giant planets and two belts of debris, both internal and external to the planets. I showed through N-body simulations that the observed outer belt cannot be explained by dynamical interactions with the four planets in their current configuration. When an additional planet (which was external to the outermost known planet) was included in the simulations, the predicted outer belt was consistent with the belt that has been observed. This led to the conclusion that the presence of a fifth planet in HR8799 predicts an outer belt of debris that agrees significantly better with observations compared with the debris predicted by the known planets in isolation. I also showed that inward scattering of material from the outer belt to the inner belt in the first $\sim$ 10Myr of HR8799 due to dynamical interactions with the planets may have produced warm dust emission at a level similar to that observed today. I concluded therefore that inward scattering of material may explain bright emission from debris for systems at $\sim$ 10Myr ages.

The work presented in this thesis has therefore shown that wide-orbit planets that have yet to be detected in planetary systems can have a significant dynamical effect on planets that have currently been observed. Dynamical interactions therefore offer the best method for constraining which types of yet to be detected planets are likely to be presence in planetary systems.

Confirmation of wide-orbit planets in planetary systems can only be made however if they are detected observationally. In Chapter 6 I introduced a survey which is looking to directly image giant planets around close-by G-, K- and M-type stars known to host super-Earth type planets. As of writing this thesis, the observations and any subsequent analysis is on-going and due to be presented as part of future work. Preliminary analysis of some targets from the survey showed however that significant mass limits in the region of 5-30au can be placed on systems with no evidence of a companion detection. These mass limits would be the best limits to date and be vital in explaining the importance of wide-orbit giant planets in the formation of close-in super-Earths. Systems which also show detections of companion objects were also presented, however it was concluded that the majority of these detections are most likely background objects observed in projection. A preliminary conclusion was made therefore that wide-orbit giant planets are not common in systems with close in super-Earths, suggesting that observed super-Earth systems form in-situ or through inward migration. Observations of all targets in the survey are expected to be completed by October 2018, including any follow-up observations required to confirm any companion detections.

7.1 Outlook for the future

Upcoming telescopes will be able to detect smaller mass planets at greater separations from the host star, allowing for the full complement of planets in a system to be found. For example, the *Gaia* space telescope, which was launched in December 2013, aims to collect precise astrometric measurements for around 1 billion stars, allowing for distances to these objects to be accurately determined. The sensitivity of *Gaia* is expected to resolve the astometric wobble of enough stars to detect thousands of giant planets on wide orbits with periods between 1.5-9 years (de Bruijne, 2012). The *James Webb Space Telescope*, due to be launched in 2019, will also provide unparalleled direct imaging of giant planets on wide orbits, which as discussed in Chapter 5 for the example of HR8799, could detect planets at $\sim 0.5 M_J$ at separations of $\sim$100au.

With the success of Kepler, many future missions plan to detect planets via the transit method (see §1.5.2). CHEOPS is a space telescope due to be launched in 2019 aimed at measuring precise radii for planets closest to the Solar System that have mass estimates only (i.e. detected with RV measurements), allowing for the bulk compositions of these planets to be determined (Broeg et al., 2013). Similarly the TESS space telescope, which is due for launch in 2018, will survey around 500,000 of the brightest G, K, and M type stars in the sky looking for potential Earth sized transiting planets. This number of stars is approximately five times that observed by Kepler, with these stars being distributed over an area of sky roughly 400 times the size of the Kepler field (Ricker et al., 2014). Further in the future with an expected launch time in 2026, the PLATO space observatory will survey up to one million stars specifically looking for transiting Earth-like planets in the habitable zone around solar type stars (Ragazzoni et al., 2016).

Future ground based telescopes will also offer an exciting contribution to the field of exoplanets. Most notably, the *Extremely Large Telescope* should be able to directly image around 20 giant planets previously observed by the radial velocity method and it is even estimated that it will be able to detect $\sim$ 10 Earth-like planets in the habitable zone around the host star (Quanz et al., 2015). Detections of planets at these separations will be milestone for direct imaging. The vast majority of radial velocity detected planets are confirmed when used in conjunction with the transit method due to the observed small separations to the host star. Confirming radial velocity planets with direct imaging will allow for non-transiting planets and planets further from the host star to be confirmed. Moreover, estimates of the true mass of planets could be constrained using evolutionary models discussed in §1.5.3.

Coupling both current and future observations of planetary systems with dynamical theory will place powerful constraints on not only the types of planets present in a given

system, but also give an insight into the formation and evolution mechanisms that have led to a planetary systems observed architecture. Through this insight we will be able to understand the diversity of exoplanetary systems, allowing us to truly conclude just how unique the Solar System really is.

I leave the reader with one final note for this thesis: it is worth remembering that the field of exoplanets would be unrecognisable compared to 30 years ago. With upcoming telescope missions and the ever expanding understanding of dynamical evolution of planetary systems, it is likely that this will also be the case once the next 30 years has passed. I have thoroughly enjoyed being able to contribute to such an exciting and rapidly progressing field of Astronomy and look forward to the revelations it will reveal in upcoming years.

Appendices

A

Further discussion of Transit equations

A.1 Central Transit Line

The centre of the transit region is defined by eq. (4.2)

$$-\sin\Delta i \sin\vartheta \sin\varphi + \cos\Delta i \cos\vartheta = 0,$$

Assuming that $\varphi = 0 \rightarrow 2\pi$ and that a corresponding value of ϑ for each value of φ can be in the range of $0 < \vartheta < \pi$, eq. (4.2) can be rearranged to give

$$\begin{aligned} \vartheta &= \arctan\left(\frac{1}{\tan\Delta i \sin\varphi}\right) && \text{for } \varphi < \pi, \\ \vartheta &= \pi + \arctan\left(\frac{1}{\tan\Delta i \sin\varphi}\right) && \text{for } \varphi > \pi. \end{aligned} \tag{A.1}$$

A.2 Upper Transit Boundary

The upper boundary of a transit region is given by eq. (4.4)

$$-\sin\Delta i \sin\vartheta_2 \sin\varphi_2 + \cos\Delta i \cos\vartheta_2 = -\chi,$$

A value of ϑ_2 for a given φ_2 can be calculated through solving a quadratic of the form

$$\left(A^2 + B^2\right) x^2 + 2A\chi x + \chi^2 - B^2 = 0 \tag{A.2}$$

where

$$x = \sin\vartheta_2, \qquad A = -\sin\Delta i \sin\varphi_2, \qquad B = \cos\Delta i.$$

Depending on the value of Δi, the calculation of ϑ_2 for a given value of φ_2 can be grouped into three different regimes, (1) Δi is small enough that the upper boundary of the transit region never crosses the fixed reference plane. (2) Δi is large enough that the upper boundary of the transit region does cross the fixed reference plane. (3) For high values of Δi the upper transit boundary only has values of ϑ_2 for $0 < \varphi_2 < \pi$. This can be thought of as the transit region going over the pole of the celestial sphere.

For regime (1), the value of ϑ_2 for a given φ_2 is equivalent to that obtained from the positive root of eq. (A.2), mirrored about $\pi/2$. The transition to regime (2) occurs for when the upper transit boundary first crosses the fixed reference plane. Here $\Delta i = \arcsin(\chi)$. As Δi is increased beyond this value the intersection between the upper transit boundary and the fixed reference plane occurs at $\varphi_2 = \varphi_0$ and $\varphi_2 = \pi - \varphi_0$, for which $\vartheta_2 = \pi/2$. From eq. (4.4) φ_0 is given by $\varphi_0 = \arcsin(\chi/\sin\Delta i)$. Therefore $\vartheta_2 < \pi/2$ for $\varphi_0 < \varphi_2 < \pi - \varphi_0$ and $\vartheta_2 > \pi/2$ otherwise. When $\varphi_0 < \varphi_2 < \pi - \varphi_0$, ϑ_2 is hence obtained from the positive solution of eq. (A.2) and by the positive solution mirrored about $\pi/2$ otherwise.

Finally the transition to regime (3) occurs when $\Delta i = \arccos(\chi)$. Similarly to regime (2) as Δi is increased beyond this value, the upper transit boundary crosses the fixed reference plane at $\varphi_2 = \varphi_0$ and $\varphi_2 = \pi - \varphi_0$ and hence ϑ_2 is only defined for when $\varphi_0 < \varphi_2 < \pi - \varphi_0$. The solution from eq. (A.2) which gives the smaller value ϑ_2 corresponds to $\vartheta_2 > \pi/2$ values and needs to be mirrored about $\pi/2$, with the solution giving the larger value of ϑ_2 corresponding to $\vartheta_2 < \pi/2$ values.

To summarize consider that for a given value of φ_2, eq. (A.2) gives two solutions for ϑ_2, denoted as ϑ_2^{*1} and ϑ_2^{*2} respectively. For $\Delta i < \arcsin(\chi)$,

$$\vartheta_2 = \frac{\pi}{2} + \left(\frac{\pi}{2} - \vartheta_2^{*1}\right) \qquad \text{for } 0 < \varphi_2 < 2\pi, \tag{A.3}$$

where $\vartheta_2^{*1} > 0$ and $\vartheta_2^{*2} < 0$.

For $\arcsin(\chi) < \Delta i < \arccos(\chi)$,

$$\begin{aligned} \vartheta_2 &= \vartheta_2^{*1} && \text{for } \varphi_0 < \varphi_2 < \pi - \varphi_0, \\ \vartheta_2 &= \frac{\pi}{2} + \left(\frac{\pi}{2} - \vartheta_2^{*1}\right) && \text{otherwise,} \end{aligned} \tag{A.4}$$

where $\vartheta_2^{*1} > 0$, $\vartheta_2^{*2} < 0$ and $\varphi_0 = \arcsin(\chi/\sin\Delta i)$.

For $\Delta i > \arccos(\chi)$,

$$\begin{aligned} &\vartheta_2 = \max\left(\vartheta_2^{*1}, \vartheta_2^{*2}\right) \\ &\text{and} \qquad\qquad \text{for } \varphi_0 < \varphi_2 < \pi - \varphi_0 \\ &\vartheta_2 = \frac{\pi}{2} + \left(\frac{\pi}{2} - \min\left(\vartheta_2^{*1}, \vartheta_2^{*2}\right)\right), \end{aligned} \tag{A.5}$$

where $\vartheta_2^{*1} > 0$, $\vartheta_2^{*2} > 0$.

A.3 Lower Transit Boundary

The lower boundary of the transit region is given by eq. (4.3)

$$-\sin\Delta i \sin\vartheta_1 \sin\varphi_1 + \cos\Delta i \cos\vartheta_1 = \chi,$$

Depending on the value of Δi, the calculation ϑ_1 for a given φ_1 can be grouped into the same regimes as described for the upper transit boundary. However now in regime (1), $\vartheta_1 < \pi/2$ for $0 < \varphi_1 < 2\pi$, in regime (2) the lower transit boundary crosses the fixed reference plane at $\varphi_1 = \pi + \varphi_0$ and $\varphi_1 = 2\pi - \varphi_0$ and in regime (3) ϑ_1 is only defined for $\pi + \varphi_0 < \varphi_1 < 2\pi - \varphi_0$. Assuming that ϑ_1^{*1} and ϑ_1^{*2} are the solutions for ϑ_1 for a given φ_1 in the modified form of eq. (A.2), then following the same discussion as for the upper transit boundary it can be shown that for $\Delta i < \arcsin(\chi)$,

$$\vartheta_1 = \vartheta_1^{*1} \qquad\qquad \text{for } 0 < \varphi_1 < 2\pi, \tag{A.6}$$

where $\vartheta_1^{*1} > 0$ and $\vartheta_1^{*2} < 0$.

For $\arcsin(\chi) < \Delta i < \arccos(\chi)$,

$$\begin{aligned} &\vartheta_1 = \frac{\pi}{2} + \left(\frac{\pi}{2} - \vartheta_1^{*1}\right) \qquad \text{for } \varphi_0 + \pi < \varphi_1 < 2\pi - \varphi_0, \\ &\vartheta_1 = \vartheta_1^{*1} \qquad\qquad\qquad\qquad \text{otherwise,} \end{aligned} \tag{A.7}$$

where $\vartheta_1^{*1} > 0$, $\vartheta_1^{*2} < 0$ and $\varphi_0 = \arcsin(\chi/\sin\Delta i)$.

For $\Delta i > \arccos(\chi)$,

$$\begin{aligned} &\vartheta_1 = \min\left(\vartheta_1^{*1}, \vartheta_1^{*2}\right) \\ &\text{and} \qquad\qquad \text{for } \varphi_0 + \pi < \varphi_1 < 2\pi - \varphi_0 \\ &\vartheta_1 = \frac{\pi}{2} + \left(\frac{\pi}{2} - \max\left(\vartheta_1^{*1}, \vartheta_1^{*2}\right)\right), \end{aligned} \tag{A.8}$$

where $\vartheta_1^{*1} > 0$, $\vartheta_1^{*2} > 0$.

B

Secular Solution for Mutual Inclination Evolution

From eq. (3.1) the evolution of complex inclinations according to Laplace-Lagrange theory is given by

$$y_j(t) = \sum_{k=1}^{N} I_{jk} e^{i(f_k t + \gamma_k)}, \tag{B.1}$$

where I_{jk} are the eigenvectors of the matrix **B** from eq. (2.16) scaled to initial boundary conditions, f_i are the eigenfrequencies of **B** and γ_k are initial phase terms. If it is assumed that all the planets and the star are point masses and that the invariable plane is taken as a reference plane, it follows that $f_3 = 0$ and $I_{j3} = 0$. From the initial conditions $|y_1(0)| = |y_2(0)| = i_1$. Hence the complex inclinations of the inner two planets respectively are given by

$$y_1(t) = I_{11} \exp\left(i\left(f_1 t + \pi\right)\right) + I_{12} \exp\left(i\left(f_2 t\right)\right), \tag{B.2}$$

$$y_2(t) = I_{21} \exp\left(i\left(f_1 t + \pi\right)\right) + I_{22} \exp\left(i\left(f_2 t\right)\right). \tag{B.3}$$

Also from the initial conditions $-I_{11} + I_{12} = i_1$ and $-I_{21} + I_{22} = i_1$. The complex mutual inclination between the inner two planets is equivalent to

$$y_1(t) - y_2(t) = \left(I_{12} - I_{22}\right)\left[\exp(i(f_1 t + \pi)) + \exp(i f_2 t)\right]. \tag{B.4}$$

Solving eq. (3.1), we propose a set of variables to represent the full solution of I_{12} and I_{22},

$$\begin{aligned} K_{1m} &= \frac{B_{13}B_{32}}{f_m + B_{31} + B_{32}}, \\ K_{2m} &= \frac{B_{13}B_{31}}{f_m + B_{31} + B_{32}}, \\ K_{3m} &= f_m + B_{12} + B_{13}, \\ K_{4m} &= f_m + B_{31} + B_{32}, \end{aligned} \tag{B.5}$$

where m = 1, 2,

$$\begin{aligned} R_{1(3-m)} &= \frac{K_{3m} - K_{2m}}{B_{12} + K_{1m}}, \\ R_{2(3-m)} &= B_{31} + B_{32}R_{1(3-m)}, \end{aligned} \tag{B.6}$$

$$\varepsilon = R_{11} + \frac{R_{21}}{K_{42}}\left(R_{12} - 1\right) + \frac{R_{22}}{K_{41}}\left(1 - R_{11}\right) - R_{12}. \tag{B.7}$$

Hence the components of the eigenvector associated with the f_2 eigenfrequency are given by

$$\begin{aligned} I_{12} &= \frac{1}{\varepsilon}\left[\Delta i(1 - R_{12})\right], \\ I_{22} &= \frac{R_{11}}{\varepsilon}\left[\Delta i(1 - R_{12})\right]. \end{aligned} \tag{B.8}$$

The non zero f_1 and f_2 eigenfrequencies of the matrix **B** from eq. (2.16) can be obtained by solving a quadratic of the form

$$\begin{aligned} &f^2 + f(B_{12} + B_{13} + B_{21} + B_{23} + B_{31} + B_{32}) + \\ &[B_{12}\left(B_{23} + B_{31} + B_{32}\right) + B_{13}\left(B_{21} + B_{23} + B_{32}\right) \\ &+ B_{21}\left(B_{31} + B_{32}\right) + B_{23}B_{31}] = 0. \end{aligned} \tag{B.9}$$

We note that the solution given by eq. (B.8) recovers exactly what is predicted when solving eq. (3.1) by numerical methods. The full solution which describes how the mutual inclination between the inner two planets according to Laplace - Lagrange theory is therefore given by

$$y_1 - y_2 = \frac{\Delta i(1 - R_{12})(1 - R_{11})}{\varepsilon}\left[e^{i(f_1 t + \pi)} + e^{if_2 t}\right], \tag{B.10}$$

with the variable K used in §4.3.3 being equivalent to $(1 - R_{12})(1 - R_{11})/\varepsilon$.

C

Reproducing the total number of single transiting planets observed by Kepler

In §4.6 we considered Kepler systems with two transiting planets which are secularly interacting with an outer planet on an inclined orbit. We found that the number of single transiting systems Kepler would be expected to observe can be dramatically increased as a result of this interaction. Figure C.1 shows the total number of single transiting objects Kepler would be expected to observe from the method outlined in §4.6.4, for when the outer planet has the same parameters as the respective panels of Figure 4.13. Again for $\Delta i \gg 20^{\circ}$, Laplace-Lagrange theory is expected to break down and is included for completeness. The white line gives where the total number of single transiting planets Kepler would be expected to observe from the model population is equal to the number in the Kepler population i.e. 1951. The red dashed lines give an estimate for an RV detection threshold.

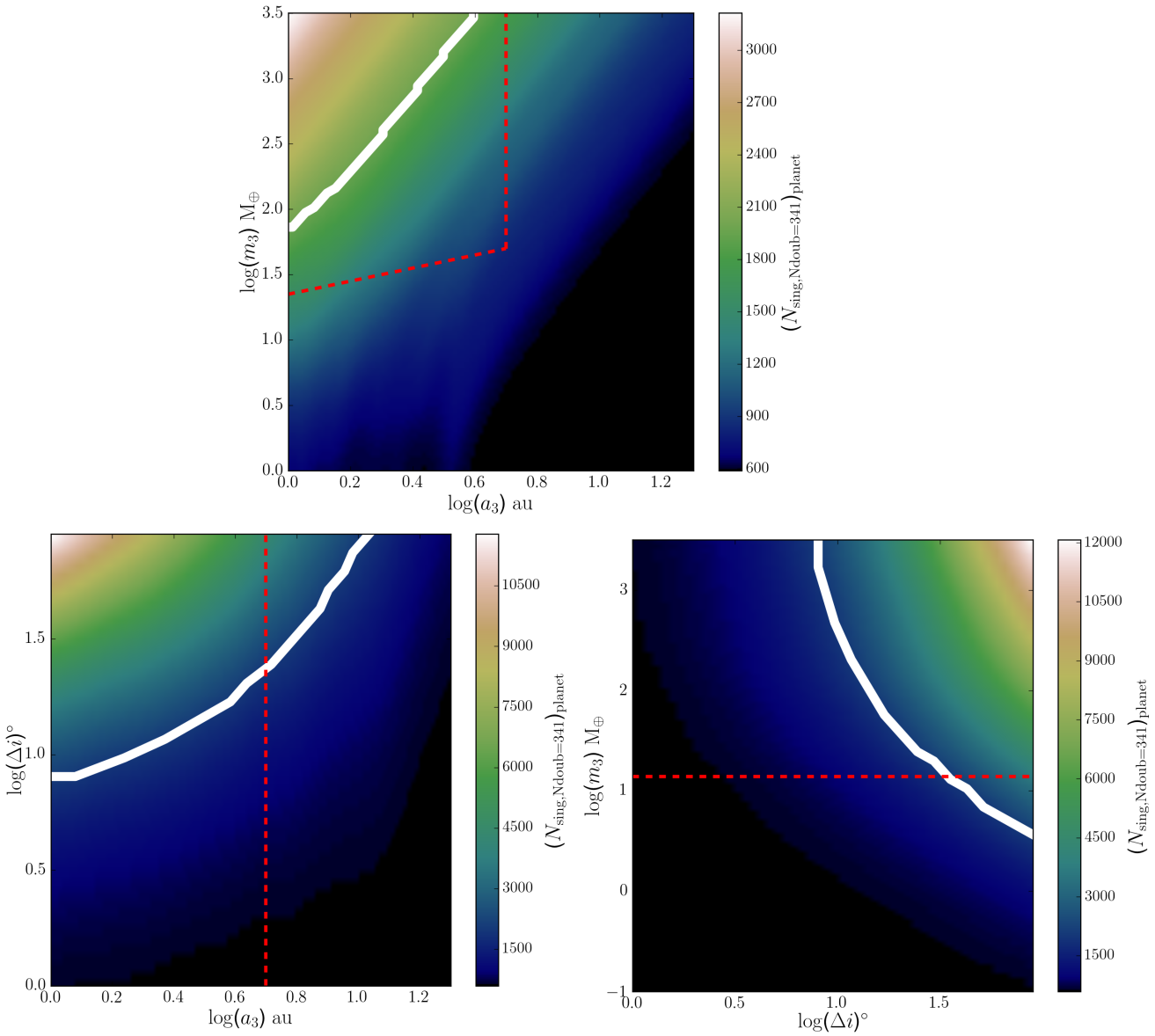

Figure C.1 The total number of single transiting planets Kepler would be expected to observe for given third planet parameters. The white line corresponds to the total number of single transiting systems currently observed by Kepler (1951). The red lines give an estimate for the detection threshold of RV surveys.

D

A younger age estimate for HR8799

Here we consider how an age estimate of HR8799 of 30Myr rather than 60Myr affects the results presented in §5.5.4. We initially show the semi-major axis vs. eccentricity distribution of particles interacting with the four known planets and an additional planet with a mass and semi-major axis of $0.1 M_J$ and 138au respectively in Figure D.1. We note that the simulated outer disk produced with this planet had an intensity profile that agreed most with the ALMA observed profile as described in §5.5.3. All lines and shaded regions are identical to those in Figure 5.2, with the semi-major axis of the fifth planet given by the black dashed line. Figure D.1 shows that few particles are scattered after 30Myr. Indeed, the intensity profile predicted after 30Myr (shown in Figure D.2, with all lines taking identical definitions to those described in Figure 5.6), is not significantly different from the profile produced after 60Myr (top left panel of Figure 5.6), highlighting that an assumed age of 30Myr rather than 60Myr for HR8799 does not significantly affect how well the intensity profile generated by this fifth planet agrees with the ALMA observed profile.

More generally, we also investigated how an assumed age of 30Myr rather than 60Myr affects the intensity profiles produced by all the fifth planets considered in this work. We repeat the method described in §5.5.3 to produce Figure 5.5, that is, calculating $\Delta\chi^2$ values for all fifth planets, which describes how well the simulated intensity profile agrees with the ALMA observed profile. However now we run simulations to 30Myr rather than 60Myr. Figure D.3 shows these $\Delta\chi^2$ values, with all contours and annotations being identical to those given in Figure 5.5 for reference. Comparing Figures 5.5 and D.3 it is clear that assuming an age of 30Myr rather than 60Myr has little effect on the types of fifth planets which produce intensity curves that strongly agree with the ALMA observed profile. We also note that the absolute χ^2 values change little between Figures 5.5 and D.3.

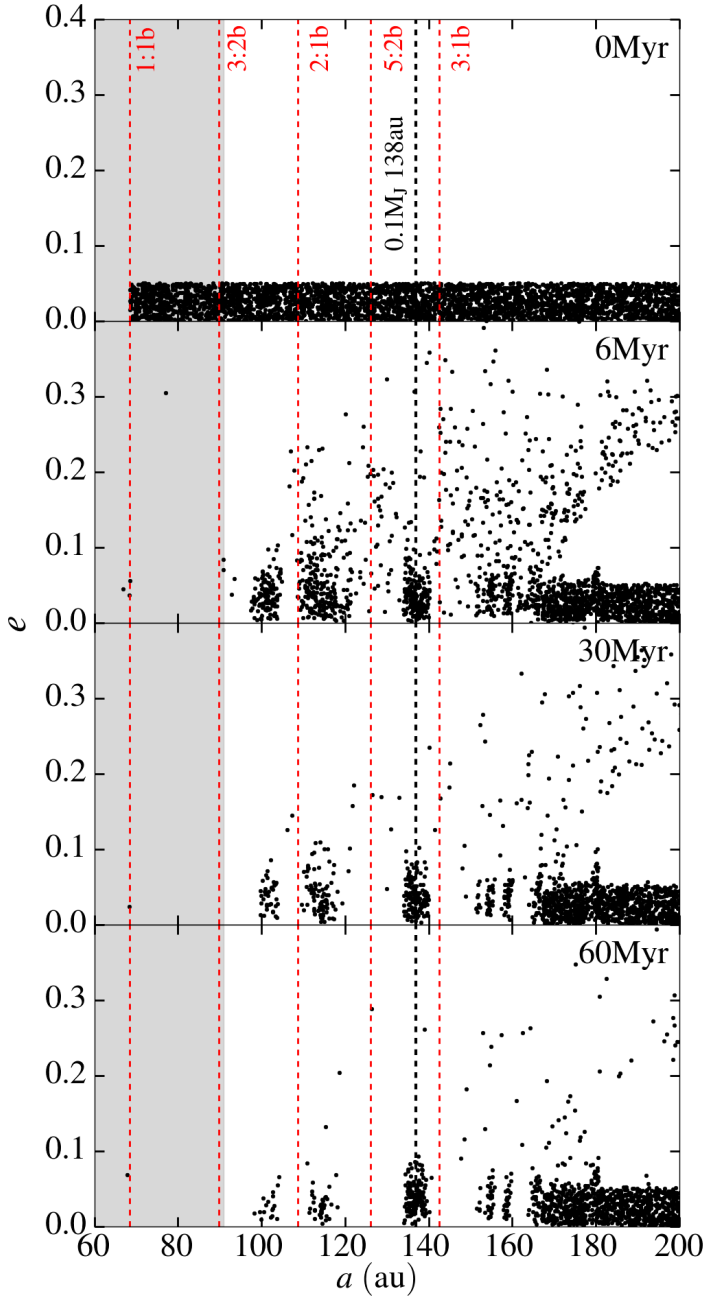

Figure D.1 Semi-major axis vs. eccentricity of particles evolving due to dynamical interactions with the four known planets and an additional fifth planet with a mass and semi-major axis of 0.1M$_J$ and 138au respectively. This fifth planet predicts an intensity profile which agrees most with the ALMA observed profile (see Figure 5.5). The red dashed lines refer to 1st order MMRs of HR8799b and the black dashed line refers to the semi-major axis of the fifth planet.

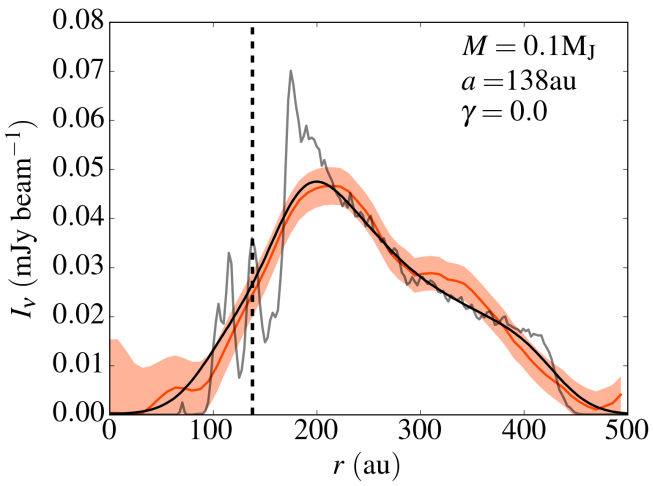

Figure D.2 Comparison of intensity profile generated by a fifth planet with a mass and semi-major axis of $0.1 M_J$ and 138au respectively after 30Myr, with and without convolving with the beam of ALMA (black and grey lines respectively), with the profile observed by ALMA (orange line). The orange shaded region gives the 1σ rms of the noise per beam. The semi-major axis of the fifth planet is given by the dashed vertical line. The value of $\gamma = 0$ refers to an initial scaling of the surface density of particles of $\Sigma(r) \propto r^{-1}$.

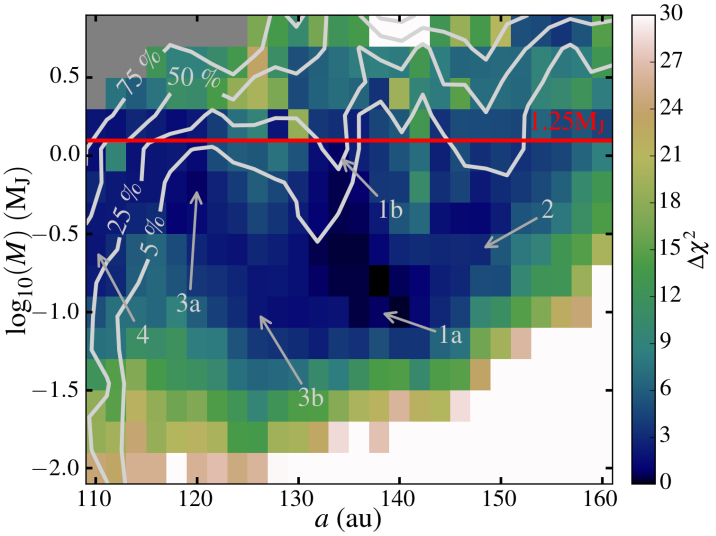

Figure D.3 Identical plot to Figure 5.5, however here simulations are run to 30Myr rather than 60Myr. Annotations and contours are identical to those shown in Figure 5.5 for reference. Running simulations to 30Myr rather than 60Myr has little effect on the types of fifth planets which predict intensity profiles that well fit the profile observed by ALMA.

Bibliography

Agnor C. B., Lin D. N. C., 2012, ApJ, 745, 143

Agol E., Fabrycky D., 2017, preprint, (arXiv:1706.09849)

Agol E., Steffen J., Sari R., Clarkson W., 2005, MNRAS, 359, 567

Allard F., Hauschildt P. H., Alexander D. R., Tamanai A., Schweitzer A., 2001, ApJ, 556, 357

Almenara J. M., Díaz R. F., Bonfils X., Udry S., 2016, A&A, 595, L5

Anglada-Escudé G., et al., 2012, ApJL, 751, L16

Bai X.-N., Stone J. M., 2010, ApJ, 722, 1437

Bailey J., Butler R. P., Tinney C. G., Jones H. R. A., O'Toole S., Carter B. D., Marcy G. W., 2009, ApJ, 690, 743

Baines E. K., et al., 2012, ApJ, 761, 57

Ballard S., Johnson J. A., 2016, ApJ, 816, 66

Baraffe I., Chabrier G., Barman T. S., Allard F., Hauschildt P. H., 2003, A&A, 402, 701

Batalha N. M., et al., 2013, ApJS, 204, 24

Becker J. C., Adams F. C., 2016, MNRAS, 455, 2980

Becker J. C., Vanderburg A., Adams F. C., Rappaport S. A., Schwengeler H. M., 2015, ApJL, 812, L18

Beichman C. A., et al., 2010, PASP, 122, 162

Bell C. P. M., Mamajek E. E., Naylor T., 2016, in Kastner J. H., Stelzer B., Metchev S. A., eds, IAU Symposium Vol. 314, Young Stars and Planets Near the Sun. pp 41–48 (arXiv:1508.00898), doi:10.1017/S1743921315006213

Beuzit J.-L., et al., 2008, in Ground-based and Airborne Instrumentation for Astronomy II. p. 701418, doi:10.1117/12.790120

Boley A. C., Morris M. A., Ford E. B., 2014, ApJL, 792, L27

Bonfils X., et al., 2007, A&A, 474, 293

Bonsor A., Wyatt M. C., 2012, MNRAS, 420, 2990

Bonsor A., Augereau J.-C., Thébault P., 2012, A&A, 548, A104

Booth M., et al., 2016, MNRAS, 460, L10

Borucki W. J., Summers A. L., 1984, Icarus, 58, 121

Borucki W. J., et al., 2011, ApJ, 728, 117

Bowler B. P., 2016, PASP, 128, 102001

Boyajian T. S., et al., 2013, ApJ, 771, 40

Brakensiek J., Ragozzine D., 2016, ApJ, 821, 47
Broeg C., et al., 2013, in European Physical Journal Web of Conferences. p. 03005 (arXiv:1305.2270), doi:10.1051/epjconf/20134703005
Bryan M. L., et al., 2016, ApJ, 821, 89
Butler R. P., Marcy G. W., Fischer D. A., Brown T. M., Contos A. R., Korzennik S. G., Nisenson P., Noyes R. W., 1999, ApJ, 526, 916
Butler R. P., et al., 2006, ApJ, 646, 505
Campanella G., Nelson R. P., Agnor C. B., 2013, MNRAS, 433, 3190
Campbell N. A., Atchley R. W., 1981, The geometry of canonical variate analysis, Systematic Zoology Vol. 30, No. 3 (Sp., 1981), pp. 268-280
Campbell B., Walker G. A. H., Yang S., 1988, ApJ, 331, 902
Carbillet M., et al., 2011, Experimental Astronomy, 30, 39
Casagrande L., Schönrich R., Asplund M., Cassisi S., Ramírez I., Meléndez J., Bensby T., Feltzing S., 2011, A&A, 530, A138
Casertano S., et al., 2008, A&A, 482, 699
Cenarro A. J., et al., 2007, MNRAS, 374, 664
Chambers J. E., 1999, MNRAS, 304, 793
Chauvin G., et al., 2017, A&A, 605, L9
Chen J., Kipping D., 2017, ApJ, 834, 17
Chen C. H., et al., 2006, ApJS, 166, 351
Christiansen J. L., et al., 2015, ApJ, 810, 95
Christou A. A., Murray C. D., 1999, MNRAS, 303, 806
Ciceri S., Lillo-Box J., Southworth J., Mancini L., Henning T., Barrado D., 2015, A&A, 573, L5
Claudi R. U., et al., 2006, in Society of Photo-Optical Instrumentation Engineers (SPIE) Conference Series. p. 62692Y (arXiv:astro-ph/0606597), doi:10.1117/12.671949
Coughlin J. L., et al., 2014, AJ, 147, 119
Coughlin J. L., et al., 2016, ApJS, 224, 12
Crossfield I. J. M., et al., 2017, preprint, (arXiv:1701.03811)
Cumming A., Butler R. P., Marcy G. W., Vogt S. S., Wright J. T., Fischer D. A., 2008, PASP, 120, 531
Currie T., et al., 2011, ApJ, 729, 128
Currie T., Fukagawa M., Thalmann C., Matsumura S., Plavchan P., 2012, ApJL, 755, L34
Dawson R. I., Chiang E., 2014, Science, 346, 212
DeMeo F. E., Carry B., 2013, Icarus, 226, 723
Decin G., Dominik C., Waters L. B. F. M., Waelkens C., 2003, ApJ, 598, 636
Delfosse X., Forveille T., Ségransan D., Beuzit J.-L., Udry S., Perrier C., Mayor M., 2000,

A&A, 364, 217
Delfosse X., et al., 2013, A&A, 553, A8
Désert J.-M., et al., 2015, ApJ, 804, 59
Dick S. J., 1996, The biological universe: the twentieth-century extraterrestrial life debate and the limits of science
Dohlen K., et al., 2008, in Ground-based and Airborne Instrumentation for Astronomy II. p. 70143L, doi:10.1117/12.789786
Dong R., Fung J., 2017, ApJ, 835, 146
Dressing C. D., Charbonneau D., 2015, ApJ, 807, 45
Drimmel R., Spergel D. N., 2001, ApJ, 556, 181
Duncan M., Quinn T., Tremaine S., 1989, Icarus, 82, 402
ESA ed. 1997, The HIPPARCOS and TYCHO catalogues. Astrometric and photometric star catalogues derived from the ESA HIPPARCOS Space Astrometry Mission ESA Special Publication Vol. 1200
Eddington A., 1928, The Nature of the Physical World. New York: Macmillan
Ellis K. M., Murray C. D., 2000, Icarus, 147, 129
Esposito S., et al., 2013, A&A, 549, A52
Fabrycky D. C., Murray-Clay R. A., 2010, ApJ, 710, 1408
Fabrycky D. C., et al., 2014, ApJ, 790, 146
Fang J., Margot J.-L., 2012, ApJ, 761, 92
Faramaz V., et al., 2014, A&A, 563, A72
Feng F., Tuomi M., Jones H. R. A., 2017, A&A, 605, A103
Figueira P., et al., 2012, A&A, 541, A139
Fogg M. J., Nelson R. P., 2009, A&A, 498, 575
Ford E. B., Rasio F. A., 2008, ApJ, 686, 621
Fragner M. M., Nelson R. P., 2010, A&A, 511, A77
Fressin F., et al., 2013, ApJ, 766, 81
Freudling W., Romaniello M., Bramich D. M., Ballester P., Forchi V., García-Dabló C. E., Moehler S., Neeser M. J., 2013, A&A, 559, A96
Fung J., Shi J.-M., Chiang E., 2014, ApJ, 782, 88
Gagné J., Lafrenière D., Doyon R., Malo L., Artigau É., 2014, ApJ, 783, 121
Gaia Collaboration et al., 2016, A&A, 595, A2
Gilliland R. L., et al., 2013, ApJ, 766, 40
Gillon M., et al., 2017, Nature, 542, 456
Gladman B., Kavelaars J. J., Petit J.-M., Morbidelli A., Holman M. J., Loredo T., 2001, AJ, 122, 1051
Gomez Gonzalez C. A., et al., 2017, AJ, 154, 7

Gonzalez G., 1996, ArXiv Astrophysics e-prints,
Götberg Y., Davies M. B., Mustill A. J., Johansen A., Church R. P., 2016, A&A, 592, A147
Goździewski K., Migaszewski C., 2009, MNRAS, 397, L16
Goździewski K., Migaszewski C., 2014, MNRAS, 440, 3140
Gray R. O., Corbally C. J., 2002, AJ, 124, 989
Gray R. O., Kaye A. B., 1999, AJ, 118, 2993
Gray R. O., Corbally C. J., Garrison R. F., McFadden M. T., Robinson P. E., 2003, AJ, 126, 2048
Guerri G., et al., 2011, Experimental Astronomy, 30, 59
Habets G. M. H. J., Heintze J. R. W., 1981, A&AS, 46, 193
Hadden S., Lithwick Y., 2014, ApJ, 787, 80
Haghighipour N., 2013, Annual Review of Earth and Planetary Sciences, 41, 469
Hamers A. S., Perets H. B., Portegies Zwart S. F., 2015a, preprint, (arXiv:1506.02039)
Hamers A. S., Perets H. B., Antonini F., Portegies Zwart S. F., 2015b, MNRAS, 449, 4221
Handler G., 1999, MNRAS, 309, L19
Hansen B. M. S., 2017, MNRAS, 467, 1531
Hatzes A. P., Cochran W. D., Endl M., McArthur B., Paulson D. B., Walker G. A. H., Campbell B., Yang S., 2003, ApJ, 599, 1383
Hayashi C., 1961, PASJ, 13
Hayashi C., Hoshi R., 1961, PASJ, 13, 442
Helled R., et al., 2014, Protostars and Planets VI, pp 643–665
Hinkley S., 2012, in Richards M. T., Hubeny I., eds, IAU Symposium Vol. 282, From Interacting Binaries to Exoplanets: Essential Modeling Tools. pp 181–188 (arXiv:1112.1765), doi:10.1017/S1743921311027293
Hinkley S., et al., 2011a, PASP, 123, 74
Hinkley S., Carpenter J. M., Ireland M. J., Kraus A. L., 2011b, ApJL, 730, L21
Hinz P. M., Rodigas T. J., Kenworthy M. A., Sivanandam S., Heinze A. N., Mamajek E. E., Meyer M. R., 2010, ApJ, 716, 417
Holczer T., et al., 2016, ApJS, 225, 9
Huang C. X., Petrovich C., Deibert E., 2016, preprint, (arXiv:1609.08110)
Huber D., et al., 2013, ApJ, 767, 127
Hughes A. M., Wilner D. J., Andrews S. M., Williams J. P., Su K. Y. L., Murray-Clay R. A., Qi C., 2011, ApJ, 740, 38
Ida S., Bryden G., Lin D. N. C., Tanaka H., 2000, ApJ, 534, 428
Izidoro A., Raymond S. N., Morbidelli A., Hersant F., Pierens A., 2015, ApJL, 800, L22
Jeans J. H., 1919, Problems of cosmogony and stellar dynamics
Johansen A., Youdin A., Mac Low M.-M., 2009, ApJL, 704, L75
Johansen A., Davies M. B., Church R. P., Holmelin V., 2012, ApJ, 758, 39

Johansen A., Blum J., Tanaka H., Ormel C., Bizzarro M., Rickman H., 2014, Protostars and Planets VI, pp 547–570
Johnson J. A., et al., 2010, PASP, 122, 149
Jurić M., Tremaine S., 2008, ApJ, 686, 603
Kane S. R., 2015, ApJL, 814, L9
Kane S. R., Ciardi D. R., Gelino D. M., von Braun K., 2012, MNRAS, 425, 757
Kane S. R., et al., 2016, ApJL, 820, L5
Kasting J. F., Catling D., 2003, ARA&A, 41, 429
Kaye A. B., Handler G., Krisciunas K., Poretti E., Zerbi F. M., 1999, PASP, 111, 840
Kennedy G. M., Kenyon S. J., 2008, ApJ, 673, 502
Kennedy G. M., Kenyon S. J., Bromley B. C., 2006, ApJL, 650, L139
Kennedy G. M., et al., 2015, MNRAS, 449, 3121
Kirsh D. R., Duncan M., Brasser R., Levison H. F., 2009, Icarus, 199, 197
Konopacky Q. M., Marois C., Macintosh B. A., Galicher R., Barman T. S., Metchev S. A., Zuckerman B., 2016, AJ, 152, 28
Kozai Y., 1962, AJ, 67, 579
Krisciunas K., Crowe R. A., Luedeke K. D., Roberts M., 1995, MNRAS, 277, 1404
Krist J. E., Stapelfeldt K. R., Bryden G., Plavchan P., 2012, AJ, 144, 45
Lagrange A.-M., et al., 2009, A&A, 506, 927
Lai D., Pu B., 2017, AJ, 153, 42
Laskar J., 1997, A&A, 317, L75
Lawler S. M., et al., 2009, ApJ, 705, 89
Leggett S. K., 1992, ApJS, 82, 351
Lestrade J.-F., et al., 2012, A&A, 548, A86
Li G., Naoz S., Valsecchi F., Johnson J. A., Rasio F. A., 2014, ApJ, 794, 131
Lidov M. L., 1962, Planet. Space Sci., 9, 719
Lillo-Box J., et al., 2014, A&A, 562, A109
Lin D. N. C., Ida S., 1997, ApJ, 477, 781
Lissauer J. J., 1993, ARA&A, 31, 129
Lissauer J. J., et al., 2011, ApJS, 197, 8
Lissauer J. J., et al., 2014, ApJ, 784, 44
Lithwick Y., Wu Y., 2011, ApJ, 739, 31
Lopez E. D., Rice K., 2016, preprint, (arXiv:1610.09390)
Macintosh B., et al., 2014, Proceedings of the National Academy of Science, 111, 12661
Maire A.-L., et al., 2015, A&A, 576, A133
Maldonado J., et al., 2015, A&A, 577, A132
Malhotra R., Fox K., Murray C. D., Nicholson P. D., 1989, A&A, 221, 348

Malik M., Meru F., Mayer L., Meyer M., 2015, ApJ, 802, 56
Malmberg D., Davies M. B., Heggie D. C., 2011, MNRAS, 411, 859
Marcy G., Butler R. P., Fischer D., Vogt S., Wright J. T., Tinney C. G., Jones H. R. A., 2005, Progress of Theoretical Physics Supplement, 158, 24
Marcy G. W., et al., 2014, ApJS, 210, 20
Marino S., Perez S., Casassus S., 2015, ApJL, 798, L44
Marino S., et al., 2016, MNRAS, 460, 2933
Marmier M., et al., 2013, A&A, 551, A90
Marois C., Lafrenière D., Doyon R., Macintosh B., Nadeau D., 2006, ApJ, 641, 556
Marois C., Macintosh B., Barman T., Zuckerman B., Song I., Patience J., Lafrenière D., Doyon R., 2008, Science, 322, 1348
Marois C., Zuckerman B., Konopacky Q. M., Macintosh B., Barman T., 2010, Nature, 468, 1080
Marshall J. P., Booth M., Holland W., Matthews B. C., Greaves J. S., Zuckerman B., 2016, MNRAS, 459, 2893
Martin D. V., Mazeh T., Fabrycky D. C., 2015, MNRAS, 453, 3554
Matsuo T., Shibai H., Ootsubo T., Tamura M., 2007, ApJ, 662, 1282
Matthews B., Kennedy G., Sibthorpe B., Booth M., Wyatt M., Broekhoven-Fiene H., Macintosh B., Marois C., 2014, ApJ, 780, 97
Mayor M., Queloz D., 1995, Nature, 378, 355
Mayor M., et al., 2003, The Messenger, 114, 20
Mayor M., et al., 2011, preprint, (arXiv:1109.2497)
Minton D. A., Malhotra R., 2009, Nature, 457, 1109
Morbidelli A., Raymond S. N., 2016, Journal of Geophysical Research (Planets), 121, 1962
Morbidelli A., Lunine J. I., O'Brien D. P., Raymond S. N., Walsh K. J., 2012, Annual Review of Earth and Planetary Sciences, 40, 251
Moro-Martín A., Rieke G. H., Su K. Y. L., 2010, ApJL, 721, L199
Morrison S., Malhotra R., 2015, ApJ, 799, 41
Morton T. D., 2012, ApJ, 761, 6
Morton T. D., Johnson J. A., 2011, ApJ, 738, 170
Morton T. D., Bryson S. T., Coughlin J. L., Rowe J. F., Ravichandran G., Petigura E. A., Haas M. R., Batalha N. M., 2016, ApJ, 822, 86
Moya A., Amado P. J., Barrado D., García Hernández A., Aberasturi M., Montesinos B., Aceituno F., 2010a, MNRAS, 405, L81
Moya A., Amado P. J., Barrado D., Hernández A. G., Aberasturi M., Montesinos B., Aceituno F., 2010b, MNRAS, 406, 566
Muñoz D. J., Lai D., 2015, Proceedings of the National Academy of Science, 112, 9264

Murray C. D., Dermott S. F., 1999, Solar system dynamics
Mustill A. J., Wyatt M. C., 2012, MNRAS, 419, 3074
Mustill A. J., Davies M. B., Johansen A., 2015, ApJ, 808, 14
Mustill A. J., Davies M. B., Johansen A., 2016, preprint, (arXiv:1609.08058)
Nelson B. E., Ford E. B., Rasio F. A., 2017, AJ, 154, 106
Nesvorný D., Morbidelli A., 1998, AJ, 116, 3029
Otor O. J., et al., 2016, AJ, 152, 165
Ozernoy L. M., Gorkavyi N. N., Taidakova T., 2000, Planet. Space Sci., 48, 993
Papaloizou J. C. B., Terquem C., 2006, Reports on Progress in Physics, 69, 119
Patience J., et al., 2011, A&A, 531, L17
Pearce T. D., Wyatt M. C., 2014, MNRAS, 443, 2541
Pearce T. D., Wyatt M. C., 2015, MNRAS, 453, 3329
Pepe F., et al., 2011, A&A, 534, A58
Pepper J., et al., 2016, preprint, (arXiv:1607.01755)
Perryman M. A. C., et al., 1997, A&A, 323, L49
Perryman M. A. C., et al., 2001, A&A, 369, 339
Perryman M., Hartman J., Bakos G. Á., Lindegren L., 2014, ApJ, 797, 14
Petigura E. A., 2015, PhD thesis, University of California, Berkeley
Petigura E. A., Howard A. W., Marcy G. W., 2013, Proceedings of the National Academy of Science, 110, 19273
Pu B., Wu Y., 2015, ApJ, 807, 44
Pueyo L., et al., 2015, ApJ, 803, 31
Quanz S. P., Crossfield I., Meyer M. R., Schmalzl E., Held J., 2015, International Journal of Astrobiology, 14, 279
Quinn S. N., et al., 2015, ApJ, 803, 49
Rafikov R. R., 2005, ApJL, 621, L69
Rafikov R. R., 2011, ApJ, 727, 86
Rafikov R. R., 2013, ApJL, 764, L16
Rafikov R. R., 2014, ApJ, 794, 76
Rafikov R. R., Silsbee K., 2015a, ApJ, 798, 69
Rafikov R. R., Silsbee K., 2015b, ApJ, 798, 70
Ragazzoni R., et al., 2016, in Space Telescopes and Instrumentation 2016: Optical, Infrared, and Millimeter Wave. p. 990428, doi:10.1117/12.2236094
Ragozzine D., Holman M. J., 2010, preprint, (arXiv:1006.3727)
Rasio F. A., Ford E. B., 1996, Science, 274, 954
Raymond S. N., Izidoro A., 2017, Science Advances, 3, e1701138
Raymond S. N., Barnes R., Armitage P. J., Gorelick N., 2008, ApJL, 687, L107

Raymond S. N., Armitage P. J., Gorelick N., 2009, ApJL, 699, L88
Raymond S. N., Kokubo E., Morbidelli A., Morishima R., Walsh K. J., 2014, Protostars and Planets VI, pp 595–618
Read M. J., Wyatt M. C., 2016, MNRAS, 457, 465
Read M. J., Wyatt M. C., Triaud A. H. M. J., 2017, MNRAS, 469, 171
Read M. J., Wyatt M. C., Marino S., Kennedy G. M., 2018, MNRAS, 475, 4953
Reidemeister M., Krivov A. V., Schmidt T. O. B., Fiedler S., Müller S., Löhne T., Neuhäuser R., 2009, A&A, 503, 247
Rein H., 2012, MNRAS, 427, L21
Rein H., Liu S.-F., 2012, A&A, 537, A128
Rein H., Spiegel D. S., 2015, MNRAS, 446, 1424
Rein H., Tamayo D., 2015, MNRAS, 452, 376
Rhee J. H., Song I., Zuckerman B., McElwain M., 2007, ApJ, 660, 1556
Ricker G. R., et al., 2014, in Space Telescopes and Instrumentation 2014: Optical, Infrared, and Millimeter Wave. p. 914320 (arXiv:1406.0151), doi:10.1117/12.2063489
Rieke G. H., et al., 2005, ApJ, 620, 1010
Robin A. C., Reylé C., Derrière S., Picaud S., 2003, A&A, 409, 523
Rodriguez D. R., Zuckerman B., Kastner J. H., Bessell M. S., Faherty J. K., Murphy S. J., 2013, ApJ, 774, 101
Rodriguez J. E., et al., 2017, preprint, (arXiv:1701.03807)
Rogers L. A., 2015, ApJ, 801, 41
Roig F., Nesvorný D., Ferraz-Mello S., 2002, MNRAS, 335, 417
Rowan D., et al., 2016, ApJ, 817, 104
Rowe J. F., Thompson S. E., 2015, preprint, (arXiv:1504.00707)
Rowe J. F., et al., 2014, ApJ, 784, 45
Sahlmann J., Triaud A. H. M. J., Martin D. V., 2015, MNRAS, 447, 287
Santerne A., et al., 2016, A&A, 587, A64
Sanz-Forcada J., Ribas I., Micela G., Pollock A. M. T., García-Álvarez D., Solano E., Eiroa C., 2010, A&A, 511, L8
Schlaufman K. C., 2014, ApJ, 790, 91
Schneider J., Dedieu C., Le Sidaner P., Savalle R., Zolotukhin I., 2011, A&A, 532, A79
Seader S., et al., 2015, ApJS, 217, 18
Shannon A., Bonsor A., Kral Q., Matthews E., 2016, MNRAS, 462, L116
Smith R., Churcher L. J., Wyatt M. C., Moerchen M. M., Telesco C. M., 2009, A&A, 493, 299
Soderblom D. R., 2010, ARA&A, 48, 581
Soummer R., Brendan Hagan J., Pueyo L., Thormann A., Rajan A., Marois C., 2011, ApJ, 741, 55

Soummer R., Pueyo L., Larkin J., 2012, ApJL, 755, L28
Sousa S. G., et al., 2008, A&A, 487, 373
Sousa S. G., Fernandes J., Israelian G., Santos N. C., 2010, A&A, 512, L5
Sozzetti A., Giacobbe P., Lattanzi M. G., Micela G., Morbidelli R., Tinetti G., 2014, MNRAS, 437, 497
Spangler C., Sargent A. I., Silverstone M. D., Becklin E. E., Zuckerman B., 2001, ApJ, 555, 932
Steffen J. H., Coughlin J. L., 2016, Proceedings of the National Academy of Science, 113, 12023
Steffen J. H., et al., 2012a, Proceedings of the National Academy of Science, 109, 7982
Steffen J. H., et al., 2012b, ApJ, 756, 186
Steffen J. H., et al., 2013, MNRAS, 428, 1077
Su K. Y. L., et al., 2009, ApJ, 705, 314
Su K. Y. L., Morrison S., Malhotra R., Smith P. S., Balog Z., Rieke G. H., 2015, ApJ, 799, 146
Sudol J. J., Haghighipour N., 2012, ApJ, 755, 38
Takeda G., Ford E. B., Sills A., Rasio F. A., Fischer D. A., Valenti J. A., 2007, ApJS, 168, 297
Terquem C., Papaloizou J. C. B., 2007, ApJ, 654, 1110
Thomas P. C., Parker J. W., McFadden L. A., Russell C. T., Stern S. A., Sykes M. V., Young E. F., 2005, Nature, 437, 224
Thorngren D. P., Fortney J. J., Murray-Clay R. A., Lopez E. D., 2016, ApJ, 831, 64
Torres C. A. O., Quast G. R., Melo C. H. F., Sterzik M. F., 2008, Young Nearby Loose Associations. p. 757
Tremaine S., Dong S., 2012, AJ, 143, 94
Trifonov T., et al., 2018, A&A, 609, A117
Valenti J. A., Fischer D. A., 2005, ApJS, 159, 141
Van Eylen V., Albrecht S., 2015, ApJ, 808, 126
Venn K. A., Lambert D. L., 1990, ApJ, 363, 234
Veras D., Armitage P. J., 2007, ApJ, 661, 1311
Veras D., Crepp J. R., Ford E. B., 2010, in Gożdziewski K., Niedzielski A., Schneider J., eds, EAS Publications Series Vol. 42, EAS Publications Series. pp 419–426, doi:10.1051/eas/1042045
Vican L., 2012, AJ, 143, 135
Vigan A., Moutou C., Langlois M., Allard F., Boccaletti A., Carbillet M., Mouillet D., Smith I., 2010, MNRAS, 407, 71
Vigan A., Gry C., Salter G., Mesa D., Homeier D., Moutou C., Allard F., 2015, MNRAS, 454, 129
Vigan A., et al., 2016, A&A, 587, A55

Vogt S. S., et al., 2010a, ApJ, 708, 1366
Vogt S. S., Butler R. P., Rivera E. J., Haghighipour N., Henry G. W., Williamson M. H., 2010b, ApJ, 723, 954
Weidenschilling S. J., 1977, MNRAS, 180, 57
Weiss L. M., Marcy G. W., 2014, ApJL, 783, L6
Weiss L. M., et al., 2016, ApJ, 819, 83
Williams J. P., Cieza L. A., 2011, ARA&A, 49, 67
Wilner D. J., MacGregor M. A., Andrews S. M., Hughes A. M., Matthews B., Su K., 2018, preprint, (arXiv:1803.00054)
Winn J. N., 2010, Exoplanet Transits and Occultations. University of Arizona Press, pp 55–77
Winn J. N., et al., 2009, ApJ, 700, 302
Wisdom J., 1980, AJ, 85, 1122
Wittenmyer R. A., Endl M., Cochran W. D., Levison H. F., Henry G. W., 2009, ApJS, 182, 97
Wittenmyer R. A., et al., 2014, ApJ, 791, 114
Wittenmyer R. A., et al., 2016, ApJ, 819, 28
Wolfgang A., Rogers L. A., Ford E. B., 2016, ApJ, 825, 19
Wolszczan A., Frail D. A., 1992, Nature, 355, 145
Wright J. T., Upadhyay S., Marcy G. W., Fischer D. A., Ford E. B., Johnson J. A., 2009, ApJ, 693, 1084
Wright N. J., Drake J. J., Mamajek E. E., Henry G. W., 2011, ApJ, 743, 48
Wright J. T., Marcy G. W., Howard A. W., Johnson J. A., Morton T. D., Fischer D. A., 2012, ApJ, 753, 160
Wuchterl G., Guillot T., Lissauer J. J., 2000, Protostars and Planets IV, p. 1081
Wyatt M. C., 2008, ARA&A, 46, 339
Wyatt M. C., Jackson A. P., 2016, Space Sci. Rev, 205, 231
Wyatt M. C., Smith R., Greaves J. S., Beichman C. A., Bryden G., Lisse C. M., 2007a, ApJ, 658, 569
Wyatt M. C., Smith R., Su K. Y. L., Rieke G. H., Greaves J. S., Beichman C. A., Bryden G., 2007b, ApJ, 663, 365
Wyatt M. C., et al., 2012, MNRAS, 424, 1206
Wyatt M. C., Bonsor A., Jackson A. P., Marino S., Shannon A., 2017, MNRAS, 464, 3385
Youdin A. N., 2011, ApJ, 742, 38
Youdin A. N., Goodman J., 2005, ApJ, 620, 459
Yu Q., Tremaine S., 2001, AJ, 121, 1736
Zakamska N. L., Tremaine S., 2004, AJ, 128, 869
Zechmeister M., Kürster M., Endl M., 2009, A&A, 505, 859

Zhu W., Wang J., Huang C., 2016, ApJ, 832, 196
Zhu W., Petrovich C., Wu Y., Dong S., Xie J., 2018, preprint, (arXiv:1802.09526)
Zuckerman B., 2001, ARA&A, 39, 549
Zuckerman B., Rhee J. H., Song I., Bessell M. S., 2011, ApJ, 732, 61
Zurlo A., et al., 2016, A&A, 587, A57
de Bruijne J. H. J., 2012, Ap&SS, 341, 31
van Leeuwen F., 2007, A&A, 474, 653